ALMA MATER STUDIORUM
UNIVERSITÀ DI BOLOGNA

DOTTORATO DI RICERCA IN
ASTROFISICA

Ciclo XXXV

Tesi di Dottorato

A HYDRODYNAMICAL VIEW ON THE MASS ACCRETION ONTO MASSIVE HALOS

Presentata da: **Matteo Angelinelli**

Coordinatore Dottorato:
Chiar.mo Prof. **Andrea Miglio**

Supervisore:
Prof. **Franco Vazza**

Co-supervisore:
Dr. **Stefano Ettori**

Esame finale Anno 2023

Settore Concorsuale: 02/C1 – Astronomia, Astrofisica, Fisica della Terra e dei Pianeti
Settore Scientifico Disciplinare: FIS/05 – Astronomia e Astrofisica

[...] Ma questa è la parte divertente del destino, le cose succedono che tu le abbia pianificate oppure no. Voglio dire, non pensavo l'avrei rivista di nuovo, ma in quel momento ero troppo vicino al puzzle per vedere la figura che si stava formando. [...]

Theodore Evelin Mosby

Di solito si fa alla fine, ma mi piace l'idea di iniziare ringraziando chi ha reso possibile questa tesi, o meglio questa esperienza chiamata Dottorato.
Iniziamo da coloro senza i quali tutto questo lavoro non sarebbe stato possibile: Dr. Stefano Ettori e Prof. Franco Vazza. A loro va tutta la mia riconoscenza per aver reso questi 3 anni un'esperienza formativa, sia personalmente che professionalmente. Nonostante la particolarità (e speriamo unicità!) del periodo in cui ho svolto il mio dottorato, mi hanno permesso di fare tante esperienze diverse e conoscere tanti colleghi. Grazie per la pazienza che avete avuto con me, la passione che mi avete trasmesso e tutto ciò che mi avete insegnato (prometto che continuo i corsi di inglese, prima o poi la smetterò di fare strafalcioni!).
Continuiamo con i miei genitori e tutta la mia famiglia, sostegno continuo di tutti questi anni, dal primo giorno di asilo all'ultimo giorno di dottorato e che sicuramente mi supporteranno anche nel tempo a venire. Grazie perché senza il vostro sostegno non sarei mai diventato ciò che sono ora (nel bene e nel male, che se no sembra che me la tiro troppo!).
Voglio ringraziare anche i tanti, tantissimi amici con i quali ho condiviso un sacco di tempo, lavorando (io poco, loro un sacco invece!) e non solo. Grazie perché siete riusciti a fare passare anche i momenti più difficili con una risata.
L'ultimo paragrafo lo voglio lasciare alla vera e sola costante di sempre, mia moglie (eh si... ora l'ho anche scritto quindi è ufficialmente ufficiale!). Questi anni sono stati assurdi per tanti versi e ci ha messo un po' (ma un po' tanto!) alla prova. Insieme però siamo riusciti a superarli uno affianco all'altra, sostenendoci e sopportandoci a vicenda. Grazie perché rendi la nostra normalità e quotidianità qualcosa di eccezionale e bellissimo!

GRAZIE!

Abstract

This Thesis presents the results of my work on how galaxy clusters form by the accretion of sub-clumps and diffuse materials, and how the accreted energy is distributed in the X-ray emitting plasma. Indeed, on scales larger than tens of millions of light years, the Universe is self-organised by gravity into a spiderweb, the *Cosmic Web*. Galaxy clusters are the knots of this Cosmic Web, but a strong definition of filaments (which link different knots) and their physical proprieties, is still uncertain. Even if this pattern was determined by studying the spatial distribution of galaxies in the optical band, recently, also in the X-rays probes of filamentary structures around galaxy clusters were obtained. Therefore, given these observational facilities, the galaxy clusters' outskirts are the best candidate regions to detect filaments and study their physical characteristics. However, from X-rays observations, we have only a few detections of cosmic filaments to date.

On the other hand, it is crucial to understand how the accreted energy is dissipated in the baryon content of galaxy clusters and groups. Indeed, it is well known that in the central region of galaxy clusters and groups the baryon fraction increases with the halo mass. On the outer region, the lack of X-rays constraints influences our understanding of the evolution of baryons in the halos volume. The standard assumption of "closed-box" system, for which the baryon fraction should approach the cosmological ratio $\Omega_{\rm bar}/\Omega_{\rm m}$, for galaxy clusters and groups seems to be too strong, especially for less massive objects. Moreover, a complete redshift evolution of baryons in galaxy clusters and groups is still missing.

In my works, I mainly focused on massive halos, whose virial masses M_{vir} at redshift $z = 0$ range from $10^{13}h^{-1}M_{\odot}$ up to $10^{15}h^{-1}M_{\odot}$, and on radii greater than $R_{500,\rm c}$, which for these massive objects spans from $250h^{-1}$kpc to $1.5h^{-1}$Mpc.

Turbulence and hydrostatic bias: how energy is dissipated in halos volume

Using simulated galaxy clusters extracted from the *ITASCA* sample, a large catalogue of clusters simulations produced with the Adaptive Mesh Refinement Code *ENZO*, I focused on the turbulence in the intra-cluster medium (ICM) and hydrostatic mass bias that affect the mass estimates of galaxy clusters and groups. I improved the algorithm developed by Vazza et al. (2012), which extracts the turbulent component of the velocity field from simulated ICM. This algorithm does not assume any a priori coherence scales for the definition of turbulent motions. I modified the algorithm to take into account the Kolmogorov theory and its result is a 3D turbulent velocity field. Starting from this, I studied the radial behaviour of the non-thermal pressure, generated by the turbulent motions. I derived a new fitting formula for the radial profile of non-thermal pressure, and I linked the coefficients of the fitting formula with the physical properties of the turbulence. I also

studied the relations between turbulent motions and hydrostatic-mass bias, the lack of reconstructed mass from X-rays observations compared to Sunyaev-Zeldovich or Weak Lensing ones. I found that turbulence, developed during mergers, is not able to completely explain the hydrostatic bias, and other non-thermal phenomena are required, for example, residual radial accelerations from infalling clumps. Finally, I compared my results with previous numerical and observational works, finding that the new filtering technique well reproduces the X-rays observations. Moreover, the new fitting formula has an easier form compared to the ones present in the literature, and it is also statistically better when applied to our data.

Clumps and filaments: sources of accretion in galaxy clusters

Using a sample of simulated galaxy clusters extracted from the *ITASCA* simulations, different from the one adopted for the turbulence and hydrostatic mass bias analysis, I studied matter clumps and filaments located in the peripheries of simulated galaxy clusters. I considered both clumps and filaments because, as already highlighted, it is very challenging in X-rays observations to identify filaments, but it is easier to identify matter's clump. Indeed, clumps are denser than the external medium and, being the X-rays emission proportional to the gas density square, their emissivity is much higher than the surrounding medium's one. Therefore, my work is as realistic a prediction as possible of the best candidates for studying cosmic filaments, with the new generation of X-ray missions. In numerical simulations is quite simple to disentangle between matter clumps, filaments and diffuse matter. I developed two algorithms to identify matter clumps and filaments in *ITASCA* simulations. The first is based on the clumps' baryon mass and clumps' dimension and I demonstrated that, in the adopted simulations, it is possible to find structures massive than $10^8 M_\odot$ and smaller than 500 kpc. The filament finder is based on gas radial velocity and entropy. Indeed, it is expected that cosmic filaments have high values of radial velocity, due to the gravity field of the central galaxy clusters, but their entropy is lower than the surrounding medium, otherwise, it would not be so challenging to detect them in the X-ray band.

Thanks to our algorithms, I studied separately the two populations, but I also compared the density and the temperature of clumps and filaments. I found a quite high level of correlations for both the quantities analysed and I concluded that, even if the used simulations do not include feedback mechanisms, the idea of using clumps as tracers for filaments seems to be quite promising. Moreover, only for the clump's populations, I studied the possible variation of density and temperature field with the distance from the central galaxy clusters. I found that up to clumps are located far from $\sim 3R_{500,\mathrm{c}}$ they are well represented by scaling relations not so different from the ones obtained for galaxy groups and clusters. Closer to the central galaxy cluster environment, the scaling relations are completely different from matter clumps and

groups or clusters. This suggests that, once the clumps interact with the ICM of the central clusters, their density and temperature are affected by the interactions with the external medium and that information about the formation's initial conditions is lost.

The Athena view of clusters peripheries: matter clumps in the next generation of X-rays observatories

To obtain a realistic observational prediction of what it would learn about clumps and filaments in the future, I simulated what the X-rays telescope ATHENA would observe on the clusters' peripheries. To perform these simulations, I used the SIXTE simulator in combination with a sample of simulated galaxy clusters, and I produced some interesting preliminary results. In detail, I developed a procedure that involves both the instruments onboard the ATHENA satellite, WFI and X-IFU. Thanks to its larger FoV, I used WFI to detect clumps in the outskirts of simulated galaxy clusters. For each of these clumps, I ran a simulated XIFU exposure to obtain spatially resolved high-resolution X-ray spectra of the plasma and to infer from them some fundamental physical quantities like gas density, temperature, metallicity, and components of the velocity both turbulent and along the line of sight.

Opening the "closed-box" of galaxy clusters and groups

I also worked on the baryon and gas budget in galaxy clusters and groups. The main assumption used in this type of analysis is the "closed-box" scenario. It is expected that, when a sufficiently large halo volume is considered, the ratio between the baryon mass over the total mass of the system is equal to the cosmological expectation. Moreover, many observational studies have shown that the baryon fraction increases with the mass of the galaxy clusters and groups, meaning that the "closed-box" assumption could be not verified in the galaxy groups regime. Using a large sample of 140 halos, with virial masses $10^{13} \leq M_{vir}/M_{\odot} \leq 10^{15}$, extracted from the simulated box *Box2b* of *Magneticum* simulations, a suite of Smoothed Particle Hydrodynamical cosmological simulations, I performed detail analysis of their baryon content. As a novelty of my work, I extended the radial analysis up to $10R_{500,\mathrm{c}}$, beyond the accretion shock position, usually assumed as a boundary of the halo volume, to include all the baryons associated with the simulated galaxy clusters and groups. I found that only for massive systems and at very larger radii ($r \geq 6R_{500,\mathrm{c}}$) the baryon fraction is equal to the cosmological expectation. In the group regime, not even when the limit of radial analysis is reached, the cosmological baryon budget is recovered.

In the *Magneticum* simulations are also available information about the gas metallicity. Combing the radial behaviour of gas metallicity and the stellar fraction, I concluded that the early enrichment scenario, for which the gas is enriched

of metal at redshift greater than two, is preferred to describe my findings. Indeed, no relation with the halo mass is found and the radial trend for radii greater than $2 \div 3 R_{500,c}$ shows a flatting, which suggests the lack of star-forming effects in recent epochs.

The cosmological evolution of baryons in massive ($M \geq 10^{13} M_{\odot}$) halos

As an extension of the previous work, I am working to assess the time evolution of baryon fraction in simulated galaxy clusters. Using the same suite of simulations adopted above, we select eight different simulated snapshots of the simulations, from redshift 3 to 0.2 and for each snapshot, I extract the 150 most massive halos and follow the baryon evolution across cosmic time. Interestingly, I find a clear evolution of the baryon fraction, without strong dependencies on halo mass. Differently from the local Universe analysis, we find that the gas fraction in high-redshift systems is not completely represented by a hot gas phase, neither in clusters nor in groups regime, but a not negligible cold component is always present. On the other hand, my findings on gas metallicity and stellar fraction still confirm that the early enrichment scenario is the preferred to describe the data. Finally, I compare the baryon and gas fraction evolution with the AGN feedback energy. Indeed, previous works have highlighted the importance of AGN feedback in the whole evolution of galaxy clusters' environment. I find a high level of correlation between AGN feedback energy and the amount of baryon, gas and all the other parameters analysed, showing how these correlations could be used as proxies to improve the AGN feedback model adopted in different numerical simulations.

Contents

Chapter 1

The large scale structure of the Universe

This Thesis is the result of my work on mass accretion phenomena in clusters of galaxies and their effects on the evolution of the intracluster medium. The chapters, which contain not only the results I published in the last three years, are organised in a way to guide the reader from the innermost regions of galaxy clusters, out to the extreme peripheries. In this Chapt. 1 I give an overview of the topics that will be discussed in the following chapters; in Chapt. 2 I introduce the numerical simulations as an efficient tool to study the large-scale structure of the Universe, highlighting the main difference of the different codes we analysed in this Thesis; in Chapt. 3 I present the results of Angelinelli et al. (2020), my work on non-thermal pressure support, turbulent gas motions and hydrostatic mass bias, all important phenomena that take place in the virialised regions of galaxy clusters; in Chapt. 4 I discuss my work Angelinelli et al. (2021), where I focus in the outskirts of galaxy clusters and I describe sources of mass accretion, such as matter clumps and cosmological filaments. Chapt. 5 covers two works, Angelinelli et al. (2022) and Angelinelli et al. (2023), in which I investigate the role of baryons in the growth of galaxy clusters and groups, following their cosmic evolution and testing the "closed box" assumption out to very large cluster radii.

Finally, in Chapt. 6 and Chapt. 7, I summarise my main results and discuss possible extensions of my works. I leave some numerical and fitting details of my analysis in the Appendices in Chapt. 8, including in the main Chapters some parts originally published as appendices as sections of this Thesis. In Chapt. 4 the reader may find some sections which are not published in the original paper Angelinelli et al. (2021) but are included in this Thesis for the sake of completeness.

1.1 Cosmological scenario and structure formation

In the modern cosmological paradigm, the Universe is considered isotropic and homogeneous. Under these assumptions, the Friedmann–Lemaître–Robertson–Walker (FLRW) metric is used as a standard metric in the form:

$$ds^2 = c^2dt^2 - a^2(t)\left(\frac{dr^2}{1-kr^2} + r^2(d\Theta^2 + sin^2\Theta d\phi^2)\right) \tag{1.1}$$

where $a(t)$ is the scale factor, which takes into account the evolution of the Universe, and k describes the curvature of the Universe and could assume positive, negative or zero values. In the General Relativity theory proposed by Einstein (1915) is possible to describe the evolution of space-time geometry of the Universe under the action of matter, using Einstein's equations:

$$-\frac{8\pi G}{c^4}T^{\mu\nu} = G^{\mu\nu} + \Lambda^{\mu\nu} \tag{1.2}$$

Assuming a perfect fluid, completely described by its density ρ and pressure p and using the Minkowski metric (Minkowski, 1915), it is possible to rewrite Einstein's equation, using the two Friedmann's equations:

$$H^2 = \left(\frac{\dot{a}}{a}\right)^2 = \frac{8\pi G}{3}\rho - \frac{kc^2}{a} + \frac{\Lambda c^2}{3} \tag{1.3}$$

$$\dot{H} + H^2 = \frac{\ddot{a}}{a} = -\frac{4\pi G}{3}\left(\rho + 3\frac{p}{c^2}\right) + \frac{\Lambda c^2}{3} \tag{1.4}$$

where H is the Hubble parameter and it measures the expansion rate of the Universe. Combining the two Friedmann's equations is possible to derive the energy conservation equation in the cosmological context.

$$\dot{\rho} + 3\frac{\dot{a}}{a}\left(\rho + \frac{p}{c^2}\right) = 0 \tag{1.5}$$

Historically, the solutions of the Friedmann equation are derived using the Eq. 1.3 and the following equation of state:

$$p = \omega\rho c^2 \tag{1.6}$$

where ω is a constant, which is 1 for a matter-dominated Universe and 1/3 for a radiation-dominated Universe. Now, combing Eq. 1.5 and Eq. 1.6, we can derive the evolution of the density as a function of a:

$$\rho = \rho_0 a^{-3(1+\omega)} \tag{1.7}$$

Introducing the "critical density" of the Universe ρ_c:

$$\rho_c = \frac{3H^2(z)}{8\pi G} \tag{1.8}$$

and defining the dark energy and curvature densities as:

$$\rho_\Lambda = \frac{\Lambda c^2}{8\pi G} \tag{1.9}$$

$$\rho_k = \frac{3kc^2}{8\pi G} \tag{1.10}$$

we can rewrite the Eq. 1.3 as:

$$E^2(a) = \left(\frac{H}{H_0}\right)^2 = \Omega_m a^{-3} + \Omega_r a^{-4} + \Omega_k a^{-2} + \Omega_\Lambda \tag{1.11}$$

where Ω_i is the ratio between matter, radiation, dark energy or curvature densities and ρ_c. Considering the equation $z = (1+a)^{-1}$, which relates redshift z and scale factor a, the Eq. 1.12 becomes:

$$E^2(z) = \left(\frac{H}{H_0}\right)^2 = \Omega_m (1+z)^3 + \Omega_r (1+z)^4 + \Omega_k (1+z)^2 + \Omega_\Lambda \tag{1.12}$$

which describes the evolution of the Universe across cosmic time.

From the observation of the Cosmic Microwave Background (CMB) presented by Planck Collaboration et al. (2020), the values of fundamental parameters for the ΛCDM paradigm are:

- $H_0 = 67.4 \pm 0.6 \frac{\text{km}}{\text{s Mpc}}$
- $\Omega_m = 0.315 \pm 0.007$
- $\Omega_\Lambda = 0.685 \pm 0.0072$

In modern cosmology, the formation of the structures is driven by the standard hierarchical structure formation scenario (see Kravtsov, Borgani, 2012, for a detailed review on galaxy cluster formation). In this scenario, the objects are formed via the gravitational collapse of peaks in the initial primordial density field characterised by the density contrast field $\delta(\mathbf{x})$, defined as:

$$\delta(\mathbf{x}) = \frac{\rho(\mathbf{x}) - \bar{\rho}_m}{\bar{\rho}_m} \tag{1.13}$$

where $\bar{\rho}_m$ is the mean mass density of the Universe. The main proprieties of $\delta(\mathbf{x})$ are completely determined by the processes that occur on the inflationary (Starobinsky,

1982) and recombination (Peebles, 1982) stages of evolution of the Universe. Under the assumption of an isotropic and homogeneous Universe, the $\delta(\mathbf{x})$ field is also an isotropic, homogeneous, and Gaussian. Thanks to these characteristics, the $\delta(x)$ could be fully characterised by its power spectrum $P(k)$, which depends only on the modulus k of the wave-vector. It is possible to define the variance of the density contrast field smoothed on the scale R as:

$$\delta_R(\mathbf{x}) \equiv \int \delta(\mathbf{x}-\mathbf{r})W(\mathbf{r},R)d^3r \tag{1.14}$$

from which follows:

$$\langle\delta_R^2\rangle \equiv \sigma^2(R) = \frac{1}{(2\pi)^2}\int P(k)|\tilde{W}(\mathbf{k},R)|^2 d^3k \tag{1.15}$$

where $\tilde{W}(\mathbf{k},R)$ is the Fourier transform of the filter function $W(\mathbf{r},R)$. When the range of the modulus k is sufficiently limited, the power spectrum $P(k)$ and $\sigma^2(R)$ are approximated to a power-law ($P(k) \propto k^n$ and $\sigma^2(R) \propto R^{-(n+3)}$). At high redshift and considering a spherical top–hat window function mass and radius are related by the equation $M = (4\pi/3)\rho_m(z)R^3$. The smoothed Gaussian density field has a probability distribution function (PDF) given by:

$$p(\delta_M) = \frac{1}{\sqrt{(2\pi)}\sigma_M}\exp\left[-\frac{\delta_M^2}{2\sigma_M^2}\right] \tag{1.16}$$

The evolution of $\delta(\mathbf{x})$ at high redshift is described by the linear growth factor $D_+(a)$ (with a scale factor):

$$D_+(a) = \frac{5\Omega_M}{2}E(a)\int_0^a \frac{da'}{[a'E(a')]^3} \tag{1.17}$$

Also, the root mean square (rms) amplitude of fluctuations $\sigma(M,a)$ follows a linear evolution:

$$\sigma(M,a) = \frac{\sigma(M,a_i)D_+(a)}{D_+(a_i)} \tag{1.18}$$

Once $\sigma(M,a) \sim 1$ the evolution is no longer linear and to follow the time evolution non-linear models or numerical simulations are needed.

The simplest non-linear model is the spherical collapse model. This model considers a spherically-symmetric density fluctuation of the initial physical radius of the perturbation R_i, amplitude $\delta_i > 0$, and mass $M = (4\pi/3)(1+\delta_i)\bar{\rho}R_i^3$, where $\bar{\rho}$ is the mean density of the Universe at the initial time. Thanks to the symmetry, the collapse of the perturbations is a one-dimensional problem and it is possible to determine the evolution of the top-hat radius $R(t)$ (Gunn, Gott, 1972). Briefly, $R(t)$ increases until the turnaround epoch t_{ta}, then it decreases until the perturbation

collapses, virializes, and approaches the final radius R_f at t_{coll}. R_f is determined by the virial theorem and it is half of the R_{ta} if $\Omega_\Lambda = 0$. The spherical collapse model helps approximate the time it takes for a halo to collapse and has been useful in creating statistical models for halo formation and evolution. However, it is a simplified model and does not include many important details and complexities of actual density peak collapse, which are typically studied using three-dimensional numerical cosmological simulations.

One of the main sources of complexities is given by the different processes that affect baryonic and dark matter masses. Indeed, once the collapse is ended, the matter approaches an equilibrium state. For the collisional baryonic component the equilibrium is approximately described by the hydrostatic equilibrium, while for the dark matter component, which is a collisionless system of particles, the equilibrium is described by the Jeans equation (Binney, Tremaine, 2008). These differences are translated in different equilibrium halo final masses: hydrostatic mass M_{HE}, Jeans mass M_J.

$$M_{HE}(< r) = -\frac{r k_b T(r)}{G\mu m_p}\left[\frac{d\ln\rho_g(r)}{d\ln r} + \frac{d\ln T(r)}{d\ln r}\right] \tag{1.19}$$

where hydrostatic mass M_{HE} inside the radius r depends on the density $\rho_g(r)$ and temperature $T(r)$ of the gas. This relation is derived from the assumption that at radius r the pressure gradient is balanced by the gradient of the gravitational potential. On the other hand, the Jeans mass is given by:

$$M_J(< r) = -\frac{r\sigma_r^2}{G}\left[\frac{d\ln\nu(r)}{d\ln r} + \frac{d\ln\sigma_r^2(r)}{d\ln r} + 2\beta(r)\right] \tag{1.20}$$

where $\beta = 1 - \sigma_t^2/2\sigma_r^2$ is the orbit anisotropy parameter defined in terms of the radial σ_r and tangential σ_t velocity dispersion components. Due to the continuous accumulation of matter and the occurrence of minor and major mergers, a halo may not fully reach a state of equilibrium over the course of the Hubble time. It is only after a few Gyr that the intracluster medium (ICM) reaches an equilibrium state following a major merger. When a cluster is not in equilibrium, it can exhibit different observable properties and this can lead to systematic errors when using equations for hydrostatic and Jeans mass to estimate the mass of the cluster.

Having strong estimations of the mass of the cluster is crucial to test the cosmological paradigm. Indeed Press, Schechter (1974) developed a statistical model for the abundance of collapsed objects as a function of their mass. The key concept behind this model is that the mass distribution of objects that form through nonlinear collapse can be directly and uniquely related to the statistical characteristics of the initial linear density contrast field, represented by $\delta(\mathbf{x})$. It is possible to determine the probability $F(M)$ that a given region within the initial over-density $\delta_M(\mathbf{x})$ will

collapse into a halo of mass M or larger, using the relation:

$$F(M) = \int_{-1}^{\infty} p(\delta) C_{coll}(\delta) d\delta \tag{1.21}$$

where $p(\delta)d\delta$ is given by Eq. 1.16 and C_{coll} is the probability that a point located in $\mathbf{x}$ with over-density $\delta_M(\mathbf{x})$ collapses. The mass function will be the fraction of the total volume collapsing into halos of mass $M \div M + dM$ (dF/dM) divided by the comoving volume within the initial density field occupied by each halo $(\frac{M}{\bar{\rho}_M})$:

$$\frac{dnM}{dM} = \frac{\bar{\rho}_M}{M} \left| \frac{dF}{dM} \right| \tag{1.22}$$

Press, Schechter (1974), assuming the spherical collapse model, concluded that the abundance of halos of mass M at redshift z is a universal function of only their peak height $\nu(M,z) \equiv \delta_c/\sigma(M,z)$, where δ_c is the collapse over-density. Under these assumptions, the fraction of mass in halos per logarithmic interval of mass becomes:

$$\frac{dnM}{d\ln M} = \frac{\bar{\rho}_M}{M} \left| \frac{dF}{d\ln M} \right| = \frac{\bar{\rho}_M}{M} \left| \frac{d\ln\nu}{d\ln M} \frac{\partial F}{\partial \ln \nu} \right| \equiv \frac{\bar{\rho}_M}{M} \left| \frac{d\ln\nu}{d\ln M} \right| g(\nu) \equiv \frac{\bar{\rho}_M}{M} \psi(\nu) \tag{1.23}$$

The shape of $\psi(\nu)$ highly depends on the model adopted for the structure's collapse. Numerical studies have highlighted that the ψ_{PS} adopted in Press, Schechter (1974) deviates by $> 50\%$ from the shape measured in cosmological simulations (e.g. Tormen, 1998; Desjacques, 2008; Corasaniti, Achitouv, 2011).

Calibrations performed on modern cosmological simulations and future observational surveys are crucial to understanding the mass function of the Universe and, in particular, galaxy clusters are critical for understanding the overall structure and evolution of the universe and the role that these massive structures play in shaping it.

1.2 Galaxy clusters and their environment

The current hierarchical paradigm of structure formation is the spatially flat Λ-Cold Dark Matter model (ΛCDM) with a cosmological constant. According to this paradigm, the Universe is composed of Dark Energy ($\Omega_\Lambda \approx 0.7$), Dark Matter ($\Omega_{\rm DM} \approx 0.25$) and baryonic matter ($\Omega_{\rm bar} \approx 0.05$), with a Hubble constant given by $\rm H_0 \approx 67\ kms^{-1}Mpc^{-1}$.

In the hierarchical paradigm of structure formation, massive objects like galaxies and galaxy clusters are formed through accretion and mergers. The first objects, formed in the early Universe from redshift 30 to 10, are supposed to be massive isolated stars of about $\sim 100 - 300 M_\odot$. The formation sites of these stars are mini

halos of Dark Matter, with masses in the $\sim 10^5 - 10^8 M_\odot$ range. In this scenario, galaxy clusters are formed by a sequence of minor and major mergers. A simplistic and commonly accepted model is the self-similar model by Kaiser (1986), which is based on Einstein-de Sitter background cosmology and a power law shape for the power spectrum of primordial density fluctuations. However, the full description of cluster formation requires detailed modelling of the nonlinear processes of collapse and the dissipative physics of baryons.

The study of galaxy clusters is complementary to other astrophysical probes (e.g. high redshift supernovae and cosmic microwave background) in the understanding and estimation of some cosmological parameters. In particular, the abundance and spatial distribution of clusters are helpful to have information about the background cosmology, gravity law, and initial conditions, while the observed discrepancies between the "closed box" assumption and the real nature of cluster gravitational potentials make it possible to assess the non-gravitational processes operating during galaxy formation and their effects on the surrounding intergalactic medium.

This Thesis mainly focused on the outskirt of galaxy clusters. These regions are the best candidates to study the accretion phenomena needed to completely understand the galaxy cluster formation and have also probes to test the cosmological scenario. I now define some of the most useful quantities, normally involved in such type of analysis (see Walker et al., 2019; Walker, Lau, 2022, for detailed reviews on galaxy cluster outskirts). Firstly, we need to refer to a radius that represents the boundary between the core and the outskirts. This definition is given in terms of over-density with respect to a background density. In particular, we can use as background density the critical density or the mean density of the Universe at a given redshift. The enclosed mass is defined as follows:

$$M_{\Delta,ref} = \frac{4\pi}{3}\Delta_{ref}\rho_{ref}R^3_{\Delta,ref} \tag{1.24}$$

where Δ define the over-density and ref could assume the meaning of c for the critical or m for the mean density of Universe. The critical density is defined as in Eq. 1.8, while the mean density is given by $\rho_m(z) = \rho_c(z)\Omega_m(z)$. A common definition of boundary is $R_{200,c}$, which is the radius at which the density is 200 times the critical density of the Universe. This follows from the assumption of the spherical collapse of the structures in a matter-dominate Universe ($\Omega_m = 1$), in which the over-density associated with the virial radius is $\Delta_c = 178$, which is approximated to 200. On the other hand, if we assume the ΛCMD model, we can rewrite $\Delta_c = 18\pi^2 + 82(\Omega_m(z) - 1) - 39(\Omega_m(z) - 1)^2$, which is approximated to 100. Another important radius, which we also assume in our analysis, is $R_{500,c}$. This radius often represents the observational limits of the X-rays facilities used nowadays. The definitions given above are not related to any particular physical phenomena

that occur in the galaxy cluster environment. Other definitions of boundary radius, derived from physical reasons, are the splashback radius R_{sp} (Adhikari et al., 2014) and the accretion shock radius R_{sh}. The R_{sp} represents the apocenters (farthest point of the particle orbit with respect to the halo potential minimum) of infalling Dark Matter through the pericenter (closest point of the particle orbit with respect to the minimum of the gravitational potential of the halo); the R_{sh} is the radius at which the infalling gas from the surrounding environment gets shock heated for the first time. All these radii could approximately be related to each other at redshift $z = 0$ by $R_{500,c} : R_{200,c} : R_{200,m} : R_{sp} : R_{sh} = 1 : 1.4 : 3 : 3 : 4.8$.

From an observational point of view, two different approaches could be used to determine the physical proprieties of galaxy cluster outskirts. On one hand, we can use the X-ray spectra from instruments with low and stable background, and good spectral resolution in the band (0.5-7.0 keV). In this respect, only Suzaku and eROSITA have the capability to achieve these requirements. Indeed, both XMM-Newton and Chandra have a too-high instrumental background, while ROSAT has a too-low spectral resolution and a covered band. Through the fitting of observed spectra, the direct measurements of temperature, density and gas metallicity could be derived. On the other hand, the second method needs a combination of X-rays maps and measurements of the Sunyaev-Zeldovich (SZ) effect. The SZ effect is the inverse Compton scattering of photons from the Cosmic Microwave Background (CMB) by the hot electrons of ICM. This method does not need any spectral information, so instruments like XMM-Newton could be used to achieve the maps of the targets. With this method, the density profiles are directly derived from the X-ray surface brightness converted into emission measure. These density profiles are combined with pressure profiles obtained from SZ measurements, and profiles of temperature and entropy could be obtained. An example of these techniques is the results part of the X-COP project (see Eckert et al., 2019; Ghirardini et al., 2019, for details on X-COP project).

In the next decades, many X-ray observatories are expected to be launched. The forerunner of this next generation of telescopes is eROSITA*, which was successfully launched in 2019. eROSITA is the first X-ray telescope to be launched to L2, the position that gives a stable background, and thanks to its large field of view (a 1.03 degree diameter circle), images of galaxy clusters and their outskirts are obtained without the need for mosaics reconstruction. For instance, eROSITA observed the Coma cluster, obtaining X-ray emission up to $2R_{200,c}$ (Churazov et al., 2021). Thanks to the high effective area in the soft X-ray band of eROSITA, Reiprich et al. (2021) studied the bridge in X-ray emission in the Abell 3391/3395 galaxy cluster system. Other X-rays missions are already planned for the next years. The

*https://erosita.mpe.mpg.de

X-Ray Imaging and Spectroscopy Mission (XRISM)[†] is a NASA and JAXA collaboration (with contributions from ESA) to replace the Hitomi satellite, supposed to be launched in 2023. It will combine an X-ray microcalorimeter, identical to that on Hitomi, and a wide field X-ray imager, with a field of view 4 times larger than the one on board Suzaku. The Advanced Telescope for High Energy Astrophysics (ATHENA)[‡] is an X-ray observatory being developed by ESA for launch in the 2030s. Nowadays, the mission suffers from some difficulties, but the original telescope was supposed to have a large collecting area and an array of microcalorimeter detectors. These instruments allow a direct measurement of line shifts and broadening due to gas motions, probing turbulence and bulk motions also in the outskirts of galaxy clusters. Other X-ray missions, such as Lynx[§], AXIS[¶] and HUBS[‖] are still being designed, but all of them would combine a large collecting area, low and stable background and a very high spatial and spectral resolution, all characteristics which allow a further improvement of our knowledge about galaxy clusters outskirts.

1.3 Non-thermal pressure in galaxy clusters and the hydrostatic mass bias problem

Turbulence plays a key role in the assembly of large-scale structures and in controlling the physics of the intracluster medium (e.g. Brunetti, Jones, 2014). The origin and evolution of turbulence in the ICM have been widely studied in the past using hydrodynamical simulations (e.g. Dolag et al., 2005b; Lau et al., 2009; Vazza et al., 2011a; Miniati, 2014; Gaspari et al., 2014). The injection and amplification of vorticity by shock waves (e.g. Ryu et al., 2008; Porter et al., 2015; Vazza et al., 2017) or ram pressure stripping (e.g. Subramanian et al., 2006; Cassano, Brunetti, 2005; Roediger, Brüggen, 2007) is a main source of turbulence in galaxy clusters. Moreover, winds from star-burst galaxies and outflows from active galactic nuclei affect the ICM, especially in cluster cores (e.g., Brüggen et al., 2005; Gaspari et al., 2011).

However, until now there are very few direct observations of turbulent gas motions are almost entirely missing. The Soft X-ray Spectrometer (SXS) onboard *Hitomi* satellite has detected turbulent gas motions in the core of the Perseus cluster. Using the broadening of atomic lines, the root-mean square velocities were found to be ~ 200 km/s on ≤ 60 kpc scales (e.g. Hitomi Collaboration et al., 2016; ZuHone et al., 2018). This is related to a $2-6\%$ of non-thermal pressure support in the case of isotropic turbulent motions, or to an $11-13\%$ non-thermal pressure support in

[†] https://xrism.isas.jaxa.jp/en/
[‡] https://www.the-athena-x-ray-observatory.eu/
[§] https://www.lynxobservatory.com/
[¶] https://axis.astro.umd.edu/
[‖] http://hubs.phys.tsinghua.edu.cn/en/

case the motions are generated by larger-scale sloshing (Hitomi Collaboration et al., 2018). Unluckily, its failure in 2016 has prevented the telescope to complete the planned mission. In the next years, the X-Ray Imaging and Spectroscopy Mission (XRISM) is supposed to recover the science capability lost with the Hitomi, focusing mainly on the soft X-ray bands.

Indirect evidence of turbulence motions in the ICM can be inferred from the radio observations of Faraday Rotation. Polarised sources located behind galaxy clusters hint at a tangled magnetic field in the ICM, with typical coherence scales in the range of $\sim 10 - 50$ kpc (e.g. Murgia et al., 2004; Vogt, Enßlin, 2005; Bonafede et al., 2010). This is naturally explained by volume-filling stretching motions induced by turbulence (e.g. Dolag et al., 2001; Donnert et al., 2018; Domínguez-Fernández et al., 2019). In order to explain their observed morphology and strength, other indirect probes of turbulent motions are obtained from highly resolved X-ray surface brightness fluctuations. These are interpreted as indications of moderate density fluctuations induced by turbulence (e.g. Schuecker et al., 2004; Churazov et al., 2012; Gaspari et al., 2014; Zhuravleva et al., 2014). From a comparison between X-ray and radio observations, it has been suggested that the surface brightness fluctuations correlate with the diffuse radio emission (Eckert et al., 2017b; Bonafede et al., 2018). This suggests that turbulence detected in X-ray emission could be linked to the re-acceleration of radio-emitting particles, via different mechanisms (e.g. Brunetti, Lazarian, 2011; Brunetti, Vazza, 2020).

Moreover, the reconstruction of the hydrostatic mass bias could be affected by turbulent motions in ICM. Indeed, turbulence is expected to contribute to the total pressure of the ICM (Morandi et al., 2011; Parrish et al., 2012; Shi, Komatsu, 2014; Shi et al., 2015, 2016; Fusco-Femiano, Lapi, 2018; Ota et al., 2018; Fusco-Femiano, 2019).

In Eckert et al. (2019) and Ettori et al. (2019), the results of a systematic study of non-thermal support and hydrostatic mass bias in a sample of nearby, relaxed, massive galaxy clusters observed for the XMM-Newton Large Program X-COP (Eckert et al., 2017a) are presented. The observed mass bias implies that the non-thermal pressure support in the outskirts galaxy clusters should vary between 5 to 15%. Such values are a factor of 2 to 3 below what is found in numerical simulations (e.g. Lau et al., 2009; Vazza et al., 2011a; Nelson et al., 2014a; Biffi et al., 2016a; Kay et al., 2004; Faltenbacher et al., 2005; Rasia et al., 2006; Hallman et al., 2006; Nagai et al., 2007). This discrepancy may be related to missing physics in the simulations such as physical viscosity, and magnetic fields, or due to an incorrect separation of turbulent and bulk motions. Indeed, different numerical techniques used to disentangle bulk from turbulent motions could yield non-thermal pressures that differ by factors of 2 to 3, even within the same simulations (Vazza et al., 2018a).

Valdarnini (2019b) studied turbulent motions in galaxy clusters simulated with

(radiative and non-radiative) N-body/SPH codes, using a multi-scale filtering technique. Their results are consistent with Vazza et al. (2018a), suggesting that advanced filtering techniques to study the internal dynamics of the simulated ICM are fundamental to correctly reconstructing the mass bias in galaxy clusters.

Recently, Vallés-Pérez et al. (2021), using an adaptive mesh refinement cosmological simulation, explored the generation and dissipation of turbulence in galaxy clusters connecting these phenomena with the assembly history of such systems. They find that major mergers are the main process driving turbulence in ICM, confirming a scenario in which turbulence is generated by baroclinicity and compression given by external and internal shocks and later by vortex stretching downstream of them.

In Angelinelli et al. (2020) (see Chapt. 3 of this Thesis) I studied the role of turbulent motions as sources of non-thermal pressure in ICM. Furthermore, I investigated how turbulence influences the estimation of the cluster's mass and the impacts of the hydrostatic mass bias. I found that corrections related to turbulence may not completely solve the hydrostatic mass bias, but other non-thermal phenomena, such as gas radial accelerations, are needed to reconstruct the real cluster mass starting from ICM derived proprieties.

1.4 Matter clumps and cosmic filaments

On large scales, the matter in the Universe is organised into web-like patterns, the so-called Cosmic Web (Bond et al., 1996). This structure is now mostly observed thanks to large optical surveys such as Sloan Digital Sky Survey (SDSS, Tegmark et al., 2004), 2 Micron All-Sky Survey (2MASS, Huchra et al., 2012), and VIMOS Public Extragalactic Redshift Survey (VIPERS, Guzzo et al., 2014), in which the large-scale distribution of the galaxies suggests the presence of filaments and knots. The knots of this web are associated with the galaxy clusters, while filaments are over-density regions which link different knots. The spatial distribution of the galaxies traces the presence of cosmic filaments and, in recent years, also diffuse gas filaments have been observed in the far-UV (Nicastro et al., 2018), by way of O VI absorption systems (Danforth, Shull, 2005; Tripp et al., 2006) and in thermal soft X-rays (Eckert et al., 2015a). This gas is characterised by densities $\sim 10^{-5}$ cm^{-3} and temperatures from 10^5 to 10^7 K, values which allow defining this gas phase as a warm-hot intergalactic medium (WHIM). The low X-ray emissivity of the gas which composes these filamentary regions makes the physical description of the WHIM very challenging. Cosmological simulations correctly reproduce the cosmic web structure, enabling the study of the evolution and proprieties of the WHIM (e.g., Cen, Ostriker, 1999; Davé et al., 2001). Predictions by numerical simulations suggest that ∼30-40% of cosmic baryons are in the WHIM phase (Martizzi et al.,

2019), and the mass density associated with this phase might be efficiently estimated through absorption features in spectra obtained from background sources such as AGN or gamma-ray bursts (GRB, e.g., Branchini et al., 2009).

Despite some difficulty due to their low X-ray emissivities, in galaxy cluster outskirts, matter clumps and cosmic filaments have been observed. For such cluster-embedded filaments, detection in the X-ray band requires sophisticated techniques such as deep, mosaiced observations (see Walker et al., 2019, for details on cluster outskirts). On the other hand, matter clumps have been found in the outskirts of the Coma cluster using Subaru weak-lensing mass maps by Okabe et al. (2014), which identified sub-halos with masses around $10^{12}\ M_{\odot}$. Also, Eckert et al. (2015b), using a sample of 31 galaxy clusters imaged by ROSAT, were able to estimate the clumping factor by comparing the median and mean of the surface brightness profile. They found comparable results with Suzaku observations and theoretical predictions from previous numerical works (Roncarelli et al., 2013; Vazza et al., 2013b). Recently, Simionescu et al. (2017), using a combined analysis of Suzaku X-ray observations and Sunyaev-Zel'dovich (SZ) effect maps derived from Planck telescope data for the Virgo cluster, found an excess in the pressure profile. This behaviour is explained by the presence of substantial gas density fluctuations in the cluster's peripheries. However, existing data do not yet provide a full characterisation of matter clumps and cosmic filaments in cluster outskirts.

Numerical simulations are used to study the impact of the clumps on the clusters' growth (Nagai, Lau, 2011; Vazza et al., 2013b; Zhuravleva et al., 2013; Roncarelli et al., 2013). Nagai, Lau (2011) showed that to correctly reproduce the observed profiles of gas density and entropy derived from X-ray observations, matter clumps have to be considered. Indeed, the average density as a function of radius is typically over-estimated and spurious flattening of the gas entropy profile is observed if matter clumps are not removed from the analysis.

Zhuravleva et al. (2013) compared the median values of density and pressure to the mean values of the same quantities. They found that the gas proprieties in radial shells are well reproduced by a log-normal PDF (Probability Density Function), plus a tail. This tail represents the 1% of the matter in each radial shell and it is related to the gas inhomogeneities or matter clumps. Thanks to this approach the clumped component of the matter is easily separated from the diffuse medium.

Roncarelli et al. (2013) studied the relations between clumps and the measurement of the clusters' masses. They find that the reconstruction of the density profile introduces a bias in the estimate of the mass on the order of $\sim 10\%$ when the gas inhomogeneities are not well excluded by the analysis. Moreover, to describe the density inhomogeneities in the ICM they introduce the *residual clumpiness factor*. Correlations between this parameter and the y-parameter profile derived from the SZ observations and with the azimuthal scatter in the X-ray surface brightness stud-

ies are observed, and thanks to these correlations, they proposed both y-parameter and azimuthal scatter as proxies for the residual clumpiness factor.

Vazza et al. (2013b) studied the relations between matter clumps and baryon fraction, clump detectability for some X-ray missions and test the effects of cooling, feedback and numerical resolution on the estimates of clump proprieties. They found that the presence of clumps in the cluster's outskirts affects the estimation of the baryon fraction because of spurious contributions given by clumps at the derivation of the gas mass. They also found different impacts in relaxed and perturbed systems. Indeed, in relaxed systems, the introduced error by the gas clumps is $\sim 10\%$, while it reaches $\sim 20\%$ in disturbed ones. Producing mock X-ray maps in the soft X-ray band ($[0.5 - 2]$ keV), they investigate the detectability of the clumps. Relations between the number of bright clumps and the dynamical state of the host cluster are observed, but it seems that no relations are present with the cluster's mass. They also find that the majority of the clumps are located in the radial range $0.6 \leq R/R_{200} \leq 1.2$. This finding suggests that for past and current X-ray missions (e.g., ROSAT, XMM-Newton, Chandra) disentangling diffuse from clumped emissions is challenging, due to the required high brightness contrast. They also studied the effects of cooling, feedback and numerical resolution on observable clump proprieties, finding that numerical simulations which include AGN feedback produce over-densities in agreement with the observed ones and in agreement also with the non-radiative simulations. On the other hand, simulations in which only cooling mechanisms are considered, reproduce substantially different numbers and proprieties of matter clumps and also they introduce behaviour not observed (e.g., clusters' cooling flow problem Fabian, 2012).

Even though cosmic filaments are even harder to isolate observationally than clumps, an ever-increasing number of works could detect the presence of filaments. They could be divided into two main groups: filaments in clusters' pair, such as A399-A401, A222-A223 and A3391-A3395 (Bonjean et al., 2018; Werner et al., 2008; Sugawara et al., 2017, and reference therein), single filamentary structures around some individual clusters, such as Abell 2744, Abell 1750 and Abell 133 (Eckert et al., 2015a; Bulbul et al., 2016; Connor et al., 2019, respectively).

Filaments represent the major contributors to Cosmic Web, so it is expected that their components in regions adjacent to individual clusters would be observed, as well as within clusters, where filamentary mass is accreting. An example of this is proposed by Eckert et al. (2015a). They observe filaments extending outside the viral radius of Abell 2744. This gas structure spanning ~ 8 Mpc with a temperature $\sim 10^7$K. They also estimate that the baryon fraction of this filament is $\sim 15\%$, and this allows them to conclude that a non-negligible part of the missing baryon mass in the Universe is in cosmic filaments.

Tanimura et al. (2020) study a large sample of about 24000 filaments identified in

the SDSS survey. They select structures on scales from 30 to 100 Mpc. They exclude the contributions from galaxy clusters and groups using SZ information finding, for the gas in filaments temperatures of $\sim 10^6$ K, typical over-density of $\delta \sim 20$ and a baryon fraction of about 8%.

Recently, Tanimura et al. (2022), using the publicly available eROSITA Final Equatorial Depth Survey (eFEDS) data, detect the stacked X-ray emissions at the position of 463 filaments. They interpret the detected X-ray signal as an emission from hot gas in the filaments with a gas temperature of ~ 1.0 keV and a gas over-density of ~ 20 at the centre of the filaments, confirming their previous finding discussed in Tanimura et al. (2020).

Many numerical algorithms have been developed to study the complex hierarchy of structures in the simulated Cosmic Web (e.g., Cautun et al., 2014; Libeskind et al., 2018, for reviews). While marking the knots of the cosmic web is a relatively simple task, isolating filaments involves more complex procedures, owing to the different possible definitions. Available algorithms evidently do not reconstruct filaments in similar ways, but it is also important to note that there are important consistencies among those structure-detecting algorithms. Indeed, all the algorithms agree on the basic proprieties of the cosmic web's voids and knots.

In Angelinelli et al. (2021) (see Chapt. 4), I presented the results of the analysis that I performed on matter clumps and filaments in the outskirts regions of simulated galaxy clusters. After developing dedicated tools to disentangle between clumps, filaments and diffuse medium, I studied the physical proprieties of these different populations, finding that the density and temperature of matter clumps and filaments show high level of correlation. This suggests that clumps population may be used as a proxies to constrain the physical proprieties of unobserved filaments. On this respect, in Chapt. 4 of this Thesis, I will present some preliminary results about the pipeline that I developed to perform prediction of what the Athena satellite will be observe on the next future.

1.5 The "closed box" assumption across the cosmic time

The baryon content of groups and clusters of galaxies is a fundamental key to connecting their evolution and cosmology. It is expected that the ratio between the amount of baryons they contain and their total mass, must be equal to the ratio between the cosmological baryon density $\Omega_{\rm bar}$ and the total matter density $\Omega_{\rm m}$. Moreover, galaxy clusters and groups could be treated as "closed boxes" (Gunn, Gott, 1972; Bertschinger, 1985; Voit, 2005) and any additional time-integrated effect of feedback from galaxy formation (e.g. Allen et al., 2011) could be neglected only when large volumes are being considered. It is expected that any deviation from the condition of "closed box" should affect the distribution and the budget of

baryon in galaxy clusters and groups, both as a function of radius and halo mass (Limber, 1959).

As we showed in our recent work (Angelinelli et al., 2022) (see Chapt. 5 for details), non-gravitational physics related to galaxy formation significantly alters this picture, by moving a large number of baryons well beyond the virial radius of their host halos. Only for massive systems ($M_{vir} \geq 5 \times 10^{14} h^{-1} M_{\odot}$) and at very large radii ($r \geq 6 R_{500,c}$), the baryon fraction approaches the cosmological value, verifying the condition for a "closed-box" system.

Furthermore, the galaxy groups' typical masses of $10^{13-14} M_{\odot}$ lead to a shallower gravitational potential than the one found in galaxy clusters and this makes the assumption of a "closed box" for galaxy groups even more inaccurate. Therefore, galaxy groups are unique laboratories to study the interplay of many different physical processes affecting the evolution of baryonic matter during the hierarchical structure formation (Springel, 2005), and the energetic feedback from the many galaxies that co-evolve within them. Moreover, being galaxy groups at the peak of the halo mass function makes their cosmological and astrophysical role particularly important.

Many observational studies (Sun et al., 2009; Ettori, 2015; Lovisari et al., 2015; Eckert et al., 2016; Nugent et al., 2020) have shown that the baryon fraction in the central region ($< R_{500,c}$) of galaxy clusters and groups increases with the mass of the system. On the other hand, in the external regions, the gas distribution is hardly constrained by X-rays observations because of their low signal with respect to the local background. The peripheries of galaxy clusters and groups are physically more interesting because of the increased complexity of processes that regulate the status of the gas, including some expected residual amount of non-thermal pressure (e.g. Angelinelli et al., 2020). On the groups scale the baryon content is only half of the one expected from the self-similar scenario, differently from the expectations for a self-similar formation scenario, which is reached for the most massive systems (see e.g. review by Eckert et al., 2021). Studying how it evolves with redshift is more challenging, due to the current observational limitations.

In Gonzalez et al. (2013), the authors analyse the baryon content in a sample of 12 galaxy clusters at $z \sim 0.1$ and in the mass range between 1 and 5×10^{14} $M_{\odot}$, using XMM-Newton. They report a dependence of baryon fraction on the cluster's mass, with a slope of ~ 0.16. Moreover, they find that less massive systems ($M_{500} \leq 2 \times 10^{14}$ $M_{\odot}$) show a larger scatter in baryon fraction, with values which span from 60% to 90% of the WMAP7 (Komatsu et al., 2011) cosmological expectation $\Omega_{\rm bar}/\Omega_{\rm m}$. Nevertheless, also massive systems show a depletion with respect to the cosmological expectation of $\sim 18\%$. However, if the assumed cosmology is derived from Planck results (Planck Collaboration et al., 2013), the scatter for less massive system spans from 65% to 100% and the depletion for massive objects decrease to 7%,

becoming consistent with the cosmological expectation, because of the systematic errors associated with the masses measurements.

Chiu et al. (2016) study a sample of 14 galaxy clusters (with a median redshift of $z = 0.9$ and masses $M_{500} = 6 \times 10^{14}\ M_{\odot}$) selected from the South Pole Telescope (SPT) with follow-up data from XMM-Newton and Chandra telescope. They find a baryon fraction of 10.7% with a dependency on the clusters' mass but not on the redshift. In particular, the authors suggest that the slope of the $f_{\rm bar} - M_{500}$ relation is ~ 0.22, while the uncertainties on the mass estimations introduce an uncertainty in the redshift trend parameter which is larger than the statistical uncertainty, making impossible any clear evidence of a redshift dependency. Given the relations, the authors conclude that a simple hierarchical structure formation merger model is not sufficient to completely describe the accretion of galaxy clusters or groups. Significant accretion of galaxies and intracluster medium (ICM) from the field, combing with the loss of stellar mass from galaxies through stripping, are needed to completely explain the observational finding they discussed.

More recently, Akino et al. (2022) study a sample of 136 galaxy clusters and groups with M_{500} masses between 10^{13} up to $10^{15}\ M_{\odot}$ and a redshift range which spans from 0 to 1. They perform a joint analysis using HSC-SSP weak-lensing mass measurements, XXL X-ray gas mass measurements, and HSC and Sloan Digital Sky Survey multiband photometry. They find that the baryon fraction systems mass relation shows steeping of the slope moving from group regime to cluster one. Moreover, they find that the baryon fraction is $\sim 50\%$ for $\sim 10^{13}\ M_{\odot}$, $\sim 60\%$ for $\sim 10^{14}\ M_{\odot}$ and $\sim 100\%$ for $\sim 10^{15}\ M_{\odot}$ systems with respect to the cosmological expectation $\Omega_{\rm bar}/\Omega_{\rm m}$, assumed from Planck Collaboration et al. (2020). Even if the relation between the baryon fraction and the systems' mass is observed, for the baryon fraction-redshift it is not possible to obtain strong constraints because of uncertainties in the mass estimations.

Using a semi-analytic model that connects the "universal" behaviour of the thermodynamic profiles with the integrated properties of the ICM by modelling the departure from self-similarity also including a dependency of the gas mass fraction within R_{500} on the gas temperature and redshift, Ettori et al. (2022) constrain the former to be about $T^{0.4}$ and the latter in being almost negligible through the calibrations with a collection of recent published scaling laws.

Even if, from an observational point of view, constraining the gas content of galaxy groups and clusters is challenging and only for the most massive systems is available with the current X-rays facilities (Ghirardini et al., 2019), numerical simulations are able to correctly reproduce many different observed physical proprieties of the gas enclosed in such systems (see e.g. Oppenheimer et al., 2021; Gastaldello et al., 2021). Galaxy groups are the environment where the physical mechanisms that occur on galactic scale become less dominant, but still important, with respect

to the gravity that rules on the clusters scale. Therefore, numerical cosmological large-scale simulations are then needed to recover the physical properties of these elusive and numerous systems (Ettori et al., 2006; Planelles et al., 2013; Haider et al., 2016; McCarthy et al., 2017; Pillepich et al., 2018a; Biffi et al., 2018c; Vallés-Pérez et al., 2020; Galárraga-Espinosa et al., 2022; Wicker et al., 2022, and references therein), also to feed realistic prediction for next X-rays observatories generation (Roncarelli et al., 2018a).

Moreover, by connecting the co-evolution of galaxies and AGN in groups and clusters of galaxies and the induced circulation of baryons, many numerical works have explored the evolution of baryon fraction across cosmic time.

Duffy et al. (2010) used a sample of galaxy clusters extracted from the Over-Whelmingly Large Simulations project (Schaye et al., 2010). They find that simulations with strong feedback (both from AGN or Supernovae) decrease the baryon fraction on galaxy-scale haloes by a factor of 2 or 3. On groups and cluster scales, only simulations that include appropriate levels of AGN feedback can reduce the observed baryon fraction, at least within a factor ~ 2. Simulations that include inefficient cooling and stellar feedback, as well as the ones with strong feedback models, well reproduce the stellar fraction for massive objects. On the other hand, only the simulations with strong AGN feedback reproduce the observed star formation efficiencies.

Planelles et al. (2013) use a set of simulations using the TreePM–SPH GADGET-3 code, including a combination of stellar and AGN feedback and non-radiative effects. They find that for non-radiative and stellar-only feedback runs, the baryon fraction with R_{500} does not show any strong dependencies by the mass of the central clusters and it deviates from the cosmological expectation at large at $\sim 10\%$. On the other hand, AGN feedback is responsible for the depletion of baryon content in galaxy group mass regime, and only for massive systems, the cosmic value is reached. Moreover, they study possible dependencies of baryon fraction with radius from cluster's centre, system's mass, and redshift. They do not find any particular trend and they suggest that further improvements could be related to the extension of the simulations with other feedback models.

Henden et al. (2020) analyse the baryon content in the Feedback Acting on Baryons in Large-scale Environments (FABLE) simulations. These simulations are performed using the AREPO code (Springel, 2010). The prescription for stellar and AGN feedback are revisited versions of the models (Henden et al., 2018) adopted in the Illustis simulations (Vogelsberger et al., 2014). They find a good agreement between their findings and the observational proxies given by the X-ray observations. This implies that, when weak lensing measurements are considered and the hydrostatic mass bias is taken into account, the systems they analysed result too gas-rich, meaning that the models must be revisited in order to reproduce the most accurate

observational constraints. Moreover, their findings suggest that there is a different evolution with cosmic time in systems with different masses. Indeed, for massive systems ($M_{500} > 3 \times 10^{14}\ M_{\odot}$) the total gas and stellar mass are approximately independent of redshift at $z \leq 1$. Otherwise, less massive systems show a significant redshift evolution. The authors conclude that this is important for understanding the different growth of massive galaxy clusters and smaller systems. For the former is expected that they accumulated mass accreting low mass systems, while these later seem to show little redshift evolution themselves.

Davies et al. (2020) compare results from EAGLE (Schaye et al., 2015; Crain et al., 2015) and Illustris-TNG (Pillepich et al., 2018b; Nelson et al., 2018; Springel et al., 2018) simulations. Even if these simulations share aims and scope, they are very different in the recipes adopted for hydrodynamics solvers and the solutions of the physical processes included, mainly for the feedback one. In their work, the authors focus on the properties of the circumgalactic medium (CGM) and the quenching and morphological evolution of central galaxies. They find that in both EAGLE and Illustris-TNG simulations, the influence of halo properties on central galaxies is mainly driven by the expulsion of CGM. Moreover, feedback is also responsible for the heating of the remaining CGM, which contributes to the growth of the cooling time and inhibits the accretion of gas. The results are similar in both the suits used, but there are also some differences which will be in principle tested from an observational point of view. Indeed, studying the scaling relations between the column density of CGM OVI absorbers and the specific star formation rate of central galaxies at fixed halo mass, or between the CGM mass fraction of haloes and the accretion rate of their central Black Hole (BH), it is possible to disentangle between the different models adopted in the different simulations, which predict different scenario for these relations. The authors conclude that, even if some differences are observed between these simulations, the role of the AGN feedback on the CGM and central galaxies is dominant in the entire cosmic evolution of such systems.

Recently, Robson, Davé (2023) study a sample of simulated galaxy clusters and groups, with masses M_{500} from $10^{12.3} M_{\odot}$ to $10^{15} M_{\odot}$, extracted from the SIMBA simulations (Davé et al., 2019). They analyse the evolution of the X-ray scaling relations and X-ray profiles from $z = 3$ to $z = 0$. Moreover, they study the impact of different feedback models in comparison with the self-similar evolution. They find that halos show a consistent slope with the self-similar one for $z > 1.5$, while at lower redshifts the number of groups that deviate from self-similarity increases. Regarding the relation between gas fraction and halo mass, they observe a drop and increasing in the scatter with redshifts $z < 1.5$, especially for halos with $M_{500} < 10^{13.5} M_{\odot}$. Comparing simulations which include or exclude different feedback models, they observe that only the AGN feedback is able to highly influence the scaling relations they analysed. In particular, they find that for halos with $M_{500} < 10^{13.5} M_{\odot}$ the gas

fraction is lowered by the AGN feedback, meaning the reduction of X-rays luminosity and temperature of these systems. On the other hand, the gas metallicity seems to be the only parameter that is more influenced by stellar feedback with respect to AGN one. Robson, Davé (2023) highlight that their analysis wants to address the connection between galaxy quenching and X-ray properties across cosmic time and their results could be useful as a basis for comparison with other physical models and future observations.

In Angelinelli et al. (2023) (see Chapt. 5 for details) I studied the evolution of baryons across cosmic time in a sample of massive halos ($10^{13-15} M_{\odot}$) extracted from the *Magneticum* simulations. Interestingly, I found a clear time evolution in the baryon content of galaxy clusters and groups. Moreover, I studied the relations between the energy injected in the halos volume by the central AGN and the baryon, gas, and stellar contents. The comparison between my analysis and previous literature works highlights the needed of future X-rays deep observations to fully understand the AGN feedback processes.

Chapter 2

Cosmological simulations: numerical approach for large scale studies

In this chapter, I summarise the main proprieties of the simulations used in my Thesis. In Angelinelli et al. (2020) and Angelinelli et al. (2021), I analysed a sample of simulated galaxy clusters extracted from the *"Itasca Simulated Clusters"*, while in Angelinelli et al. (2022) and Angelinelli et al. (2023) I worked with galaxy groups and clusters selected from the *Magneticum* simulations suite. These simulations are based on very different numerical codes. *"Itasca Simulated Clusters"* is developed using the *ENZO* fluid dynamics code (Bryan et al., 2014), while *Magneticum* is based on the Smoothed Particle Hydrodynamical (SPH) code GADGET-3 (Springel, 2005). In Sect. 2.1 I discuss the main differences between the Eulerian and Lagrangian approaches, following the works by Dolag et al. (2008) and Vazza et al. (2011b); while in Sect. 2.2 and Sect. 2.3 I present the details of the different simulations used in our works.

2.1 Generalities of cosmological simulations: Eulerian vs Lagrangian techniques

Being the Universe's evolution dominated by dark matter, each cosmological simulation has first to solve the evolution of dark matter. The Cold Dark Matter (CDM) in the standard ΛCDM scenario can be described as a collisionless, non-relativistic fluid of particles of mass m, position $\mathbf{x}$ and momentum $\mathbf{p}$. Assuming an expansion of the Universe described by the Friedmann-Lemaître model, the fundamental equations that have to be solved to follow the evolution of dark matter are the Boltzmann equation:

$$\frac{\partial f}{\partial t} + \frac{\mathbf{p}}{ma^2}\nabla f - m\nabla\Phi\frac{\partial f}{\partial \mathbf{p}} = 0 \tag{2.1}$$

where $a = (1+z)^{-1}$ is the Universe scale factor, and the Poisson equation:

$$\nabla^2\Phi(\mathbf{x},t) = 4\pi G a^2[\rho(\mathbf{x},t) - \bar{\rho}(t)] \tag{2.2}$$

where Φ is the gravitational potential and $\bar{\rho}(t)$ is the background density. The proper mass density is given by:

$$\rho(\mathbf{x},t) = \int f(\mathbf{x},\mathbf{p},t)d^3p \tag{2.3}$$

The solutions of these equations are given by the equation of the motion of the particles, in the following forms:

$$\frac{d\mathbf{p}}{dt} = -m\nabla\Phi \tag{2.4}$$

and

$$\frac{d\mathbf{x}}{dt} = \frac{\mathbf{p}}{ma^2} \tag{2.5}$$

After introducing the peculiar velocity $\mathbf{v} = a\dot{\mathbf{x}}$, we can derive

$$\frac{d\mathbf{v}}{dt} + \mathbf{v}\frac{\dot{a}}{a} = -\frac{\nabla\Phi}{a} \tag{2.6}$$

where the Friedmann equation gives the time derivative of a:

$$\dot{a} = H_0\sqrt{1 + \Omega_0(a^{-1}-1) + \Omega_\Lambda(a^2-1)} \tag{2.7}$$

There are different methods to solve these equations. Indeed, it is possible to directly solve the Poisson equation or to trace the particles' motions. Briefly, these methods can be divided as following (see Dolag et al., 2008, for details of different techniques):

- Direct sum
- Tree
- Particle-Mesh
- TreePM/P^{3}M.

Dark matter and baryons evolution are solved differently in numerical simulations. Indeed, the Dark matter particles are assumed to be a collisionless and non-relativistic fluid, whereas the evolution of baryons is assumed to be described as an ideal fluid. The hydrodynamic equations that regulate the time evolution of baryons are the Euler equation, the continuity equation and the first law of thermodynamics:

$$\frac{d\mathbf{v}}{dt} = -\frac{\nabla P}{\rho} - \nabla\Phi \tag{2.8}$$

$$\frac{d\rho}{dt} + \rho\nabla\mathbf{v} = 0 \tag{2.9}$$

$$\frac{du}{dt} = -\frac{P}{\rho}\nabla\cdot\mathbf{v} - \frac{\Lambda(u,\rho)}{\rho} \tag{2.10}$$

where $\Lambda(u,\rho)$ is the cooling function which describes the radiative losses and the set of equations is closed if we assume an equation of state, which relates pressure and internal energy per unit mass u. The standard assumption is:

$$P = (\gamma - 1)\rho u \tag{2.11}$$

with $\gamma = 5/3$ for an ideal and mono-atomic gas. The solutions of the equations described above for dark matter and baryons component could be performed using two different families of numerical schemes: particle or grid-based methods. The former, also defined smoothed particle hydrodynamics (SPH) method solves the Lagrangian form of the Euler equations. These methods reach a good spatial resolution in high-density regions, whereas they achieve less strong results in low-density regions. The grid-based methods solve the fundamental equations based on grids, which represent the proprieties of the fluids. Using as examples the two different codes used to develop the simulations I analysed in my works, I describe the different approaches of the Eulerian and Lagrangian solvers in the next sections.

2.1.1 *ENZO*: the grid approach

ENZO is an adaptive mesh refinement (AMR) cosmological code (see Bryan et al., 2014, for the details of the code version adopted to develop the *Itasca* simulations), which combines a particle-mesh (PM) solver with an adaptive mesh method for ideal fluid dynamics.

The PM approach follows the dynamics of collisionless systems, a technique that is more effective than a straight solution of the Boltzmann equation because it directly computes the trajectories of a representative sample of individual DM particles. Using the cloud-in-cell (CIC) interpolation technique the DM particles are distributed in a grid, generating a DM density field. After this step, the baryons are added using the hydro solver of the code and the gravitational potential is calculated on the periodic root grid using fast Fourier transform algorithms. Lastly, the elliptic Poisson's equation is solved. When AMR simulations are performed, the potential is computed recursively within sub-grids at a higher resolution, and the boundary conditions are extrapolated using the parent grid's potential values. The gravitational force is then calculated for each cell inside sub-grids using a multi-grid relaxation technique. This makes it possible to utilise a gravitational softness of the order of the simulation's greatest resolution.

The Eulerian Piecewise Parabolic method (PPM) (Colella, Woodward, 1984) is

the main hydrodynamic solver adopted in *ENZO*. The PPM algorithm is one of a group of techniques that incorporate non-linear wave interaction and propagation calculations into the numerical method to enable accurate modeling of flow discontinuities. It is a more advanced variation of Godunov's shock-capturing technique (Godunov, Bohachevsky, 1959). It is at least second-order accurate in time and space, up to the fourth-order in the case of smooth flows and small time steps). As a result, energy conversion processes are treated optimally, inaccuracies caused by the grid's finite cell size are minimised, and a spatial resolution that is close to the nominal one is achieved.

Although the spatial resolution of the grid-based approaches is often poor, they perform remarkably well in both high and low-density regimes and shocks. In cosmological simulations, accretion flows which generate strong shocks with Mach numbers greater than 100 are very common. These strong shocks combined with numerical discretisation errors may cause inaccurate thermal energy estimations when the kinetic energy dominates the total energy. In these circumstances, the numerical techniques typically switch from formulations based on solving the total energy to formulations based on solving the internal energy in these hypersonic flow regions (Ryu et al., 1993; Bryan et al., 1995).

Other examples of grid-based codes are *Zeus* (Stone, Norman, 1992), *COSMOS* (Ricker et al., 2000), *FLASH* (Fryxell et al., 2000), *AREPO* (Weinberger et al., 2020).

2.1.2 GADGET3: the particles approach

The parallel TreeSPH code GADGET-3 (Springel, 2005) combines SPH with a hierarchical TreePM algorithm for gravitational forces. SPH samples the mass components of the fluid using a collection of tracer particles. From the Lagrangian of such systems, it is possible to recover the equation of motion for these tracer particles. A kernel interpolation approach is used to estimate the continuous fluid quantities (Monaghan, 1992). Each fluid element's thermodynamic state can be expressed in terms of either its thermal energy per unit mass, u_i, or its entropy per unit mass, s_i, which is considered as the independent thermodynamic variable (Springel, Hernquist, 2002). Moreover, the particle's adaptive smoothing lengths h_i are designed to have kernel volumes that contain a constant mass for the estimated density.

Discontinuities are easily developed by the flow of ideal gases and entropy is generated by micro-physics phenomena. In SPH code the generated shocks need to be captured by artificial viscosity. This viscosity acts only when fluid elements are in close proximity to one another in space, preventing particle interpenetration, and converting kinetic energy irreversibly into heat (Monaghan, Gingold, 1983). GADGET-3 uses an artificial viscosity based on an analogy with Riemann solutions

of compressible gas dynamics, as proposed by Monaghan (1997) and additional viscosity-limiters in presence of strong shear flows to alleviate spurious angular momentum transport (Steinmetz, White, 1997). Being the collisionless DM and the baryonic fluid represented by particles, the self-gravity of both components is computed by gravitational N-body methods. Moreover, GADGET-3 allows a hybrid method consisting of a combination of the PM method and the tree algorithm, which significantly reduces the computational time.

2.2 Details on the cosmological simulations used in this Thesis: the Itasca suite of Simulated Clusters

The *"Itasca Simulated Clusters"* sample (ISC)* is a set of simulated galaxy clusters in the $5 \cdot 10^{13} \leq M_{100}/M_{\odot} \leq 4 \cdot 10^{14}$ mass range simulated at uniformly high spatial resolution with Adaptive Mesh Refinement and the PPM in the *ENZO* fluid dynamics code (Bryan et al., 2014). These simulations do not include radiative processes and assumed the WMAP7 ΛCDM cosmology (Komatsu et al., 2011), with $\Omega_{\rm bar} = 0.0445$, $\Omega_{\rm DM} = 0.2265$, $\Omega_{\Lambda} = 0.728$, Hubble parameter $h = 0.702$, $\sigma_8 = 0.8$ and a primordial index of $n = 0.961$. Each cluster was generated from two levels of nested grids as initial conditions (each with 400^3cells and Dark Matter particles and covering 63^3 Mpc^3 and 31.5^3 Mpc^3, respectively). At run time, it is also imposed two additional levels of *static* mesh refinement in a 6.3^3 Mpc^3 box around each object, for a fixed $\Delta x = 19.6$ kpc/cell comoving resolution. More information on the ISC sample can be found in Vazza et al. (2017), Wittor et al. (2017) and Vazza et al. (2018a).

These simulations do not include radiative gas cooling, nor the effect of heating from star-forming regions, reionization or active galactic nuclei. Several studies have shown that the influence of non-gravitational effects is very limited in affecting the global properties of turbulence on the $\gg 100$ kpc scales of interest here, and outside of cluster cores, compared to the impact of mergers and accretion phenomena in the ICM (e.g. Vazza et al., 2012, 2013a; Valdarnini, 2019a). Even if cooling and feedback mechanisms tend to increase the number of density substructures and the clumping of gas in the ICM (e.g. Nagai, Lau, 2011; Roncarelli et al., 2013), the gas velocity fields produced by these simulations can be considered realistic enough for regions outside of the cluster core. Otherwise, the gas pressure model of these simulations is known to be smoother than in reality.

Moreover, as discussed in Vazza et al. (2013b), cooling, heating and numerical resolutions may affect the results of the analysis of the clump physics. The authors showed that in numerical simulations in which only cooling phenomena are con-

*http://cosmosimfrazza.myfreesites.net/isc-project

sidered, the number and the density of the clumps are substantially different from non-radiative simulations, both for perturbed systems and relaxed ones. However, considering only cooling processes is not representative of the observed Universe (e.g., clusters' cooling flow problem Fabian, 2012). On the other hand, numerical simulations that include AGN feedback, produce over-densities in agreement with the observed ones and in agreement also with the non-radiative simulations.

2.3 Details on the cosmological simulations used in this Thesis: the *Magneticum* suite of cosmological simulations

The sample of galaxy clusters and groups analysed as part of the simulated *Box2b/hr* of *Magneticum*[†] simulations. In Angelinelli et al. (2022) we used only the last available snapshot of these simulations at redshift $z = 0.25$, while in Angelinelli et al. (2023) we used eight different snapshots, corresponding at eight different redshifts (2.79,1.98,1.71,1.18,0.90,0.67,0.42,0.25). The high-resolution run of *Box2b* includes a total of $2 \cdot 2880^3$ particles in a volume of $(640\ h^{-1}\mathrm{cMpc})^3$. The particles masses are $6.9 \cdot 10^8\ h^{-1}\mathrm{M}_\odot$ and $1.4 \cdot 10^8\ h^{-1}\mathrm{M}_\odot$, respectively for dark matter and gas component and the stellar particles have softening of $\epsilon = 2\ h^{-1}\mathrm{ckpc}$. The cosmology adopted for these simulations is the WMAP7 from Komatsu et al. (2011), with a total matter density of $\Omega_\mathrm{m} = 0.272$, of which 16.8% of baryons, the cosmological constant $\Lambda_0 = 0.728$, the Hubble constant $\mathrm{H}_0 = 70.4$ km/s/Mpc, the index of the primordial power spectrum $n = 0.963$ and the overall normalisation of the power spectrum $\sigma_8 = 0.809$. In *Magneticum* several physical mechanisms are included and hereafter we highlight the more relevant ones: cooling, star formation and winds with velocities of 350 km/s (Springel, Hernquist, 2002); tracing explicitly metal species (namely, C, Ca, O, N, Ne, Mg, S, Si and Fe) and following in detail the stellar population and chemical enrichment by SN-Ia, SN-II, AGB (Tornatore et al., 2003, 2007) and cooling tables from Wiersma et al. (2009); black holes and associated Active Galactic Nuclei (AGN) feedback (Springel et al., 2005) with various improvements (Fabjan et al., 2010; Hirschmann et al., 2014) for the treatment of the black hole sink particles and the different feedback modes; isotropic thermal conduction of 1/20 of standard Spitzer value (Dolag et al., 2004); low viscosity scheme to track turbulence (Dolag et al., 2005c; Beck et al., 2016); higher order SPH kernels (Dehnen, Aly, 2012); passive magnetic fields (Dolag, Stasyszyn, 2009). Halos are identified using SUBFIND (Springel et al., 2001; Dolag et al., 2009), where the centre of a halo is defined as the position of the particle with the minimum of the gravitational potential. The virial mass, M_vir is defined through the spherical overdensity as predicted by the generalised spherical top-hat collapse model (Eke et al., 1996) and, in particular, it is referred to R_{vir}, whose overdensity to the critical density follows Eq. 6 of Bryan,

[†] http://www.magneticum.org

Norman (1998), which correspond to ≈ 117 at $z = 0$ for the given cosmology.

Many studies show that the galaxy physics implemented in the *Magneticum* simulations successfully reproduce the basic galaxy properties like the stellar mass-function (Naab, Ostriker, 2017; Lustig et al., 2022), the environmental impact of galaxy clusters on galaxy properties (Lotz et al., 2019) and the appearance of post-starburst galaxies (Lotz et al., 2021) as well as the associated AGN population at various redshifts (Hirschmann et al., 2014; Steinborn et al., 2016; Biffi et al., 2018a). At cluster scale, the *Magneticum* simulations have demonstrated to reproduce the observable X-ray luminosity-relation (Biffi et al., 2013), the pressure profile of the ICM (Gupta et al., 2017) and the chemical composition (Dolag et al., 2017; Biffi et al., 2018b) of the ICM, the high concentration observed in fossil groups (Ragagnin et al., 2019), as well as the gas properties in between galaxy clusters (Biffi et al., 2022). On larger scales, the *Magneticum* simulations demonstrated to reproduce the observed SZ-Power spectrum (Dolag et al., 2016) as well as the observed thermal history of the Universe (Young et al., 2021).

Chapter 3

Turbulent motions and their effects on hydrostic mass bias

Mass modelling of combined X-ray and Sunyaev Zel'dovich observations provides an estimate of turbulent pressure support in the outer regions of several galaxy clusters, but a clear description of this pressure given by residual gas motions is still missing. In Angelinelli et al. (2020), we test two different filtering techniques to disentangle bulk from turbulent motions in a sample of simulated galaxy clusters extracted from the *ITASCA* simulations (see 2.2 for details). We find that the radial behaviour of the ratio of non-thermal pressure to total gas pressure as a function of distance from the cluster's centre can be described by a polynomial function. The typical non-thermal pressure support in the centre of clusters is $\sim$5%, increasing to $\sim$15% in the outskirts, in line with the pressure excess found in recent X-ray observations. Moreover, we find that a relation between turbulent motions and hydrostatic bias can be established using the median properties of a sample of objects. We also estimate the contribution of radial accelerations to the non-thermal pressure support and conclude that it decreases moving outwards the cluster's core to its outskirts, from $\sim$40% to $\sim$15% respectively. Combing this contribution to the one provided by turbulence, we show that it might account for the entire observed hydrostatic bias in the innermost regions of the clusters, and for less than 80% in the peripheries. In this chapter, I will go through the methods, the results and related conclusions I presented in Angelinelli et al. (2020).

3.1 Methods

3.1.1 Cosmological selection of independent clusters

We take a new approach to building a large sample of galaxy clusters by treating clusters at different redshifts as dynamically independent. Under certain assumptions and for the sake of analysing the properties of turbulent motions in the ICM, these clusters can then be regarded as independent objects (Giocoli et al., 2012a; De Boni et al., 2016). Hence, we obtained a sample of 68 clusters from $z \simeq 2$ to $z = 0$ which are separated in redshift by $\langle \Delta z \rangle \simeq 0.12$ that, for the ΛCDM cosmology, it corresponds to $\langle \Delta t \rangle \simeq 0.91$ Gyr.

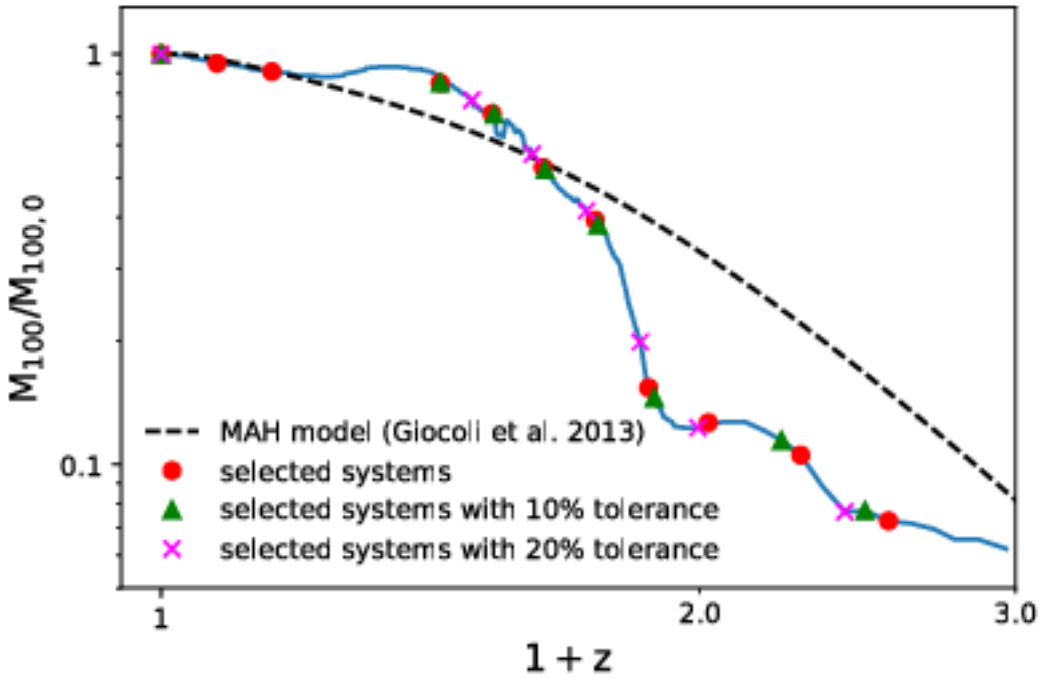

Figure 3.1: Example of real mass growth history (blue solid line) against the theoretical one (black dashed line) for one galaxy cluster of our sample. The different points represent the selected snapshots for a different level of tolerance (red points 0%, green triangle 10%, pink cross 20%, see Sect. 3.1.1 for details).

First, we computed $R_{100,c}$ and $M_{100,c}$ of each available snapshot for each object in the $z \leq 1$ range and reconstructed the mass growth of each cluster. Based on this, we could also compute the dynamical time of the cluster in each snapshot, assuming $t_{\rm dyn} \approx R_{100}/\sigma_v$, with $\sigma_v = \sqrt{G\ M_{100}/R_{100}}$, which gives us an estimate for the time between two dynamically independent realisations of the same object. Going back in time from $z = 0$, we selected those snapshots that are separated by one dynamical

time.
Finally, we have to verify that the mass growth between the snapshots is compatible with the expected growth. In particular, we checked that the corresponding M_{100} mass is *below or equal to* the predicted mass, within some tolerance ($0 \div 20\%$), based on the theoretical mass growth for a given M_{100} at $z = 0$ for the given cosmology, as outlined in Giocoli et al. (2012a) and De Boni et al. (2016).

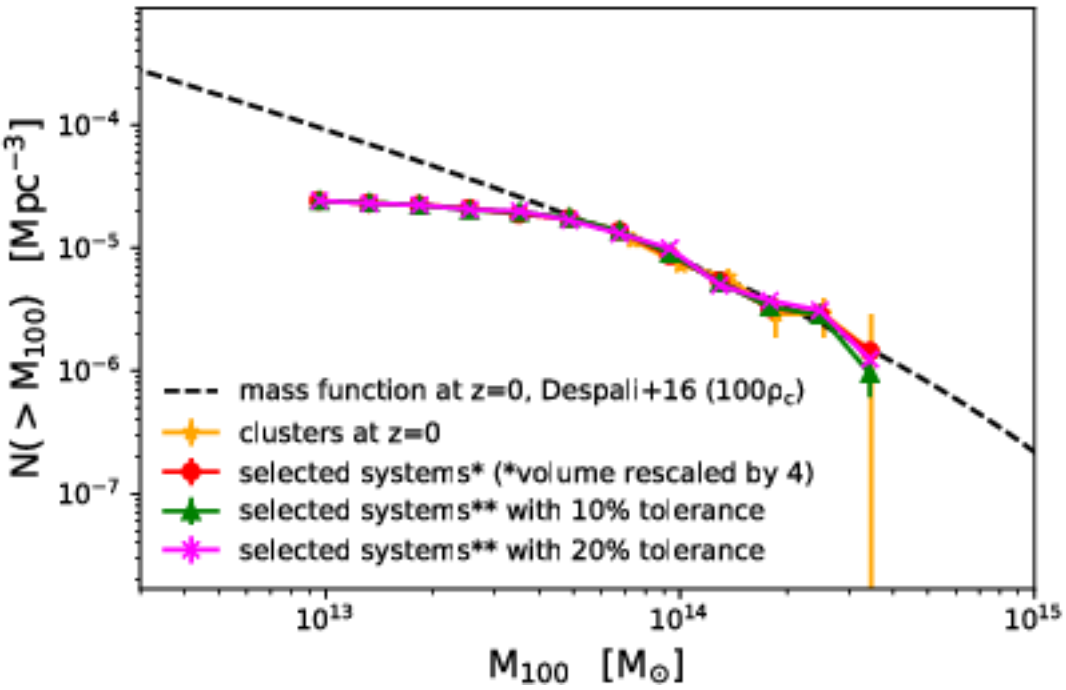

Figure 3.2: Mass functions of selected clusters at different levels of tolerance (i.e. the difference between the expected cosmological mass growth over a given time interval and the measured one). For comparison, the dashed black line gives the theoretical mass function for the cosmology used in our analysis at $z = 0$.

We treat each newly selected cluster, along with the mass growth, as independent from the previous one when calculating the theoretical mass accretion history (Giocoli et al., 2012b). In Fig. 3.1 the blue curve displays the mass growth history of one of our clusters from $z = 0$ to $z = 2$. The dashed black line shows the corresponding mass accretion history model starting from the $z = 0$ system. The various data points indicate the selected independent clusters along the growth with different tolerance thresholds. Thus, we obtained a final sample of 68 clusters (with 0% tolerance), yielding the total mass function shown in Fig. 3.2.

For comparison, the Despali et al. (2016) mass function at $z = 0$ for the same cosmology and total volume is shown as a black dashed line, and this suggests that our final sample is sufficiently mass completely for $M > 5 \cdot 10^{13} M_\odot$. This allows us

to proceed with a statistical study of the dependence of turbulence on mass, redshift and dynamical state parameters in sub-samples.

3.1.2 Identifying turbulence in the ICM

To disentangle turbulent from bulk motions, we use a small-scale filtering approach. In this technique, we assume that turbulent velocities are approximated as those parts of the gas velocities that fluctuate on the smallest scales, while bulk motions on the largest scales are approximately laminar. The validity of such an approach in cosmological simulations of galaxy clusters is supported by a large body of works on this subject (e.g. Dolag et al., 2005b; Lau et al., 2009; Vazza et al., 2011a, 2012; Miniati, 2014; Vazza et al., 2017). With the use of an appropriate small-scale filter, it is possible to define the velocity of the bulk motions and to calculate the velocity of turbulent motions as the difference between the total velocity and the one associated with the bulk motions. In this section, we discuss the updated filtering technique which we used to disentangle turbulent to bulk motions and the parameters that we tuned to limit the spurious contributions by shocks and clumps.

Iterative multi-scale filtering of turbulent motions

The non-thermal to total pressure ratio, α, is given by

$$\alpha \equiv \frac{P_{nt}}{P_{tot}}, \tag{3.1}$$

where P_{nt} is the non-thermal pressure caused by turbulent motions and P_{tot}=P_{nt}+P_{th} is the total pressure of the gas. P_{th} is the thermal gas pressure, computed as:

$$P_{th} = \frac{k_b}{\mu\, m_p} \cdot \rho \cdot T, \tag{3.2}$$

where ρ is the gas density, T is the gas temperature, k_b is the Boltzmann constant, m_p is the proton mass, μ is the mean molecular mass for electrons gas and its value is 0.59.

The non-thermal pressure P_{nt} is estimated as

$$P_{nt} = \frac{1}{3} \cdot \rho \cdot \delta v^2 \tag{3.3}$$

where δv is the local turbulent velocity; its estimate is in general non-trivial, and in the following, we discuss our fiducial procedure to reconstruct it in simulation, as well as test another method used in the literature (see Sec.3.1.2).

We use an adaptive, iterative filtering to disentangle turbulent from laminar motions in hydrodynamical grid simulations, which follows from previous works

by our group (e.g. Vazza et al., 2012, 2018a). The algorithm does not assume any a-priori coherence scale and the local mean velocity field around each cell is reconstructed with a multi-scale filtering technique, yielding the maximum scale of turbulent eddies by means of iterations in the smoothing scale length. The key assumption is that the gas flow in these simulations is generally part of a cascade of kinetic energy starting from scales much larger than the cell size.

In the original work, we applied a fixed tolerance on the increase of the local rms velocity amplitude with the filtering scale to stop the iterations, and find the smoothing scale of each cell (Vazza et al., 2012). For better removal of spurious contribution from shock waves, the method has been later combined with a velocity-based shock finder (Vazza et al., 2017).

As a novelty of this work, we apply here instead a more physical definition for the tolerance needed by our iterative algorithm to stop and converge on the local turbulent velocity field. In particular, we modify the multi-scale adaptive filtering by Vazza et al. (2012) to include the scale-dependent expected to increase in the local rms velocity. In the original work, we applied a fixed tolerance of 1% to stop the iterations and find the smoothing scale of each cell. Here instead, we adopt a more physical condition and, based on Kolmogorov's theory, we define a variable tolerance ϵ_w for each iteration from the following equation:

$$\epsilon_w = \frac{w^f - (w-1)^f}{w^f}, \tag{3.4}$$

where w is the size of the smoothing scale in the cell's unit and f is the exponent of the Kolmogorov-like relations, which we fix to 0.77 based on our test, as detailed in the Appendix 8.1. At the lower smoothing scale, this value is too high and the best choice is the minimum value between ϵ_w and the fixed tolerance used in Vazza et al. (2012). We verified that only for scales smaller than 200 kpc, ϵ is greater than 1%. As discussed in Vazza et al. (2012), we define the turbulent velocity in each cell as:

$$\delta \mathrm{v} = \mathrm{v} - \mathrm{v}_{sm}, \tag{3.5}$$

where v is the velocity field obtained from simulations and v_{sm} is the velocity field obtained by a 3D spatial filtering around each i-cell, defined as (in the simple 1D case):

$$\mathrm{v}_{sm;i} = \frac{1}{w} \Sigma_{j=i-\frac{w}{2}}^{i+\frac{w}{2}} \mathrm{v}_j, \tag{3.6}$$

where w is the size of the smoothing scale in the cell's unit, which determines the number of cells on which v_{sm} is calculated at each iteration step. We compute the relative variation of the turbulent local velocity δv between two successive iterations

$w-1$ and w as:

$$\delta_w = \frac{\delta \mathrm{v}_w^2 - \delta \mathrm{v}_{w-1}^2}{\delta \mathrm{v}_w^2}. \tag{3.7}$$

Wherever $\delta_w < \epsilon_w$, we find the value of turbulent velocity and the value of the smoothing scale. We test this procedure with two different exponents for the definition of the tolerance and also with a fixed tolerance as described in Vazza et al. (2012). The distribution of smoothing scales reconstructed by our algorithm is shown in Fig. 3.3.

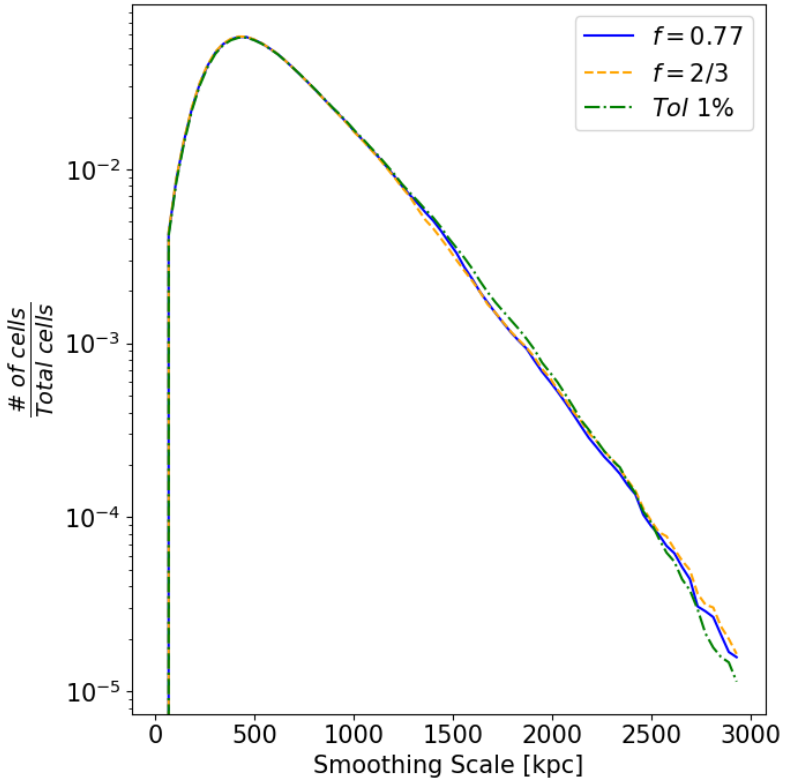

Figure 3.3: Median distribution of smoothing scales for a sub-sample of clusters at $z = 0$. The different colours identify different definitions of tolerance, i.e. by varying the exponent for the expected trend of the local rms velocity field as a function of the filtering scale, as explained in Sect. 3.1.2.

The reconstruction of the turbulent velocity before the application of other filtering techniques is shown in Fig. 3.4 for different configurations of the filtering.

Both Fig. 3.3 and Fig. 3.4 show that the definitions of tolerance have a minor effect on the distribution of the scales or the reconstruction of the turbulent velocity field. This behaviour is also visible in the radial profile of α, as shown in Fig. 3.5.

Here, it is clear that variations in the tolerance lead to small effects on the resulting non-thermal pressure. We also tested if this new definition of tolerance could affect the radial behaviour of the smoothing scales. We noticed an increase in

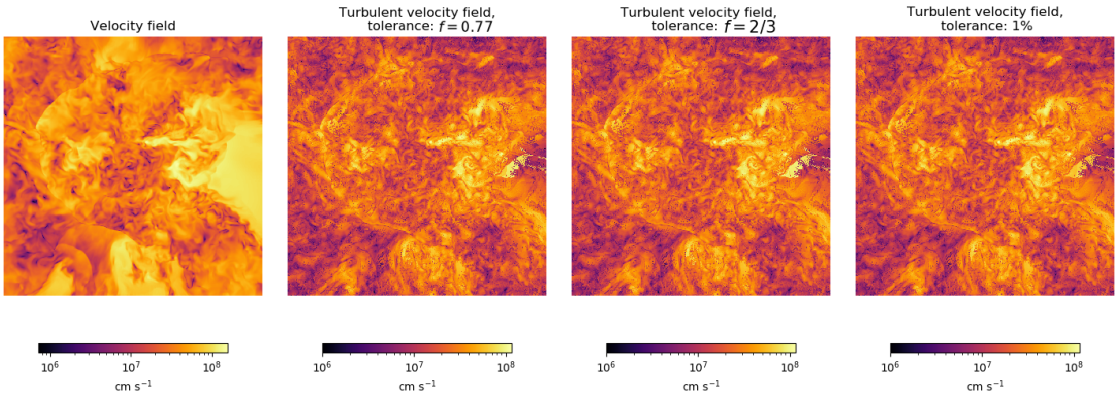

Figure 3.4: Maps of central slice of IT92_0 at $z = 0$. From left to right: First panel: Unfiltered velocity field [cm s^{-1}]; Second Panel: Filtered velocity field for tolerance determined by Kolmogorov relation with 0.77 exponent [cm s^{-1}]; Third panel: Filtered velocity field for tolerance determined by the standard Kolmogorov relation [cm s^{-1}]; Forth panel: Filtered velocity field for fixed tolerance equal to 1% [cm s^{-1}]

the smoothing scale of $\leq 20\%$ from the centre of the cluster to the outskirts, which also results in an average increase of the non-thermal pressure at most by $\leq 30\%$ (e.g. Vazza et al., 2012). However, the radial trend of the turbulent pressure support measured in our data (see the following Section) is not an artefact of the filtering procedure: when no filtering is applied, the predicted radial increase of non-thermal support from gas motions in our data (Vazza et al., 2018a) as well as in other works (e.g. Nelson et al., 2014a) is much steeper. In the following, we use the variable tolerance referred to in the $f = 0.77$ case, and combine this with the additional filtering of shocks and gas clumps, to better disentangle turbulent motions from other small-scale hydrodynamical features.

Radial filtering of turbulent motions

Other types of filtering techniques are available in the literature. For the sake of comparison, we also consider the model proposed by Nelson et al. (2014a, herefater N14) to our dataset. The definition of the fraction of the non-thermal pressure support in N14 is

$$\alpha_{\rm Tot} = \frac{P_{rand}}{P_{rand} + P_{therm}} = \frac{\sigma^2_{gas}}{\sigma^2_{gas} + (3k_bT/\mu m_p)}, \tag{3.8}$$

where the gas velocity dispersion σ_{gas} within radial shells is estimated as

$$\sigma_{gas} = \sqrt{\frac{\sigma_r^2 + \sigma_t^2}{3}} \tag{3.9}$$

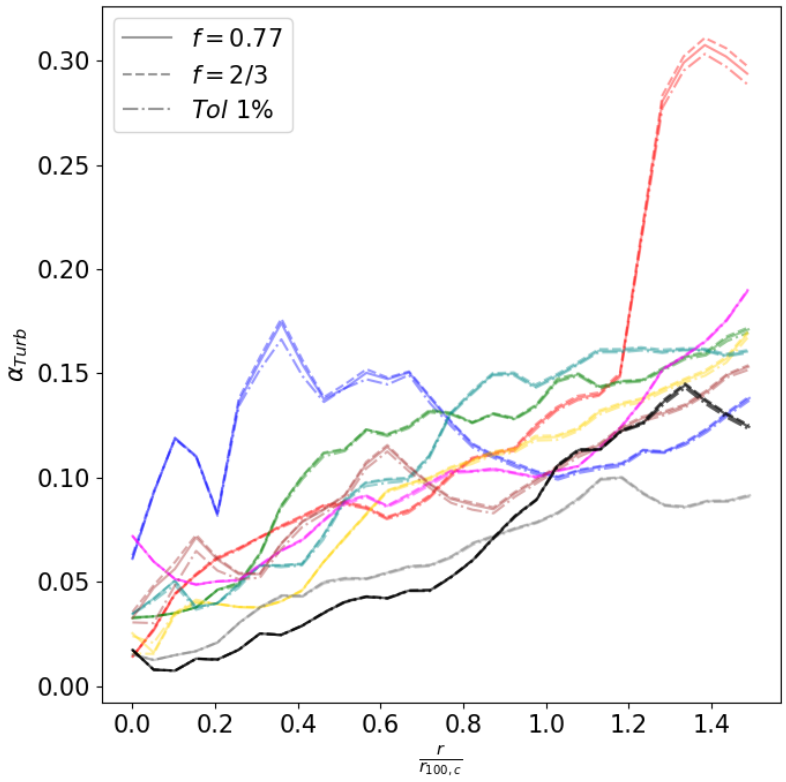

Figure 3.5: Radial profile of non-thermal pressure support for each cluster at $z = 0$ for different definitions of the tolerance, ϵ_w (Eq.3.4) used to stop out iterations on the local turbulent velocity field.

with σ_r and σ_t that are the radial and the tangential velocity component, respectively. These components are computed as:

$$\sigma_i = \sqrt{\langle v_i^2 \rangle - \langle v_i \rangle^2}, \tag{3.10}$$

where $\langle v_i^2 \rangle$ is the mean-square gas velocity, while $\langle v_i \rangle$ is the mean gas velocity, computed in each radial bin, both in radial and tangential direction. Both mean and mean-square gas velocity are weighted by the mass of each gas cell.

In the remainder of the Chapter, we will compare our definition of $\alpha_{\rm Turb}$ to the definition of $\alpha_{\rm Tot}$ above, in which the main difference between them stems from the definition of the "turbulent" velocity. In the N14 model, the turbulent velocity is basically the gas velocity dispersion within radial shells, while we filter out also motions which are coherent on small scales (e.g. bulk flows associated with clumps). The differences between these types of definitions will be discussed in more detail in the following sections (for additional discussion see also Vazza et al. 2018a).

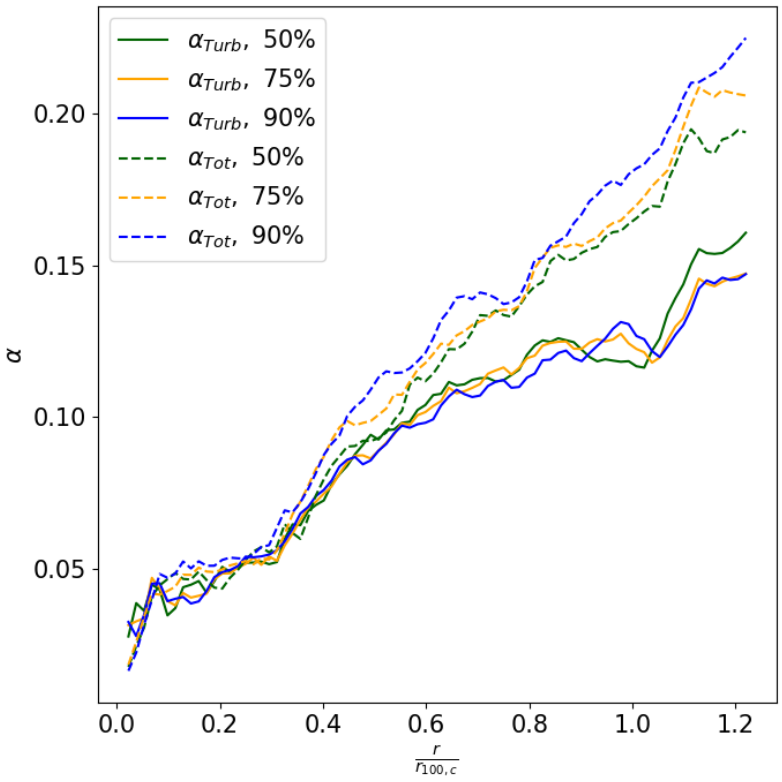

Figure 3.6: Radial profile of the median value of non-thermal pressure support for a sub-sample of clusters at $z = 0$, obtained by considering the 50%, 75% or 90% least dense cells at each radial bin from the centre of clusters. The solid lines are the result for α_{Turb}, while the dashed lines are the α_{Tot} ones.

Spurious contributions: shocks and density clumps filtering

Shock identification

In the study of turbulence, shocks can introduce spurious terms in the estimate of turbulent kinetic energy. In the presence of shocks, it is possible to use the Rankine-Hugoniot conditions and use velocity or temperature jumps to determine the Mach number. The Mach number is used to calculate the flux of kinetic energy that is dissipated into gas thermal energy. Here we use the shock finding algorithm based on the velocity jump between neighbouring cells (Vazza et al., 2009, 2017, 2018a). Detecting shocks with high Mach numbers is a relatively easy task in grid simulations with a uniform resolution (and all clusters in the *ITASCA* sample were simulated with uniform resolution in the "zoom" region), yet the detection of shocks with small Mach numbers is made uncertain by several factors such as numerical errors due to strong gradients or oblique directions of the shocks. In order to reduce the potential noise in the reconstruction of the local turbulent velocity field due to weak shocks sweeping our volume, we set a lower limit to the Mach number of $\mathcal{M}_{\rm thr} = 1.3$. We refer the reader to Vazza et al. (2017) and to Vazza et al. (2018a) for an overview

of this shock-finding method.

Clump excision
Dense clumps associated with infalling structures can introduce a bias in the estimate of the local velocity field (e.g. Dolag et al., 2005b), due to the fact that these structures are correlated with large bulk motions, mostly in the inwards radial direction (e.g. Vazza et al., 2018a). These spurious terms could lead to an overestimate of the non-thermal pressure support. Clumps in simulations are routinely identified as peaks with high-density contrast in the radial gas density distribution of the host cluster (e.g. Ruszkowski, Oh, 2011; Zhuravleva et al., 2011). Therefore, restricting the analysis to a fraction of the gas density distribution at every radius, obtained after excising the highest percentiles in the gas distribution at each radius, is a practical way to limit the bias from the most *clumpy* structures in the ICM. Hence, we tested three different values for masking the densest cells (considering gas density only) at each radius from the cluster centre: the cells in the top 50%, 25% or 10% of the gas density distribution at every radius. As shown in Fig. 3.6, the profile of non-thermal pressure support α_{Turb} we can derive in our clusters at $z = 0$ is overall quite robust against a more restricting selection of cells in the low-density part of the distribution at each radius. On the other hand, when we use the same cells selection to compute the radial profile of α_{Tot}, we notice a larger impact of the gas clumping factor, shown by the increase of non-thermal support when denser cells are retained in the procedure (see Zhuravleva et al., 2013, for a detailed study on the ICM inhomogeneities). This suggests that α_{Tot} is susceptible to clump expulsions, while α_{Turb} is more stable with respect to the presence of clumps. Based on our results and previous work (e.g., Zhuravleva et al., 2013; Roncarelli et al., 2013), we will use the 90% masking in our analysis which roughly mimics the approach applied to the X-ray spatial analysis (e.g., Ghirardini et al., 2017; Eckert et al., 2019). Our tests show that the adoption of $\mathcal{M} \geq 1.3$ and the exclusion of cells in the top 10 percentile in density in each shell yields the best filtering combination. In the following, we will refer to the results of our best filtering configuration as the turbulent velocity.

3.2 Results

Our projected maps of gas density, dark matter density, gas temperature and unfiltered velocity field, as well as the turbulent velocity field and shocks for one of the objects in our sample, are given in Fig. 3.7. The maps well illustrate the complex gas flow patterns that are typically found in the simulated clusters at all epochs, with expanding shocks that mark recent heating episodes in the ICM (top and lower right panels) and a mixture of large-scale bulk flows (lower left panel) and small-scale turbulent motions (lower central panel).

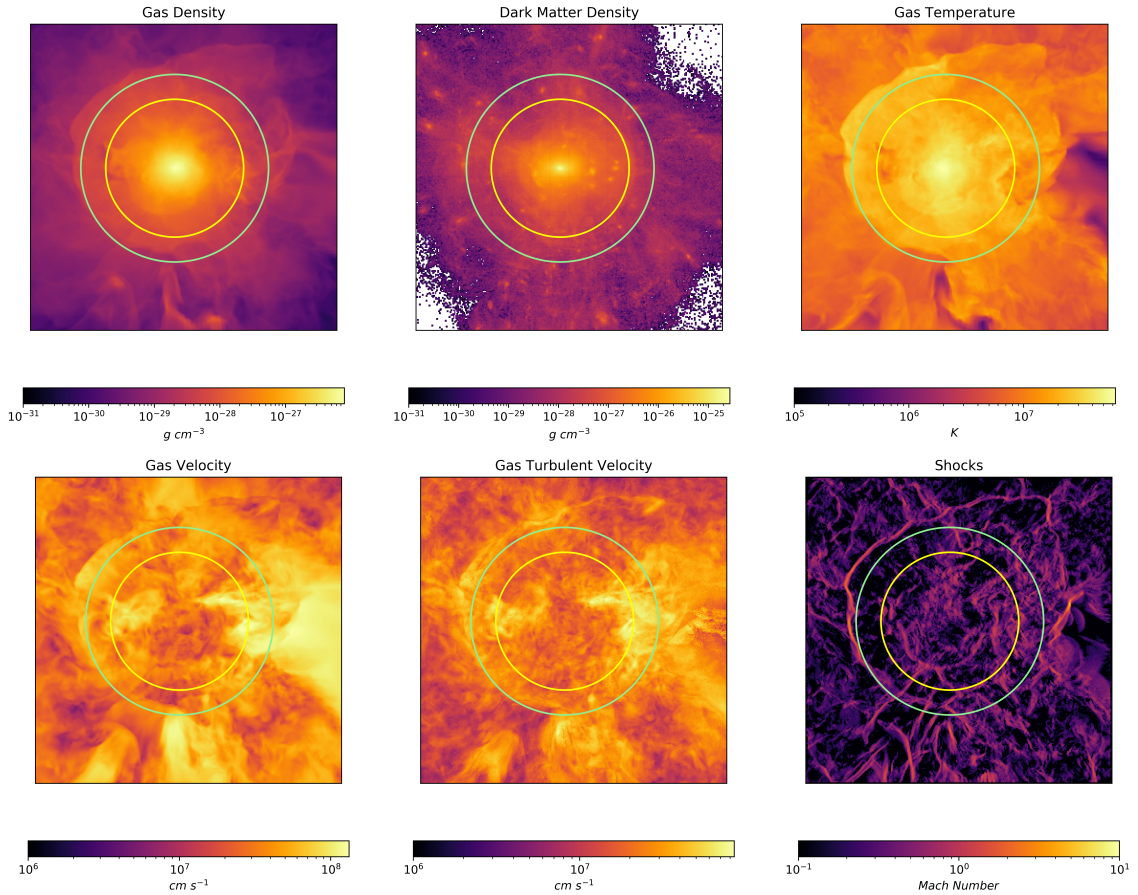

Figure 3.7: Maps of the central region in IT92_0 at $z = 0$. The inner circle is $R_{200,c}$, while the outer one is $R_{100,c}$. From top left to bottom right: First panel: gas density in $g\ cm^{-3}$; Second Panel: dark matter density in $g\ cm^{-3}$; Third panel: gas temperature in K; Forth panel: unfiltered velocity field in $cm\ s^{-1}$; Fifth panel: turbulent velocity field in $cm\ s^{-1}$; Sixth panel: Shocks Mach Number.

To extract the radial profiles of α, we first define the cluster centre based on the maximum value of the thermal energy of the gas at each snapshot since this definition of the centre results makes the most stable, in highly perturbed systems, as well.

We consider mass-weighted values of the pressures, estimated on the same cells selected with our turbulent filtering technique (see Sec.3.1.2).

In the following analysis, we consider two methods to estimate the ratio $\alpha = P_{nt}/P_{tot}$: (i) either applying our filtering technique ($\alpha_{\rm Turb}$) or the N14 model ($\alpha_{\rm Tot}$); (ii) by comparing the mass estimated from the hydrostatic equilibrium equation with the total mass distribution ($\alpha_{\rm HS,Turb}$ or $\alpha_{\rm HS,Tot}$). Furthermore, when we refer to α or $\alpha_{\rm HS}$, we are considering both "Turb" and "Tot" quantities at the same time. Otherwise, if we consider only one of these quantities, we will indicate it with the related pedice. In Fig. 3.8, we show values of mass and non-thermal pressure

support $\alpha_{\rm Turb}$ at radius $R_{100,\rm c}$ in the function of redshift. We notice that there is a strong relation between mergers and an increase of $\alpha_{\rm Turb}$. Instead, when the cluster is not affected by mergers the value of $\alpha_{\rm Turb}$ decreases. The red points in Fig. 3.8 are the selected snapshots obtained by the selection described in Sect. 3.1.1. In the following, we will refer to three different typical radii $R_{500,\rm c}$, $R_{200,\rm c}$, $R_{100,\rm c}$ and $R_{200,\rm m}$. From the cluster's centre to the peripheries we find $R_{500,\rm c}$:$R_{200,\rm c}$:$R_{100,\rm c}$:$R_{200,\rm m}$ and they are related by these approximated ratios 1:1.4:1.9:3 (see Walker et al., 2019, and references therein). Hereafter, we will show in the plots, the median or mean value and the related σ dispersion of data for the different quantities. To have an asymmetric dispersion, which well represents the real distribution of the data, the σ dispersion is computed as the 16th quantile and 84th one, of the distributions in each radial shell, for the -1σ and +1σ respectively.

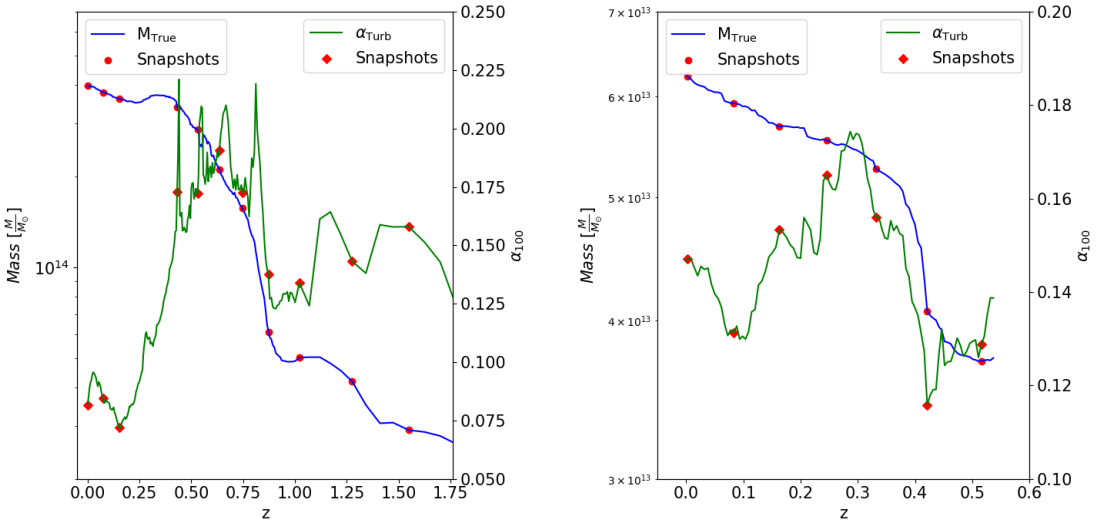

Figure 3.8: $M_{100,c}$ growth (blue solid line) and non-thermal pressure support at $R_{100,\rm c}$ time behaviour (green solid line) for IT92_0 and IT90_4. The red points are the selected snapshots as explained in Sect. 3.1.1

3.2.1 Parametrising the profile of non-thermal pressure support in galaxy clusters

The radial distribution of non-thermal pressure support we find in our cluster sample is so regular that an analytic formula reproduces well the trend of $\alpha_{\rm Turb}$ with radius:

$$\alpha_{\rm Turb}(r) \;=\; a_0 \;\cdot\; \left(\frac{r}{R_{200,\rm m}}\right)^{a_1} \;+\; a_2. \tag{3.11}$$

The physical meaning of our parameters is straightforward: a_0 represents the normalisation of $\alpha_{\rm Turb}$ at $R_{200,\rm m}$, a_1 gives the slope of the profile and a_2 gives the

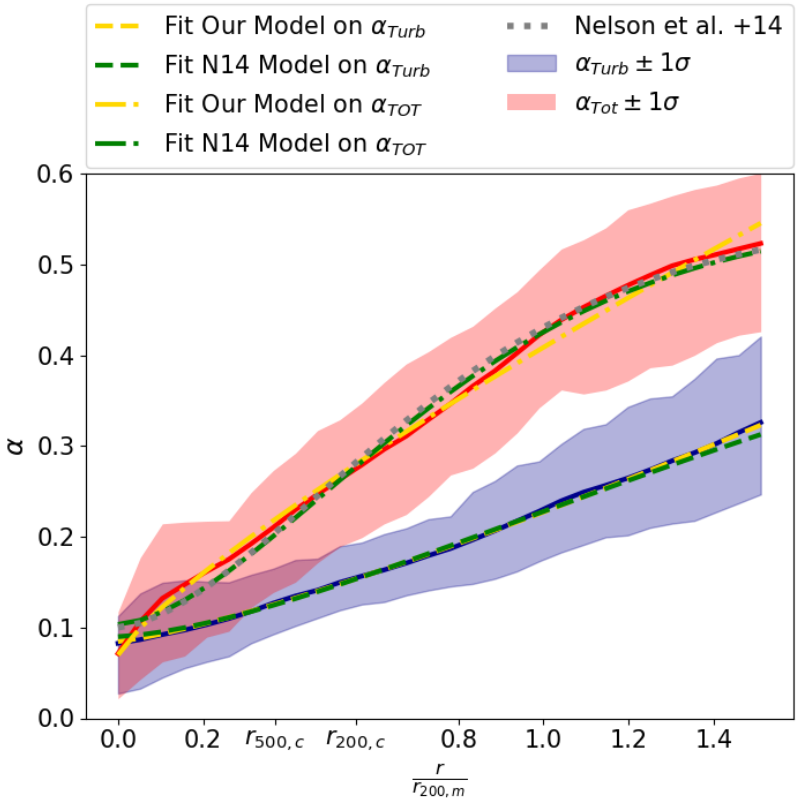

Figure 3.9: Radial profile of median value of $\alpha_{\rm Turb}$ (blue solid line) and $\alpha_{\rm Tot}$ (red solid line). The shadow regions represent the 1σ distribution of the sample. The yellow and green dashed lines are the best fits of our model and N14's one on $\alpha_{\rm Turb}$ profile, while the dash-dotted ones are the fits of the models on the $\alpha_{\rm Tot}$ profile. The dotted grey line is the profile obtained in N14. As described in Sect. 3.2, the σ values are asymmetric compared to the median. The scatter around the median is here represented by the 16th and 84th percentiles. The median values of the radial distribution of the relative errors are -0.24 and $+0.26$.

value of non-thermal support in the cluster centre. We notice that Shi, Komatsu (2014) develop an analytic model to describe the trend of $\alpha_{\rm Turb}$ with the radius. They use three fundamental time scales to develop their model: turbulence dissipation time-scale, $\rm t_d$, also controlled by the efficiency of energy transfer from the largest scales, where most of the turbulence energy is stored, to smaller scales; the time elapsed between the initial time and the time of observation, ($\rm t_{obs} t_i$), which characterises the age of the cluster; and a time-scale characterising the mass growth rate of the cluster defined by $\rm t_{growth}$, which also determines the rate at which turbulence energy grows. They define also turbulence injection efficiency η, a parameter that should be determined primarily by the Mach number of the internal shocks, and which they constrain to be $\eta \approx 0.5 - 1$ based on simulations. However, the turbulence injection efficiency is strongly correlated with the slope of the fitting formula, and compared to Shi, Komatsu (2014) we report a lower injection efficiency, which

may also be connected to the role of numerical dissipation of our hydro scheme on small scales. We also notice that in real systems, and especially at low mass, the turbulence in the core may be dominated by the interplay of cooling and feedback (e.g., Brighenti, Mathews, 2002; Brüggen, 2003; Gaspari et al., 2018), hence our a_2 may be underestimated. However, we notice that, although our simulations do not include feedback mechanism or cooling, our estimate for a_2 is close to the only available direct spectral measurement from the *Hitomi* (Hitomi Collaboration et al., 2016).

Nelson et al. (2014a) present the following analytical fit to the radial distribution of the non-thermal pressure in a data set of 65 simulated galaxy clusters with masses in a range similar to ours:

$$\frac{P_{rand}}{P_{tot}}(r) = 1 - A\left\{1 + \exp\left[-\left(\frac{\frac{r}{R_{200,\mathrm{m}}}}{B}\right)^{\gamma}\right]\right\}, \tag{3.12}$$

with best-fit values $A = 0.452 \pm 0.001$, $B = 0.841 \pm 0.008$ and $\gamma = 1.628 \pm 0.019$. This fit formula is based on three-dimensional gas velocity fields without explicitly filtering out bulk motions (for details see Sect. 3.1.2). The same function also fits our data after filtering, albeit with a slightly higher χ^2 value (see Tab. 3.1). In Fig. 3.9, we show the different fits over-plotted to the median radial profiles of our objects.

From the comparison of the χ^2, it appears that our model yields a better fit to the data than, or as good as, the model in N14. The fit suggested by N14 can also fit our data, albeit with different parameters. However, the advantage of our best-fit form is that the fit parameters have a simple physical meaning.

As we discussed already in Vazza et al. (2018a), the differences between our results and N14 stem from the different choices in filtering velocities, and the two methods yield formally the same result if no filtering is applied to the 3-dimensional velocity field in our simulations. However, our work suggests that our filtering yields the isotropic part of the turbulent pressure while filtering out the spurious contribution to the non-thermal pressure support by inward radial motions.

We apply our model also to the profile of α_{Tot} and compare the results with the fit obtained by the N14 model. The results are shown in Fig. 3.9 and Tab. 3.1. We notice that our model can reproduce also the α_{Tot} trend. From the comparison of χ^2 we can notice that, as for α_{Turb} case, our model is slightly preferred over the N14 model.

We investigated the possible correlations between the non-thermal pressure and mass, redshift and sparsity of each cluster in our sample. The Sparsity is defined as

Our model

	a_0	a_1	a_2	χ^2
$\alpha_{\rm Turb}$	$(1.427\pm0.002)\cdot10^{-1}$	1.246 ± 0.005	$(8.44\pm0.02)\cdot10^{-2}$	10^{-4}
$\alpha_{\rm Tot}$	$(3.388\pm0.009)\cdot10^{-1}$	0.822 ± 0.004	$(6.97\pm0.08)\cdot10^{-2}$	0.001

N14 model

	A	B	γ	χ^2
$\alpha_{\rm Turb}$	$(4.550\pm0.003)\cdot10^{-1}$	1.966 ± 0.004	1.508 ± 0.005	$2\cdot10^{-4}$
$\alpha_{\rm Tot}$	$(4.483\pm0.003)\cdot10^{-1}$	0.865 ± 0.002	1.633 ± 0.006	0.046
N14	0.45	0.84	1.63	

Table 3.1: Parameters and values of χ^2 statistical test for the different formula used to fit the radial behaviour of $\alpha_{\rm Turb}$ and $\alpha_{\rm Tot}$. We show also the values of the parameters presented in N14. The errors on the parameters are the values at 3σ confidence.

the ratio between the total mass within $R_{100,\rm c}$ and $R_{200,\rm c}$:

$$s = \frac{M_{100,c}}{M_{200,c}}. \tag{3.13}$$

For all of these quantities, we divided our samples into three sub-samples which contain the same number of objects. The results are discussed in Sect. 3.2.3. Here we just note that our model reproduces the radial behaviours of α for all subselections of our sample. The same best-fit parameters are valid for all subsamples, suggesting that no strong dependencies between the non-thermal to total pressure ratio and the cluster mass, the redshift or the mass sparsity can be detected in our sample.

Recently, Eckert et al. (2019) present some constraints on the non-thermal pressure support in a sample of 12 massive, nearby and mostly relaxed clusters observed in X-rays with XMM-Newton and in SZ with Planck. They compare the values of the hydrostatic mass, recovered up to $R_{200,\rm c}$ by using a combination of the SZ pressure profile and X-ray based thermodynamical properties (see for details Ettori et al., 2019), with mass estimates based on the assumption that hydrodynamical simulations provide the correct baryon fraction distribution in clusters. In the latter estimate, the gas mass is inferred directly from X-ray measurements and the contribution of the mass in stars is evaluated statistically from published work. From the mismatch between the two estimates of the total mass, it is then possible to infer the hydrostatic bias, which turns out to be, on average, consistent with the results obtained by other methods (see Ettori et al., 2019).

If we attribute the origin of this hydrostatic bias to the contribution from a non-thermal pressure component, $P_{\rm nt}(r)$, we can write (e.g. Eckert et al., 2019):

$$\frac{d}{dr}(\mathrm{P_{th}(r)} + \mathrm{P_{nt}(r)}) = -\rho\frac{GM_T(<r)}{r^2}, \tag{3.14}$$

where $\mathrm{P_{th}}$ is the thermal pressure component, and M_T is the total mass. By defining $\alpha(r) = \mathrm{P_{nt}}(r)/\mathrm{P_{tot}}(r) = \mathrm{P_{nt}}(r)/[\mathrm{P_{nt}}(r)+\mathrm{P_{th}}(r)]$, the equation above can be rewritten as:

$$M_T(< r) = M_H(< r) + \alpha(r) M_T(< r) - \frac{\mathrm{P_{th}} r^2}{(1-\alpha)\rho G}\frac{d\alpha}{dr}, \tag{3.15}$$

where M_H is the hydrostatic mass:

$$M_H(i) = -\frac{\left(\frac{d\mathrm{P_{th}}}{dr}\right)_i r_i^2}{G\rho_{i-1}}. \tag{3.16}$$

From the equations above and using our radial profiles of total mass and hydrostatic mass, we can then define $\alpha_{\rm HS}$ at each radius r as:

$$\alpha_{\rm HS} = 1 - \frac{M_H + \sqrt{(M_H)^2 - 4M_T \mathrm{P_{th}} \frac{r^2}{\rho G}\frac{d\alpha}{dr}}}{2M_T}, \tag{3.17}$$

and link it to the parameter b, which is usually used in literature to identify the hydrostatic mass bias (e.g., Salvati et al., 2019; Pratt et al., 2019) and defined as

$$M_H = (1-b)M_T, \tag{3.18}$$

to obtain

$$b = \frac{\alpha + A}{1 + A}, \tag{3.19}$$

where A encloses the pressure's contributions

$$A = (\mathrm{P_{th}} + \mathrm{P_{nt}})\frac{d\alpha/dr}{d\mathrm{P_{th}}/dr}. \tag{3.20}$$

We notice that if α is radially constant, then $b = \alpha$. However, α is not generally constant with radius in our sample (see Fig. 3.9). Hence the $d\alpha/dr$ term plays a small but non-negligible role here. As described below, we use both $\alpha_{\rm Turb}$ and $\alpha_{\rm Tot}$ profiles to estimate $d\alpha/dr$ and propagate it to the measurement of $\alpha_{\rm HS}$. We show in Fig. 3.10 the radial profile of the term A, where the different effect of the radial derivative of α allows us to distinguish between the "Turb" and "Tot" cases.

We compute the hydrostatic mass M_H through the radial derivative of thermal pressure associated with a spectroscopic-like temperature profile and computed as

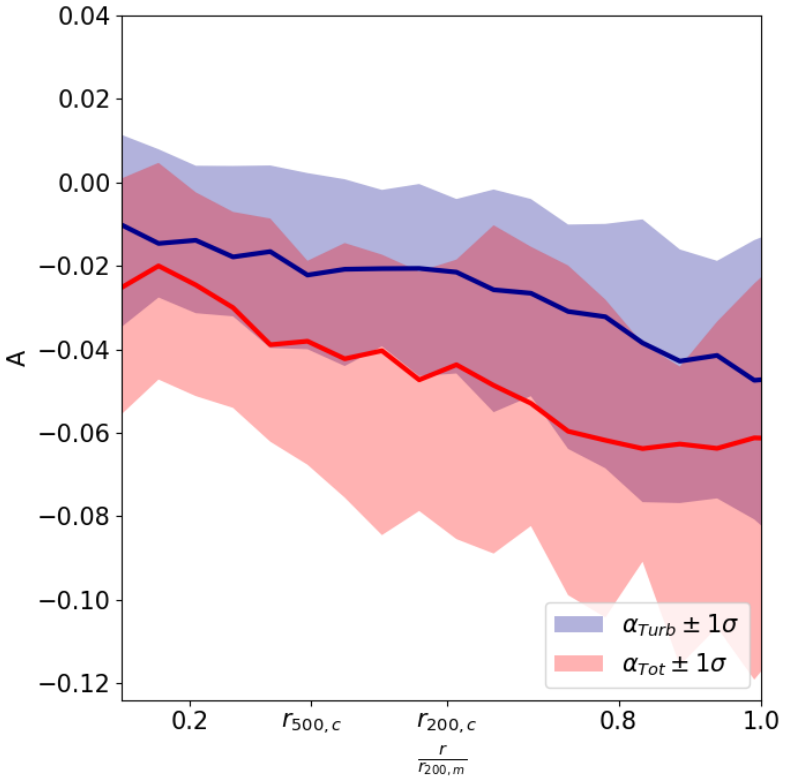

Figure 3.10: Radial profiles of A pressure correction term of Eq. 3.19. In blue solid line, the profile computed for the radial derivative of $\alpha_{\rm Turb}$, while in red solid line the profile computed for the $\alpha_{\rm Tot}$. The shadow regions represent the 1σ distribution of the data.

follows*:

$$\left(\frac{d\mathrm{P_{th}}}{dr}\right)_i = \frac{\mathrm{P_{th},}_{i-2} - 6\ \mathrm{P_{th},}_{i-1} + 3\ \mathrm{P_{th},}_{i} + 2\ \mathrm{P_{th},}_{i+1}}{6r_i}, \tag{3.21}$$

where $\mathrm{P_{th}}$ is the thermal pressure defined as in Eq. 3.2 and i represents each radial shell. To limit the contribution from dense, self-gravitating clumps, we use the same masking procedure of Sect. 3.1.2, in order to consider only the thermal pressure exerted by the gas within the cluster. We also applied a box-averaged smoothing function along ten radial shells at density, thermal pressure and $\alpha_{\rm Turb}$ or $\alpha_{\rm Tot}$ profiles, in order to reduce numerical fluctuations in the profiles. This procedure allows us to obtain smoothing profiles which are more similar to the typical profile obtained in observational works and which are also less affected by spurious numerical effects.

*We tested this procedure in idealised (semi-analytically generated) control atmospheres and we verified that our approach is robust to recover the correct mass bias (within a few $\sim 0.01\%$) for the typical pressure profile of ICM. Furthermore, we also tested smoothing our data on scales larger than our spatial resolution (19.6 kpc/cell), in order to mimic was can be realistically done by X-ray observations, *worsens* the match between the hydrostatic mass and the total mass, especially in 3-dimensional simulated clusters as the smoothing the accuracy with which the internal substructures orbiting in the cluster potential well can be modelled.

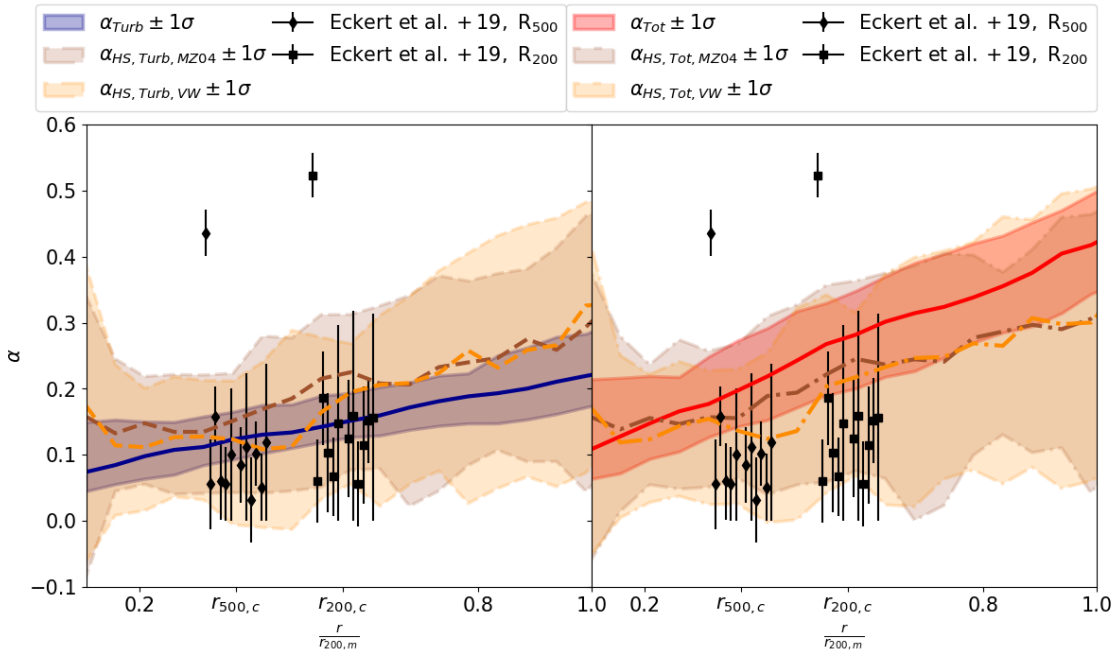

Figure 3.11: On the left panel, we show the comparison between $\alpha_{\rm Turb}$ (blue solid line) and $\alpha_{\rm HS,Turb}$ computed with volume-weighted profile (orange dashed line) and with the spectroscopic-like temperature (brown dashed line). On the right panel (with the same colour-coded legend of the left panel) the result for $\alpha_{\rm Tot}$ against $\alpha_{\rm HS,Tot}$. The shadowed regions give the 1σ distribution of the sample for all the profiles. The black points represent the results of Eckert et al. (2019).

For each radius, we computed the value of $\alpha_{\rm HS}$ applying the Eq. 3.17. The radial derivative of α allows us to define two different $\alpha_{\rm HS}$, already presented above, $\alpha_{\rm HS,Turb}$ and $\alpha_{\rm HS,Tot}$. To check the dependencies of $\alpha_{\rm HS}$ on physical quantities such as mass, redshift and mass sparsity of clusters, we used the sub-samples analysis presented in Sect. 3.2.3. We notice that the variance of the $\alpha_{\rm HS}$ data is larger with respect to the α ones. As for α profiles, also for $\alpha_{\rm HS}$ ones, we could not identify any strong correlation with the physical properties of host clusters.

Several factors may influence the comparison between observational results with numerical ones. To test different choices to compute radial profiles of thermodynamical quantities, in a way similar to what is commonly feasible with observations, we built both a volume-weighted version of $\alpha_{\rm HS}$, as well as one using the "spectroscopic-like" temperature suggested by Mazzotta et al. (2004) (hereafter MZ04), which approximately takes into account the real spectroscopic response of X-ray detectors in determining the average gas temperature in the ICM. The results are shown in Fig. 3.11.

We notice that there are no strong differences between the volume-weighted pressure profile and the pressure profile based on the spectroscopic-like temperature.

This is consistent with the finding that the hydrostatic mass bias is relatively small in AMR grid-based simulations, while the temperature bias could be large in SPH simulations, owing to the enhanced formation of substructures there (Rasia et al., 2014a). We also notice how our definition of turbulent motions is more in agreement with the radial trend of $\alpha_{\rm HS}$, mostly in the inner regions that are more accessible to the present X-rays observations. Instead, the $\alpha_{\rm Tot}$ is larger than $\alpha_{\rm HS}$ at any radius. In the following sections, we will use the $\alpha_{\rm HS}$ parameter to easily compare our results to the ones in Eckert et al. (2019), as shown in the plots (black points with error-bars).

Similarly to Vazza et al. (2018a), but extended in the present study to the full set of simulated clusters, the scatter in the simulations is typically larger than the one observed in real cluster data, with the exception of A2319 (Ghirardini et al., 2018), which probably comes from the intrinsic difference in the two samples: the X-COP sample contains by selection mostly relaxed clusters, while our sample contains a larger variety of objects. Despite this promising average agreement between these two samples, in the next section, we investigate the caveats which may lead to a mismatch between observational estimates of $\alpha_{\rm HS}$ and the underlying presence of turbulent motions in single objects.

It shall be noticed that all approaches are in better agreement in the centre of clusters, although the scatter is large for the distribution of $\alpha_{\rm HS}$. Interestingly, the central median values of $\alpha_{\rm Turb}$ and $\alpha_{\rm Tot}$ for the sample are in the $5-8\%$ range, which is reasonably close to the most recent estimates from the centre of the Perseus cluster, i.e. $\sim 2-6\%$ (Hitomi Collaboration et al., 2018). This trend is well explained by Lau et al. (2017) and Bourne, Sijacki (2017).

3.2.2 On the relation between turbulence and hydrostatic bias

To investigate the relation between turbulence and hydrostatic bias in a more systematic way, we compare the radial dependence of α and $\alpha_{\rm HS}$. We consider the median values of the entire sample of α and $\alpha_{\rm HS}$ in each radial shell. The results are shown in the left panel of Fig. 3.12.

If turbulence and hydrostatic bias were perfectly correlated, the data would closely follow the bisector of the plot. Instead, we find that their relation is well described by a function $\alpha_{\rm HS} = a_0 \times (\alpha/0.2)^{a_1} + a_2$ (see Fig. 3.12). This suggests that in general both our definition of turbulence and the N14 model do not trace in a 1-to-1 relation the hydrostatic bias. From Fig. 3.12, it also appears that the N14 definition of turbulence is much closer to the 1-to-1 relation between turbulence and hydrostatic bias. Considering that the N14 model includes not only turbulent motions but also the kinetic pressure associated with bulk motions, we conclude that the latter represents an important ingredient for the mass bias, especially when

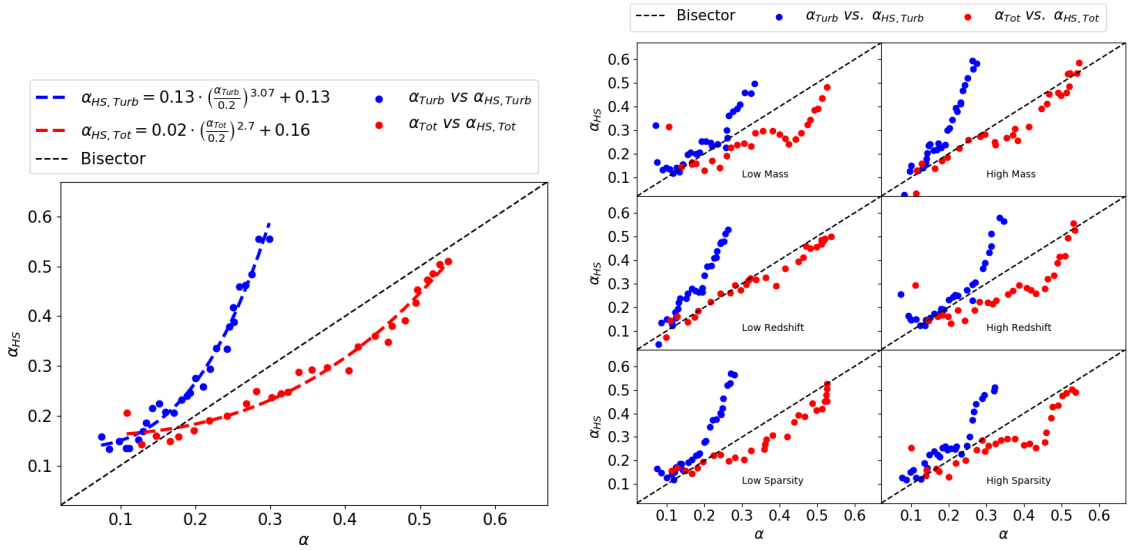

Figure 3.12: Relation between α and $\alpha_{\rm HS}$ computed as described in Sect. 3.2.2. In the left side the whole sample, where the blue points are obtained from $\alpha_{\rm Turb}$ and $\alpha_{\rm HS,Turb}$, while the red ones are obtained from $\alpha_{\rm Tot}$ and $\alpha_{\rm HS,Tot}$. The dashed lines are the fits made as described in Sect. 3.2.2, where the coefficients are given in the legend. The black dashed line is the bisector. In the right panel, there are six sub-samples, as described in Sect. 3.2.2. Top panels: low mass on the left, high mass on the right; central panels: low redshift on the left, high redshift on the right; bottom panels: low sparsity on the left, high sparsity on the right. Also in these plots, the blue points represent the "Turb" quantities, while the red dots represent the "Tot" ones. The dashed lines are the plots' bisectors.

large values of $\alpha_{\rm HS}$ are considered (which happens most often at larger radii).

We divide further our sample into two mass, redshift or sparsity sub-samples (see right panel of Fig. 3.12). We observe that, as opposed to the analysis of the complete sample, $\alpha_{\rm Tot}$ is able to reproduce the 1-to-1 relation with $\alpha_{\rm HS,Tot}$ in some sub-samples. This confirms that $\alpha_{\rm Tot}$ is a more accurate tracer of hydrostatic bias compared to our definition of $\alpha_{\rm Turb}$. This is supported by the plot in Fig. 3.13 where we show the ratio between $\alpha_{\rm Turb}$ and $\alpha_{\rm Tot}$ against $\alpha_{\rm HS}$ (here we used $\alpha_{\rm HS,Turb}$ but the results are almost the same for the $\alpha_{\rm HS,Tot}$ case). Combining the information from Fig. 3.12 and Fig. 3.13, we notice that our definition of turbulent motions give a value of α which is always a fraction of the value obtained from the N14 filtering technique, $\sim 50-70\%$ from case to case. From Fig. 3.13 we also notice that the less the hydrostatic bias, the greater the support from purely turbulent motions to non-thermal pressure. Indeed, the higher is $\alpha_{\rm HS}$, the lower is the ratio $\alpha_{\rm Turb}$ against $\alpha_{\rm Tot}$. This ratio has also a dependence on distance from the cluster's core. Indeed, the greater the radius and lower the ratio. Therefore, the role of the turbulent motions in the non-thermal pressure support is less important in cluster outskirts than in the innermost regions.

We made also a sub-sample analysis of these relations and the results are shown

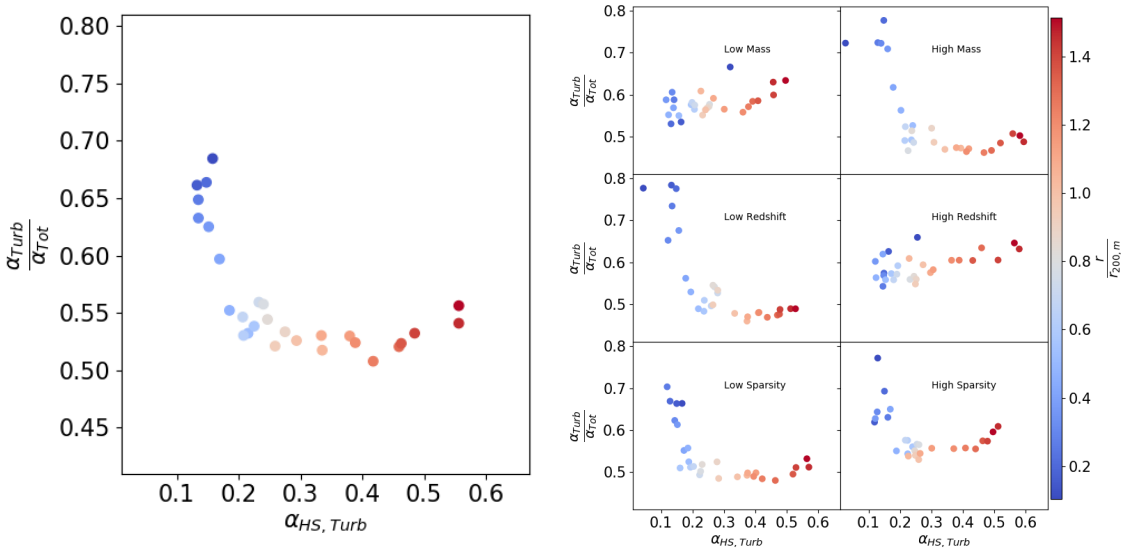

Figure 3.13: Relation between the ratio $\alpha_{\rm Turb}/\alpha_{\rm Tot}$ and $\alpha_{\rm Hs,Turb}$. On the left side the whole sample, while on the right one there are six sub-samples, as described in Sect. 3.2.2. Top panels: low mass on the left, high mass on the right; central panels: low redshift on the left, high redshift on the right; bottom panels: low sparsity on the left, high sparsity on the right. The colours represent the distance from the cluster's centre.

in the right panel of Fig. 3.13. We notice that for all the sub-samples the above conclusions still hold. In the case of low mass or high redshift clusters, we also notice that the ratio $\alpha_{\rm Turb}$ against $\alpha_{\rm Tot}$ is almost constant with the hydrostatic bias.

We conclude that the relation between turbulence and hydrostatic bias can be statistically detected only with a typical number of ≥ 20 objects, at least in the mass range probed by our sample. On the other hand, when applied to single objects the analysis presented above appears not suitable to give accurate correction factors for the hydrostatic bias, as we will show in the next chapter.

3.2.3 Sub-samples analysis of α radial profiles

As described in Sect. 3.2.1, we adopt our model as the best fitting function both for $\alpha_{\rm Turb}$ and $\alpha_{\rm Tot}$. In Fig. 3.14 we shown the radial profiles of α and $\alpha_{\rm HS}$. Here the profiles of $\alpha_{\rm HS}$ are computed using a spectroscopic-like definition of the temperature profile. As already discussed in Sect. 3.2.1, the differences between a spectroscopic-like profile and a volume-weighted one are as small as they allow us to use either of the two profiles. The sub-samples used in this section are built to have the same number of objects in all the bins. The values which allow us this selection are shown in Tab. 3.2.

Both from Fig. 3.14 and Tab. 3.2, we conclude that our fitting formula well reproduces the radial behaviour of $\alpha_{\rm Turb}$ and $\alpha_{\rm Tot}$ at any sub-samples. For $\alpha_{\rm Turb}$

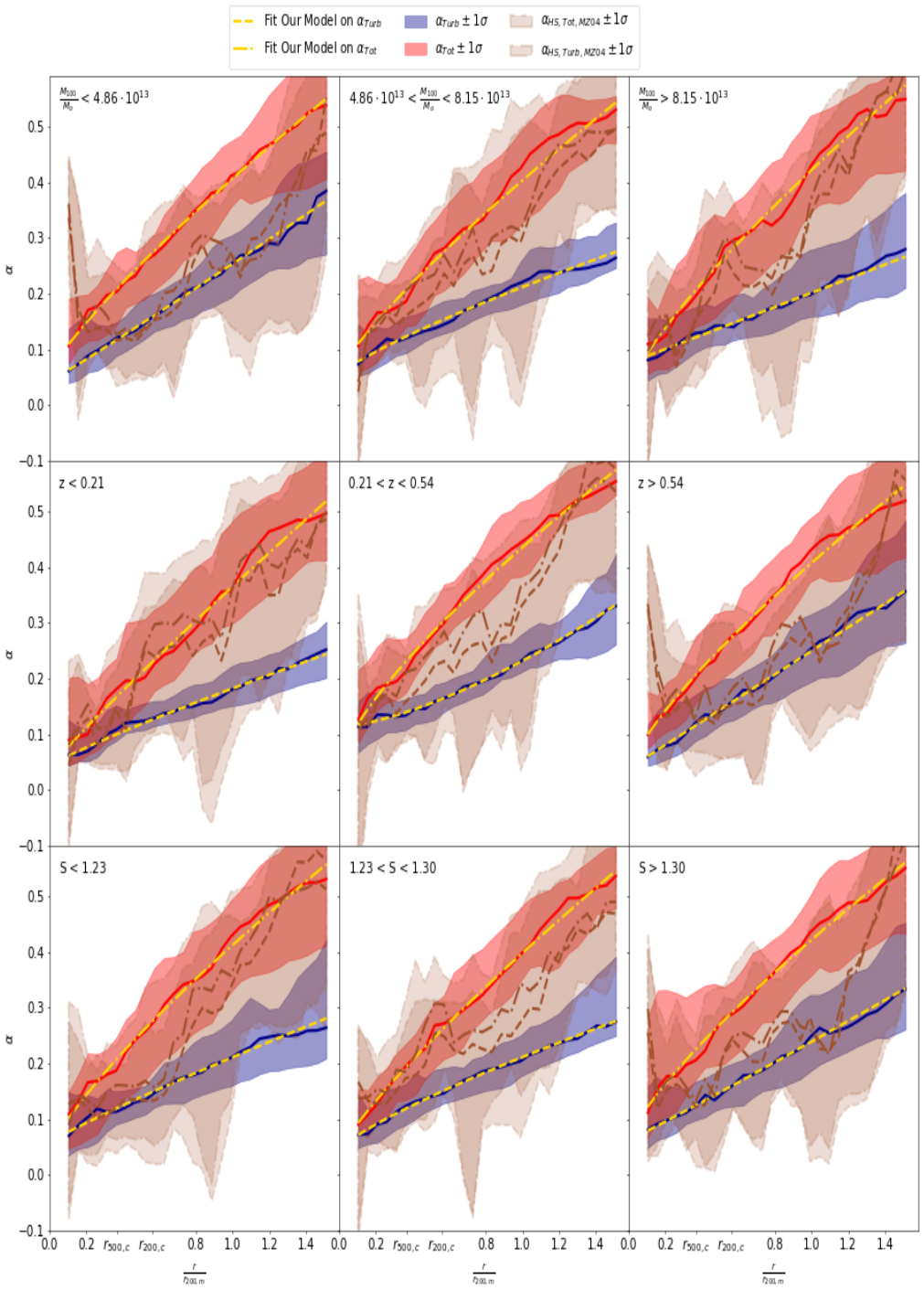

Figure 3.14: Radial profile of the median value of $\alpha_{\rm Turb}$ (blue solid line) and $\alpha_{\rm Tot}$ (red solid line) for different bins of mass (top panels), redshift (central panels) and sparsity (bottom panels). The yellow dashed lines are the fits of our model on $\alpha_{\rm Turb}$ profile, while the dash-dotted ones are the fits of the model on the $\alpha_{\rm Tot}$ profile. The brown dashed and dash-dotted lines are the profile of median $\alpha_{\rm HS,Turb}$ and $\alpha_{\rm HS,Tot}$ computed as described in Sect. 3.2.1. The shadow regions represent the 1σ distribution of the sub-sample.

we observe a slight decrease at any radii with an increase of mass or a decrease of redshift. However, no other strong dependencies are observed between the radial profiles and the quantities used for the selection. We notice also that $\alpha_{\rm Turb}$ shows the lowest scatter at any radii, while both $\alpha_{\rm HS,Turb}$ and $\alpha_{\rm HS,Tot}$ are affected by high scatters.

3.3 Discussion

We can finally study the relation between the non-thermal pressure, the turbulence we identify in our data and the X-ray derived proxy (e.g. Eckert et al., 2019). To address this, we compute the values of $\alpha_{\rm HS}$ and α at the radii $R_{200,\rm c}$ and $R_{500,\rm c}$ in each object. The results are shown in Fig. 3.15

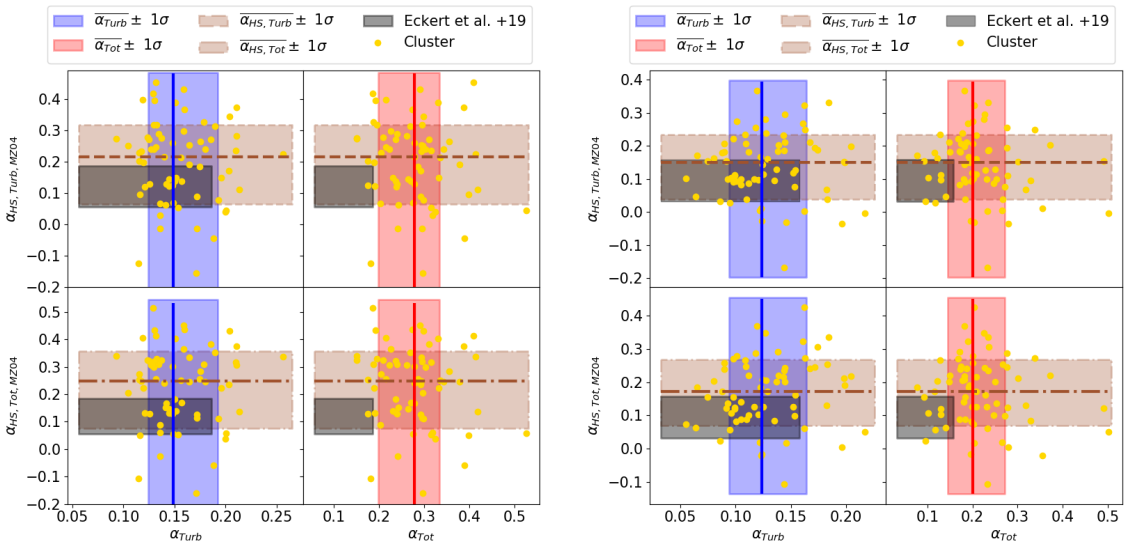

Figure 3.15: Comparison between median $\alpha_{\rm Turb}$ (blue solid line) or $\alpha_{\rm Tot}$ (red solid line) and $\alpha_{\rm HS,Turb}$ (brown dashed line) or $\alpha_{\rm HS,Tot}$ (brown dash-dotted lines) at $R_{200,\rm c}$ (left panels) and $R_{500,\rm c}$ (right panels). The shadow regions represented 1σ variance. The black shadowed regions represented the range values presented by Eckert et al. (2019), while the yellow dots refer to singles clusters (we notice that one cluster of the sample is found to be well outside the plot limits and is discarded given its very peculiar shape).

At first glance, there are almost no correlations between the two proxies (α and $\alpha_{\rm HS}$) for the non-thermal pressure support, even if the two distributions span a similar range of values, and also are in the same ballpark of the XCOP results discussed in Eckert et al. (2019). We also notice that while α is defined as a positive quantity by construction, $\alpha_{\rm HS}$ can be measured with negative values (in $\sim$10% of the sample) due to local fluctuations in the reconstructed thermodynamical profiles that are responsible for the scatter in the distribution of the estimated $\alpha_{\rm HS}$ at a given radius.

Sample		a_0	a_1	a_2	χ^2
$M_{100}/M_\odot < 4.86 \cdot 10^{13}$	$\alpha_{\rm Turb}$	$(2.100 \pm 0.005) \cdot 10^{-1}$	1.041 ± 0.003	$(0.430 \pm 0.003) \cdot 10^{-1}$	0.010
	$\alpha_{\rm Tot}$	0.351 ± 0.001	0.825 ± 0.004	0.054 ± 0.001	0.008
Mass $4.86 \cdot 10^{13} < M_{100}/M_\odot < 8.15 \cdot 10^{13}$	$\alpha_{\rm Turb}$	$(1.582 \pm 0.001) \cdot 10^{-1}$	0.815 ± 0.002	$(0.532 \pm 0.001) \cdot 10^{-1}$	0.034
	$\alpha_{\rm Tot}$	$(3.467 \pm 0.003) \cdot 10^{-1}$	0.821 ± 0.001	$(0.589 \pm 0.001) \cdot 10^{-1}$	0.035
$M_{100}/M_\odot > 8.15 \cdot 10^{13}$	$\alpha_{\rm Turb}$	$(1.261 \pm 0.004) \cdot 10^{-1}$	1.003 ± 0.007	$(0.755 \pm 0.005) \cdot 10^{-1}$	0.014
	$\alpha_{\rm Tot}$	0.395 ± 0.001	0.786 ± 0.004	0.027 ± 0.001	0.036
$z < 0.21$	$\alpha_{\rm Turb}$	$(1.398 \pm 0.001) \cdot 10^{-1}$	0.884 ± 0.001	$(0.424 \pm 0.001) \cdot 10^{-1}$	0.024
	$\alpha_{\rm Tot}$	$(3.271 \pm 0.005) \cdot 10^{-1}$	0.929 ± 0.004	$(0.386 \pm 0.003) \cdot 10^{-1}$	0.030
Redshift $0.21 < z < 0.54$	$\alpha_{\rm Turb}$	$(1.186 \pm 0.001) \cdot 10^{-1}$	1.488 ± 0.002	$(1.130 \pm 0.001) \cdot 10^{-1}$	0.023
	$\alpha_{\rm Tot}$	$(3.875 \pm 0.008) \cdot 10^{-1}$	0.743 ± 0.002	$(0.474 \pm 0.008) \cdot 10^{-1}$	0.040
$z > 0.54$	$\alpha_{\rm Turb}$	$(2.113 \pm 0.003) \cdot 10^{-1}$	0.998 ± 0.004	$(0.380 \pm 0.004) \cdot 10^{-1}$	0.012
	$\alpha_{\rm Tot}$	0.373 ± 0.001	0.769 ± 0.004	0.034 ± 0.001	0.027
$s < 1.23$	$\alpha_{\rm Turb}$	$(1.537 \pm 0.003) \cdot 10^{-1}$	0.903 ± 0.004	$(0.573 \pm 0.003) \cdot 10^{-1}$	0.023
	$\alpha_{\rm Tot}$	$(3.730 \pm 0.006) \cdot 10^{-1}$	0.793 ± 0.002	$(0.392 \pm 0.001) \cdot 10^{-1}$	0.019
Sparsity $1.23 < s < 1.30$	$\alpha_{\rm Turb}$	$(1.674 \pm 0.002) \cdot 10^{-1}$	0.791 ± 0.002	$(0.435 \pm 0.003) \cdot 10^{-1}$	0.012
	$\alpha_{\rm Tot}$	$(3.587 \pm 0.003) \cdot 10^{-1}$	0.836 ± 0.001	$(0.390 \pm 0.003) \cdot 10^{-1}$	0.023
$s > 1.30$	$\alpha_{\rm Turb}$	$(1.761 \pm 0.003) \cdot 10^{-1}$	1.046 ± 0.005	$(0.629 \pm 0.004) \cdot 10^{-1}$	0.014
	$\alpha_{\rm Tot}$	$(0.361 \pm 0.002) \cdot 10^{-1}$	0.785 ± 0.006	0.061 ± 0.002	0.014

Table 3.2: Parameters and values of χ^2 statistical test for our model applied to mass, redshift and mass sparsity sub-samples of our data. The errors on the parameters are the values at 3σ confidence.

This introduces crucial problems for the $\alpha_{\rm HS}$ estimate. First, the spherical symmetry and the coincidence between the centre of the gas pressure and of the gravitational mass (and between gas and dark matter densities) are often violated for systems which had only a little time to relax. Gas substructures are also more prominent, as they are often found in their first crossing of the ICM. This also leads to an ICM with a multi-phase structure, also correlated with the crossing of shocks. In summary, most of the assumptions on which the hydrostatic equilibrium analysis is based are violated at high-z, while on the other hand the above factors little affect our estimate of α, because through our filtering procedure the measure of turbulence is local and do not rely in assumptions of symmetry or isothermality. Interestingly, the above problems should also play an important role in the mass modelling of high-z galaxy clusters in real observations (e.g. Maughan et al., 2006; Jee et al., 2011; Schrabback et al., 2018).

To further investigate the physical origin of the deviations from hydrostatic equilibrium, we added a few important dynamical proxies to characterise the dynamics of our systems. More specifically, we computed the radial profile of gas acceleration, and derived the residual acceleration from gas motions which are out of equilibrium in the presence of mergers, following Biffi et al. (2016a). While Biffi et al. (2016a) could directly access the acceleration values of single smoothed-particle-hydrodynamics (SPH) particles from the hydrodynamical solver, we rely on the post-processing of Eulerian data, taking the derivative of two close time-steps. We defined the gravitational acceleration in each radial shell as:

$$g(r) = -\frac{GM_T}{r^2}, \tag{3.22}$$

while the residual gas acceleration is computed by first taking the radial velocity in each cell, and then reconstructing the radial profile of this quantity for every selected snapshot. To define the residual gas acceleration in the radial direction, we take the difference in each radial shell, between two snapshots, $\delta(r)$ as:

$$\delta(r) = \frac{Vr(t_2) - Vr(t_1)}{(t_2 - t_1)}. \tag{3.23}$$

In order to follow a convention consistent with Biffi et al. (2016a), we defined an acceleration term consistent with the one extracted from their SPH simulations:

$$H(r) = g(r) + \delta(r). \tag{3.24}$$

From the above we can thus introduce a factor, δ_{HE}, which compensates for the residual gas radial acceleration by motions which are not in equilibrium with the

gravitational pull of the cluster:

$$\delta_{HE}(r) = \frac{g(r)}{H(r)} - 1. \tag{3.25}$$

From this definition, we notice that when the gas is in hydrostatic equilibrium δ_{HE} is equal to 0. Finally, as in Biffi et al. (2016a) we define ξ_r:

$$\xi_r = \mid \alpha_{\rm HS}(r) - \delta_{HE}(r) \mid, \tag{3.26}$$

which allows us to consider at the same time the contributions given at the hydrostatic bias from the acceleration terms and the term obtained from $\alpha_{\rm HS}$. In Sect. 3.3.1, we show in more detail how this procedure can well highlight the presence of out-of-equilibrium conditions in the ICM; in particular, we can relate large residual acceleration terms to the local gas conditions in the proximity of powerful shock waves crossing the cluster. We can thus conclude that these terms are likely to be crucial for an accurate estimate of hydrostatic mass, but also that they are hard to model for a perfect correction of the hydrostatic mass bias, in most realistic cases.

We attempted to incorporate residual gas accelerations in the previous modelling of the hydrostatic bias, by defining α_ξ as the fraction of the total pressure due to purely radial accelerations:

$$\alpha_\xi(r) = \mid \overline{\delta_{HE}}(< r) \mid \tag{3.27}$$

where $\overline{\delta_{HE}}$ is defined starting from the Eq. 3.25 and it represents the median value of the contributions of residual radial accelerations within the radius r. In Fig. 3.16 we show the behaviour of the ratio $\alpha_\xi/\alpha_{\rm Tot}$ against $\alpha_{\rm HS}$.

From the left panel of Fig. 3.16 we notice that the contribution of radial accelerations to the non-thermal pressure support span from ∼40% in the innermost regions of the cluster to ∼15% in the outskirts. Two effects are likely at play here. First, strong acceleration terms originate from expanding shocks, which are typically launched during mergers starting from the core cluster region (or close to it). Therefore, when a cluster is disturbed by ongoing merger activity, such terms can be more significant in the core regions than in more external ones, due to their larger volume-filling fraction there. Additionally, we expect an irreducible level of spurious radial acceleration at the scale of cluster cores, due to the fact that in perturbed systems (i.e. with many substructures in the core etc) it is not always trivial to exactly track the position of the centre as a function of time, which may introduce noise in our procedure to measure $\delta_{HE}(< r)$ above.

As for the turbulent contributions, which are discussed in Sect. 3.2.2, also for the radial accelerations one, the higher is the hydrostatic bias and the lower is the

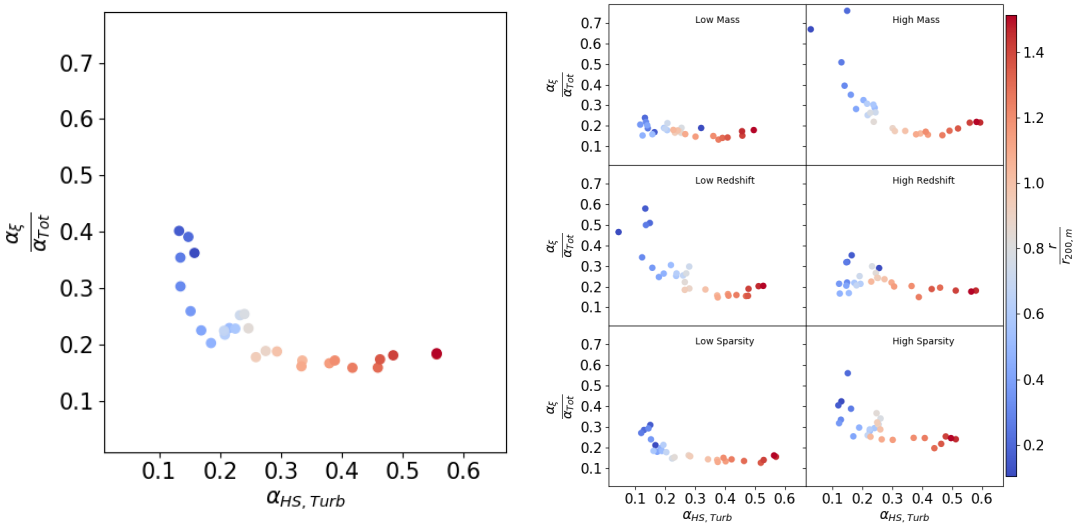

Figure 3.16: Relation between the ratio α_ξ against $\alpha_{\rm Tot}$ and $\alpha_{\rm Hs,Turb}$. On the left side the whole sample, while on the right one there are six sub-samples, as described in Sect. 3.2.2. Top panels: low mass on the left, high mass on the right; central panels: low redshift on the left, high redshift on the right; bottom panels: low sparsity on the left, high sparsity on the right. The colours represent the distance from the cluster's centre.

contribution. The sub-sample analysis revealed that for high masses and low redshift samples, in the innermost regions of the clusters where the hydrostatic bias is lower, the contribution of radial accelerations seems to be higher than for low masses and high redshifts.

Combining the contribution from turbulence and radial accelerations, we obtained the results shown in Fig. 3.17. In the clusters' outskirts, where the hydrostatic bias is higher, turbulence and radial accelerations are not able to completely trace the hydrostatic bias. Due to the filtering techniques, the residual 30% of the hydrostatic bias is generated by the bulk motions, which are filtered out from our filtering technique, but they are considered in the filter proposed by N14. However, in the innermost regions, the hydrostatic bias is completely described by the combination of turbulence and radial acceleration contributes.

We performed the same sub-sample analysis used above. For low masses and high redshift clusters, the combination of turbulence and radial accelerations is not still enough to account for the hydrostatic bias. On the other hand, for high masses, low redshift or low sparsity objects, where the hydrostatic bias is lower, turbulence and radial accelerations trace the hydrostatic bias. However, even then, turbulence and radial accelerations are not still sufficient to explain the hydrostatic bias.

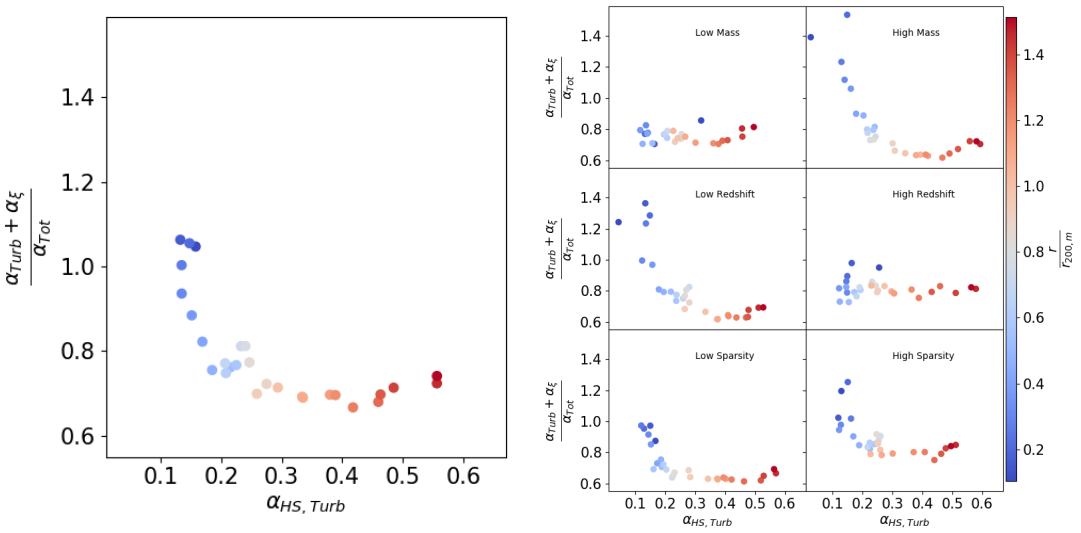

Figure 3.17: Relation between the ratio $\alpha_{\rm Turb} + \alpha_\xi$ against $\alpha_{\rm Tot}$ and $\alpha_{\rm Hs,Turb}$. On the left side the whole sample, while on the right one there are six sub-samples, as described in Sect. 3.2.2. Top panels: low mass on the left, high mass on the right; central panels: low redshift on the left, high redshift on the right; bottom panels: low sparsity on the left, high sparsity on the right. The colours represent the distance from the cluster's centre.

3.3.1 On the relation between hydrostatic bias and radial acceleration

The presence of shocks in the ICM is important for their dynamical equilibrium since the passage of a shock provides a thrust, usually in the outward direction. This effect generates a radial acceleration of the gas that could affect the computation of the hydrostatic mass, mimicking an excess of thermal pressure if the hydrostatic equilibrium is (wrongly) imposed on the structure (Nelson et al., 2014b).
As written in Sect. 3.3, we apply the same formalism presented in Biffi et al. (2016a) on our clusters. We quantify the amount of departure from the hydrostatic equilibrium in each shell through the median value of ξ_r within the shell, ξ.

As an example, in Fig. 3.18 we show the central slice of Mach Number, which allows us to identify shocks sweeping the clusters volume at a given epoch. In the left panel we can see wide $\mathcal{M} \approx 3$ shocks in the inner part of cluster IT90_0 at the epoch of $z \simeq 0.15$, while in right slight through cluster IT92_0 at $z \simeq 0.07$ there are no relevant shocks inside $R_{200,\rm c}$. We can therefore expect in the first case a stronger departure from equilibrium, following the gas dynamical acceleration downstream of the shock wave. These trends are well captured in Fig. 3.19, which gives the radial behaviour of total mass (blue solid line), hydrostatic mass (red solid line) and $\mathcal{M}_{\rm w}$ (green solid line). In the bottom panels of Fig. 3.19, we also show the radial profiles of $\alpha_{\rm HS}$ and of the radial acceleration term.

From there we can quantify how shocks in the inner parts of the cluster influence

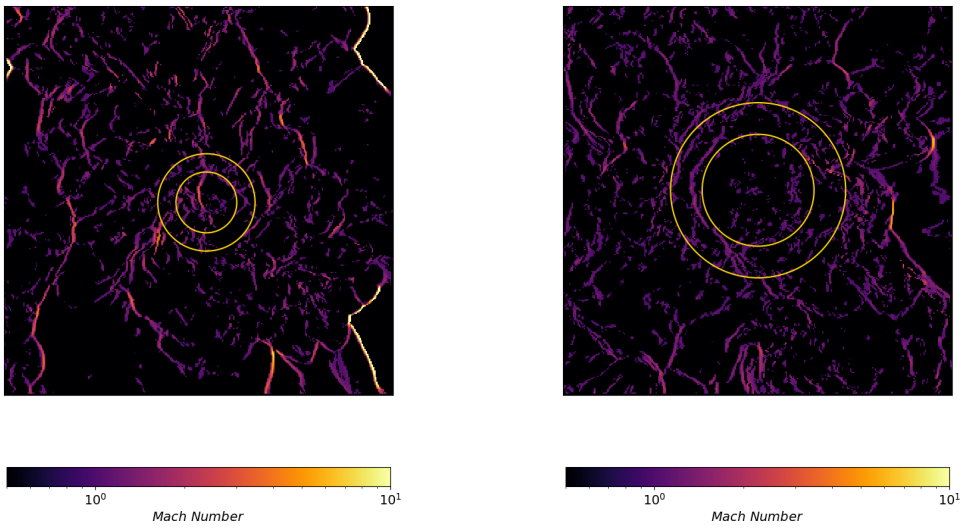

Figure 3.18: Maps of shock Mach number in a slice through the centre for cluster IT90_0 at $z \simeq 0.15$ (left panel), and through the centre of IT92_0 at $z \simeq 0.07$ (right panel). The inner circle shows the location of $R_{500,c}$, while the outer one shows $R_{200,c}$.

the hydrostatic mass. There is a strong correlation between the maximum values of the Mach Number and a *negative* hydrostatic mass bias, meaning that the total mass that would be inferred through a standard hydrostatic equilibrium analysis would be larger than the total (true) mass, as shown by the radial trend of $\alpha_{\rm HS}$. These behaviours are also observed for the more relaxed cluster in the right panel, but only in the regions close to $R_{200,c}$, where a shock front is visible in the right panel of Fig. 3.18. Therefore, shocks introduce an additional term that one must consider when inferring non-thermal pressure from the hydrostatic mass bias. We remark that such behaviours in the radial profile would hardly be detected in realistic X-ray analysis of observed clusters because observations are usually fitted through a (smooth) Navarro-Frank-White profile, which cannot produce such a sharp increase in the hydrostatic mass profile.
Thanks to the analysis of radial acceleration terms, we used ξ as correcting factor of hydrostatic bias. We compared the α terms with the sum of $\alpha_{\rm HS}$ plus ξ. The goal of this comparison is to obtain a closer relation between the turbulent proxy α and the hydrostatic bias counterpart $\alpha_{\rm HS}$. The results are shown in Fig. 3.20.

From the comparison between Fig. 3.20 and Fig. 3.15, we notice that the negative terms of hydrostatic bias are not present anymore. However, we do not find a strong correlation between turbulence and hydrostatic bias yet.

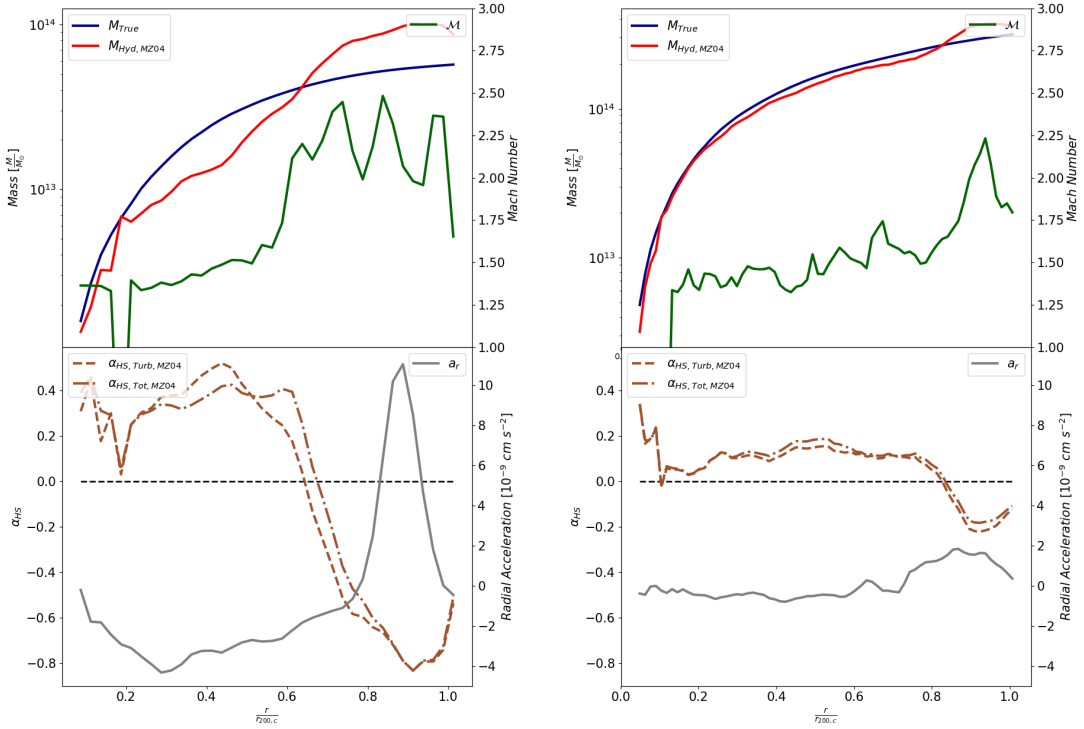

Figure 3.19: Total mass profile (blue solid line), hydrostatic mass profile (red solid line) and median Mach Number profile (green solid line) in the top panel, and radial acceleration (blue solid line) and $\alpha_{\rm HS,Turb}$ (brown dashed line) and $\alpha_{\rm HS,Tot}$ profiles (brown dash-dotted line) in the bottom panel, for IT90_0 at $z \simeq 0.15$ (left panel) and IT92_0 at $z \simeq 0.07$ (right panel).

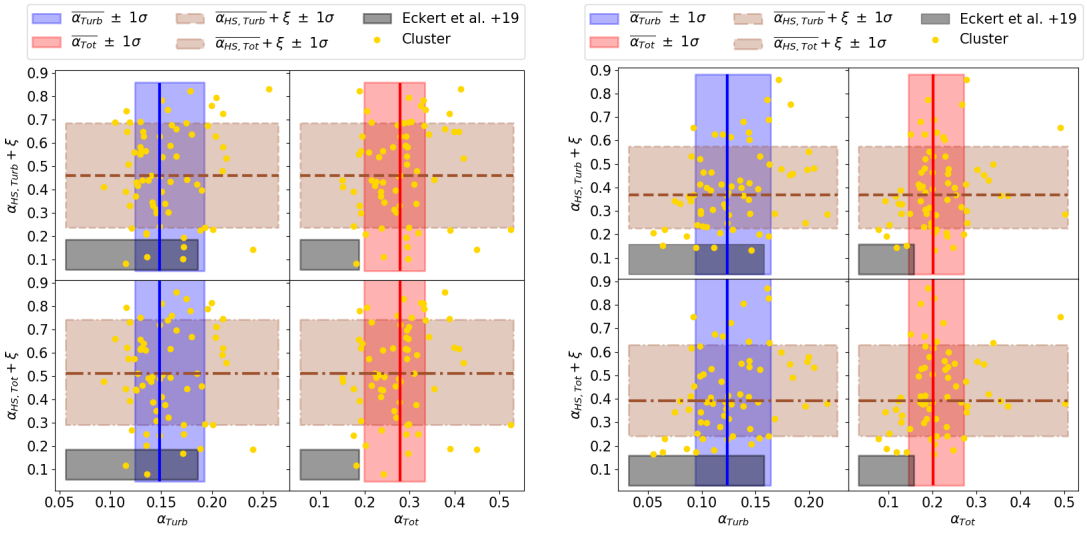

Figure 3.20: Comparison between median $\alpha_{\rm Turb}$ (blue solid line) or $\alpha_{\rm Tot}$ (red solid line) and $\alpha_{\rm HS,Turb}$ (brown dashed line) or $\alpha_{\rm HS,Tot}$ (brown dash-dotted lines) corrected for the radial acceleration term ξ, at $R_{200,\rm c}$ (left panels) and $R_{500,\rm c}$ (right panels). The shadow regions represented 1σ variance. The black shadow regions represented the range values inferred with X-ray observations by Eckert et al. (2019), while the yellow dots refer to single clusters.

Chapter 4

Proprieties and relations between matter clumps and filaments

In this chapter, following Angelinelli et al. (2021), I report on the possibility of studying the proprieties of cosmic diffuse baryons by studying self-gravitating clumps and filaments connected to galaxy clusters. While filaments are challenging to detect with X-ray observations, the higher density of clumps makes them visible and a viable tracer to study the thermodynamical proprieties of baryons undergoing accretion along cosmic web filaments onto galaxy clusters. We developed new algorithms to identify these structures and applied them to a set of non-radiative cosmological simulations of galaxy clusters at high resolution. We find that in those simulated clusters, the density and temperature of clumps are independent of the mass of the cluster where they reside. We detected a positive correlation between the filament temperature and the host cluster mass. The density and temperature of clumps and filaments also tended to correlate. Both the temperature and density decrease moving outward. We observed that clumps are hotter, more massive, and more luminous if identified closer to the cluster centre. Especially in the outermost cluster regions ($\sim 3R_{500,c}$ or beyond), X-ray observations might already have the potential to locate cosmic filaments based on the distribution of clumps and to allow one to study the thermodynamics of diffuse baryons before they are processed by the intracluster medium. Sect. 4.1.3, Sect. 4.2.4 and Sect. 4.2.5 are a novelty of this thesis. Indeed, the results of Sect. 4.2.4 obtained by the procedure described in Sect. 4.1.3 were not included in the original paper Angelinelli et al. (2021). Moreover, the results presented in Sect. 4.2.5 were supposed to be part of the Athena Red Book (one of the steps needed for a new mission to be accepted). Unfortunately, due to some issues suffered by the ATHENA mission, the adoption is postponed and nowadays it is not already clear when and with which characteristics the mission will be approved. For completeness, I decided to include them as results of this chapter.

4.1 Methods

In this section, we describe the numerical algorithms we develop to disentangle clumps from the diffuse gas in filaments. In the following analysis, we consider the baryon mass component only; that is to say, we neglect the dark matter mass contribution to the masses of clumps and filaments. This reflects the fact that our clump finder algorithm searches for baryon density peaks, while the filament finder focuses on gas entropy, so it is also baryon-based. Considering that because collisional, baryonic matter and collisionless, dark matter do not obey exactly the same dynamics, there could be mismatches between the positions of peaks in the two distributions. This could in turn introduce a bias in the estimate of the total masses of the clumps, which we want to minimise here. When and if necessary, we highlight different assumptions on the mass estimation.

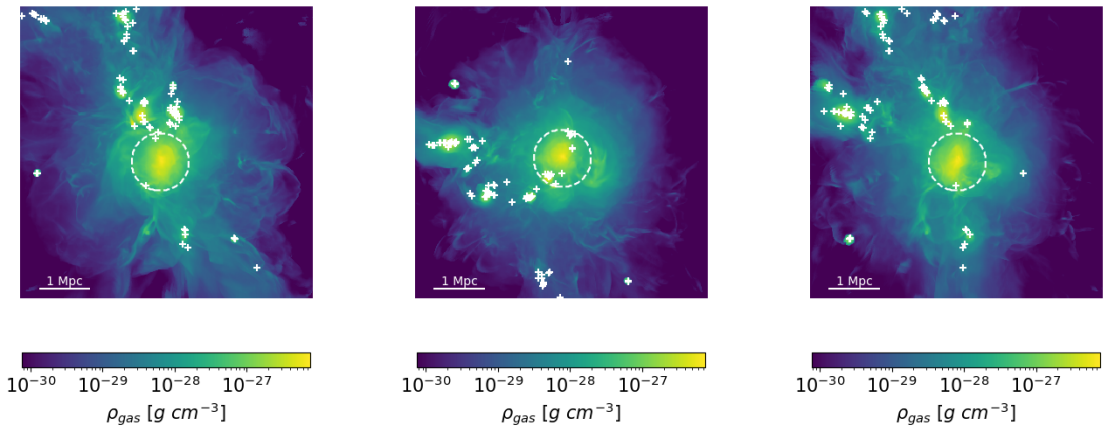

Figure 4.1: Projected emission weighted gas density for the simulated cluster IT90_2 a z=0.1, along three different lines of sight. The dashed circles represent $R_{500,c}$, while the white crosses are at the centres of the identified clumps.

4.1.1 Identifying the clump structures

In this analysis we consider clumps as the top 1% of the densest regions within each radial shell from a given cluster centre, following well-established evidence that clumps occupy the high-density tail of the gas density distribution in the simulations (e.g., Zhuravleva et al., 2013). Then, we add a second filter on the temperature of these structures. In the regions selected by the density threshold, we exclude all the cells with a temperature below 0.1 keV. This selection ensures us to identify regions which are comparable with the X-ray observations. To identify individual clumps, we have to implement a second, complementary algorithm which separates the initially identified region into specific clumps. This algorithm groups all the cells which are at a defined maximum distance from the initial reference cell. We also

add a second criterion to exclude all the clumps which have a mass below a defined threshold mass. Figure 4.1 shows the results of this process, where the position of the clump's centre (defined as the position of the maximum density in each clump) is identified for three different lines of sight of one of the clusters in our sample.

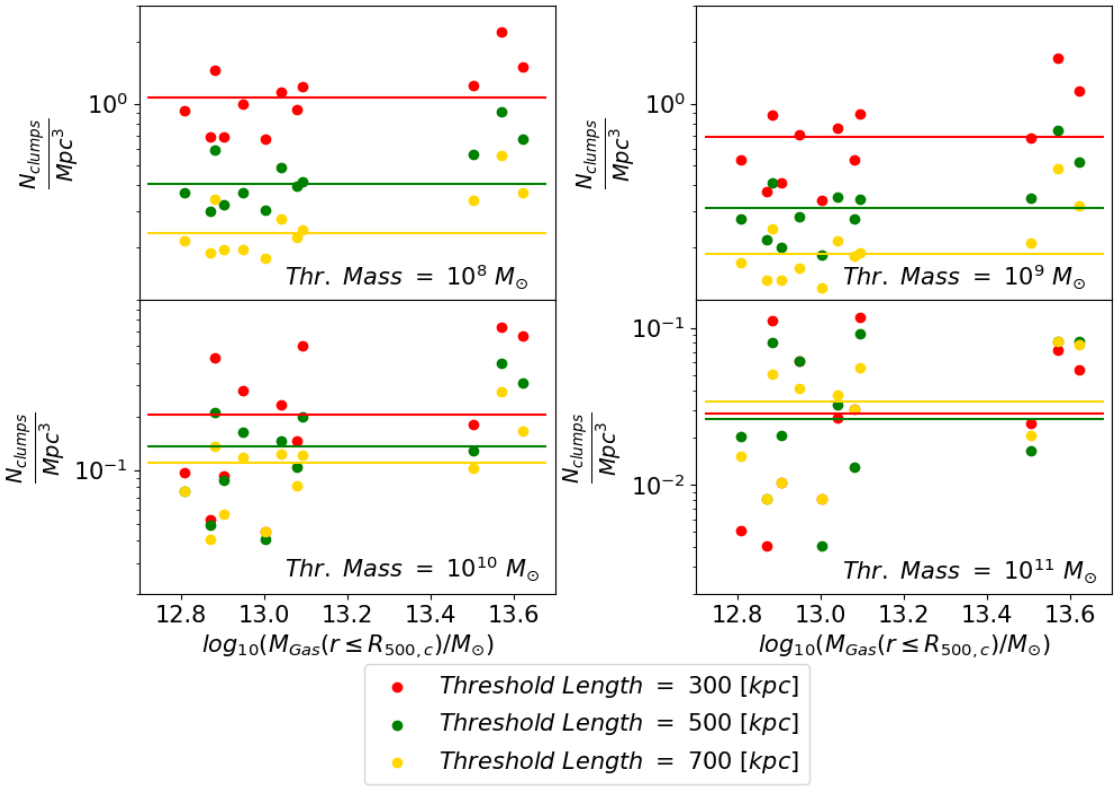

Figure 4.2: Number of identified clumps per Mpc^3, as a function of the simulated host cluster's mass. The different panels show different threshold masses (top left: 10^8 $M_\odot$; top right: 10^9 $M_\odot$; bottom left: 10^{10} $M_\odot$; bottom right: 10^{11} $M_\odot$), while the different colours represent different threshold maximum distances (red: 300 kpc; green: 500 kpc; gold: 700 kpc). The solid lines, which have the same colour-coding as the threshold maximum distances, represent the median values of clumps per Mpc^3 for the related threshold mass, computed on the whole simulated cluster sample.

We test our algorithm with different values of maximum distance and mass threshold, and the results are reported in Fig. 4.2. It is apparent that increasing the host cluster's mass increases the number of identified clumps. This is observed for all the maximum distance thresholds when the threshold mass is below 10^{11} $M_\odot$. Moreover, for these threshold masses, we also notice a decrease in the number of identified structures with an increase in the maximum distance threshold. Indeed, by increasing the maximum distance threshold, nearby structures, which are considered as different structures for small maximum distance threshold, are grouped into single, larger structures. For a fixed mass threshold, this behaviour reduces the total number of identified structures with an increase of the maximum distance thresh-

old. From the last panel of Fig. 4.2, we observe that none the relations between the number of identified clumps and the host cluster's mass or maximum distance thresholds are observed for the mass threshold 10^{11} $M_{\odot}$. This is, in fact, a consequence of the large magnitude of this threshold mass. Indeed, in some clusters in our sample, the algorithm does not detect clumps with masses exceeding 10^{11} $M_{\odot}$, especially for smaller maximum distances. This suggests that, for these clusters, the clump threshold mass 10^{11} $M_{\odot}$ is larger than any clumps that have formed.

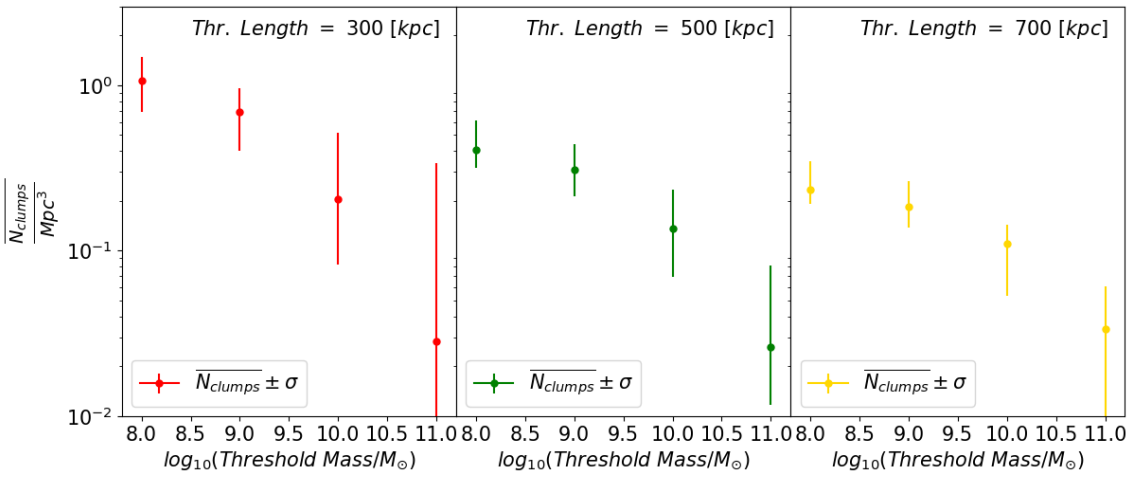

Figure 4.3: Median number of identified clumps per Mpc^3, as a function of the threshold mass for the different maximum distance thresholds (left: 300 kpc; centre: 500 kpc; right: 700 kpc). The error bars represent the 1σ dispersion of the data.

In Fig. 4.3, we show the median number of identified clumps in our sample, as a function of the threshold mass. We notice that the number of identified clumps decreases when the threshold mass is increased for all the maximum distance thresholds. Moreover, as already observed for Fig. 4.2, the number of clumps decreases with increasing maximum distance threshold. Comparing Fig. 4.2 and Fig. 4.3, we identify a threshold mass of 10^8 $M_{\odot}$ and a maximum distance threshold of 500 kpc as the best thresholds to identify clumps in our cluster sample. The chosen maximum distance threshold is in agreement with our previous work (Angelinelli et al., 2020), where we studied turbulent motions in the same simulated clusters used here. In particular, we showed in that work how the peak of the Kolmogorov spectrum, which relates to the scale of the dominant energy-containing structures in the ICM, is on scales around 500 kpc. Those structures are, indeed, the same clumps studied in the current chapter. Therefore, from the results presented in Angelinelli et al. (2020) and the ones obtained from the algorithm presented above we can conclude that the maximum distance threshold of 500 kpc properly represents the typical upper scales of clumps in these clusters. Regarding the threshold mass, we assume 10^8 $M_{\odot}$ to avoid neglecting any appropriate clump structures. Indeed, if we compare the top panels of Fig. 4.2 (which illustrate the results with a threshold mass of

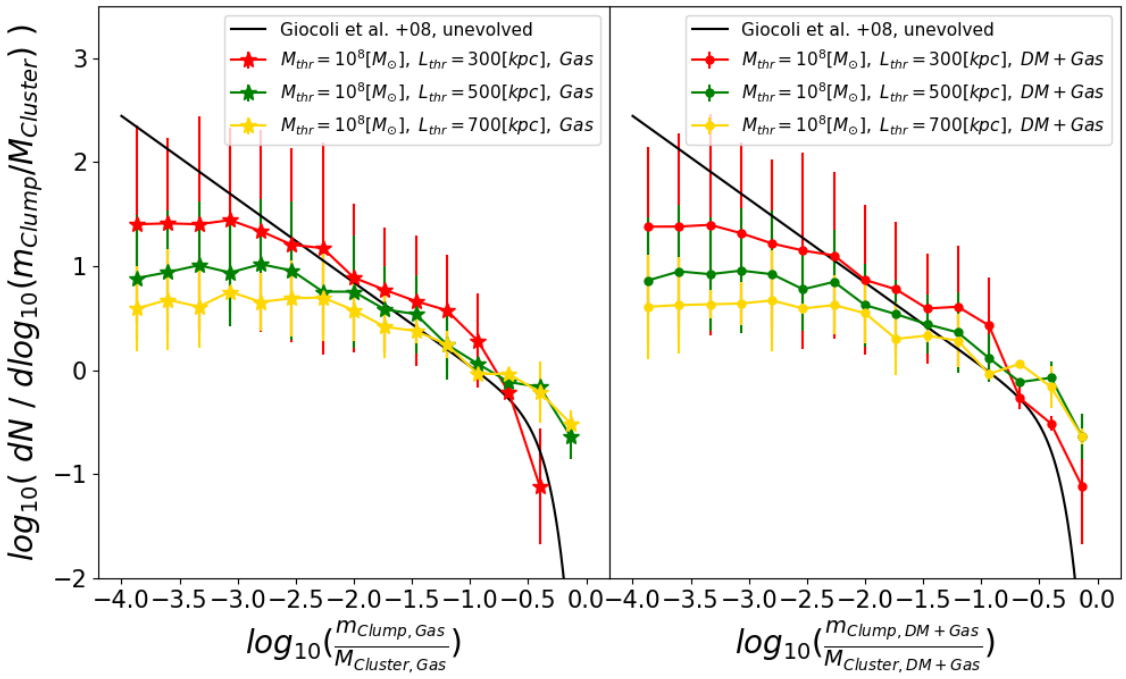

Figure 4.4: Clump mass function for the 10^8 $M_\odot$ mass threshold with different maximum distance thresholds (red: 300 kpc; green: 500 kpc; gold: 700 kpc. In the left panel, we consider only the gas component of the mass, while on the right side we show the results for combined baryon and dark matter components. In both panels, the black solid line represents the fitting formula proposed by Giocoli et al. (2008).

10^8 $M_\odot$ and 10^9 $M_\odot$, respectively), we notice that the number of clumps in an Mpc^3 volume is almost the same. When we increase the threshold mass (bottom panels of Fig. 4.2), the number density of clumps drops quickly, suggesting that most of the clumps have masses lower than 10^{10} $M_\odot$. Therefore, to sample properly the clump population in these clusters, we adopt the minimum threshold mass of 10^8 $M_\odot$.

Using these thresholds, we compare the mass function of the identified clumps with the results presented by Giocoli et al. (2008). In that work, the authors studied a sample of N-body simulated dark-matter-only galaxy clusters. They focused on the mass-loss rate and the related mass function of the sub-halos present in their simulation boxes. They demonstrated that the mass function of sub-halos is universal, and they described it with the following fitting formula:

$$\frac{dN}{d\ln(m_v/M_0)} = N_0\, x^{-\alpha}\, e^{-6.283\cdot x^3}, \qquad x = \left|\frac{m_v}{\alpha \cdot M_0}\right| \tag{4.1}$$

where m_v is the clumps' mass and M_0 is the cluster's mass, while α=0.8 and N_0=0.21. We compare this fitting formula with our mass distributions. The results are plotted in Fig. 4.4.

Our results including both baryons and dark matter are consistent with the

fitting formula presented by Giocoli et al. (2008) (right panel of Fig. 4.4). However, some differences in the distribution at low masses appear because of different mass resolutions in the two studies. When we consider only the gas component of our simulations, the mass distribution is well-described by the fitting formula proposed by Giocoli et al. (2008). This consistent behaviour is explained by a relative baryon component of clump mass that is almost the same as for the central, host cluster. Indeed, as this would suggest, the curves in the left and the right panel of Fig. 4.4 have similar trends.

As the next step in this analysis, we compute the clumping factor for our full cluster sample. We define the clumping factor at each radius r as:

$$C_\rho(r) = \sqrt{\frac{\langle \rho(r)^2 \rangle}{\langle \rho(r) \rangle^2}}, \tag{4.2}$$

where the means are computed within a shell with radius r (e.g., Nagai, Lau, 2011).

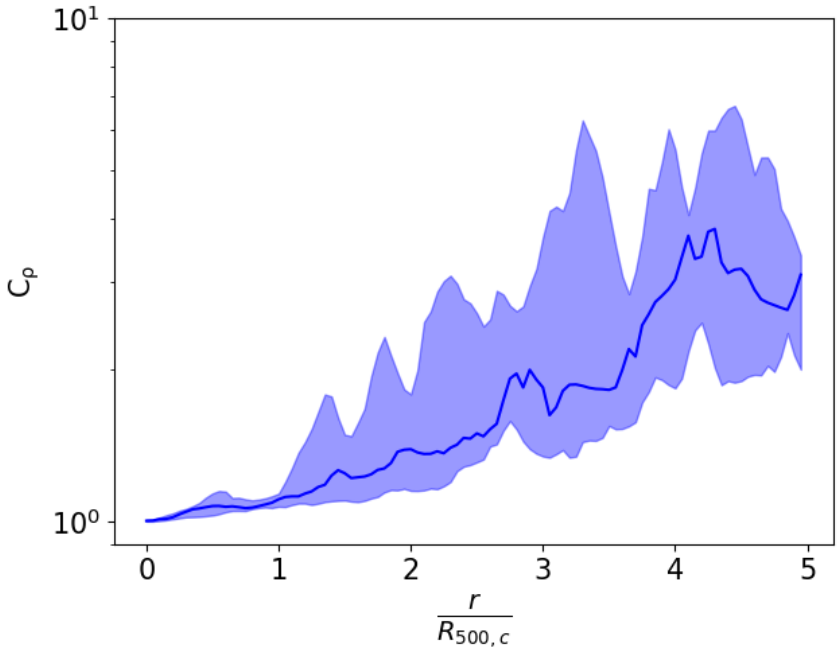

Figure 4.5: Radial profile of clumping factor for the whole clusters sample. The blue solid line represents the median value, while the shadow region is enclosed between the 16th and the 84th percentile of the distribution at any radii.

In Fig. 4.5, we show the median value of C_ρ, along with the 16th and 84th percentiles, at each radius. Similar to Vazza et al. (2013b), we observe an increment of clumping factor with the radial distance, and measure values which are in good agreement with the ones estimated in, for example, Nagai, Lau (2011) and Vazza et al. (2013b).

In Fig. 4.6 we also present the relation obtained for our clusters between the

clump number density and the radial distance from the cluster centre. We adopt the distance and mass thresholds described above and we use ten equally spaced radial shells from $R_{500,c}$ up to $5R_{500,c}$. It is clear that the clump number density decreases with the radial distance, that is by a factor $\simeq$3 from the inner to the outer bin.

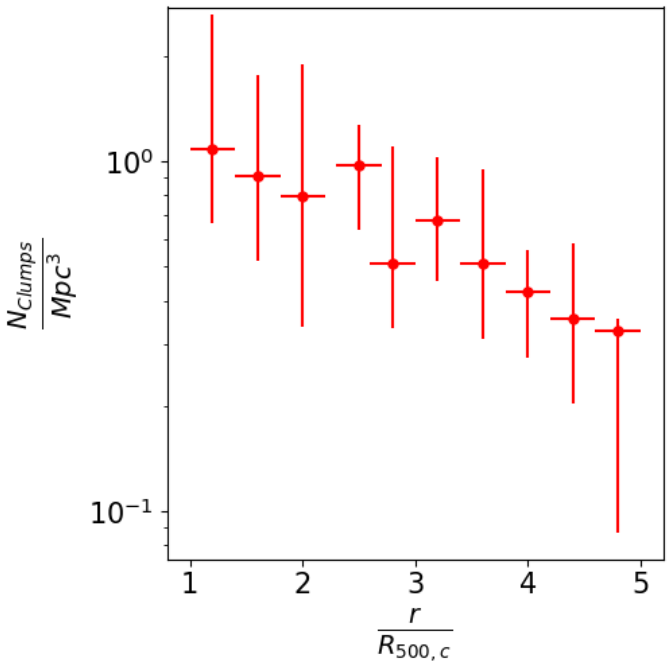

Figure 4.6: Number density of clumps computed on ten radial bins between $R_{500,c}$ and $5R_{500,c}$. The red dots are the median clumps' number density in each bin. The x-axis errors represent the length of radial bins, while the y-axis ones represent the 16th and 84th percentiles of the bin's number density distribution.

Comparing Fig. 4.5 and Fig. 4.6 we conclude that, even though the clumping factor increases with radius, the clump number density decreases. These different behaviours suggest that the observed decreased number of clumps with the radial distance is not an artefact of our clump finder algorithm, but, rather, is a true property of the clump population. To further test the dependence of our results on the numerical resolution, in Appendix 8.2 we computed the clumping factor, as well as the clumps number density, for four different re-simulations of the same cluster, at increasing spatial resolution. Briefly, we find that the Itasca cluster simulation sample numerical resolution ($\sim$19.6 comoving kpc) is sufficient to study the structures which our clump finder algorithm identifies. That is, our detected trends are not found to depend significantly on resolution, for $\Delta x \leq 32$kpc.

4.1.2 The $\frac{V_{rad}^2}{K}$ estimator

In this section, we use the simulated cluster IT90_2 as an example to explore a novel *filament* identifier tool. IT90_2 is described at $z = 0.1$ by density and temperature radial profiles shown in Fig. 4.7. These profiles follow well the rescaled universal cluster profiles proposed by Ghirardini et al. (2019).

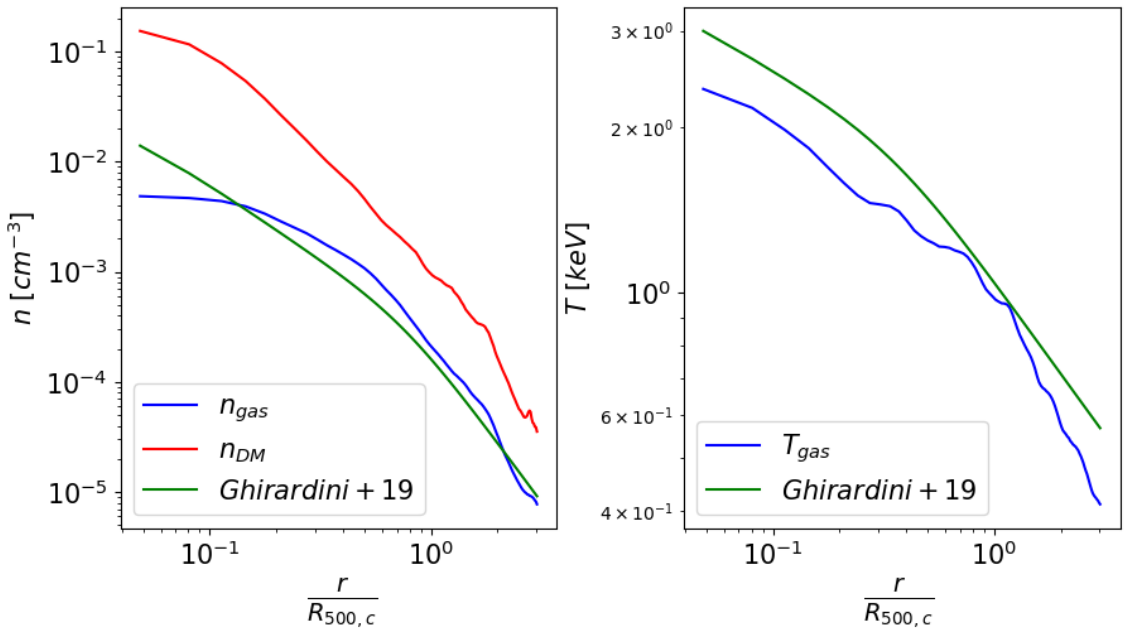

Figure 4.7: Comparison between density and temperature profiles of the simulated cluster IT90_2 ($M_{Tot,500,c} = 6.68\ 10^{13} M_{\odot}, R_{500,c} = 555$ kpc, $z = 0.1$) and the universal profile proposed by Ghirardini et al. (2019). (Left) Gas density (blue), dark matter density (red) and universal (green) profiles in cm^{-3} units. (Right) Gas temperature (blue) and universal (green) profiles in keV units. In both panels, the profiles are computed from the cluster's centre out to $3R_{500,c}$

The projected IT90_2 gas density and dark matter density maps at $z = 0.1$ are shown in Fig. 4.8, together with the projected entropy map.

To identify the diffuse gas in the filaments within and adjacent to the clusters, we define a proxy based on gas entropy and gas radial velocity. Indeed, we expect that these structures, having "fallen" out of the web, are moving toward the cluster centre mainly in the radial direction, and with a velocity determined by gravity, comparable with the local in-fall velocity. Furthermore, the absence of a strong X-ray detection of filaments in real clusters so far suggests that their densities and temperatures are quite different from clump densities and temperatures. Specifically, the filaments are expected to be relatively cooler and very likely with low entropy. In our entropy-radial-velocity-based filament finding algorithm we define gas entropy,

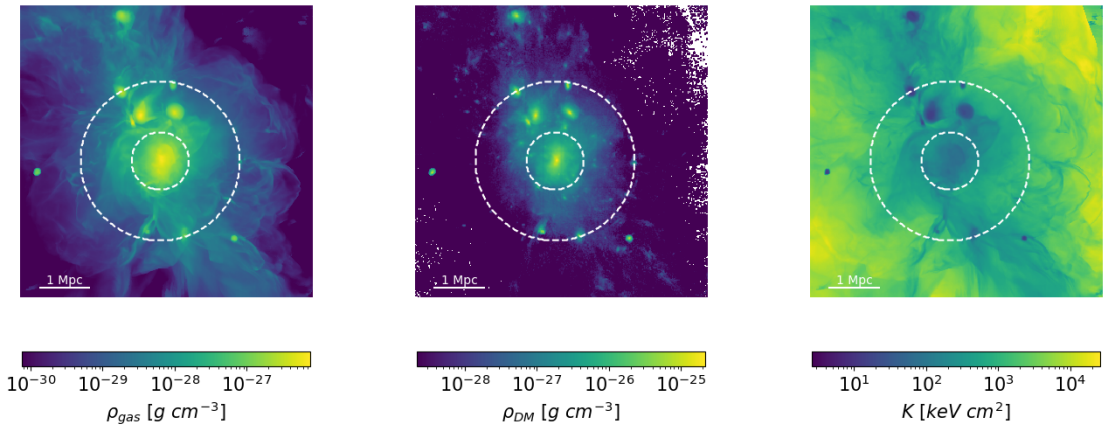

Figure 4.8: Projected emission weighted gas density (left panel), dark matter density (central panel) and entropy (right panel) for the cluster IT90_2 at $z = 0.1$. The dashed circles represent $R_{500,c}$ and $2.8R_{500,c}$.

$K(i)$ in volume element i, as

$$\mathrm{K(i) = T(i) \cdot n(i)^{-2/3}} \tag{4.3}$$

and the radial velocity, $V_{rad}(i)$, as the radial projection of the velocity field, relative to the cluster centre. The centre was defined as the position of the maximum thermal energy density of the gas.

Now we consider the ratio between the V^2_{rad} and K. In the self-similar cluster formation approximation, the ratio of entropy to free-fall velocity is independent of the host cluster mass:

$$\frac{\mathrm{V^2_{rad}}}{\mathrm{K}} \propto \frac{\mathrm{M^{2/3}}}{\mathrm{M^{2/3}}} = \mathrm{CONST.} \tag{4.4}$$

In Fig. 4.9, we show the projected emission weighted map of the ratio $\frac{\mathrm{V^2_{rad}}}{\mathrm{K}}$. We note that filaments show higher values of this ratio than those of their ICM surroundings, especially reflecting reduced filament entropy. Utilising this bias toward large V^2_{rad}/K, we include as filaments the regions in each radial shell j, with

$$\frac{\mathrm{V^2_{infall}(j)}}{0.05 \cdot \overline{\mathrm{K(j)}}} < \frac{\mathrm{V^2_{rad}(j)}}{\mathrm{K(j)}} < \frac{\mathrm{V^2_{infall}(j)}}{0.01 \cdot \overline{\mathrm{K(j)}}} \tag{4.5}$$

where $\mathrm{V^2_{infall}(j)}$ is the free-in-fall velocity in the radial shell j given by

$$\mathrm{V^2_{infall}(j)} = \frac{\mathrm{G \cdot M(<j)}}{\mathrm{r(j)}} \tag{4.6}$$

and $\overline{\mathrm{K(j)}}$ is the mean entropy in the radial shell j. As noted our selection is mainly based on the gas entropy, because clumps and filaments have comparable radial

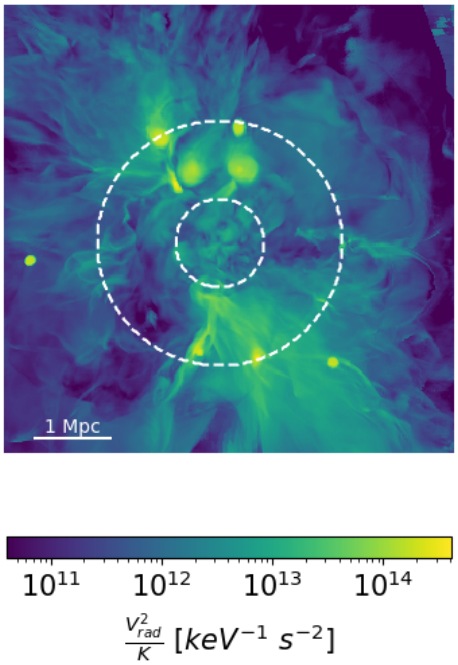

Figure 4.9: Projected emission weighted V_{rad}^2/K for the cluster IT90_2 at z=0.1. The dashed circles represent $R_{500,c}$ and $2.8R_{500,c}$.

velocities close to the free-in-fall velocity. But, they do differ by their entropy. The limits of 1% and 5% are imposed to exclude clumps and diffuse gas from the filament analysis. Indeed, as observed from Fig. 4.9, filamentary structures are described by high values of V_{rad}^2/K, but the highest values are actually reached in the presence of clumps. Therefore, we exclude the regions with the highest values of V_{rad}^2/K in order to avoid the presence of clumps (Fig. 4.9). But, we need also a lower limit to select only filaments and to exclude the diffuse gas.

We also add a filter on the density of the gas. We consider gas to be part of a filament only when it has a density greater than the critical density of the Universe $\rho_c(z)$, in order to avoid selecting under-dense regions, especially in the cluster outskirts. In Fig. 4.10 we compare the map of the clumpy region against the map of the filamentary structure. We also add a third panel in which we display regions selected using the standard definition of WHIM (10^5 K$\leq$T$_{gas}$ $\leq$ 10^7 K). We note that our definitions of clumps, derived by the clump finder algorithm, and filaments, based on the V_{rad}^2/K proxy, select regions distinct from the standard definition of WHIM gas, which is based only on a temperature criterion. In fact, looking at the right-most panel in Fig. 4.10, we observe how the standard definition of WHIM highlights relatively diffuse regions not directly associated with clumps or filaments.

In Fig. 4.11, we present a gas-phase diagram analysis for the cluster IT90_2 at $z = 0.1$ in order to characterise these distinct distributions. We observe how clumps

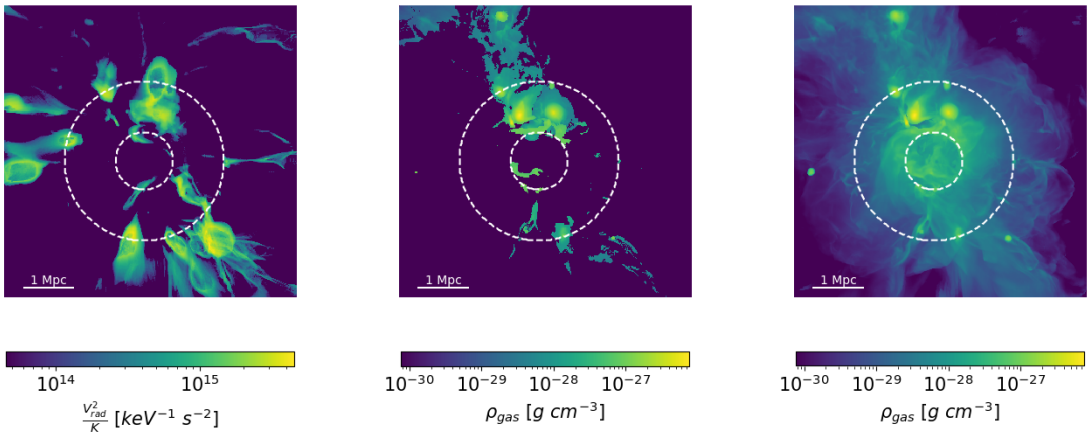

Figure 4.10: Visual comparison between filaments, clumps, and WHIM. Left panel: projected integrated V_{rad}^2/K for the filaments; centre panel: projected emission-weighted density for the clumps; right panel: projected emission-weighted density for the gas with temperature between 10^5K and 10^7K. The cluster used is IT90_2 at z=0.1. The dashed circles represent $R_{500,c}$ and $2.8R_{500,c}$.

and filaments occupy different regions in the phase diagram. Indeed, filament temperatures are mainly below 0.1 keV, while clump temperatures reach peaks greater than 1 keV. However, the density distributions are actually quite similar, with values between 10^{-5} cm^{-3} and 10^{-2} cm^{-3}. These differences assure us that our selection algorithms do not confuse the phases. In addition, we notice that the clumps seem to lie physically at the tips of the filaments pointing to related origins for these two phases. We study this finding in more in detail in Sect. 4.2.1. Moreover, the last panel of Fig. 4.11 shows the phase diagram for the gas component which we called "Diffuse". This gas is located at radii beyond $R_{500,c}$ and it is not organised into clumps or filaments.

4.1.3 Identify over-density regions in surface brightness images

To produce the mock X-rays maps of our clusters, we use two different steps. The first one generates a map in physical units erg s^{-1}, while the second one allows us to convert the X-rays emissivity in Photons Counts (in the following we will refer to it with "Cnt"), as it is obtained from the X-rays observations. We focus on the soft X-rays band from [0.3-2.0] keV. In the first step of our algorithms, we consider the density and temperature fields in the simulated box and we derive the X-rays emissivity from the sum of the following components:

$$\mathrm{EmX_{ff,i}} = \mathrm{n_i^2} \times \Lambda_{\mathrm{ff}}(\mathrm{T_i}) \tag{4.7}$$

$$\mathrm{EmX_{lin,i}} = \mathrm{n_i^2} \times \Lambda_{\mathrm{lin}}(\mathrm{T_i}) \tag{4.8}$$

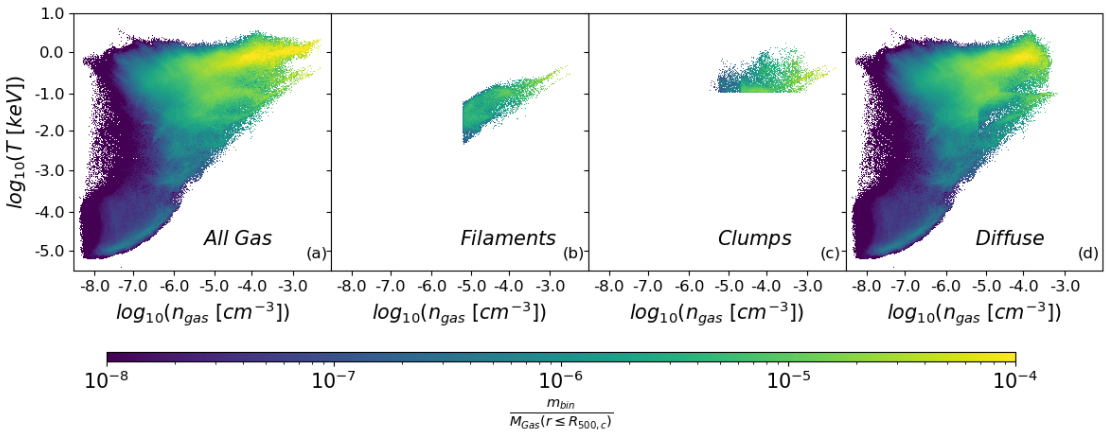

Figure 4.11: Phase diagrams for the cluster IT90_2 at z=0.1. (a): all gas present in the simulated box enclosing IT90_2; (b): filaments selected by the V_{rad}^2/K proxy; (c): clumps identified as described in Sect. 4.1.1; (d): Diffuse gas located on radii over $R_{500,c}$ and not organised into clumps or filaments. The colour-coding identifies the mass enclosed in every single bin, normalised by the central cluster's gas mass.

where i is the index which identifies each cell in the box, n is the gas density in cm^{-3}, T is the gas temperature in K and $\Lambda_{ff}(T_i)$ and $\Lambda_{lin}(T_i)$ are respectively the conversion factor for the free-free emission and the lines one, at a given temperature. The $\Lambda_{ff}(T_i)$ and $\Lambda_{lin}(T_i)$ are computed as in Vazza et al. (2019), by assuming for simplicity a single temperature and a single (constant) composition for every cell in the simulation using the APEC* emission model. We adopt a constant metallicity across all cluster volumes, $Z/Z_\odot = 0.3$, where $Z_\odot$ is the solar abundance in Anders, Grevesse (1989).

In the second step of our algorithm, we convert the X-rays emissivity in Cnt. The conversion needs three fundamental quantities: gas temperature, redshift, and selected instrument. We decide to produce maps for the Wide Field Imager (WFI), which will be on board on the ATHENA telescope (Rau et al., 2013). We fix the redshift of each cluster at z=0.05, conventionally used for simulated bright nearby sources. The conversion factor is also related to the gas temperature and to determine it, we used the *XSPEC* model *PHABS(APEC)*, in which we fix the galactic absorption at $n_H = 2 \times 10^{20}$ and the redshift at z=0.05. We produced emission-weighted maps of the temperature field and, starting from these images, we produce images in which the value in each pixel is the corresponding conversion factor. Combining the cluster's image in erg s^{-1} with the image with the conversion factor values, we obtain the image in Cnt s^{-1}. Finally, we convert each pixel dimension in $arcsec^2$ and the results are shown in the left panel of Fig. 4.12.

We produce the X-rays map for our sample, considering three different lines of

*https://heasarc.gsfc.nasa.gov/xanadu/xspec/manual/Models.html

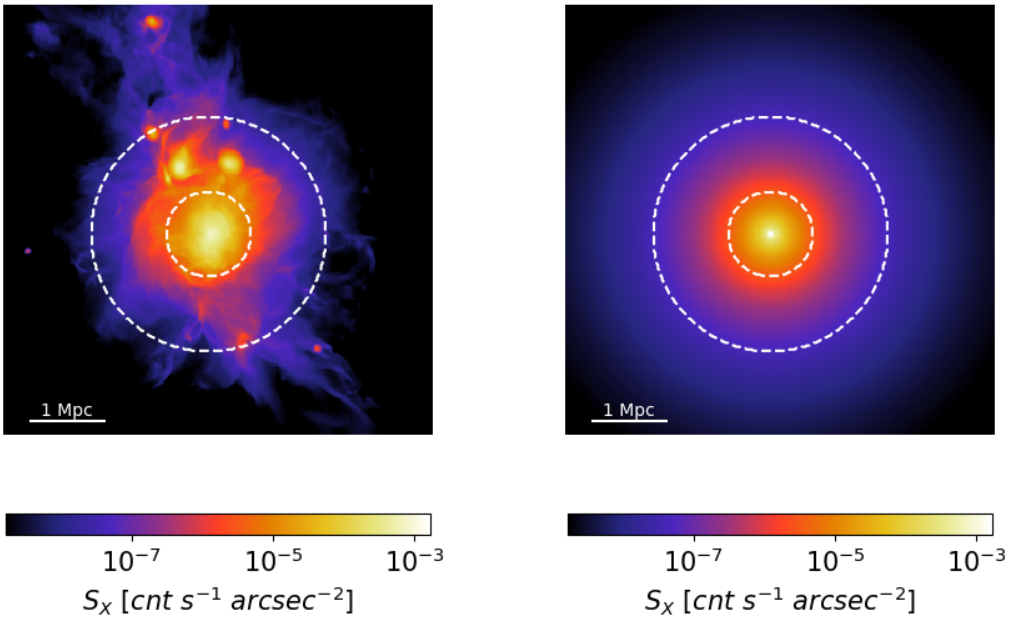

Figure 4.12: X-rays emission in the soft band [0.3-2] keV for the cluster IT90_2, in Cnt s^{-1} arcsec^{-2} units. On the left panel is the emission of the simulated cluster, and on the right one is the emission of the related background, computed as described in Sect. 4.1.3. The dashed circles represent $R_{500,c}$ and $2.8\times R_{500,c}$. The white cross is the centre of the cluster, identified as the maximum of the thermal energy in the box (as already discussed in Angelinelli et al., 2020). The colour scales are the same to help a visual comparison between the two panels.

sight (LOS), along the main axes of the box. For each LOS, we use the *CIAO* tool *WAVDETECT* (Freeman et al., 2002) to identify the over-density regions in our maps. *WAVDETECT* is based on the combination of two different *CIAO* tool: *WTRANSFORM* and *WRECON*. The first one correlates the input image with a Mexican-Hat wavelet function with different scales. All the pixels with enough large values of correlations are assumed as sources. This procedure is called "cleansing". At the end of the *WTRANSFORM* process, a catalogue of possible sources is generated for each wavelet scale. *WRECON* compares the different scales' catalogs and it combines all the information of a single source in a unique final catalogue. In the following, we report the main parameters which we equally set for all the images.

- *scales* = 2.828, 4.0, 5.657, 8.0, 11.314, 16.0, 22.62, 25.0;
- *ellsigma* = 5.0;
- *sigthresh* = 9.76e-6;
- *iterstop* = 0.001;
- *bkgsigthresh* = 0.01.

where the used parameters are:

- *scales*: the wavelet radii in units of the pixel; smaller scales detect small sources, while greater scales identify larger structures;
- *ellsigma*: the size of the elliptical identified regions, in units of pixels; this parameter is a multiplicative factor applied to the standard deviation σ of the data distribution;
- *sigthresh*: threshold applied to determine if a pixel belongs to the identified source;
- *iterstop*: the minimum ratio of pixels identified in new sources over the total number of pixels in the image; when the ratio is less than this parameter, the procedure stops;
- *bkgsigthresh*: the minimum statistical significance of the cleaning procedure on each iteration.

We differently set for each image the input background image. Starting from mock maps, we have to define a mock background. We define the background as the emission of the host cluster, and we do not consider any other source of background. To produce the X-ray map of the host cluster, we use the same procedure presented above. In this case, we use input density and temperature fields derived from the universal profile proposed by Ghirardini et al. (2019). An example result is shown in the right panel of Fig. 4.12. We will discuss the results of the procedure described above in Sect. 4.2.4.

4.2 Results

In the following, we refer to "clumps" when we present results associated with the cells selected by the clump finder algorithm. Otherwise, when we refer to cells selected by the V_{rad}^2/K estimator, we use the term "filaments". In Sect. 4.2.2, we compare the results obtained in two different radial shells of our clusters. As mentioned above, we define the centre of a cluster as the position of the peak in the thermal energy of the gas. This definition of the centre provides the most stable identification criterion, including highly perturbed systems. As outlined above, we focus on cluster peripheries. Hence, the inner shell considers all the radii enclosed in $R_{500,c} \leq r \leq 2.8R_{500,c}$, whereas the outer shell encloses radii between $2.8R_{500,c} \leq r \leq 5R_{500,c}$. This radial analysis allows us to better assess the dependence of physical proprieties on distance from the cluster centre.

Unless specified otherwise, we shall use the median, along with 16th and 84th distribution percentile boundaries to quote the results of our statistical analysis.

These measures are justified by the distribution forms of physical proprieties we are studying. An example is given in Fig. 4.13 for the cluster IT90_2. We notice that the distributions of both density and temperature are far from being described by symmetrical Gaussians, making the mean and standard deviation values weaker representative measures than the median and the two above percentiles to describe these distributions.

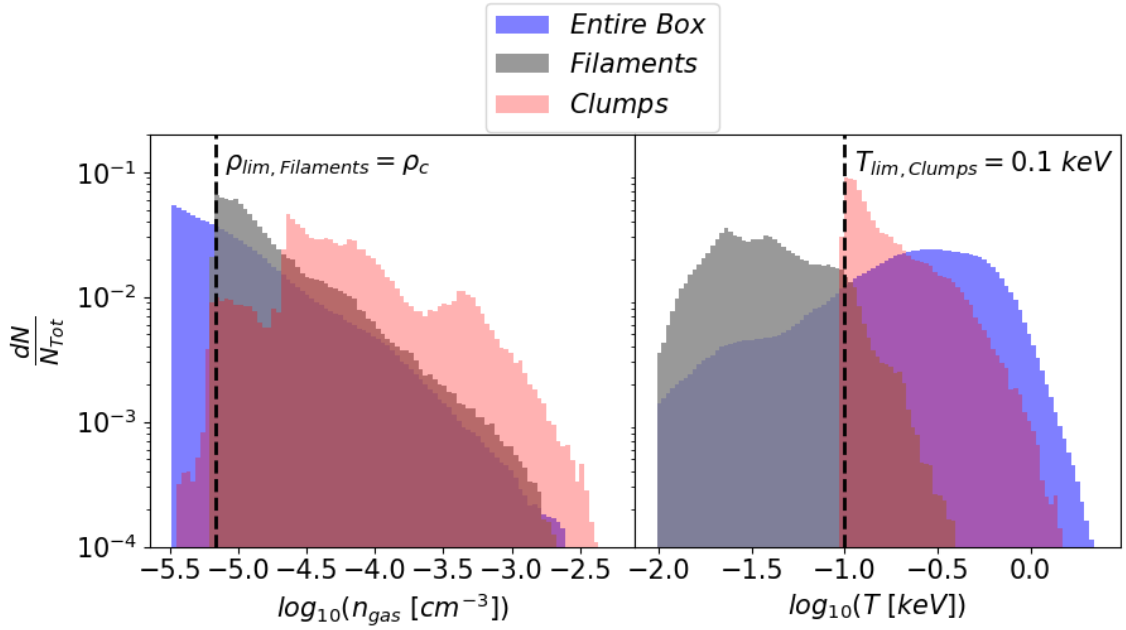

Figure 4.13: Density and temperature distributions for the different selected regions for the IT90_2 cluster at z=0.1: the blue areas represent the entire contents of the simulated box, grey areas characterise regions identified as filaments and red areas characterise clumps. Each histogram is normalised to the total number of cells present for the specified selection. The black dashed line in the left panel represents the $\rho_c(z)$, used as the lower limit for the density in the V_{rad}^2/K procedure. On the right panel, the black dashed line is the lower temperature limit of 0.1 keV, adopted for the clump finder algorithm as explained in the text.

Sometimes in the analysis, we use Pearson's correlation index, a powerful tool to verify the level of correlation between two different distributions. We compute Pearson's correlation index as:

$$\rho_{\mathrm{X,Y}} = \frac{\sigma_{\mathrm{XY}}}{\sigma_{\mathrm{X}} \cdot \sigma_{\mathrm{Y}}} \tag{4.9}$$

where $\sigma_{\mathrm{X,Y}}$ is the covariance between the quantities X and Y, while σ_{X} and σ_{Y} are the standard deviations of X and Y. Then, the test statistic t^* is given by the following equation:

$$\mathrm{t}^* = \frac{\rho_{\mathrm{X,Y}} \cdot \sqrt{\mathrm{n}-2}}{\sqrt{1-\rho_{\mathrm{X,Y}}^2}} \tag{4.10}$$

where "$\rho_{X,Y}$" is Pearson's correlation index and "n" is the total number of clusters in the sample. We compare the computed t* values with the tabulated Student's t distribution for the relative number of freedom degrees (12, $N_{Cluster}$-1) and we derive the P-value for each Pearson's correlation index shown in Tab. 4.1. As we discuss in Sect. 4.2.1, many of the studied relations show a strong level of correlation, which is also confirmed by the significance given by the P-value.

4.2.1 Physical proprieties of clumps and filaments

We now consider the density and temperature of the cells selected by the clump finder algorithm. For each cluster, we compute the median values of the density and temperature distributions and identify the locations of their 16th and 84th percentiles. We also determined the masses of individual clumps. In Fig. 4.14, we show the median values of density and temperature as functions of cluster mass. We notice an almost flat distribution of the density against cluster mass around a value of $0.6^{+1.6}_{-0.4}$ 10^{-4} cm^{-3}.

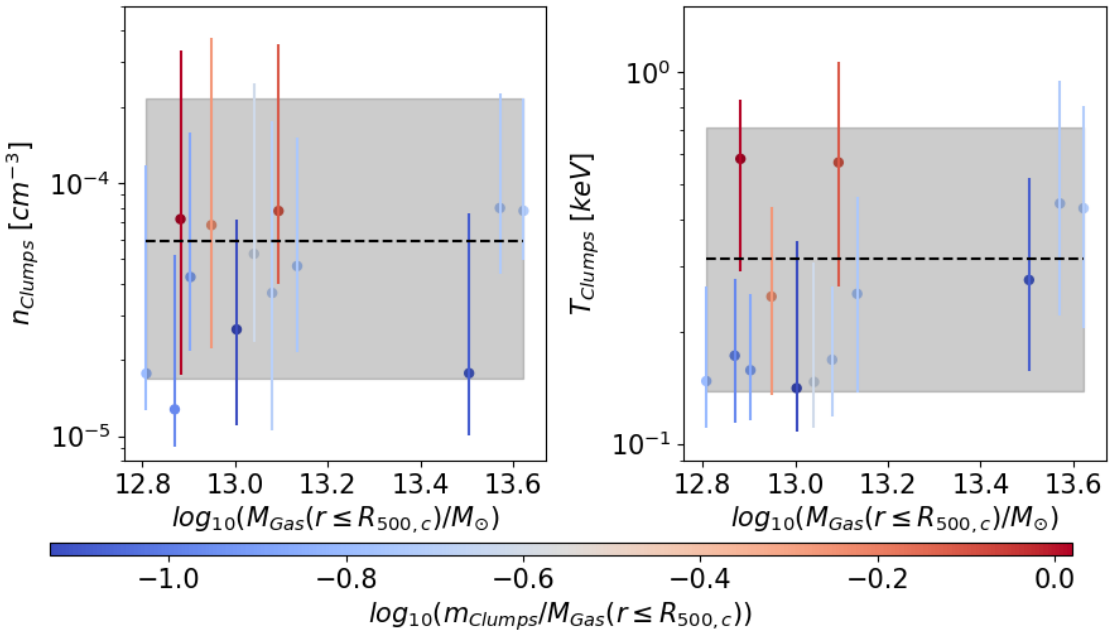

Figure 4.14: Clump density (on the left, in cm^{-3}) and temperature (on the right, in keV) as a function of $M_{500,c}$ cluster gas mass. In both the panels, the dots represent the median value, while the error bars are the 16th and 84th distribution percentiles. The colour-coding is the same for both panels and it identifies the ratio between the total clump mass and the $M_{500,c}$ cluster mass. The black dashed lines represent the median values of density and temperature for the whole clump population. The shadow grey regions are enclosed in the 16th and 84th of the density and temperature distributions.

We also observe that relatively few objects are far from this value. From the colour-coding of Fig. 4.14, we can see that those objects have larger ratios of clump

mass over cluster mass. In fact, they are merging systems, for which our clump finder algorithm can consider the baryons in the less massive interacting object as a mass clump rather than a component of a merging halo. This will bias the total clump baryon mass estimation for those clusters.

The relation between cluster mass and clump temperature is shown in Fig. 4.14 (right panel). The clump temperature distribution can be characterised as $0.3^{+0.4}_{-0.2}$ keV. We note that the median value ≈ 0.3 keV, while a factor three larger than the 0.1 keV lower temperature limit we adopted in our clump identification algorithm (see Sect. 4.1.1), is still quite small. So, it is clear that any X-ray detection of clumps, although possible, will be very challenging. As already discussed for the density distribution, now for the temperature distribution, we have some clumps with median values far from the median of the full clump population with similar masses. We believe these outliers represent merging objects.

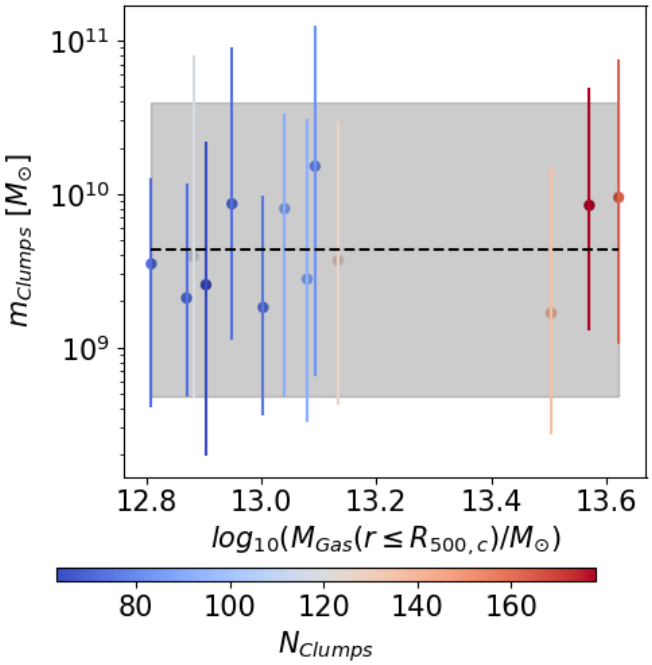

Figure 4.15: Clump mass as a function of central cluster mass. The dots represent the median value, while the error bars are the 16th and 84th distribution percentiles. The colour-coding identifies the total number of clumps found by the clump finder algorithm. The black dashed line represents the median value computed for the entire clump population. The grey shadow region is enclosed between the 16th and 84th percentiles of the clump mass distribution.

For each identified clump, we compute both mass and volume. We study the distributions of these quantities also in relation to the cluster's mass. The results are shown in Fig. 4.15 for the masses and in Fig. 4.16 for the volumes. For both distributions, we obtain median values quite independent of the host cluster's mass. For the clump masses, the median value is $0.44^{+3.53}_{-0.38}$ 10^{10} $M_\odot$, while for the volumes

it is $0.4^{+1.6}_{-0.3}$ 10^{-2} Mpc^3. In the following, using the V^2_{rad}/K criterion introduced above, we investigate the relations between the proprieties of clumps and those of the surrounding medium.

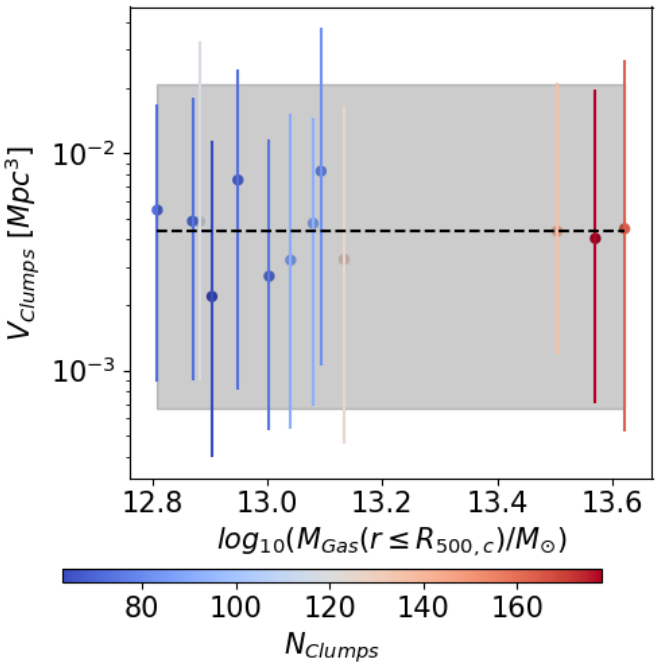

Figure 4.16: Clump volume as a function of central cluster mass. The dots represent the median value, while the error bars are the 16th and 84th distribution percentiles. The colour-coding identifies the total number of clumps identified by the clump finder algorithm. The black dashed line represents the median value computed for the entire clump population. The grey shadow region is enclosed between the 16th and 84th percentiles of the clump volume distribution.

For both clumps and filaments, we analyse the relations between the density and the temperature of the selected regions, including their dependence on the host cluster's mass. The results of these analyses are shown in Fig. 4.17. The density distribution appears to be independent of cluster mass (left panel of Fig. 4.17) with a median value of $1.3^{+3.4}_{-0.5}$ 10^{-5} cm^{-3}.

On the other hand, the temperature of the filaments seems to increase slightly with the cluster's mass (with a Pearson's correlation index $\rho_{XY} = 0.88$; see also Tab. 4.1) around a median value of $0.04^{+0.05}_{-0.02}$ keV (right panel of Fig. 4.17). This value is less than 0.1 keV, the lower limit we adopt for X-ray detection, confirming that the observations of X-ray emitting filaments are on average very challenging with current (and even future) X-ray telescopes. These behaviours also are consistent with the fact that the few significant observational X-ray confirmations that exist are typically associated with massive cluster systems.

The colour-coding of Fig. 4.17 identifies the ratio between filament masses and

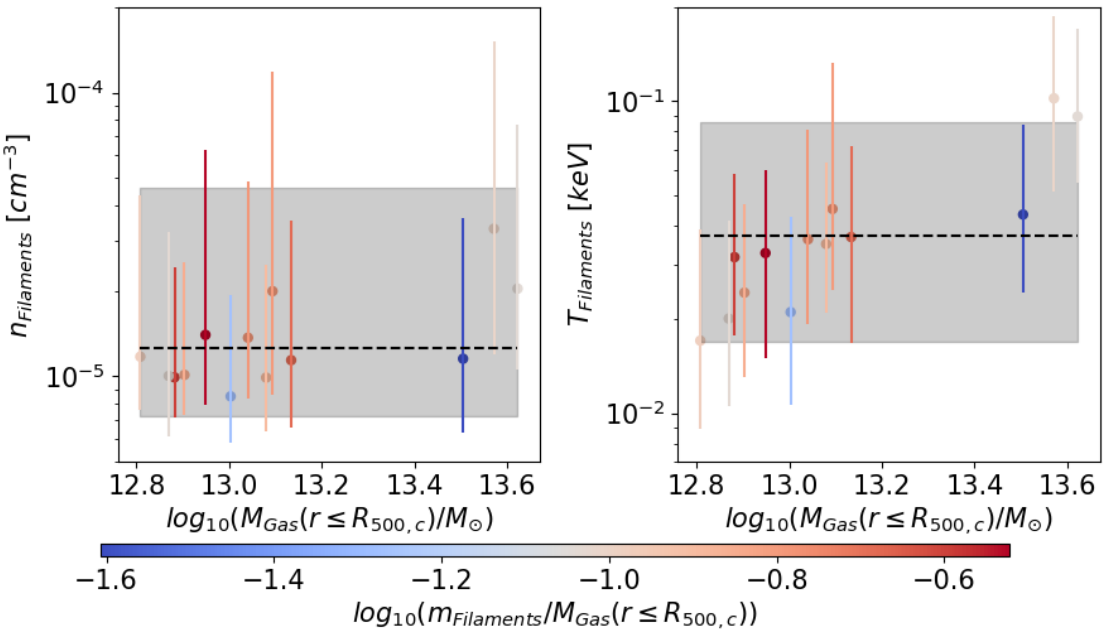

Figure 4.17: Filament density (on the left, in cm^{-3} units) and Filament temperature (on the right, in keV units) as functions of $M_{500,c}$ cluster *gas* mass. In both panels, the dots represent the median value, while the error bars are the 16th and 84th distribution percentiles. The colour-coding is the same for both panels. It identifies the ratio between the total filament gas mass and the $M_{500,c}$ cluster gas mass. The black dashed lines represent the median population values of density and temperature for the whole filament population. The shadow grey regions are enclosed in the 16th and 84th of the density and temperature distributions.

cluster masses. Distinct from the clump situation, our selection is not able to separate filaments as single, isolated objects, so we need to consider the total gas mass of all filaments connected to a given cluster. By comparing Fig. 4.14 and Fig. 4.17, we observe that some typical values can characterise the entire populations of clumps and filaments. Moreover, we do not find a strong correlation between clump or filament proprieties with the host cluster mass, excepting the filament temperature relation mentioned above. Even so, for these quantities, we could reasonably describe the full filament population using single values.

Proprieties	$\rho_{X,Y}$	t^*	**P-value**
Filaments' temperature vs. cluster's mass	0.88	6.15	$\leq$0.001
Density clumps vs. filaments	0.66	2.91	$\leq$0.02
Temperature clumps vs. filaments	0.54	2.13	$\leq$0.1

Table 4.1: Pearson's correlation index $\rho_{X,Y}$, test statistic t^* and P-value for the different correlations analysed in Sect. 4.2.1

Up until this point we have concentrated on issues specific to either clumps

or filaments. We now briefly compare the relative densities and temperatures for clumps and filaments populations of every single cluster. In Fig. 4.18, we present the results of these analyses. Both for the density and the temperature, there appear to be moderate correlations between clump and filament proprieties. For the density comparison between clumps and filaments we measure a Pearson's index, $\rho_{XY} = 0.66$, while for temperature, we estimate a somewhat weaker correlation with $\rho_{XY} = 0.54$ (see also Tab. 4.1).

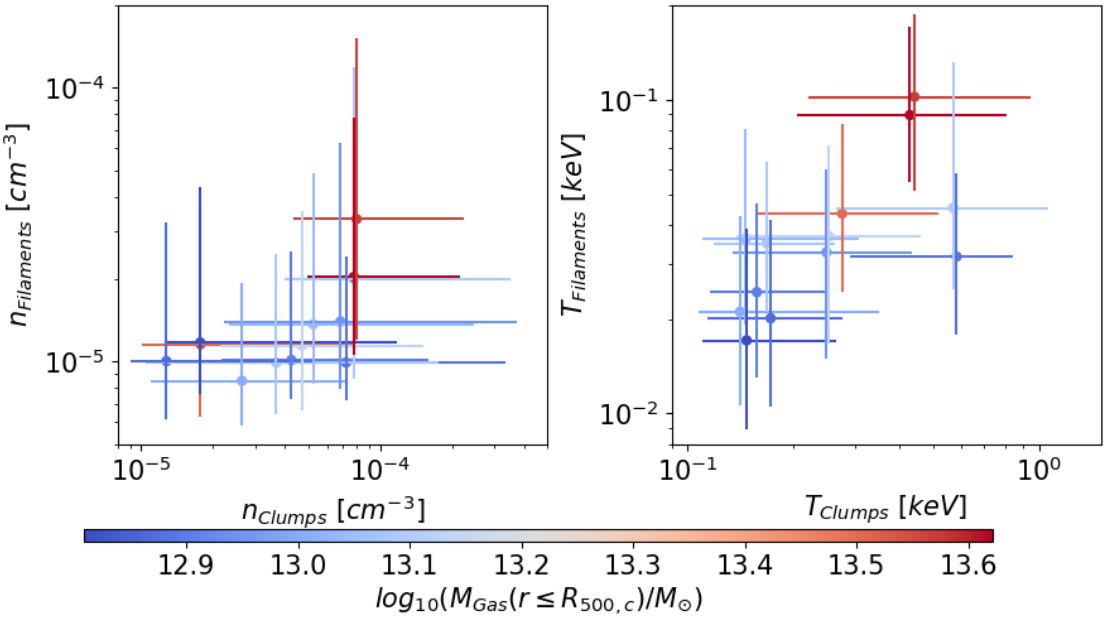

Figure 4.18: Comparison of density (in cm^{-3} units) and temperature (in keV units) for clumps (on the x-axis) and filaments (on the y-axis), for every single cluster. The dots are the median values, while the error bars are the 16th and 84th percentiles on both axes. The colour-coding is the same for both the panels and it identifies the $M_{500,c}$ cluster gas mass.

4.2.2 Analysis of the radial trends

We next study the proprieties of clumps as a function of their distance from the cluster centre, collecting the clumps into two radial shells. The inner shell goes from $R_{500,c}$ to $2.8R_{500,c}$, while the outer one spans from $2.8R_{500,c}$ to $5R_{500,c}$. As a first step, we analyse the number density of clumps per Mpc^3. The results are shown in Fig. 4.19.

The median number of identified clumps does not depend significantly on the host cluster's gas mass. However, it decreases with the growing distance from the cluster centre. Moreover, if we consider the whole volume outside the $R_{500,c}$ sphere, the clump number density slightly increases with the cluster's mass. This suggests that massive clusters roughly have the same number of clumps within $R_{500,c} - 5R_{500,c}$, but

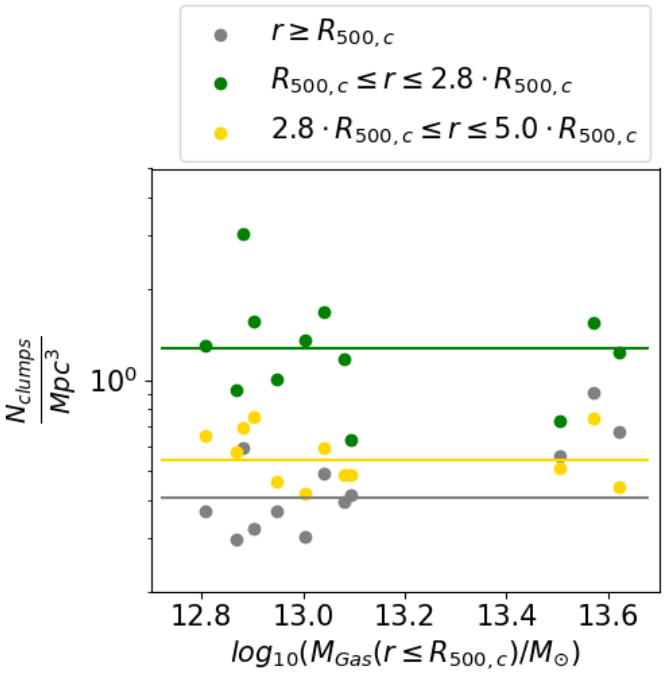

Figure 4.19: Number density of identified clumps per Mpc^3 (dots), as a function of the host cluster gas mass. The different colours show different radial selections: grey: $r \geq R_{500,c}$; green: $R_{500,c} \leq r \leq 2.8R_{500,c}$; gold: $2.8R_{500,c} \leq r \leq 5R_{500,c}$. The solid lines represent the median values of clumps per Mpc^3, computed on the whole cluster sample, using the same colour-coding adopted for the dots.

have more clumps outside $5R_{500,c}$ compared to less massive ones. Furthermore, we observe that the median clump density values for both the inner and outer shells are greater than what we obtain for the full simulation boxes around the clusters. This indicates, as expected, that clumps tend to be concentrated in the near-vicinities of host clusters.

We also investigate possible variations in clump density and temperature with distance from the cluster centre. In Fig. 4.20 we show the results of this analysis. Both density and temperature show a dependence on the radial distance from the cluster centre. We estimate median density and temperature values for the different shells. The clumps in the inner shell are described by a median density of $1.1^{+2.9}_{-0.5}$ 10^{-4} cm^{-3} and a temperature of $0.43^{+0.65}_{-0.25}$ keV. In the outer shell, we obtain analogous density $0.6^{+1.1}_{-0.4}$ 10^{-4} cm^{-3} and temperature $0.31^{+0.34}_{-0.17}$ keV, revealing a decrease of the median density and temperature with radial distance. By combining the analysis of Fig. 4.19 and Fig. 4.20, we conclude that clump X-ray detection is expected to be easier in regions closer to a cluster centre.

Indeed, in these regions, the number of clumps per Mpc^3 is higher than the outer regions and both density and temperature are higher than in the external regions. Higher values of density and temperature imply higher X-ray emissivity. On the

other hand, the closer we get to the cluster centre, the greater the X-ray emission due to the cluster itself.

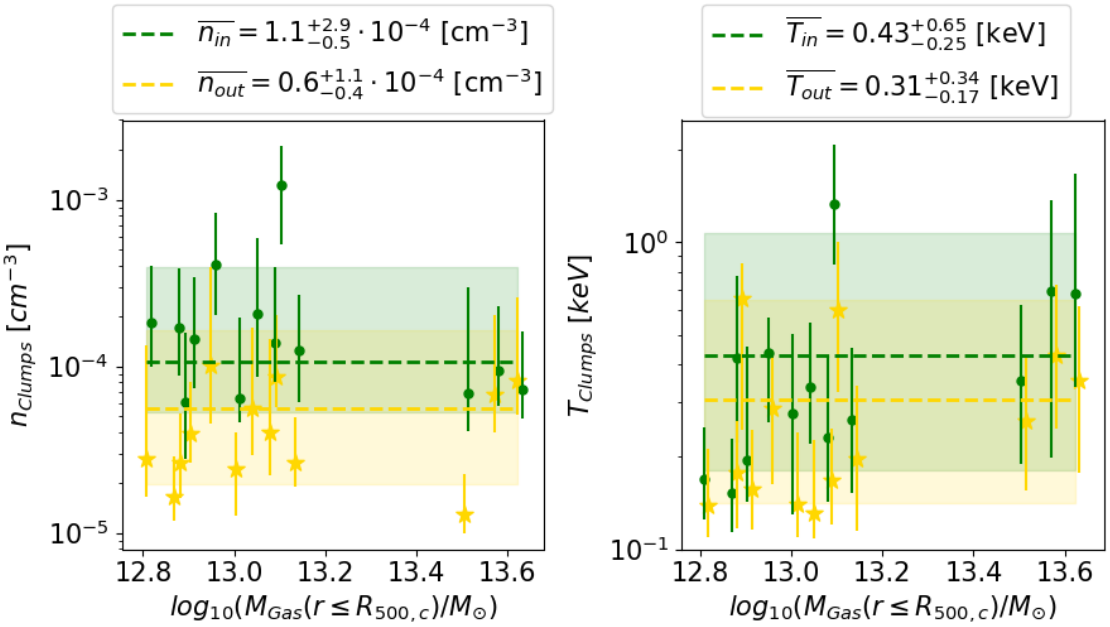

Figure 4.20: Clump density (on the left, in cm^{-3} units) and temperature (on the right, in keV units) as functions of $M_{500,c}$ cluster gas mass, for the different radial shells. In both panels, the dots represent the median value, while the error bars are the 16th and 84th distribution percentiles. The colours are the same for both panels: green represents the inner shell ($R_{500,c} \leq r \leq 2.8R_{500,c}$), while gold represents the outer shell ($2.8R_{500,c} \leq r \leq 5R_{500,c}$). The dashed lines represent the median values of density and temperature for the different clump populations (using the same colour-code of the dots). The shadow regions are enclosed in the 16th and 84th of the density and temperature distributions.

To evaluate the volume and mass contributions of clumps and filaments in different shells, we define a dimensionless function f as

$$f = \frac{\mathrm{m_k}}{\mathrm{M_{Shell}}} \tag{4.11}$$

where $\mathrm{m_k}$ in the numerator represents the (baryon) mass in clumps or filaments, while the denominator is the total baryon mass in the inner or the outer shell, combining the contributions of clumps, filaments and the diffuse gas for the same cluster. We studied also the volume filling factor, Φ, of the structures, defined as:

$$\Phi = \frac{\mathcal{V}_\mathrm{k}}{\mathcal{V}_\mathrm{Shell}}. \tag{4.12}$$

As done for the f, mass fraction metric, $\mathcal{V}_\mathrm{k}$ represents the volume occupied by clumps or filaments, and the denominator is the surveyed volume in each shell.

In Fig. 4.21 we show the results for both the adopted shells. We observe different

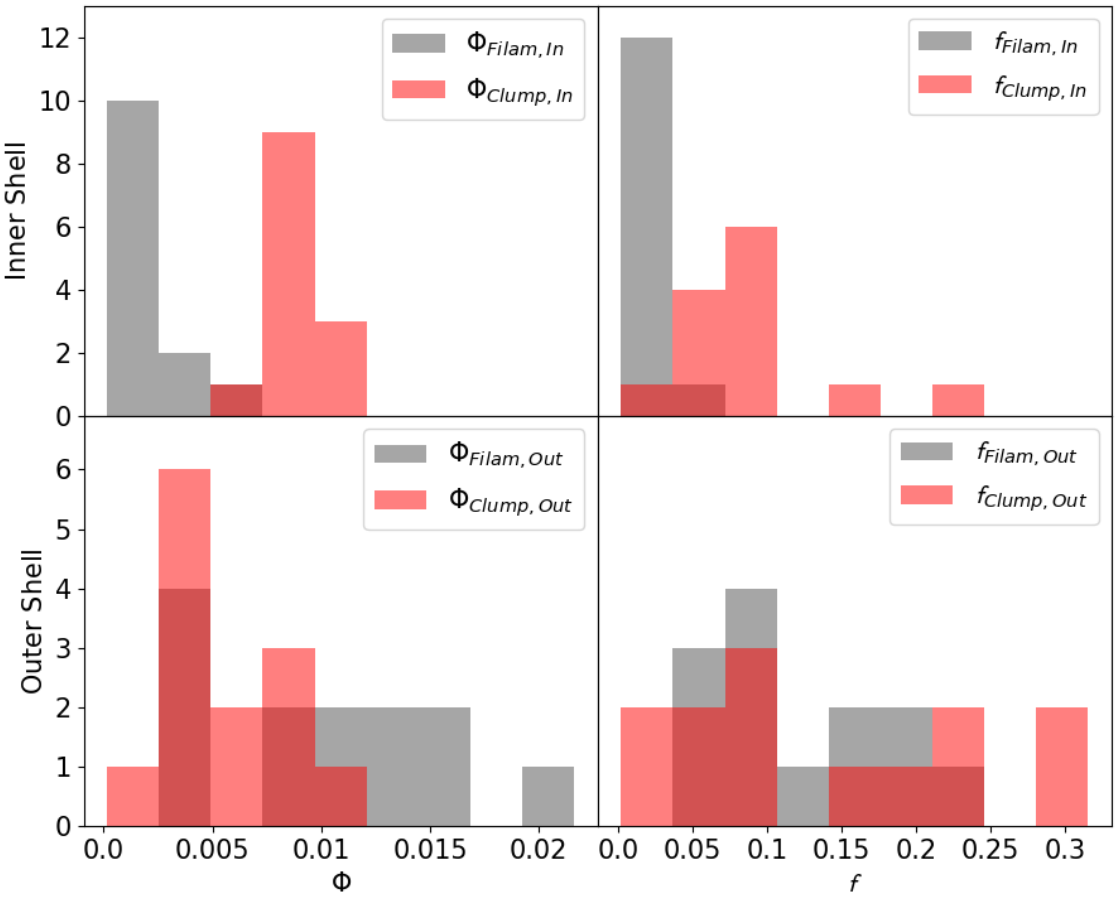

Figure 4.21: Comparison between clump and filament volume filling factor distributions, Φ and their mass contributions, f, for the different adopted shells. In all panels, the red histogram represents the clump distribution, while the grey colour identifies the filament distribution. The upper panels show Φ (on the left) and f (on the right) for the inner shell, while the bottom panels show the same distributions in the outer shell.

trends for different shells. In particular, in the inner shell (upper panels of Fig. 4.21) the filament contributions for both Φ and f, are negligible compared with those from the clumps. On the other hand, when we move to the outer shell (bottom panels of Fig. 4.21), these behaviours are quite different. The volume filling factor, Φ of filaments is now twice that for clumps. However, due to the filaments' lower densities, the mass contribution of filaments, f is comparable to that of clumps. From these results, we conclude that closer to the central cluster only clumps survive interactions with the ICM gas, while in the outer regions both clumps and filaments coexist. Moreover, the detection of filaments is easier far from the cluster's centre due to the larger occupied volume. In contrast, the detection of clumps is facilitated in the inner shells thanks to their intrinsic higher densities and temperatures.

4.2.3 Observable X-ray emission proprieties of clumps

We investigate the proprieties of the observable X-ray emission of clumps in our simulated sample of clusters. We compute the soft X-ray emissions in the band [0.3-2.0] keV for clumps in the radial range $(R_{500,c}, 5R_{500,c})$. The procedure is the same described in step 1 of Sect. 4.1.3. Then, we consider as X-ray emission from the clump the sum of the contribution of all cells belonging to the identified clump. In Fig. 4.22, we show clump X-ray emission as a function of the central cluster mass. Similar to what we found for clump masses and volumes, the X-ray emissions do not show a strong correlation with the total mass of host clusters. The median emission of our sample of clumps is found to be $0.11^{+4.83}_{-0.10}$ 10^{40} erg s^{-1}.

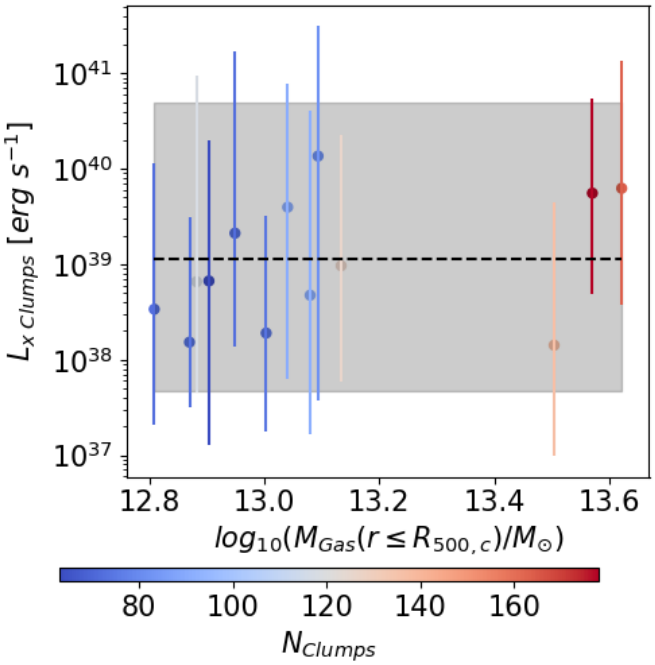

Figure 4.22: Clump soft X-ray emission ([0.3-2.0] keV band) as a function of the central cluster gas mass. The dots represent the median value, while the error bars are the 16th and 84th distribution percentiles. The colour-coding identifies the total number of clumps identified by the clump finder algorithm. The black dashed line represents the median value computed for the entire clump population. The grey shadow region identifies the 16th and 84th percentile boundaries of the clump soft X-ray emission distribution.

We study three different scaling relations for the sample of clumps: X-ray luminosity vs mass (L_x-M_{Gas}), X-ray luminosity vs gas (mass-weighted) temperature (L_x-T_{mw}), and mass vs gas (mass-weighted) temperature (M_{Gas}-T_{mw}), as shown in Fig. 4.23.

We also perform the same analysis on the full clusters in the sample. In that case, we compute the same quantities (L_x, M_{Gas} and T_{mw}) within $R_{500,c}$. Dots in Fig. 4.23 are colour coded according to clump radial distance from cluster centres.

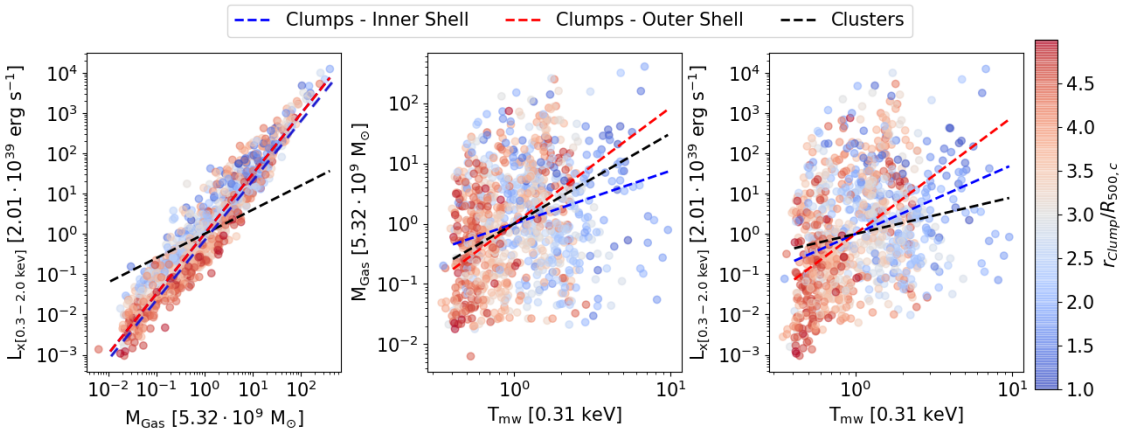

Figure 4.23: Scaling relations L_x-M_{Gas}, M_{Gas}-T_{mw} and L_x-T_{mw}, from left to right panel, respectively. The dashed lines identify different selections: clumps selected in the inner region in blue (from $R_{500,c}$ to $2.8R_{500,c}$), clumps selected in the outer region in red (from $2.8R_{500,c}$ to $5R_{500,c}$), cluster sample in black. The colourful dots represent a single clump. They are colour-coded as a function of the clump's radial distance from the cluster centre, normalised to $R_{500,c}$. We note that in the left panel, the blue dashed line is shifted arbitrarily for visual purposes. Indeed, it is perfectly over-posted on the red one, due to their identical slope.

Radial trends are apparent for all quantities displayed. The fitted trends are shown with the dashed lines with proprieties listed in Table 4.2. To prescribe such scaling relations, we use linear fitting functions. For the clump population, we sample the range of mass and temperature with 20 equally spaced logarithmic bins. Comparing the slopes obtained for the cluster sample and those proposed by Lovisari et al. (2015), we notice that our results are in good agreement with the slopes expected for simulations. However, they do not match observations. These conflicting behaviours are expected because observed clusters are influenced by radiative energy loss processes that are not included in our non-radiative simulations.

Clusters	**Clumps**	
	$\mathbf{1.0 \leq r/R_{500,c} \leq 2.8}$	$\mathbf{2.8 \leq r/R_{500,c} \leq 5.0}$
$L_x \propto M_{Gas}^{0.59}$	$L_x \propto M_{Gas}^{1.49}$	$L_x \propto M_{Gas}^{1.49}$
$M_{Gas} \propto T_{mw}^{1.49}$	$M_{Gas} \propto T_{mw}^{0.88}$	$M_{Gas} \propto T_{mw}^{1.93}$
$L_x \propto T_{mw}^{0.91}$	$L_x \propto T_{mw}^{1.71}$	$L_x \propto T_{mw}^{2.89}$

Table 4.2: Scaling relations (M_{Gas}-L_x), (M_{Gas}-T_{mw}) and (L_x-T_{mw}) for the entire cluster sample and the two clumps subsamples obtained by the inner and the outer shells.

To obtain a physical interpretation of these scaling relations, we compare the computed relations with similar ones measured by Eckmiller et al. (2011) and Lovisari et al. (2015) in samples of X-ray galaxy groups. Eckmiller et al. (2011) used

Chandra observations of 26 objects and combined those results with results derived from the HIFLUGCS clusters sample. They found that physical differences appear when groups and clusters are studied separately, but that these differences do not affect the proprieties of the scaling relations. Specifically, they found $L_x \propto M_{500}^{1.34}$, $L_x \propto T^{2.25}$ and $M_{500} \propto T^{1.68}$ for their group sample. Lovisari et al. (2015) used a sample of 20 groups observed with the XMM-Newton telescope, and reported $L_x \propto M_{500}^{1.5}$, $L_x \propto T^{2.5}$ and $M_{500} \propto T^{1.65}$, with a small dependence on the different fitting procedures adopted.

Comparing our results from our entire sample of clumps with those obtained observationally by Eckmiller et al. (2011) and Lovisari et al. (2015), we conclude that only the M_{Gas}-L_x relation seems to be in agreement, while the observed L_x-T_{mw} and M_{Gas}-T_{mw} are significantly shallower than our simulation-based results. Nevertheless, we point out that the cluster sample mass ranges of the work by both Eckmiller et al. (2011) and Lovisari et al. (2015) are different from our clump mass range. However, to further probe the validity of our scaling relations for clumps in a more massive cluster atmosphere, future dedicated X-ray observations will be necessary.

We also looked for any dependencies of the above scaling relations on distance from the cluster centre. Clearly, only the M_{Gas}-L_x relation is unchanged from small to large radii. Both L_x-T_{mw} and M_{Gas}-T_{mw} relations are steeper in the outer analysed regions, in line with Eckmiller et al. (2011) and Lovisari et al. (2015). This suggests that outside $\sim 3R_{500,c}$ clumps have not interacted with the central cluster and their physical proprieties follow the self-similar assumption, so they can be considered as mass-rescaled galaxy clusters. Recently, using data from THE THREE HUNDRED project, a collection of 324 simulated galaxy clusters, Mostoghiu et al. (2021) conclude that infalling sub-haloes lose their gas quicker when they are closer than $\sim 1.5R_{200}$. This suggests that closer than $\sim 2.5R_{500}$ the clump-cluster gas interactions could strongly change the physical proprieties of clumps and consequently the estimation of the scale relations. From Fig. 4.23, we also note that clumps are less massive, colder and less luminous with increasing radial distance from the cluster centre. All these trends influence their chance of detection around galaxy clusters. By combining the trends shown in Fig. 4.23 and the results of Sect. 4.2.2, the shell just outside $R_{500,c}$ seems to be the region that might ensure the best conditions for the detection of gas clumps using X-rays. Nevertheless, the study of clumps beyond $\sim 2.5R_{500}$ enables the reconstruction of physical proprieties which are not affected by interaction with the central galaxy cluster's gas.

4.2.4 Properties of the X-ray emission from the clumps

Thanks to the procedure described in Sect. 4.1.3, we compare the results obtained from projected quantities and the ones obtained directly from the simulated boxes.

These comparisons are useful to make predictions on future observations, but also to take into account some possible systematic uncertain that could affect present observational results.

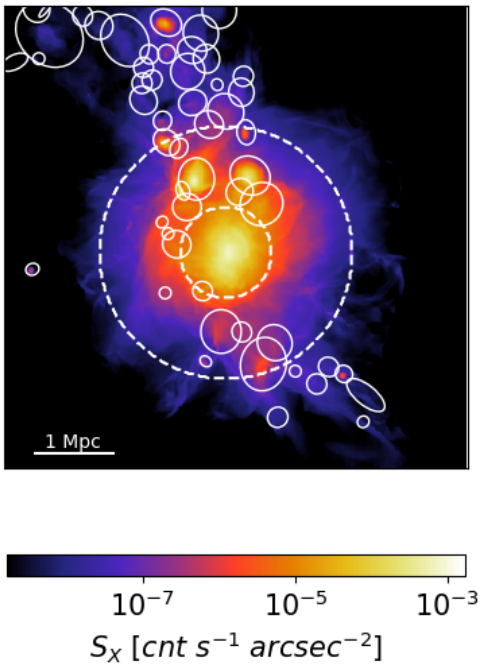

Figure 4.24: X-rays emission in the soft band [0.3-2.0] keV for the cluster IT90_2 at z=0.05, in Cnt s^{-1} $arcsec^{-2}$ units. The white ellipses are the over-density regions selected as described in Sect. 4.1.3. The dashed circles represent $R_{500,c}$ and $2.8\times R_{500,c}$. The white cross is the centre of the cluster. The colour scale is the same as Fig. 4.12.

In Fig. 4.24 we show the results of *WAVDETECT* procedure applied on cluster IT90_2 (the same presented in Sect. 4.1.2) along a line of sight (LOS). We notice how the spatial distribution of the identified sources seems to be quite filamentary. This suggests that different clumps could be visible in some LOS and obscured in others ones.

In Fig. 4.25 we show the number of identified sources along three different LOS for each cluster. We observe that the number of sources is quite different when we consider different LOS. This is due to the peculiar pattern in which clumps are organised around a host cluster. We expect a constant value of the source for each cluster only if the spatial distribution of clumps is isotropic. However, different quantity of sources in different LOS implies that the clumps' spatial distribution follows a preferential pattern described by a filamentary accretion into the host cluster. Indeed, if the pattern is described by filaments, depending on the LOS, we could or could not observe some clumps due to their projected position.

Combing the information from the three different LOS for each cluster, we compare the soft X-ray emissivity (considering the band [0.3-2.0] keV) and temperature

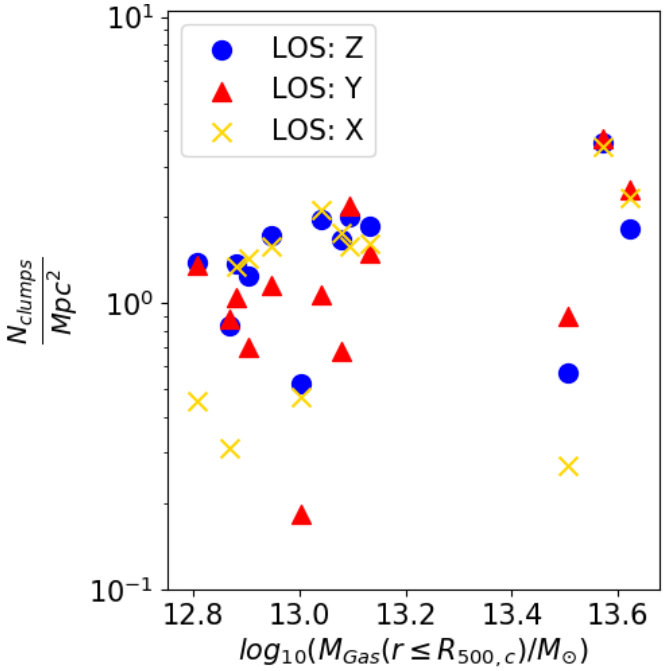

Figure 4.25: Number of identified sources along three different LOS on the unit of projected surface, for each cluster in our sample. Different markers and colours represent different LOS.

obtained from the *WAVDETECT* procedure and the clump finder algorithm. From the *WAVDETECT* procedure, we derive the emissivity as the sum of the values enclosed in each selected region, while for the temperature we considered the temperature at the centre of each region. The centre of the elliptical regions is determined automatically by the *WAVDETECT* procedure and it represents the local maximum of the overdensity region. In a similar way, also for the information derived from the clump finder algorithm, we consider the sum of the X-ray emissivity of each cell that is composed of every single clump and the temperature as the maximum in every single clump. We compare the distributions obtained from the different techniques and the results are presented in Fig. 4.26.

If the proprieties' projection has no effect, we should expect a one-to-one relation between the information obtained from the *WAVDETECT* procedure and the clump finder algorithm. However, we do not reconstruct this relation. Otherwise, we describe the correlation using Pearson's correlation index. In particular, we obtain a ρ_{XY}=0.25 and ρ_{XY}=0.72, for the X-ray emissivity and the temperature, respectively. These values suggest that the temperature is less affected by projection effects, while the X-ray emissivity is strongly dependent on the observer's line of sight. For the reconstruction of the real clumps' emissivity, starting from 2D information, we have to take into account the effects that the medium between observer and clump generates on the final estimations. The X-ray emissivity is the observable

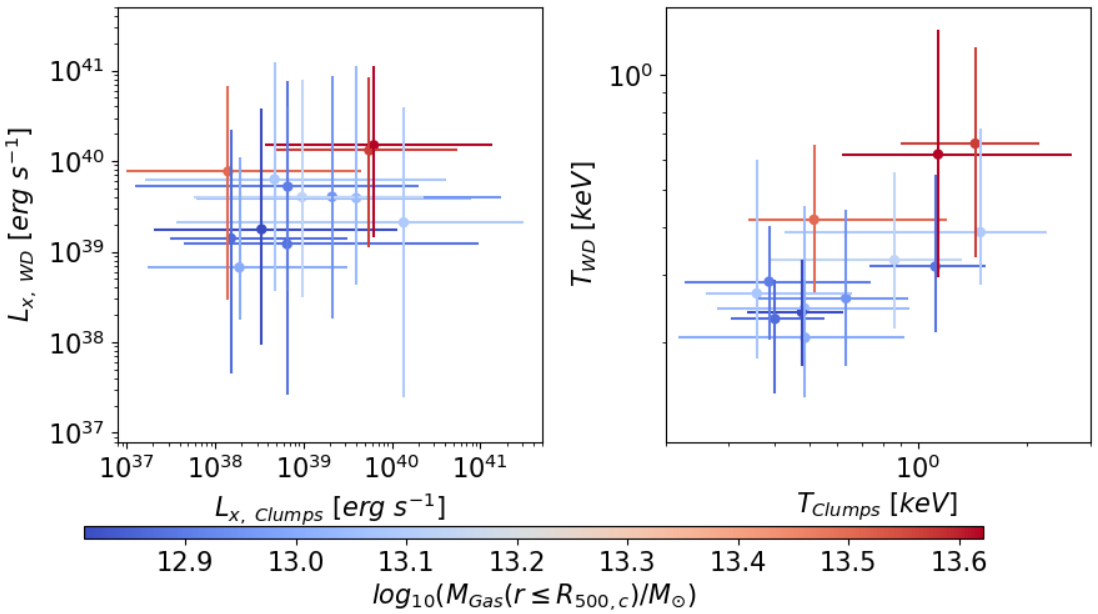

Figure 4.26: Comparison between the X-ray emissivity in the soft band [0.3-2.0] keV (on the left, in erg s^{-1} units) and temperature (on the right, in keV units) for the clumps identified by the clump finder algorithm (x-axis) and *WAVDETECT* procedure (y-axis). In both panels, the dots represent the median value, while the error bars are the 16th and 84th percentiles. The colour-coding is the same for both the panels and it represents the $M_{500,c}$ cluster's mass (computed as described in Sect. 4.1.1). As discussed in Sect. 4.2.4 the Pearson's index is $\rho_{XY} = 0.25$ for the X-ray emissivity, and $\rho_{XY} = 0.72$ for the temperature.

directly linked to the clumps' density. Small uncertainty on the X-ray emissivity could strongly affect the estimation of the clump's density.

4.2.5 The Athena view of matter clumps in clusters outskirts

To obtain a realistic observational prediction of what we would learn about clumps and filaments in the future, we simulated what the X-rays telescope Athena would observe on the clusters' peripheries. To perform these simulations, we use the SIXTE simulator (Dauser et al., 2019) in combination with a sub-sample of the clusters used in Angelinelli et al. (2021), and we produce some interesting preliminary results.

In detail, we developed a procedure that involves both the instruments onboard the Athena satellite, the Wide Field Imager (WFI; Rau et al., 2013) and the X-ray Integral Field Unit (X-IFU; Barret et al., 2018). Thanks to its large field of view, we use WFI to detect clumps in the outskirts of simulated galaxy clusters. For each of these clumps, we run a simulated X-IFU exposure to obtain spatially resolved high-resolution X-ray spectra of the plasma and to infer from them some fundamental physical quantities like gas density, temperature, metallicity, and components of the velocity both turbulent and along the line of sight.

We extract from the sample of simulated galaxy clusters adopted in our work Angelinelli et al. (2021) a couple of systems that present prominent matter clumps in their peripheries.

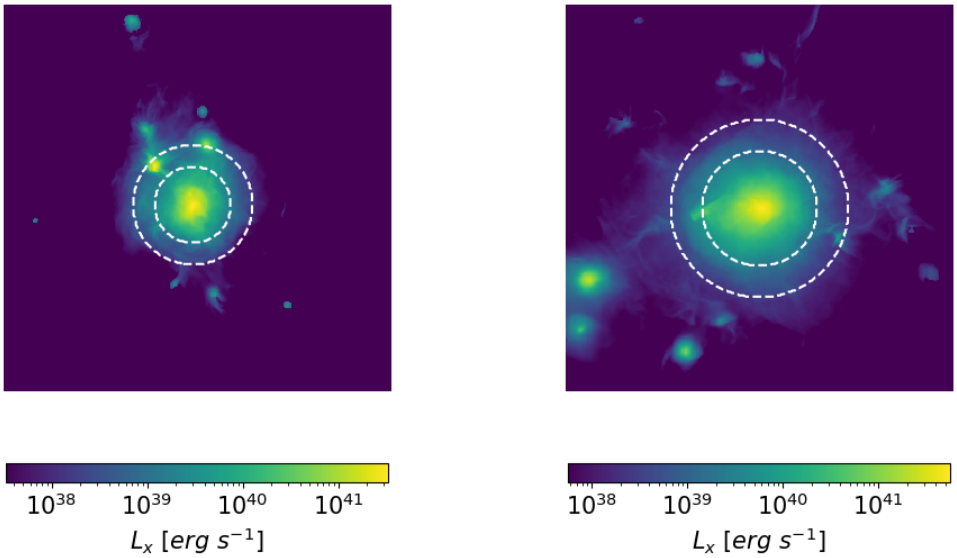

Figure 4.27: X-ray emission maps (in $erg\ s^{-}1$) of the target selected to perform the simulations of Athena satellite. On the left the cluster IT90_2, while on the right IT92_0. In both panels, the dashed white circles represent $R_{500,c}$ and $R_{200,c}$.

In Fig. 4.27 we show the X-rays emission maps of these galaxy clusters. The IDs of these systems are "IT90_2" (the same used above) and "IT92_0", which we use as identifiers in the following. We fixed the redshift of both galaxy clusters at $z = 0.05$ and the metallicity to $Z = 0.3Z_{\odot}$, to consider them as objects in the local Universe. IT90_2 has $R_{500,c} = 541.1kpc$ and $M_{500,c} = 5.6 \times 10^{13} M_{\odot}$, while IT92_0 is more massive, with $R_{500,c} = 820.9kpc$ and $M_{500,c} = 1.9 \times 10^{14} M_{\odot}$. Another difference between the selected target is the projected position of the matter clumps in which we are interested. Indeed, we selected a target with matter clumps close to $R_{500,c}$ (IT90_2) and the other one with clumps far from the cluster's centre (IT92_0). This allows us to evaluate possible effects on the estimation of matter clumps' proprieties due to their relative position with respect to the cluster's centre.

Once identified the target of our analysis, following a procedure similar to the one presented in Roncarelli et al. (2018b), we convert the simulated density, temperature and velocity fields in a SIMPUT[†] files, the input needed to perform SIXTE simulations. These files are FITS-based standards for handling source descriptions for simulations of astronomical observations. They are optimised for X-Ray simulations, but they can be used also for different bands. Then, we run the simulations using the WFI RMF and ARF available[‡].

[†] http://hea-www.harvard.edu/heasarc/formats/simput-1.1.0.pdf
[‡] https://www.sternwarte.uni-erlangen.de/sixte/instruments/

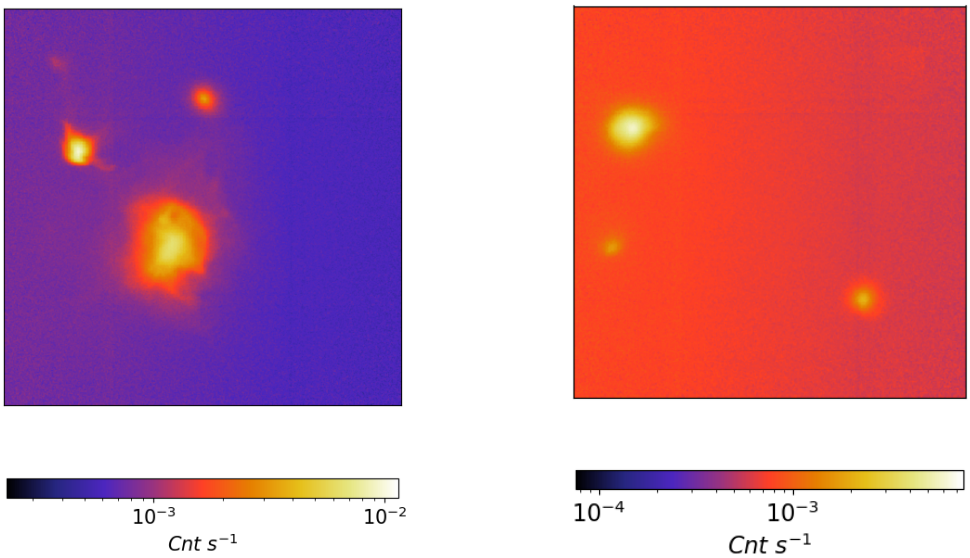

Figure 4.28: X-ray emission maps (in $Cnt\ s^{-}1$) of the targets selected to perform the simulations of Athena satellite. On the left the cluster IT90_2, while on the right IT92_0. Both maps reproduce the entire FOV of WFI, meaning a map's side of 40 arcmin.

In Fig. 4.28 we show the maps of IT90_2 and IT92_0. To perform simulations as realistically as possible, we fix an exposure time of 100ks. Being WFI a combination of four different chips with buffering regions between them, we also use the dithering technique to avoid the presence of dark regions in the final images. Moreover, for IT90_2 we fix the central pointing to the centre of the cluster, while for IT92_0, the one with the matter clumps far from the system's centre, we point our observation out of $R_{200,c}$. We also included the background, considering both the particle and instrumental components. In particular, the diffuse X-ray background consists of a soft thermal spectrum at low energies ($<$ 1keV), associated with the galactic plane and halo hot plasma, and of a hard power-law spectrum at higher energies produced by the integrated emission of many faint hard spectra of unresolved extra-galactic point sources. The background spectrum is shown in Fig. 4.29.

On the WFI maps, we run the *CIAO* tool *WAVDETECT* (see Sect. 4.1.3 for details on this tool). Thanks to this tool, we obtain the position of each over-density region presented in the maps. These regions are the matter clumps in which we are interested. On each one of these identified regions, we run a second simulation. The input SIMPUT file is the same one used for the WFI case, but now the RMF and ARF files, which described the instrument settings, are the ones delivered for the X-IFU instrument. Also for these simulations, the exposure time is fixed to 100ks and the background (with its two components) is included. Being the field of view of X-IFU is much smaller than the one of WFI, the dithering technique is not used in this case. As a result of these simulations, we obtained event files, in the same format used for real X-rays observations. From these event files, we can reconstruct

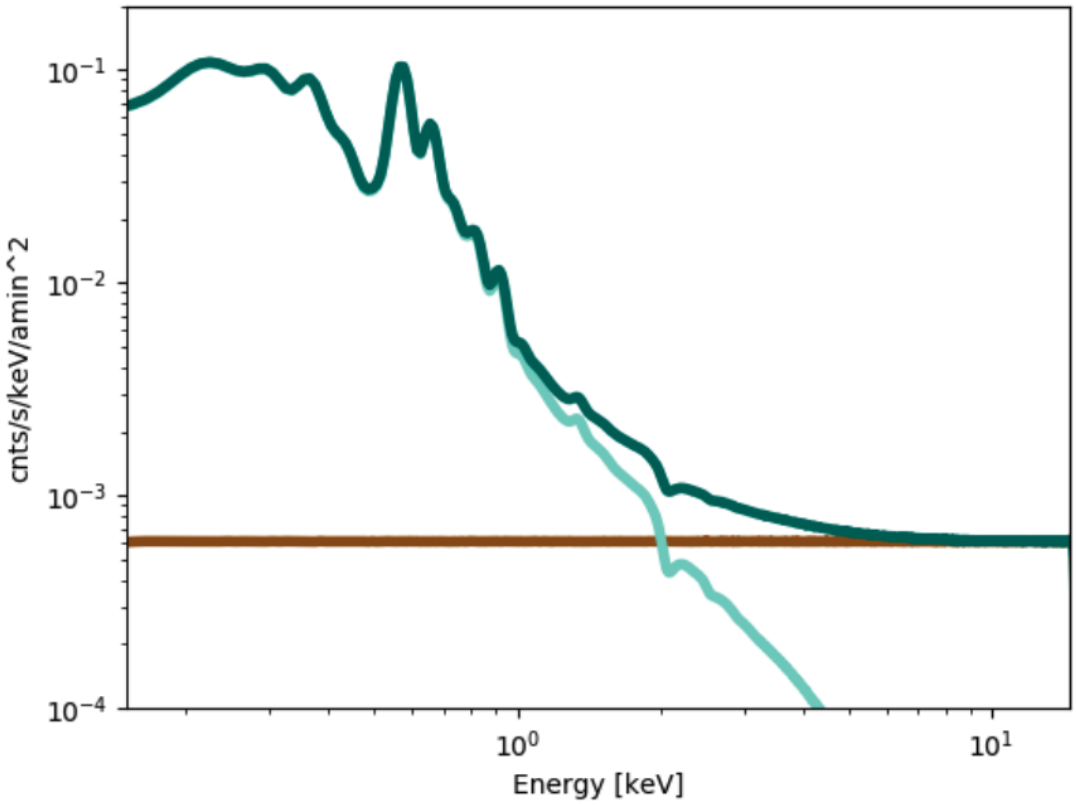

Figure 4.29: Background components for extended sources, on-axis, without external optical blocking filter, in units of $cnt\ s^{-1}\ keV^{-1}\ arcmin^{-2}$. The photon background (light green), the particle background (brown), and the sum of both (dark green) are shown. Credits: WFI consortium, preparation files for background simulations.

both the images and the spectra of the targets. In Fig. 4.30 we show the images and the spectra of one of the clumps located in the outskirts of IT90_2. We limit the spectral analysis in the soft energy band, between 0.1 and 2.0 keV.

Indeed, this energy range is the preferred one to study the physical proprieties of matter clumps, due to their expected combination of density and temperature. We also plan a detailed analysis of the velocity field inside the matter clumps. To perform this analysis, we divide the X-IFU observed in 60 squared sub-regions and we extract single spectra for each one of these sub-regions. These sub-regions are visible in the left panel of Fig. 4.30. However, the results of detailed analysis on the velocity fields are not already available.

Once the spectra are extracted, we use the B-APEC[§] model implemented in the XSPEC (Arnaud, 1996) software to fit the spectra and derived the physical characterisation of the observed matter clumps. B-APEC allows the fitting of a continuum with a thermal broadening of the lines. This allows us to determine

[§]https://heasarc.gsfc.nasa.gov/xanadu/xspec/manual/node136.html

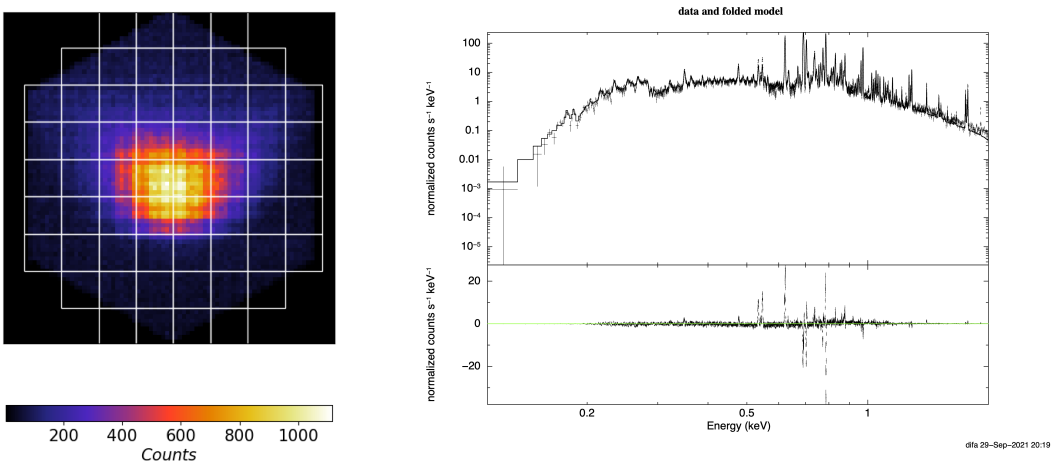

Figure 4.30: X-ray emission maps (in Cnt) and the spectra in the energy band 0.1-2.0keV of one clumps located in the outskirts of IT90_2. The squares in the maps are described in Sect. 4.2.5.

the temperature, density and velocity of the matter clumps. In particular, the density is related to the normalisation of the spectra, while the velocity field is split into two components. The first component is related to the bulk motion of the matter clump and it is described by the redshift of the source in the fitting result, while the second component, related to the σ parameter, gives us information about the velocity field inside the matter clump. Moreover, we have to subtract the contribution from the background. We run dedicated simulations in empty regions, to mimic what is done in observations when the background is determined using blank fields. Another possibility that we have planned to investigate is the determination of the background using one (or more) of the sub-regions in which we divide our X-IFU simulations. This will allow us to achieve a better estimation of the background because a residual emission from the central galaxy clusters could affect the background subtraction, especially when the matter clumps are located in the proximity of the central cluster. However, this technique is still in progress and the results we discuss later are only obtained using a background from blank fields. To evaluate the robustness of our results, we compare the results obtained from the fitting procedure with the one directly obtained by the *ITASCA* simulations, which we use as input. The results are presented in Fig. 4.31

We have to convert the temperature, density and velocity simulated field in quantities related to the one that results from the fitting procedure. Indeed, we have to convert three-dimensional information into quantities that depend on the line of sight. For the temperature, we refer to Mazzotta et al. (2004), where the

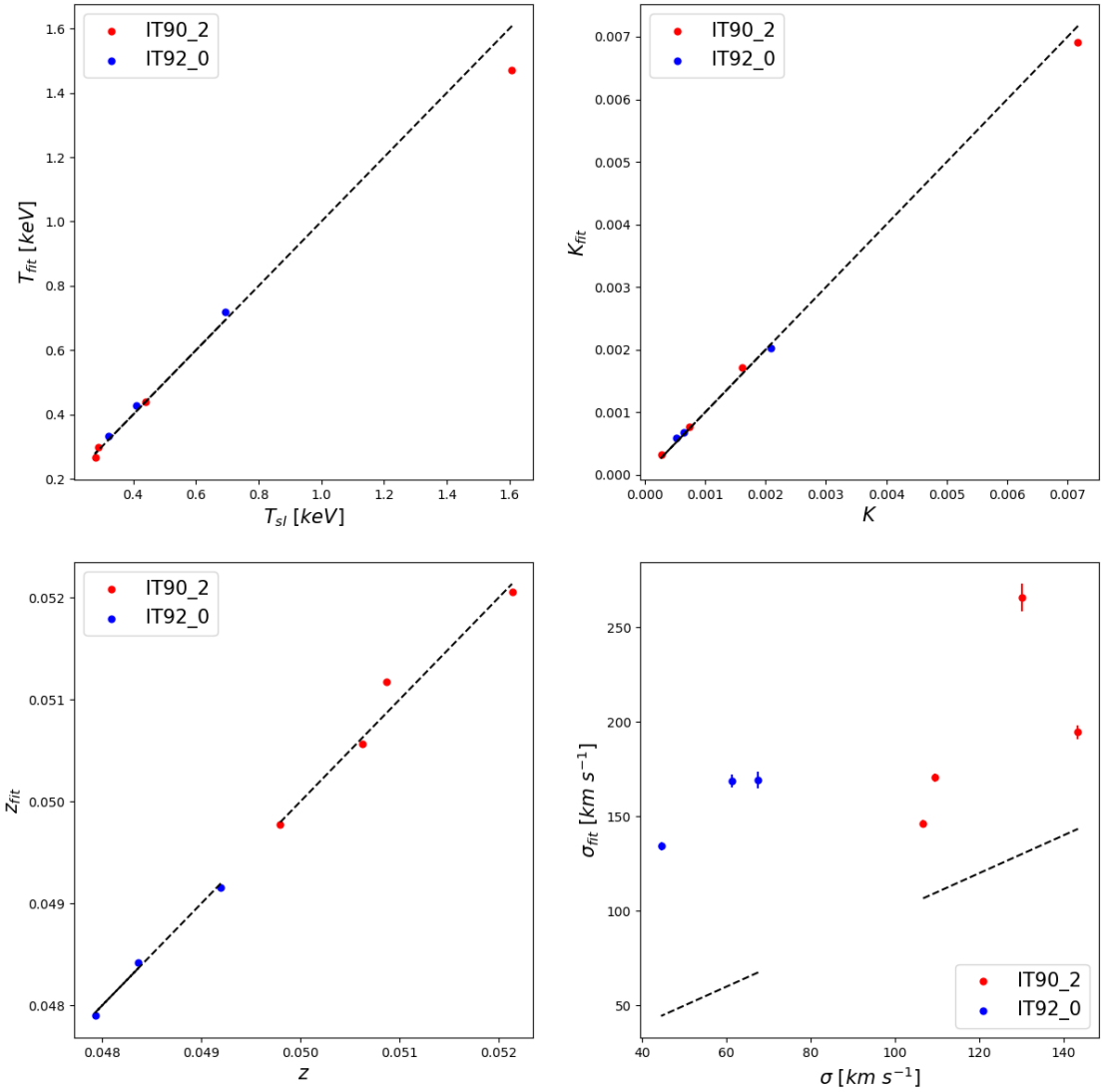

Figure 4.31: Comparison between the results obtained from the *ITASCA* simulations (x-axis) and the fitting procedure applied to the X-IFU spectra (y-axis), applied to cluster IT90_2 (red dots) and IT92_0 (blue dots). (Top-left) Temperature, computed as spectroscopic like temperature (Mazzotta et al., 2004) for the *ITASCA* simulations and directly derived from the fit. (Top-right) Normalisation K, the gas density is related to the normalisation of the spectra. (Bottom-left) Redshift, the velocity field projected along the line of sight in the *ITASCA* simulations is related to the redshift of the source determined by the fit. (Bottom-right) σ, the velocity field of matter clumps is related to the broadening of the lines traced by the *sigma* parameter in the fitting procedure.

authors give a definition of spectroscopic-like temperature, defined as:

$$T_{sl} = \frac{\int \rho^2 T^{0.25} dl}{\int \rho^2 T^{0.75} dl} \tag{4.13}$$

where ρ is the gas density, T is the temperature and integrals are computed on dl which represent the line of sight. In the top-left panel of Fig. 4.31 we note how the fitting procedure is completely able to match the input results. For the B-APEC model we applied to the data, it is possible to relate the 3D gas density to the normalisation of the spectra following this relation:

$$K = \frac{10^{-14}}{4\pi[D_A(1+z)]^2} \int n_H n_e dV \tag{4.14}$$

where D_A is the angular diameter distance to the source (cm), n_e and n_H are the electron and H densities (cm^{-3}), respectively. In the top-right panel of Fig. 4.31 we show the match between input and output. As for the temperature, also the density of the matter clumps is well recovered by the fitting procedure. It is possible to relate the redshift of the source estimate by the B-APEC model with the velocity projected along the line of sight, using the following relation:

$$z = \int v_{los} dl \tag{4.15}$$

As for the cases of temperature and density, also the velocity field is well reconstructed. This velocity represents the bulk motion of matter clumps, while to have information about the internal velocity field, we need the *sigma* parameter. This fitting parameter is related to the simulated velocity field by the relation:

$$\sigma = \int v_{los}^2 dl - \left(\int v_{los} dl \right)^2 \tag{4.16}$$

The results of σ are shown in the bottom-left panel of Fig. 4.31. Here, we note that the fitting procedure overestimates the input values for all the matter clumps observed. This discrepancy could be associated with the internal motion of the gas that is not completely due to the thermal motion, as assumed by the B-APEC model, or a not well subtraction of the background implemented in our analysis. We already planned a better estimation of the local background, as discussed above.

All the results presented in this section have to be considered preliminary and the conclusions we proposed are still under investigation.

4.3 Discussion

The presence of clumps and filaments in the proximity of galaxy clusters, and physically connected to the gas atmosphere of the host halo was predicted early on by cosmological simulations and more recently supported by X-ray observations (Eckert et al., 2015b; Simionescu et al., 2017; Reiprich et al., 2020). However, due to the low X-ray emissivity of such structures, a complete physical picture of these structures supported by observations is still missing. In this work, we use a catalogue of 13 galaxy clusters simulated at uniformly high resolution with the cosmological code *ENZO* (see Sect. 2.2; Vazza et al., 2017; Wittor et al., 2017; Vazza et al., 2018a) to introduce and test novel strategies that could be used to identify and characterise such clumps and filaments both from simulations and through observations.

We have verified (see Appendix 8.2) that the spatial resolution used in our simulations is suitable to capture and characterise clumpy and filamentary accretions formed in these non-radiative simulations, in a reasonably converged way. We expect, however, that some of the statistics extracted from our sample (especially the thermodynamical proprieties of clumps) may change after the adoption of more sophisticated treatments of chemistry, cooling and galaxy-formation related processes.

Specifically, we have introduced two different algorithms to robustly identify, and distinguish between, clumps and filaments in each of our simulated cluster volumes. Our clump finder algorithm is based on work by Zhuravleva et al. (2013) and Roncarelli et al. (2013), where clumps were classified as a tail of the log-normal mass density probability distribution function, corresponding to the densest 1% of cells within each radial shell around a cluster centre. In order to associate cells in our simulations with individual clumps, we implement a clustering procedure for neighbouring selected cells, based on the baryon mass within a chosen enclosure radius (Sect. 4.1.1).

Owing to their more complex and extended morphology, filaments are more challenging to define than clumps, both observationally and numerically. While clumps can be robustly identified by local over-density conditions, filaments require a more sophisticated approach (see Libeskind et al., 2018, for a detailed review on numerical definitions of filaments), especially when they overlap with the cluster ICM. We have, thus, developed a new proxy tool targeting the parameters of radial velocity and entropy associated with gas undergoing accretion from cosmic web filaments onto our simulated galaxy clusters (as in Eq. 4.5).

We stress that detailed physical analysis of clumps and filaments in our work is limited by the restricted range of physical processes included in our (non-radiative) suite of cluster formation simulations.

Galárraga-Espinosa et al. (2020) recently applied simulations with a richer set of physical processes from the Illustris-TNG suite (Nelson et al., 2019). The phase dia-

grams of gas in their simulations show proprieties distinct from our work (Fig. 4.11), supporting the notion that non-gravitational physical processes related to galaxy formation, as well as radiative gas cooling, can significantly affect the evolution of gas thermodynamics. In their work, those authors divided the gas component into five different phases, based on threshold values of density and temperature. We note that in our simulations their "halo gas" phase is completely missing, while the warm circumgalactic medium (WCGM) is significantly reduced. We would, indeed, expect those phases to depend on details of gas thermodynamics. In our work we focus on simpler and numerically less expensive non-radiative simulations, thus assessing the impact of the processes described above on the observational proprieties of filaments that will be a mandatory step to consider. We can refer to an earlier inspection of the effects of radiative gas physics and AGN feedback on the distribution of density fluctuations in (similar) ENZO simulations of galaxy clusters (Vazza et al., 2013b). This analysis found, on the one hand, that the physical proprieties of clumps are modified by details of baryon physics, but also that the large-scale organisation of clumps and filaments around them is not significantly modified by this. Concerning the effect of spatial resolution, our simulations are robust in the sense that they adopt a fixed spatial resolution in the cluster region, rather than adaptive mesh refinement. Additional resolution tests presented in Appendix 8.2 also show that the impact of spatial/force resolution on the distribution of the gas clumping factor and on the formation of single clumps is small once a resolution ≤ 20 kpc is considered throughout their development.

The combination of the above results suggests that the suite of simulations we used for this work can provide a robust initial characterisation of the morphology, distribution and large-scale correlation of clumps and filaments, which are largely dominated by purely gravitational processes. However, the detailed thermodynamical proprieties of clumps (and, to a lesser extent, also of filaments) are expected to depend on specific prescriptions for baryonic physics. In this respect, our non-radiative simulation setup can only be considered as a toy model to study the feasibility of future observational investigations. Incidentally, we note that early tests presented in Vazza et al. (2013b) compared the average number of clumps detected in high-resolution non-radiative cosmological simulations (similar to the ones analysed in this work) and the catalogue of point-like sources identified by the X-ray analysis of ROSAT exposures of A2142, finding an agreement within a factor ~ 2 across the cluster volume (see their Fig. 11).

Chapter 5

Radial distribution of the baryons in massive halos: dependencies on mass and redshift

In this chapter, I report on the results presented in Angelinelli et al. (2022) and in another work recently accepted (Angelinelli et al. 2023).

In Angelinelli et al. (2022), we analyse the distributions of the baryons in massive halos ($M_{vir} > 10^{13}\ h^{-1}M_{\odot}$) in the *Magneticum* suite of Smoothed Particle Hydrodynamical cosmological simulations, out to the unprecedented radial extent of $10R_{500,c}$. As already discussed in the literature, also in our sample, we find that, under the action of non-gravitational physical phenomena, the baryon mass fraction is lower in the inner regions ($< R_{500,c}$) of increasingly less massive halos, and rises by moving outwards, with values that span from 51% (87%) in the regions around $R_{500,c}$ to 95% (100%) at $10R_{500,c}$ of the cosmological value in the systems with the lowest (highest; $M_{vir} \sim 5 \times 10^{14}\ h^{-1}M_{\odot}$) masses. The galaxy groups almost match the gas (and baryon) fraction measured in the most massive halos only at very large radii ($r > 6R_{500,c}$), where the baryon depletion factor $Y_{\rm bar} = f_{\rm bar}/(\Omega_{\rm bar}/\Omega_{\rm m})$ approaches the value of unity, expected for "closed-box" systems. Moreover, we find that both the radial and mass dependency of the baryon, gas and hot depletion factors are predictable and follow a simple functional form. Lastly, the star mass fraction is higher in less massive systems, decreases systematically with increasing radii, and reaches a constant value of $Y_{\rm star} \approx 0.09$, where also the gas metallicity is constant, regardless of the host halo mass, as a result of the early ($z > 2$) enrichment process.

Additionally, in Angelinelli et al. (2023), we study the redshift evolution of the baryon budget in a large set of galaxy clusters from the *Magneticum* suite. At high redshifts ($z \gtrsim 1$), we obtain “closed box” systems independently by the mass of the systems on radii greater than $3R_{500,c}$, whereas at lower redshifts, only the most

massive halos could be considered as "closed box". Furthermore, in the innermost regions ($r < R_{500,c}$), the baryon fraction shows a general decrease with the redshift and, for less massive objects, we observe a much more prominent decrease than for massive halos (Y_{bar} decreases by $\sim 4\%$ from $z \sim 2.8$ to $z \sim 0.2$ for massive systems and by $\sim 15\%$ for less massive objects in the same redshift range). The gas depletion parameter $Y_{gas} = f_{gas}/(\Omega_{bar}/\Omega_{tot})$ shows a steeper and highly scattered radial distribution in the central regions ($0.5R_{500,c} \leq r \leq 2R_{500,c}$) of less massive halos with respect to massive objects at all redshifts, while on larger radii ($r \geq 2R_{500,c}$) the gas fraction distributions are independent of the masses or the redshifts. We divide the gas content of halos into the hot and cold phases. The hot, X-rays observable, component of the gas traces well the total amount of gas at low redshifts (e.g. for $z \sim 0.2$ at $R_{500,c}$, in the most massive sub-sample $-4.6 \times 10^{14} \leq M_{500,c}/M_{\odot} \leq 7.5 \times 10^{14}$ / less massive sub-sample $-6.0 \times 10^{14} \leq M_{500,c}/M_{\odot} \leq 1.9 \times 10^{14}-$ we obtain: $Y_{gas} \sim 0.75/0.67$, $Y_{hot} \sim 0.73/0.64$, and $Y_{cold} \sim 0.02/0.02$). On the other hand, at higher redshifts, the cold component provides a not negligible contribution to the total amount of baryon in our simulated systems, especially in less massive objects (e.g. for $z \sim 2.8$ at $R_{500,c}$, in the sub-sample of the most massive objects $-2.5 \times 10^{13} \leq M_{500,c}/M_{\odot} \leq 5.0 \times 10^{13}$ / less massive sub-sample $-5.8 \times 10^{12} \leq M_{500,c}/M_{\odot} \leq 9.7 \times 10^{12}-$, we measure: $Y_{gas} \sim 0.63/0.64$, $Y_{hot} \sim 0.50/0.45$, and $Y_{cold} \sim 0.13/0.18$). Moreover, the behaviour of the baryonic, entire gas, and hot gas phase depletion parameters as a function of radius, mass, and redshift are described by some functional forms for which we provide the best-fit parametrization. The evolution of metallicity and stellar mass in halos suggests that the early ($z > 2$) enrichment process is dominant, while more recent star-formation processes give negligible contributions to the enrichment of the gas metallicity. In addition, Active Galactic Nuclei (AGN) have an important role in the evolution of galaxy clusters' baryon content. Thereby, we investigate possible correlations between the time evolution of AGN feedback and the depletion parameters in our numerical simulations. Interestingly, we demonstrate that the energy injected by the AGN activity shows a particularly strong positive correlation with Y_{bar}, Y_{cold},Y_{star} and a negative one with Y_{hot}, Z_{Tot}. Y_{gas} shows the less prominent level of negative correlation, a result which is highly dependent on the mass of the halos. The radial trends of depletion parameters and the relations between baryon distribution and AGN feedback are consistent with previous theoretical and numerical works (Lapi et al., 2005; Castro et al., 2021; Ragagnin et al., 2022; Ayromlou et al., 2022), meaning that our results, combined with findings derived from current and future X-rays observations (e.g. measurements of f_{gas} inside $R_{500,c}$ for galaxy groups and high-z systems; constraints of f_{gas} in outskirt regions $> R_{500,c}$; proxies of radial distributions of metals), represent possible proxies to test the AGN feedback models used in different suites of numerical simulations. Below, I describe the numerical

dataset and the methods applied to it to recover the baryonic distribution studied in Angelinelli et al. (2022) and Angelinelli et al. (2023). I present in Chapt. 6 the discussions of, and the conclusions derived from, the results obtained.

5.1 Methods

In Angelinelli et al. (2022), we analyse a catalogue of galaxy clusters and groups extracted from the simulated box *Box2b* of *Magneticum* simulations (see Sect. 2.3 for details), at last, available snapshot ($z = 0.25$). To build our sample, we divide the mass range between $M_{\rm vir}$, from $10^{13}\ h^{-1}M_{\odot}$ and $> 5{\cdot}10^{14}\ h^{-1}M_{\odot}$ (corresponding to $M_{500,\rm c}$ between $4.2 \cdot 10^{12}\ h^{-1}M_{\odot}$ and $5.4 \cdot 10^{14}\ h^{-1}M_{\odot}$ for the less massive and the most massive system, respectively) in 14 equal bins in the logarithmic space. For each bin, we randomly selected 10 objects from simulated *Box2b*. Therefore, the final sample is composed of a total of 140 galaxy groups and clusters where the smallest halo is represented by $4.6 \cdot 10^4$ particles in the radial range shown in Fig. 5.1, which gives the density profiles for each object, as well as the median values computed in the 14 mass bins.

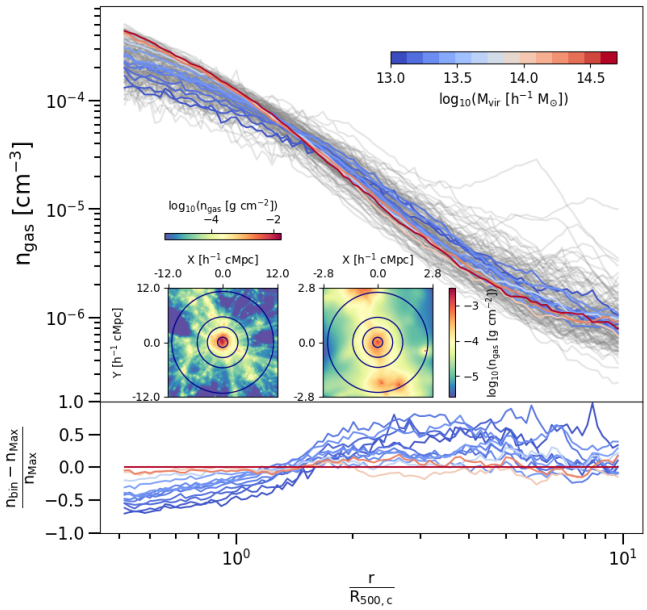

Figure 5.1: (Top) Radial profiles of gas density from $0.5R_{500,c}$ up to $10R_{500,\rm c}$. Grey lines indicate profiles of single objects, while coloured lines are the median values computed in different mass bins (see colour legend); (Bottom) Median radial profiles of the gas density of different mass bins computed with respect to the median radial profile of the most massive bin (same colour legend of the upper plot); (Insets) Projected 2D electron gas density maps for the most (left; $M_{vir} = 9.8 \cdot 10^{14}\ h^{-1}M_{\odot}$, $R_{500,\rm c} = 1120.4\ h^{-1}$ckpc) and the less (right; $M_{vir} = 10^{13}\ h^{-1}M_{\odot}$, $R_{500,\rm c} = 252.5\ h^{-1}$ckpc) massive objects in our sample. The blue circles represent 1, 3, 5 and 10 $R_{500,\rm c}$.

In addition, Fig. 5.1 also shows two gas density maps for the most massive and less one object in our sample, produced using the software SMAC (Dolag et al., 2005a). To have also an upper limit for the radial range of our analysis, we consider the boundary of our system as the position of the accretion shocks. Different definitions of the position of accretion shock could be found in literature (Zhang et al.,

2020; Aung et al., 2021). In our work, we assume that the position of the accretion shock is located at the same radius at which the gas entropy profile reaches the peak (Vazza et al., 2011b). Expressing this distance in the function of $R_{200,\mathrm{m}}$, we find that the median distance of accretion shock from the system centre is $3(\pm1)R_{200,\mathrm{m}}$. Moreover, for our sample, we find also that $R_{200,\mathrm{m}}$ is $2.3(\pm0.1)R_{500,\mathrm{c}}$. Combing these values and wanting to characterise the baryon and gas fraction inside the entire volume of our galaxy groups and clusters, we extend our analysis up to $10R_{500,\mathrm{c}}$.

The dynamics of accreting gas, which mostly gets shock heated during its first infall, is different from that of the collisionless dark matter. Thus, while the radius of accretion shocks defines the spatial extent of the gas in the DM halos, a different boundary must be defined using DM particles only (e.g. Walker et al., 2019). One example is the splashback radius R_{sp} (Adhikari et al., 2014), which represents the apocenters (farthest point of the particle orbit with respect to the halo potential minimum) of infalling Dark Matter through the pericenter. Many different works* have demonstrated that R_{sp} is $\sim 2.5R_{200,\mathrm{c}}$. Being $R_{200,\mathrm{c}} \sim 1.6R_{500,\mathrm{c}}$, R_{sp} is $\sim 4R_{500,\mathrm{c}}$, which is closer to halo centre compared to the radius of the accretion shock. This means that the assumption of the accretion shock radius as a boundary of the halo, combined with an extension of the analysis on radii larger than the accretion shock position, ensures we consider in our work all the baryons that are enclosed in the simulated halos. A more detailed study about the position of accretion shock in our sample will be part of a forthcoming and dedicated paper.

In Angelinelli et al. 2023, we have extended the work Angelinelli et al. (2022) (hereafter defined as *PaperI*) by selecting a sub-sample of galaxy clusters part of the simulated *Box2b/hr* of *Magneticum* simulations at eight different snapshots, corresponding at eight different redshifts $(2.79, 1.98, 1.71, 1.18, 0.90, 0.67, 0.42, 0.25)$. For each one of the selected snapshots, we selected the 150 most massive galaxy halos (see Tab. 5.1 for details on the mass range). The final sample (combining all the different snapshots) is composed of 1200 galaxy clusters, described by a $M_{500,\mathrm{c}}$ mass range between $\sim 10^{13}h^{-1}M_{\odot}$ and $\sim 10^{15}h^{-1}M_{\odot}$. Moreover, for each snapshot, we divided the sample into 10 equal bins in the logarithmic space, so that each bin contains 15 objects.

For both the works, we define the baryon, gas and star fractions as:

$$f_{\mathrm{bar}}(<r) = (m_{\mathrm{gas}}(<r) + m_{\mathrm{star}}(<r) + m_{\mathrm{BH}}(<r))/m_{\mathrm{tot}}(<r) \tag{5.1}$$

$$f_{\mathrm{gas}}(<r) = m_{\mathrm{gas}}(<r)/m_{\mathrm{tot}}(<r) \tag{5.2}$$

$$f_{\mathrm{star}}(<r) = m_{\mathrm{star}}(<r)/m_{\mathrm{tot}}(<r) \tag{5.3}$$

where r is the radial distance from the cluster or group centre. The different $m_{\mathrm{i}}(<r)$

*see http://www.benediktdiemer.com/research/splashback/ for a complete bibliography about the splashback radius

	$M_{500,c}$ $[h^{-1}M_\odot]$		M_{vir} $[h^{-1}M_\odot]$	
z	Min	Max	Min	Max
2.79	5.8×10^{12}	6.3×10^{13}	9.2×10^{12}	8.0×10^{13}
1.98	9.8×10^{12}	1.2×10^{14}	1.8×10^{13}	1.8×10^{14}
1.71	1.2×10^{13}	1.5×10^{14}	3.0×10^{13}	2.4×10^{14}
1.18	2.1×10^{13}	3.2×10^{14}	4.6×10^{13}	4.5×10^{14}
0.90	4.5×10^{13}	3.5×10^{14}	9.7×10^{13}	5.6×10^{14}
0.67	4.5×10^{13}	4.6×10^{14}	1.2×10^{14}	7.0×10^{14}
0.42	6.1×10^{13}	7.4×10^{14}	1.5×10^{14}	1.3×10^{15}
0.25	6.0×10^{13}	1.4×10^{15}	1.5×10^{14}	2.0×10^{15}

Table 5.1: Minimum and maximum halos masses ($M_{500,c}$ and M_{vir}) for each selected redshift.

are referred to as different particles type (gas, stars or black holes), while $m_{\rm tot}(< r)$ is the sum of the previous masses and the dark matter up to the radial shell r. Regarding the black holes, which are no longer considered in our analysis, their median mass is $7 \cdot 10^8\ h^{-1}M_\odot$ (at $z = 0.25$), while their contribution to the total baryon budget rapidly decreases with the radial distance from the centre of the system, from 0.2% to 0.02%, without strong dependencies with the halo mass. Focusing on the gas component of our systems, we define $f_{\rm hot}$ and $f_{\rm cold}$:

$$f_{\rm hot}(< r) = m_{\rm hot}(< r)/m_{\rm tot}(< r) \tag{5.4}$$

$$f_{\rm cold}(< r) = m_{\rm cold}(< r)/m_{\rm tot}(< r) \tag{5.5}$$

meaning a selection of gas particles based on the temperature, *hot* for particles with a temperature greater than 0.1 keV and *cold* for the others. In the following, we use the depletion parameter Y, defined as:

$$Y(< r) = f(< r)/(\Omega_{\rm bar}/\Omega_{\rm m}) \tag{5.6}$$

where $f(< r)$ could assume any definition given above and $\Omega_{\rm b}/\Omega_{\rm m} = 0.168$, the cosmological value of baryon over total matter adopted for *Magneticum* simulations. The 0.1 keV ($\sim 10^6 K$) threshold is used as a conservative lower limit on the gas temperature to consider the gas that can be detected by X-rays observatories (see Mazzotta et al., 2004; Rasia et al., 2014b; Biffi et al., 2022, for details on the comparison between simulations and X-rays observations).

5.2 Results

Being the findings of Angelinelli et al. (2022) and Angelinelli et al. (2023) closely related to each other, in this section I collect the results presented in each one of the papers.

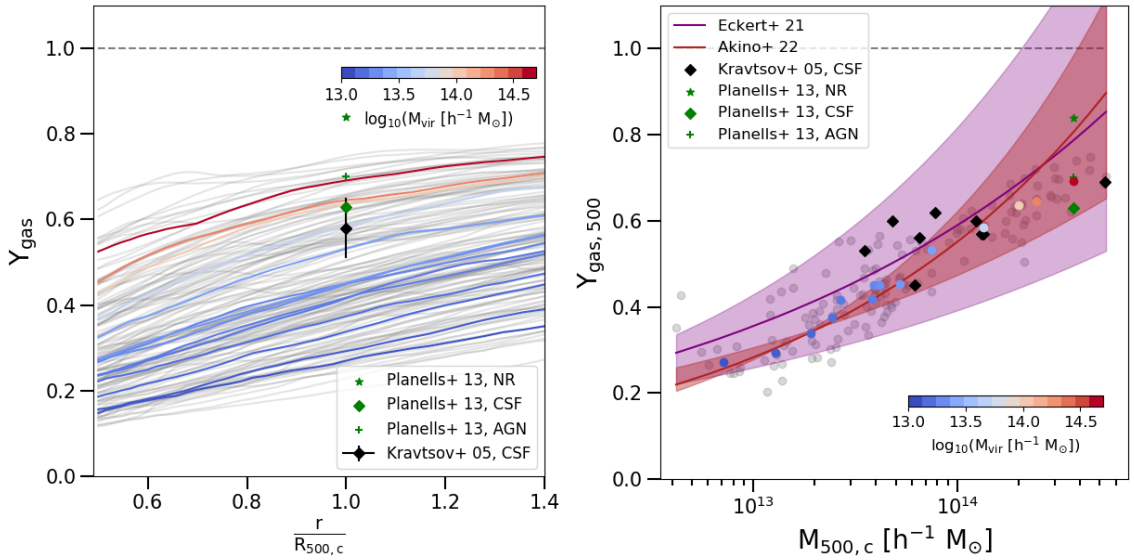

Figure 5.2: (Left) Radial profiles of gas depletion, from $0.5R_{500,c}$ up to $1.4R_{500,c}$. Grey lines represent single objects in our sample, while the coloured ones are the median values computed in mass bins. Comparison numerical estimates from the literature are given by different symbols (black, Kravtsov et al. 2005; green, Planelles et al. 2013). From Kravtsov et al. (2005), we consider the mean value and its scatter for Y_{gas} at $R_{500,c}$ in the simulations with gas dynamics and several physical processes (CSF). From Planelles et al. (2013), we plot the non-radiative run (NR), star formation and feedback from supernova explosion one (CSF) and a run with the additional contribution from AGN (AGN). (Right) Gas depletion parameter at $R_{500,c}$ as function of $M_{500,c}$. Grey dots represent single objects in our sample, while the coloured ones are the median values computed in mass bins. The constraints from Kravtsov et al. (2005) (black points) are indicated in correspondence with the mass of single clusters in their analysis, whereas for Planelles et al. (2013) (green points) are indicated in correspondence with our most massive bin. The lines and related shadow regions are the best fit proposed by Eckert et al. (2021) (purple; $f_{gas,500} = 0.079^{+0.026}_{-0.025}(M_{500}/10^{14}M_\odot)^{0.22^{+0.06}_{-0.04}}$) and Akino et al. (2022) (firebrick; $ln(M_{gas}/10^{12}M_\odot) = 1.95^{+0.08}_{-0.08} + 1.29^{+0.16}_{-0.10}ln(M_{500}/10^{14}M_\odot)$.

5.2.1 The gas and baryon fractions out to $10R_{500,c}$ in the local Universe

Firstly, we compare our results with the numerical and observational literature. In particular, in the left panel of Fig. 5.2, we compare our gas depletion with the values reported by Kravtsov et al. (2005) and Planelles et al. (2013). From the left panel

of Fig. 5.2, we can conclude that the gas depletion factor we recover at $R_{500,c}$ for the most massive systems is in line with the numerical literature. However, we expect that on group mass scales, the potential well is less effective in bounding the accreting baryons and balancing the dispersive actions of feedback from AGN and winds from star formation activity. Therefore, we expect a decrease of the gas depletion factor moving towards lower mass scales (see e.g. Eckert et al., 2021; Akino et al., 2022). In Fig. 5.2, we show how our simulated dataset is able to recover the expected and observed behaviour within $R_{500,c}$.

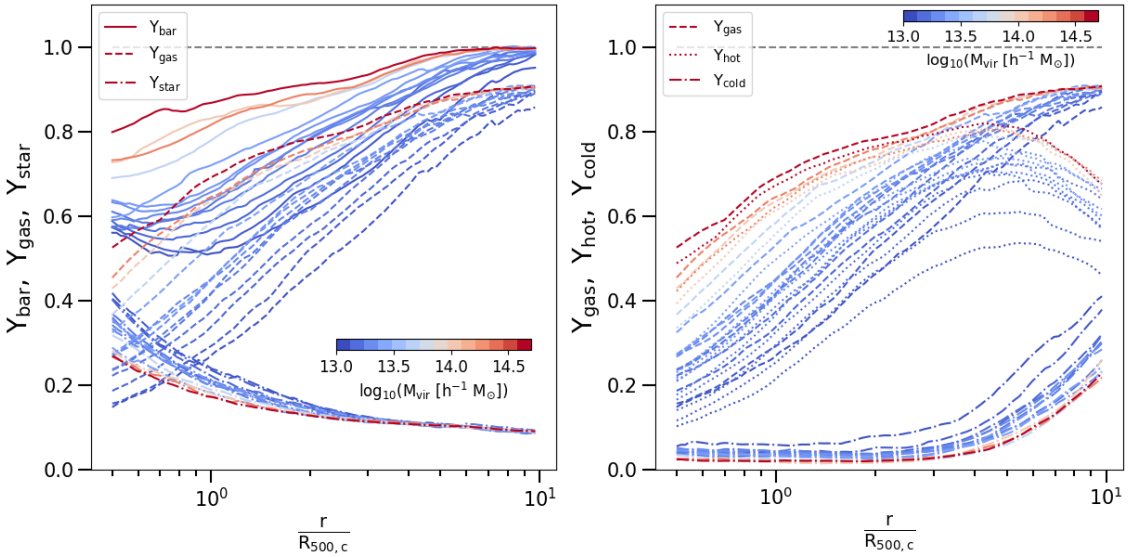

Figure 5.3: (Left) Radial profiles of baryon, gas and star depletion, from $0.5R_{500,c}$ up to $10R_{500,c}$. The lines represent the median profiles in each mass bin, while the different line styles represent baryon (solid), gas (dashed) or star depletion (dash-dotted). (Right) Same as the plot on the left, but represents only three different gas particle selections: gas particles are in dashed, hot gas with a temperature greater than 0.1 keV is in dotted, while cold gas with a temperature below 0.1 keV is in dash-dotted.

In Fig. 5.3, we show the distributions of the baryon ($Y_{\rm bar}$), gas ($Y_{\rm gas}$) and star ($Y_{\rm star}$) depletion factors as function of the radius (between $0.5R_{500,c}$ and $10R_{500,c}$) and halo mass. We show that, although the baryon fraction always is $\geq 50\%$ of the cosmological value $\Omega_{\rm bar}/\Omega_{\rm m}$ in each mass bin, it reaches the cosmological value only at radii larger than $5R_{500,c}$ and only in the most massive systems. Indeed, $Y_{\rm bar}$ is greater than 0.99 at $r > 5R_{500,c}$ in the sub-sample D (more massive systems in our catalogue), whereas it has a value of about 0.83 at $5R_{500,c}$ and 0.95 at $10R_{500,c}$ (see Tab. 8.2). Similar trends are observed for the gas depletion factor $Y_{\rm gas}$. Also, in this case, the larger the radii and higher the depletion factor. Both for the baryonic matter and for the hot gas alone, less massive systems show a steeper increase in the depletion factor with the radius. On the contrary, the stellar depletion factor $Y_{\rm star}$ decreases with the radius and is higher in less massive systems. At larger radii, this

behaviour is less prominent and both galaxy groups and clusters show constant and similar values of $Y_{\rm star} = 0.09^{+0.01}_{-0.01}$, confirming that the in situ enrichment does not play a significant role, and its uniform metal abundance is rather the consequence of the accretion of pre-enriched (at z > 2) gas (see Biffi et al., 2018c). On the other hand, more efficient production of stars is required by the larger $Y_{\rm star}$ estimated in less massive halos within $R_{500,c}$.

On the right panel of Fig. 5.3, we show the radial behaviour of $Y_{\rm hot}$ and $Y_{\rm cold}$ compared to $Y_{\rm gas}$. We note that the cold component of gas content became important at very large radii, over $6R_{500,c}$. Moreover, this cold component shows larger values for galaxy groups, for which it is larger than 0.2 at radii greater than $8R_{500,c}$. The hot phase presents a drop for all the mass bins at radii larger than $6R_{500,c}$, where we locate the accretion shocks on average in our systems (see Sect. 5.1). This means that at larger radii we are investigating also the contribution from the environment in which galaxy groups and clusters reside, with a decreasing contribution to the expected gas emissivity in X-ray.

5.2.2 The time-evolution of depletion parameters within $R_{500,c}$ at different redshift

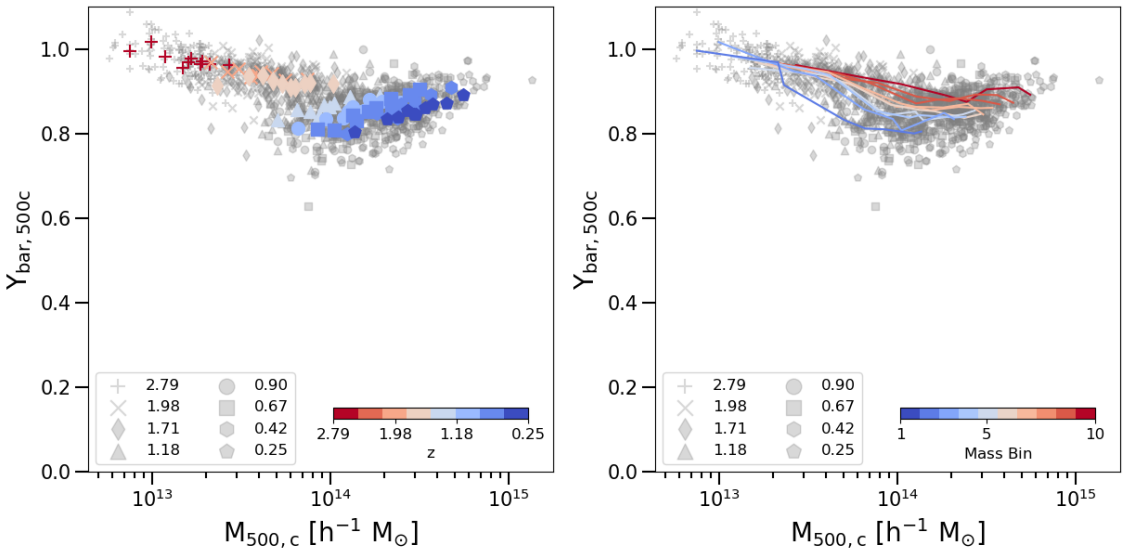

Figure 5.4: Baryon depletion parameter inside $R_{500,c}$. The grey dots represent single galaxy clusters, identified by different markers, accordingly to the legend in the bottom left corner. (Left) The coloured dots represent the median values computed in each of the mass bins of a single snapshot. The colour coding is given by the snapshot's redshift, following the colourbar in the bottom right corner. (Right) The coloured lines represent the redshift evolution of each mass bin. The colour coding is given by the mass bin, following the colourbar in the bottom right corner.

We now focus on the innermost regions of galaxy clusters. In Fig. 5.4 we show

the baryon depletion parameter inside $R_{500,c}$ as a function of the host cluster's mass. From the left plot of Fig. 5.4, we observe a general decrease of the baryon depletion parameter across cosmic time. From the right panel, we follow the redshift evolution of the baryon depletion parameter of a single mass bin. Massive objects show a flatter behaviour than less massive systems, and for the latter, the baryon depletion parameter decreases by $\sim 15\%$ from $z = 2.79$ to $z = 0.25$ (see Tab. 8.4).

We compare our findings with the observational constraints within $R_{500,c}$, from recent work by Eckert et al. (2021) and Akino et al. (2022), where different best fits were proposed to describe the gas fraction as a function of the host cluster's mass. In Fig. 5.5, we show these best fits against our findings on gas and hot gas phase depletion parameters, also including the results proposed by Chiu et al. (2016) and already introduced in Sect. 1.5. As in *PaperI*, our results are able to correctly reproduce the observational findings, and for low redshift ($z < 1.2$) halos show an increase of the gas fraction with the cluster's mass. On the other hand, in high redshift ($z > 1.2$) halos the gas fraction appears to be independent of the mass of the central cluster, with values $Y_{\rm gas} \sim 0.65$. In the right plot of Fig. 5.5, we show the hot gas phase depletion parameter inside $R_{500,c}$ as a function of cluster mass. Comparing the left and right plots of Fig. 5.5, we notice that, for low redshift systems, the hot gas phase is able to completely recover the total gas depletion fraction. On the other hand, for high redshift systems, the hot component is always a fraction of the total gas amount of galaxy clusters. This implies that for high redshift systems the cold gas component is far from negligible, not even from the most massive halos. This suggests that in forming systems closer to their formation time the virialization process is far from complete, and large fractions of the gas mass are still cold; this also suggests that our earlier findings in *PaperI* become increasingly less accurate moving to higher redshifts.

In this respect, the differences between the hot gas phase component and the total amount of gas embedded in high redshift galaxy clusters have particular importance in the study of proto-galaxy clusters. Indeed, these objects, characterised by relatively low masses and high redshifts, seem to show the highest displacement between the real amount of gas and the one which is recovered by X-rays observations. Further investigations are needed to completely assess these differences and understand how to take into account them in the computation of real proto-cluster masses (see Overzier, 2016, for a review on proto-clusters).

5.2.3 The time-evolution of depletion parameters up to $10R_{500,c}$

In Fig. 5.6, we show the median distributions of the baryon depletion parameters as a function of the radius (between $0.5R_{500,c}$ and $10R_{500,c}$) for the less massive and most massive mass bins, computed in each redshift. In Fig. 5.6, we identify a redshift evolution of the profiles. Indeed, in the innermost regions ($r < R_{500,c}$) we

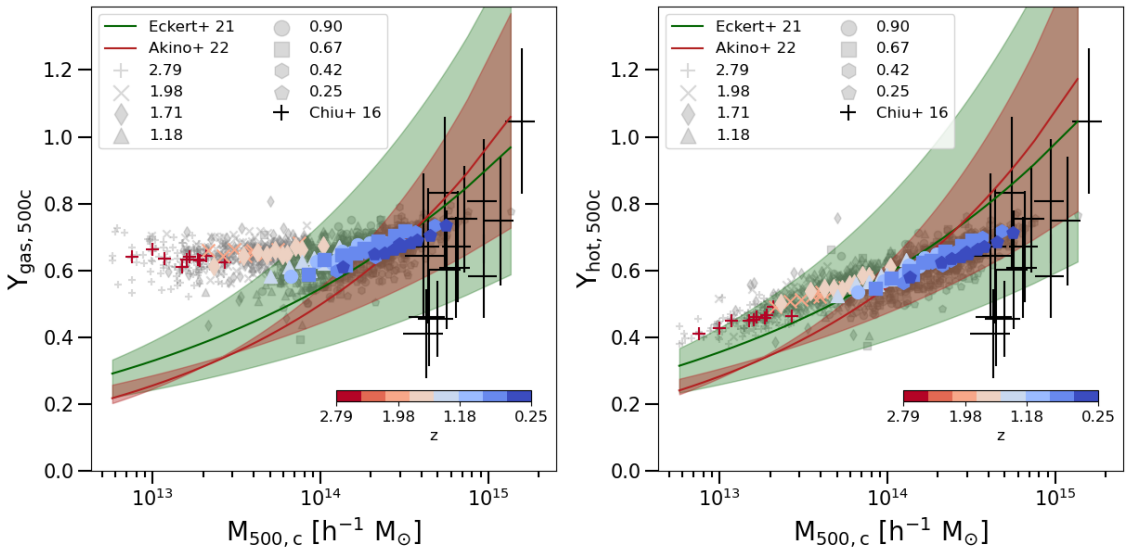

Figure 5.5: Gas depletion parameter (Left) and hot gas phase depletion parameter (right) inside $R_{500,c}$. The grey dots represent single galaxy clusters, identified by different markers, accordingly to the legend in the bottom right corner. The coloured dots represent the median values computed in each of the mass bins of a single snapshot. The colour coding is given by the snapshot's redshift, following the colourbar in the top left corner. The solid lines (and related shadow regions) represent the fit proposed by Eckert et al. (2021) ($f_{\rm gas,500} = 0.079^{+0.026}_{-0.025}(M_{500}/10^{14}M_\odot)^{0.22^{+0.06}_{-0.04}}$, shown in green) and Akino et al. (2022) ($ln(M_{\rm gas}/10^{12}M_\odot) = 1.95^{+0.08}_{-0.08} + 1.29^{+0.16}_{-0.10} ln(M_{500}/10^{14}M_\odot)$, shown in red). The black crosses represent the $f_{\rm gas}$ estimates in Chiu et al. (2016).

observe a decreasing of $\sim 0.40\%$ moving from $z = 2.79$ to $z = 0.25$. In regions far from the cluster's centre ($r < 5R_{500,c}$), the differences between low and high redshift systems are less than 10% from less massive objects and less than 5% for massive ones. At low redshifts, the "closed-box" assumption remains true only for massive objects and on radii greater than $5R_{500,c}$ (see also *PaperI*). At high redshifts, the same condition is reached independently by the halo mass and on radii closer to $3R_{500,c}$.

In Fig. 5.7, we present the median gas depletion parameters as a function of the radius, for the less massive and most massive mass bins, computed in each redshift investigated. At high redshifts, the differences between low and high mass objects are less than 10%, while, at low redshifts, the same differences are larger than 20%. Fig. 5.7 shows an increase in the gas content with the radius. This increase is steeper for less massive objects at low redshift, whereas for massive systems the trend is rather redshift-independent. In each of the analysis cases, the gas depletion parameter approaches values between 85% and 90% at $10R_{500,c}$, independent of the mass or the redshift.

In Fig. 5.8 we show the median hot gas phase depletion parameters as a function

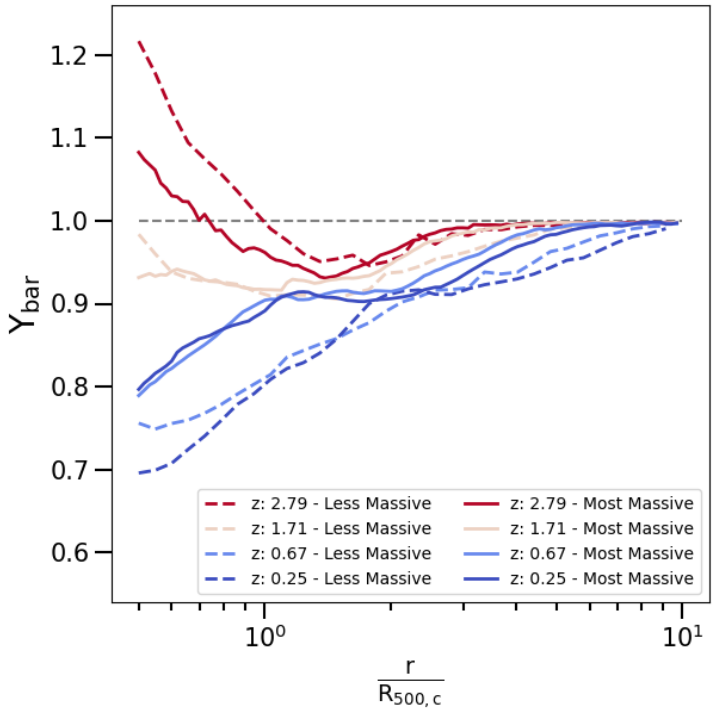

Figure 5.6: Radial profiles of baryon depletion parameter, from $0.5R_{500,c}$ up to $10R_{500,c}$, for the less massive bin (dashed lines) and most massive one (solid lines). The lines represent the median profiles at four different redshifts, accordingly to the colours in the bottom right corner (see Tab. 8.4 for the definition of the mass ranges).

of the distance from the cluster's centre, for the less massive and most massive mass bins, computed in each redshift. Differently from the profiles of baryon and gas depletion parameters presented in Fig. 5.6 and Fig. 5.7, here the profiles show a marked peak and the following drop. This trend is already discussed in *PaperI*, where we surmised that the position of the peak is closer to the position of the accretion shock. Interestingly, here we can further observe a shift to the outer regions of the peak with the decrease of redshift. This is compatible with an increase in the halo volume with cosmic time, marked by the expansion of the outer accretion regions. We also notice that most massive objects have a higher contribution of hot gas at every redshift. Moreover, comparing Fig. 5.7 and Fig. 5.8, we note that for low redshift systems the total amount of gas within the cluster's volume is quite perfectly traced by the hot component, while for high redshift objects the hot gas phase is always less than 75% of the total gas. Therefore, in high redshift galaxy clusters, the hot and X-rays observable part of the gas represents only a fraction of the total gas mass, making it indispensable to correct the derived mass in order to make any accurate cosmological use of it.

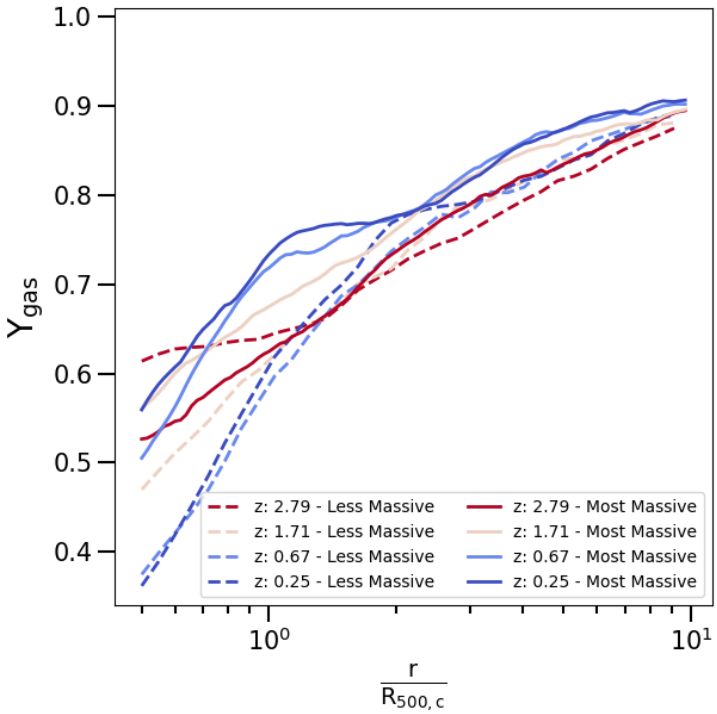

Figure 5.7: Radial profiles of gas depletion parameter, from $0.5R_{500,c}$ up to $10R_{500,c}$, for the less massive bin (dashed lines) and most massive one (solid lines). The lines represent the median profiles at four different redshifts, accordingly to the colours in the bottom right corner (see Tab. 8.4 for the definition of the mass ranges).

5.2.4 The radial trend of gas metallicity in the local Universe

The injection and evolution of metals by SN-Ia, SN-II and AGB stars in *Magneticum* simulations are modeled following Tornatore et al. (2003, 2007). Although the simulation traces various elements individually, we consider here the total metallicity, i.e. the sum of the elements heavier than helium relative to the hydrogen mass. Then, the total metallicity at each radial shell r, $Z_{\rm tot}(r)$, is the mass-weighted sum of the metallicity of the gas particles i with mass $m_{\rm gas,i}$ which belong to the radial shell r:

$$Z_{\rm tot}(r) = \frac{\sum_{\rm i} Z_{\rm tot,i} \cdot m_{\rm gas,i}}{\sum_{\rm i} m_{\rm gas,i}}. \tag{5.7}$$

The radial shells are defined to include a fixed number of 250 particles, to allow a significant statistical analysis of each of them. We normalise these values of metallicity to the solar values proposed by Asplund et al. (2009): $Z_{\odot} = 0.0142$.

In Fig. 5.9, we show the metallicity profiles recovered up to $10R_{500,c}$ in all our halos. The profiles are remarkably similar, flattening to a constant value of about $0.23^{+0.08}_{-0.08}$ at $r > 2R_{500,c}$, and with a negligible dependence upon the halo mass (see median estimates in Tab. 8.2). Some mass dependency would be expected as a consequence of any difference in star-formation activities from group to cluster

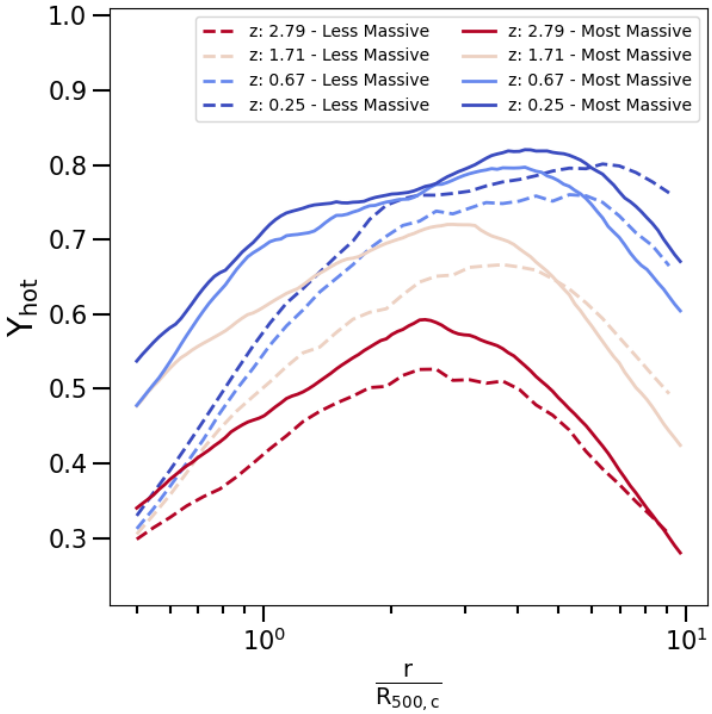

Figure 5.8: Radial profiles of the depletion parameter for the hot gas phase, from $0.5R_{500,c}$ up to $10R_{500,c}$, for the less massive bin (dashed lines) and most massive one (solid lines). The lines represent the median profiles at four different redshifts, accordingly to the colours in the top right corner (see Tab. 8.4 for the definition of the mass ranges).

scales, with the latter being less effective in producing and releasing metals in the environment. The lack of evidence of such dependency supports the expectations of the early enrichment scenario. Biffi et al. (2017) (see also Biffi et al., 2018c) found that at $r > 0.2R_{180}$ the metallicity is remarkably homogeneous, with almost flat profiles of the elements produced by either SNIa or SNII, mostly as a consequence of the widespread displacement of metal-rich gas by early ($z > 2-3$) AGN powerful bursts acting on small high-redshift halos, and with no significant evolution since redshift ~ 2. Nevertheless, we highlight the fact that even if the flattening behaviour we find is in agreement with the results proposed by Ghizzardi et al. (2021), the value we recover is lower than the one proposed by the observational work of Ghizzardi et al. (2021) ($\sim 0.38Z_{\odot}$). This difference could be related to some peculiar structure represented in our simulation that affects the overall metallicity estimate, but further analysis is needed to fully resolve this issue.

Given the large scatter observed in single radial profiles of metallicity in Fig. 5.9, we investigate the relations between the masses of the systems and metallicity. From the left panel of Fig. 5.10, where we show the metallicity in the function of gas mass, we note how the profiles are still highly scattered, but looking at the values of metallicity computed at $R_{500,c}$ (the coloured dots in the plot), we also notice that

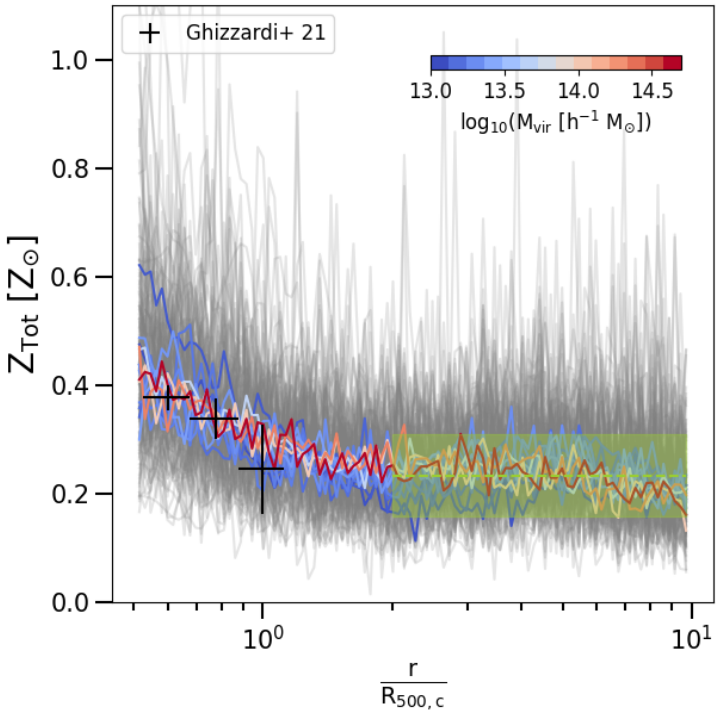

Figure 5.9: Radial profiles of gas metallicity from $0.5R_{500,c}$ up to $10R_{500,c}$. Grey lines represent single objects, while the coloured ones are the mean values computed in mass bins. The green dashed line and its related shadow region show the median, the 16th and 84th percentiles of gas metallicity distribution over $2R_{500,c}$ ($0.23^{+0.08}_{-0.08}$). The black dots are the observed estimates of gas metallicity by Ghizzardi et al. (2021) ($r/R_{500,c} = [0.60 \pm 0.08, 0.78 \pm 0.10, 0.99 \pm 0.12]$, $Z/Z_{\odot} = [0.38 \pm 0.03, 0.34 \pm 0.05, 0.26 \pm 0.12]$).

galaxy groups (bluish dots) show a higher spread in metallicity instead of galaxy clusters (reddish dots), with median values of $0.29^{+0.11}_{-0.11}$ and $0.30^{+0.06}_{-0.07}$, respectively. This trend is similar to the findings discussed by Truong et al. (2019). Here the authors focus on the iron contribution in extremely central regions of simulated galaxy clusters and groups ($r < 0.1R_{500}$) and they also compare their results with observational work by Mernier et al. (2018). On the other hand, in the central and right panels of Fig. 5.10, we present the density-temperature phase diagram, for the less (centre) and most (right) massive objects in our sample, colour-coding by the mass-weighted metallicity of each density-temperature bin. Here, we notice a high spread of metallicity values, both for galaxy groups and clusters. Even when we consider the "hot" and "cold" gas phase separately, the scatter in metallicity is still present. From the whole panels of Fig. 5.10 we conclude that the observed scatter in radial profiles of metallicity is due to an intrinsic scatter present in the gas particles. Moreover, the coexistence of different gas phases tends to enlarge the observed scatter.

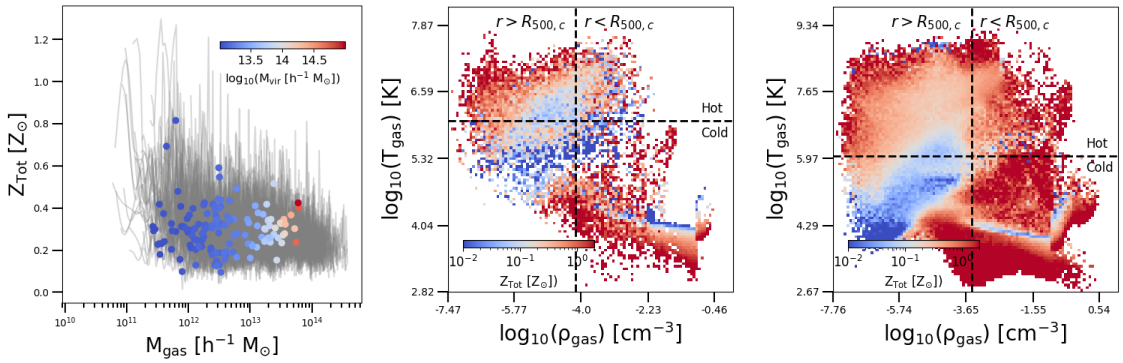

Figure 5.10: (Left) Metallicity as a function of the gas mass. The grey lines represent the profiles computed for single objects in our sample, whereas the coloured dots are the values computed at $R_{500,c}$ (again for each group and cluster present in our sample). The colour-coding is given by the virial mass (M_{vir}) of the systems; (Centre and Right) Density-temperature phase diagram for the less massive system (centre; $M_{vir} = 10^{13}\ h^{-1}M_{\odot}$) and the most massive one in our sample (right, $M_{vir} = 9.8 \cdot 10^{14}\ h^{-1}M_{\odot}$). The colour-coding is given by the mass-weighted metallicity in each density-temperature bin. The dashed horizontal black line represents the 0.1keV ($1.16 \cdot 10^6$K) temperature cut, adopted to separate "hot" and "cold" gas phases. The dashed vertical line marks the gas density at $R_{500,c}$. On the right of this line, there are the particles inside $R_{500,c}$, while on the left the particles are located at larger radii.

5.2.5 The time-evolution of gas metallicity and stellar component

In Fig. 5.11, we show the median distributions of the total metallicity as a function of the radius for the less massive and most massive mass bins, computed in each redshift. Here we note that the profiles are highly scattered, as already discussed and justified in *PaperI*. Moreover, although no strong mass dependencies are observed, we notice a clear evolution of total metallicity across time. Indeed, independently of the mass bin analysed, the values of metallicity increase towards lower redshifts. In the external part of the galaxy clusters, on radii larger than $2 \div 3R_{500,c}$, we observe a general flatting of the profiles. This trend is slightly prominent in high redshift systems.

In Fig. 5.12, we give the median distribution of stellar depletion parameter, as a function of radius, for less massive and most massive objects, computed in each redshift. Differently from the case of baryons, gas, and hot gas phases, here we observe a gradual decrease of the stellar depletion parameter with increasing distance from the cluster's center. Instead, similar to the metallicity profiles, also for the stellar depletion factor we do not observe any mass-associated trend. However, we observe a clear trend: especially in the innermost regions, the values of the stellar depletion parameter decrease with the redshift, while in the outskirts of halos the differences between different redshifts are of the order of a few percent. Halos in all mass bins approach a stellar depletion parameter $Y_{\rm star} \sim 0.1$ a the boundary of the

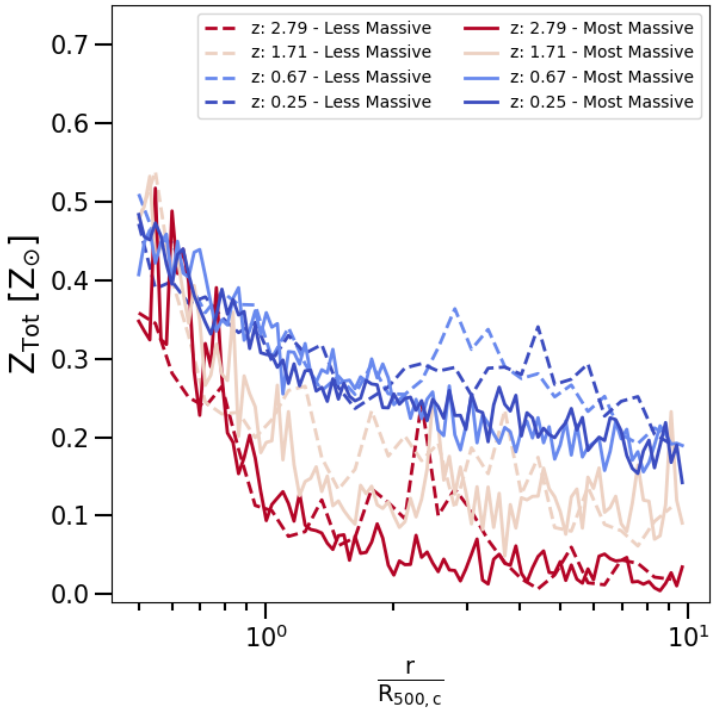

Figure 5.11: Radial profiles of gas metallicity (in Solar units), from $0.5R_{500,c}$ up to $10R_{500,c}$, for the less massive bin (dashed lines) and most massive one (solid lines). The lines represent the median profiles at four different redshifts, accordingly the colours in the top right corner (see Tab. 8.4 for the definition of the mass ranges).

analysed volumes ($\sim 10R_{500,c}$).

5.3 Discussion

Recently, many different works have explored the evolution of baryons in simulated halos (Castro et al., 2021; Ragagnin et al., 2022; Ayromlou et al., 2022; Robson, Davé, 2023). In our work, we analyse a sample of galaxy clusters extracted from *Magneticum* simulations. Compared to other works, the simulated volume of *Box2b* is large enough to allow a selection of very massive objects ($M_{500,c} > 10^{15} M_\odot/h$ at $z = 0$). Moreover, as also discussed by Robson, Davé (2023) (see their Fig.10 and related discussion), the effects of different feedback phenomena highly influence the evolution of baryons in the simulated halos. From the comparison between *Magneticum* simulations and other suites of numerical simulations, we can assess the impact of different feedback models in the evolution of baryons in simulated in halos. We select for each simulated snapshot the 150 most massive halos (see Tab. **??** for details on the mass range). This selection minimises the effect of mergers and phenomena that occur in the history of single objects. Indeed, in the most massive objects gravity can compensate for the effect of AGN feedback, and the

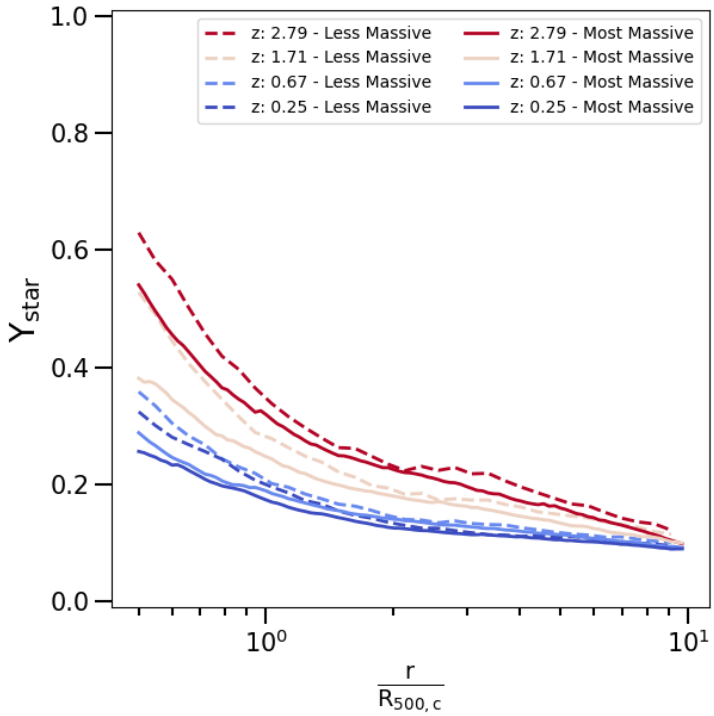

Figure 5.12: Radial profiles of stellar depletion parameter, from $0.5R_{500,c}$ up to $10R_{500,c}$, for the less massive bin (dashed lines) and most massive one (solid lines). The lines represent the median profiles at four different redshifts, accordingly to the colours in the top right corner (see Tab. 8.4 for the definition of the mass ranges).

evolution we recover is less affected by internal feedback phenomena. On the other hand, the other possible approach is to trace the time evolution of a sample of massive objects at $z = 0$. In this case, the results are probably affected by the history of the single objects, and the evolution of baryon may be influenced by mergers or peculiar phenomena that occur in specific objects, making the results less statistically robust. Moreover, this approach does not ensure that at high redshifts the sample still remains mass-complete. Indeed, since the mass growth of halos is determined by merger phenomena peculiar to individual objects, halos that at high-z belong to the most massive mass bin, may in their history not grow to sufficient masses to still belong to the most massive sub-sample at $z = 0$. Furthermore, due to observational limitations, the galaxy cluster observed samples are composed of very massive objects, especially for high-z observations. The selection we decided to adopt in our work is therefore closer to what can be reproduced to date with X-rays observations. Robson, Davé (2023) also highlight the major role of the feedback model in the estimations of proprieties of galaxy clusters and groups derived from X-rays observations. It is therefore essential to build simulated samples as similar as possible to those that can be obtained from X-rays observations. This will allow a comparison between different feedback models used in simulations that can give

results comparable with observations and thus enable a better understanding of the real effect of feedback phenomena on the evolution of baryons in halos. We defer this to future work.

Castro et al. (2021) investigate the role of AGN feedback in the halo accretion history in the *Magneticum* simulations. The energy introduced in the surrounding environment by the AGN is proportional to the mass accretion rate of the black hole $\dot{\mathrm{M}}_{\mathrm{BH}}$ (Springel, 2005; Hirschmann et al., 2014). The authors conclude that the AGN feedback has a nearly time-universal behaviour. They find that the peak of the AGN feedback occurs at a slightly higher redshift than the baryon fraction peak, and then they observe a quick decaying around $z = 1$, followed by a slow decaying phase at lower redshifts. Moreover, they note a rather universal trend response to the AGN activity. The variation of the halo mass shows a significant and negative correlation with the intensity of AGN feedback when halo progenitors reach $\sim 30 \div 50\%$ of their final mass. Castro et al. (2021) conclude that the decrease of halo mass observed in simulations is driven by the action of AGN feedback in a relatively early phase of the halo assembly when the shallower galaxy cluster's potential well can better react to the displacement of gas heated by feedback.

Recently, Ragagnin et al. (2022) study the ejection of gas from the halo, due to AGN feedback in *Magneticum* simulations. They find that the gas fraction in galaxy clusters with a redshift formation greater than 1 is lower than the one observed for systems with lower redshift formation. This difference is associated with the amount of gas present at the epoch of formation and later ejected by the AGN activity. Indeed, when the amount of ejected gas is taken into account, the distributions of gas fraction recovered are independent of the formation redshift of galaxy clusters.

Starting from the finding of Castro et al. (2021) and Ragagnin et al. (2022), we investigate the role of AGN feedback in the time evolution of the depletion parameters. In the following, we do not include the energy feedback from stellar processes, because of its minor contribution with respect to the AGN feedback at the redshifts we are interested in (see Ragagnin et al., 2022, and reference therein). We define the feedback energy as the ratio between the mass accretion rate $\dot{\mathrm{M}}_{\mathrm{BH}}$ and the thermal energy of galaxy clusters inside $R_{500,\mathrm{c}}$,

$$E_{feedback} = \frac{\dot{M}_{BH}\ c^2\ \epsilon_r\ \epsilon_f}{(M_{gas,500c}/[\mu\ m_p]) \times (T_{gas,500c}/[erg])} \tag{5.8}$$

where $\dot{M}_{BH}$ is computed as the differences of the mean black hole mass between two consecutive time steps and ϵ_r and ϵ_f are the parameters proposed by Hirschmann et al. (2014), which takes into account the amount of feedback energy thermally coupled to the surrounding gas. For each redshift, we compute the median values of depletion parameters and metallicity for the entire galaxy clusters sample.

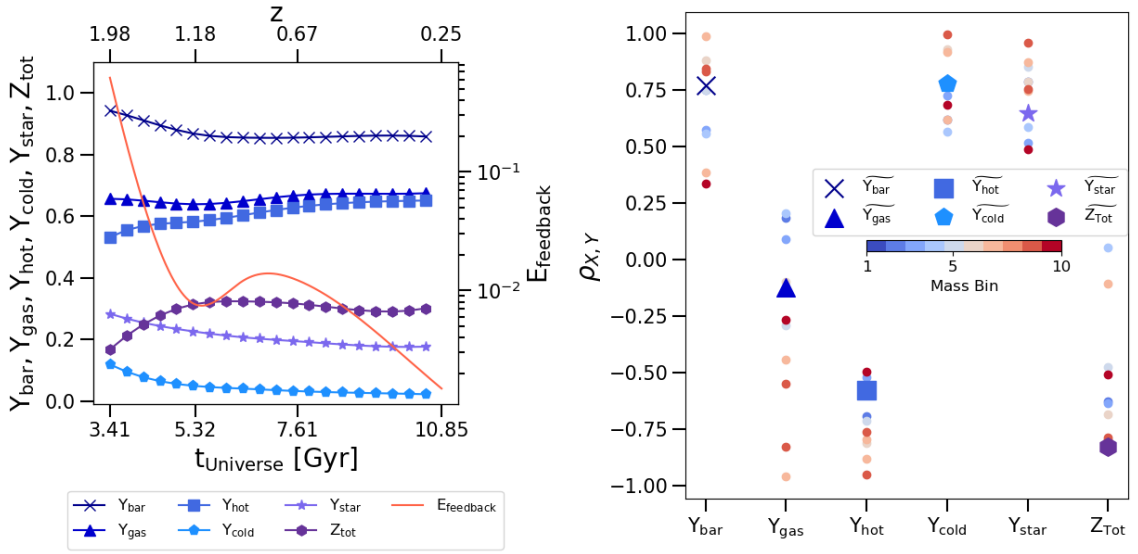

Figure 5.13: Redshfit evolution from $0.2 \lesssim z \lesssim 2$ of feedback, depletion parameters and metallicity and their correlations inside $R_{500,c}$. (Left) Median values of depletion parameters, metallicity and feedback energy proxy as a function of redshift. The different lines (accordingly the legend on the bottom) represent the median values computed on the entire galaxy clusters sample in each redshift. (Right) Pearson correlation index of the redshift evolution computed between the feedback energy proxy and depletion parameters or metallicity. The coloured dots represent the median values computed in each mass bin (following the colour coding showed by the colourbar in the middle of the plot), while the dots identified by different markers (accordingly the legend in the middle of the plot) show the median values computed for the whole sample.

The results are shown in the left panel of Fig. 5.13. Here we observe that the feedback energy, rapidly decreases with the redshift, as already observed and discussed by Castro et al. (2021). Moreover, we note that baryon, cold gas phase, and stellar depletion parameters show a decrease with redshift, whereas gas, hot gas phase, and metallicity have opposite behaviour. These trends suggest the presence of correlations between the feedback energy and the quantities analysed. In the right panel of Fig. 5.13, we show the Pearson correlation indices computed between the time evolution of the feedback energy and the depletion parameters and metallicity. Focusing on the redshift range from $z \sim 2$ up to $z \sim 0.2$, we present the results both for the galaxy clusters divided in the same 10 mass bin adopted above and for the median values of the entire sample. As already observed, but now quantified by the Pearson correlation index, we note that the baryon depletion parameter, gas cold phase, and stellar ones, show a correlation with the energy feedback, while the gas depletion parameter, hot gas phase one, and metallicity show anti-correlated trends. In particular, we observe that in all the parameters analysed, except for the gas depletion parameter, the mass of the galaxy clusters does not change the correlation or anti-correlation trend. On the other hand, for the gas depletion pa-

rameter, we note a shift from correlation to anti-correlation with the increase in the mass of systems associated with the mass bins. This trend is associated with the relative impact of the different gas phases in different galaxy cluster sub-samples. Indeed, in less massive systems we note that the hot component is less dominant than in more massive galaxy clusters. This suggests that for less massive systems, the total gas depletion parameter is driven by the cold phase, which has a high level of correlation with feedback energy. Instead, for massive systems, the hot gas phase is completely dominant with respect to the cold one. The hot gas phase shows a high level of anti-correlation with the feedback energy, and this lead to an increase in the anti-correlation observed between the total gas depletion parameter and the feedback energy. In Tab. 5.2 we report the Pearson correlation indices discussed above.

	$\rho_{X,Y}$		
	Less massive bin	Most massive bin	Entire sample
Y_{bar}	0.75	0.34	0.77
Y_{gas}	0.19	-0.27	-0.12
Y_{hot}	-0.69	-0.49	-0.58
Y_{cold}	0.62	0.68	0.78
Y_{star}	0.79	0.49	0.65
Z_{Tot}	-0.63	-0.51	-0.83

Table 5.2: Pearson correlation index of the redshift evolution computed between the feedback energy proxy and depletion parameters or metallicity, inside $R_{500,c}$, for the less massive sub-sample, the most massive one and the entire sample.

Lapi et al. (2005) proposed a model which relates the energy injected by an event of AGN activity and the fractional mass ejected by this event. In particular, the authors compute the energy introduced by an AGN event and the thermal energy of the hosting system. This quantity has the same meaning as our definition of feedback energy. Lapi et al. (2005) demonstrate that this energy ratio is related to the fractional mass ejected from the galaxy cluster environment. In detail, they demonstrate that $\Delta m/m \simeq \Delta E/2E$. To compare these findings with our analysis, we consider the fractional mass as the changing of baryon fraction over consecutive time steps and the time-integrate contribution of the feedback energy. In Fig. 5.14 we show the time evolution of time-integrate feedback energy (dE/E), the baryon fraction change (dM/M - Data) and the prediction on the fractional mass evolution given by the model of Lapi et al. (2005) (dM/M - Lapi+ 05). We note that the feedback energy rapidly increases around redshift $z = 2$, while a flat behaviour is observed on lower redshift. On the other hand, the baryon fraction change increases more slowly than both the feedback energy and the prediction of the model, depending the latter only on the energy injected. The differences between the baryon

fraction change we recover and the prediction of the model are related to the assumption adopted for the model. Indeed, the model proposed by Lapi et al. (2005) takes into account only heating phenomena, whereas at high redshift gravitational effects, such as accretion and mergers events, give not negligible contributions, making the model assumptions less effective.

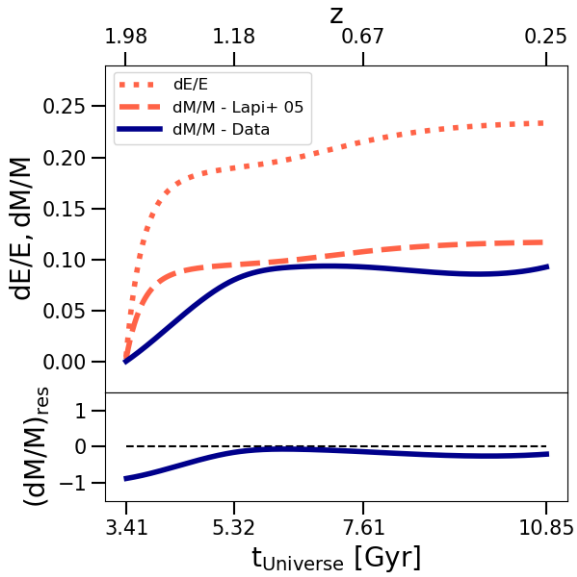

Figure 5.14: Time evolution of feedback energy and mass depletion inside $R_{500,c}$. (Top) The dotted line represents the time-integrated ratio between feedback energy and the system's thermal energy ("dE/E"), and the solid one shows the mass depletion computed as the difference between the baryon fraction in two consecutive time steps ("dM/M - Data"), the dashed line represents the expected mass depletion computed as $\frac{1}{2}$(dE/E), as proposed by Lapi et al. (2005) ("dM/M - Lapi+ 05"). The lines represent the median trends, computed over the whole galaxy clusters sample. (Bottom) The line shows the residuals of mass depletion, computed as $((\mathrm{dM/M})_{\mathrm{Data}} - (\mathrm{dM/M})_{\mathrm{Lapi+05}})/(\mathrm{dM/M})_{\mathrm{Lapi+05}}$.

Recently Ayromlou et al. (2022) compare three different suites of numerical simulations, Illustris-TNG (Pillepich et al., 2018b; Nelson et al., 2018; Springel et al., 2018), EAGLE (Schaye et al., 2015; Crain et al., 2015) , and SIMBA (Davé et al., 2019) to understand the evolution of baryon in halos with $M_{200,c}$ masses between $10^8 M_\odot$ and $10^{15} M_\odot$, from halo's centre up to $30 R_{200,c}$. They demonstrate that baryon feedback mechanisms highly influence the baryon distribution, lowering the baryon budget within the halos and accumulating matter outside the virial radius of these systems. Moreover, they find that halos with different mass ranges are influenced by different feedback mechanisms. In particular, they show that for low-mass systems ($10^8 \leq M_{200,c}/M_\odot \leq 10^{10}$) the main source of heating is given by the UV background, for intermediate mass halos ($10^{10} \leq M_{200,c}/M_\odot \leq 10^{12}$) stellar feedback becomes dominant, while for massive systems ($10^{12} \leq M_{200,c}/M_\odot \leq 10^{14}$) the main source of feedback is given by central AGN. Furthermore, they conclude that galaxy

clusters with masses $M_{200,c}/M_{\odot} \geq 10^{14}$ are less affected by feedback phenomena instead by less massive objects. They also proposed a new characteristic scale, the closure radius R_c that represents the radius at which all the baryons associated with a halo could be found. They define R_c as:

$$f_{bar}(< R_c) = f_{bar,cosmic} \pm \Delta f_{bar,cosmic} \tag{5.9}$$

where $\Delta f_{bar,cosmic}$ represents the observational uncertainty on the cosmic baryon fraction, which they assume to be 0.05 (Planck Collaboration et al., 2016). They find that the closure radius is closer to $R_{200,c}$ in massive systems, while it tends to increasingly outer regions for objects in which the mass is gradually smaller. Moreover, they show that the position of the closure radius depends also on the model adopted by different simulations. Indeed, the simulations they used give the different positions of closure radius for objects with the same masses. Starting from these findings, we compute the closure radius on our *Magneticum* sample using the same definition proposed by Ayromlou et al. (2022).

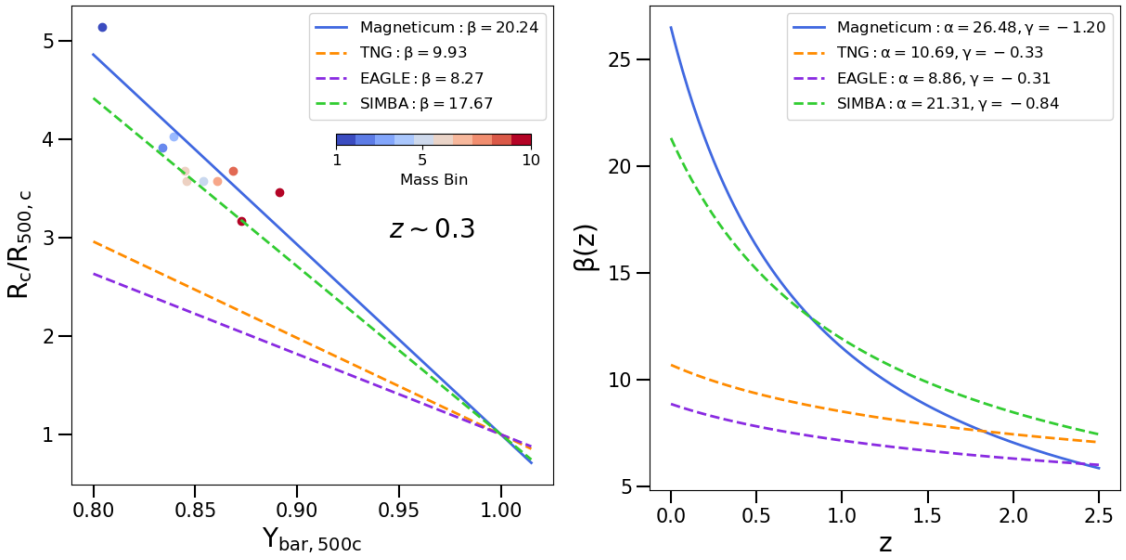

Figure 5.15: Closure radius as function of baryon depletion factor within $R_{500,c}$ and β parameter as function of redshift. (Left) The dashed lines represent the results proposed by Ayromlou et al. (2022) for Illustris-TNG (orange), EAGLE (purple), and SIMBA (green) simulations computed for redshift $z \sim 0.3$. The solid blue line shows the best fit relation between closure radius and baryon depletion factor, performed on our *Magneticum* sample at redhsift $z \sim 0.3$. The coloured dots represent the median values of closure radius computed on the 10 mass bins (according to the colourbar on the top right corner of the plot) at the same redshift of $z \sim 0.3$. (Right) Redshift evolution of β parameter. The dashed lines show the results proposed by Ayromlou et al. (2022) for TNG (orange), EAGLE (purple), and SIMBA (green) simulations, whereas the solid blue line represents the findings we obtained as best fit on our *Magneticum* sample.

To compare our results with their finding, we also consider the universal relation they proposed, which relates to baryon fraction and closure radius:

$$R_c/R_{500,\mathrm{c}} - 1 = \beta(z)\ (1 - f_{bar}(< R_{500,\mathrm{c}})/f_{\mathrm{bar},cosmic}) \tag{5.10}$$

with $\beta(z)$ is defined as:

$$\beta(z) = \alpha(1+z)^{\gamma} \tag{5.11}$$

where α and γ are free parameters that we use to perform the fit on our simulations. In Fig. 5.15 we show the comparison between our findings and the results proposed by Ayromlou et al. (2022). In the left panel, we present the closure radius, normalised to $R_{500,\mathrm{c}}$, as a function of baryon depletion factor Y_{bar} for the four different suites of numerical simulations at redshift $z \sim 0.3$. The results for Illustris-TNG, EAGLE, and SIMBA simulations are derived from the best-fit parameters of α and γ proposed by Ayromlou et al. (2022), while we perform the fitting procedure on our *Magneticum* sample. We obtain values of $\alpha = 26.48$ and $\gamma = -1.20$, which also determine the redshift evolution of $\beta(z)$ parameter proposed on the right panel of Fig. 5.15. As also discussed by Ayromlou et al. (2022), different models adopted for the treatment of AGN feedback highly influence the position of closure radius and cosmic time evolution of the β parameter. Being the AGN model one of the main differences from the four different simulations analysed, this also suggests that the AGN feedback in galaxy clusters and groups represents the major source of energy responsible for the redistribution of baryon in the halo's environment. Moreover, the existence of the universal relation between closure radius and baryon fraction proposed by Ayromlou et al. (2022) shows how will be crucial the next generation of X-rays observatories to observe clusters and groups peripheries and disentangle between different AGN feedback models.

Chapter 6

Summary and conclusions

I present here a summary of the results obtained from my Thesis work illustrated in the previous Chapters.

I first focused on the properties of accreting material around galaxy groups and clusters, and the physical phenomena connected to it. Due to observational caveats related to the external regions of massive halos (see Sect. 1.2 for details and references), in my works I used different halo samples extracted from either *"Itasca Simulated Clusters"* (Sect. 2.2) or *Magneticum* (Sect. 2.3) simulations.

First, using *ITASCA* simulations, I designed a procedure to extract a large sample of objects and conduct detailed statistical studies, by considering multiple snapshots of the same objects with a sufficiently large time separation, which allows us to treat them as dynamically independent clusters (see Sect. 3.1.1). This way we could study total sample of 68 independent cluster snapshots in Angelinelli et al. (2020) and 13 objects in Angelinelli et al. (2021). On the other hand, in Angelinelli et al. (2022) and Angelinelli et al. (2023) we used samples of simulated halos extracted from the *Magneticum* simulations. In particular, in Angelinelli et al. (2022) we selected the simulated *Box2b* (see Sect. 2.3) at the last available snapshot ($z = 0.25$) and we divided the mass range $10^{13} < M_{vir}/M_{\odot} < 10^{15}$ in 14 equal bins in the logarithmic space, and for each bin we extract 10 random objects, having a final sample of 140 massive halos. In Angelinelli et al. (2023) we extended the analysis proposed in our previous work to different redshifts. Using the same *Box2b*, we selected 8 different simulated snapshots (from $z \sim 3$ to $z = 0.25$) and for each snapshot, we extracted the 150 most massive halos. This overall gives a full coverage of the properties of clusters and groups of galaxies, across a wide range of spatial and temporal scales, and also including many physical prescriptions for baryon physics.

For each work, I developed new dedicated numerical tools. In Angelinelli et al. (2020) I improved the iterative small-scale filtering techniques to identify turbulent motions, introduced in Vazza et al. (2018a), by linking the tolerance parameter in

our multi-scale iterative analysis of turbulence to the expected increase of velocity with scale, following Kolmogorov theory (Sect. 3.1.2). I thus extracted the three-dimensional distribution of turbulent velocities from which I computed the non-thermal contribution of pressure, $\alpha_{\rm Turb}$, as a function of cluster-centring distance. I also compared this definition of turbulence using different filtering techniques, specifically to the one proposed in Nelson et al. (2014a), which we defined as $\alpha_{\rm Tot}$. In Angelinelli et al. (2021) I developed two different algorithms to disentangle matter clumps from filaments populations to the surrounding medium. The first algorithm is based on the baryon mass and size of the clumps and I showed that structures as massive as 10^8 solar masses and as small as 500 kpc can be found in *ITASCA* simulations. The second algorithm is used to find filaments and is based on the radial velocity and entropy of the gas. Filaments are expected to have high radial velocities due to the gravity of central galaxy clusters but have lower entropy compared to their surroundings, which makes them difficult to detect in X-ray emissions. Lastly, in Angelinelli et al. (2022) and Angelinelli et al. (2023) I expanded the radial analysis to cover an area up to $10R_{500,\rm c}$, which is beyond the location of the accretion shock, which is commonly considered as the boundary of the halo volume. This expansion allows me to include all of the baryons associated with the simulated galaxy clusters and groups in my analysis.

In the following, I summarise the main results of each work presented in this Thesis.

- Angelinelli et al. (2020) (discussed in Chapt. 3):
  - The average non-thermal pressure support in our sample is in agreement with the recent X-ray observational campaign by Eckert et al. (2019), both at $R_{500,\rm c}$ and $R_{200,\rm c}$, albeit with a large scatter which is probably due to a larger variety of simulated dynamical states, compared to the X-COP sample used by Eckert et al. (2019) (Fig. 3.11). Different choices in filtering generate very different non-thermal pressure support (see Vazza et al., 2018a), and we show that the other filtering technique for turbulence yield values of non-thermal pressure support which are $\sim 2 \div 3$ times larger. Our analysis of sub-samples in mass, redshift and sparsity sub-samples does not highlight particular trends. Despite having a different selection bias for clusters, the comparison between the non-thermal pressure support obtained by Eckert et al. (2019) yields rather similar results.
  - Following on Eckert et al. (2019), we computed $\alpha_{\rm HS}$ for our objects, defined as in Eq. 3.17. When averaged over the sample, the median $\alpha_{\rm HS}$ is not far from the values obtained by X-ray observations, i.e. $\alpha_{\rm HS} \sim 10-20\%$ at $R_{500,\rm c}$ and $R_{200,\rm c}$, albeit with a large scatter. The hydrostatic

mass bias does not show strong dependencies on the cluster mass or the cluster dynamical status (see Sect. 3.2.1 and Sect. 3.3 for details).

  - **We conclude that, when compared with available observations, our simulations match the currently inferred level of non-thermal pressure support, and they allow us to identify its origin (predominantly) with residual gas turbulent motions.**

- Angelinelli et al. (2021) (discussed in Chapt. 4):

  - By comparing the density and temperature distributions of clumps and filaments populations in each cluster of our sample, we investigated the possible correlations between these quantities. We use Pearson's correlation index to describe these correlations and we obtain $\rho_{\rm XY}$=0.66 and $\rho_{\rm XY}$=0.54, for density and temperature respectively.
  - When the simulated volume of each cluster is divided into a pair of radial shells, we observe a significant drop (a factor of two or more) in the number of clumps going from the inner ($1.0 \leq r/R_{500,\rm c} \leq 2.8$) to the outer shell ($2.8 \leq r/R_{500,\rm c} \leq 5.0$). We study the variations in clump density and temperature with distance from the cluster centre. In both, we also report a decrease (by a factor $\sim$2) in the typical density and temperature of clumps as a function of distance from the cluster centre, as well as in their mass and volume filling fraction. We observe how in the inner shell the contribution of filaments, both in mass and volume, is less than for the clumps. On the other hand, in the outer shell, the volume occupied by filaments is on average $\sim$ 2 times the one occupied by clumps.
  - **We conclude that gas clumps in clusters of galaxies can efficiently be used to track and study the underlying, more diffuse and yet to be detected population of filaments.**

- Angelinelli et al. (2022) (discussed in Chapt. 5):

  - We verify that the baryon fraction is always >50% of the cosmological value adopted in our simulations at $r > R_{500,\rm c}$ and at any mass bin, and reaches that value at $\sim 5R_{500,\rm c}$, but only in the most massive ones. $Y_{\rm bar}$ in less massive systems, although shows steeper radial profiles, remains 5% below $\Omega_{\rm bar}/\Omega_{\rm m}$ even at $10R_{500,\rm c}$ (see Fig. 5.3 and Tab. 8.2). Similar trends are observed for the gas component.
  - $Y_{\rm star}$ decreases systematically with increasing radii. While the contribution of the stellar mass fraction in the central region ($< 2R_{500,\rm c}$) is higher in less massive systems, this difference disappears at larger radii,

and both galaxy groups and clusters reach a value of $Y_{\rm star} = 0.09^{+0.01}_{-0.01}$. In these regions, the metal distribution becomes constant, with a median value of $0.23^{+0.08}_{-0.08}$ at $r > 2R_{500,c}$, with no dependency on the halo mass (see Fig. 5.9 and Tab. 8.2). These flat mass-independent metallicity profiles support a scenario in which the gas present in massive halos is early enriched, with a negligible contribution from recent star-formation processes (that is indeed expected to be mass-dependent). This result confirms, and extends to much larger radii, what has been obtained from recent work on numerical simulations (see e.g. Biffi et al., 2017, 2018c).

  - **Our results support that matter halos behaves as "closed boxes" only when volume much larger than their virial volume are considered, and that especially in low mass systems the effect of feedback controls the distribution of baryons up to very large distances from the cluster centre.**

- Angelinelli et al. (2023) (discussed in Chapt. 5):

  - In the central region of galaxy clusters ($r < R_{500,c}$) the baryon fraction shows a general decrease with the redshift, with a decrease for less massive objects which is ~ 4 times larger than in massive ones (see Fig. 5.4 and Tab. 8.4). The gas depletion parameter we recover inside $R_{500,c}$ is an agreement with observations of low redshift halos (Eckert et al., 2021; Akino et al., 2022) (see Fig. 5.5). At high redshift ($z > 1.2$) instead, the contribution given by the cold gas phase ($kT < 0.1$ keV) is non-negligible. For instance, at $z \sim 2.8$ the cold component accounts for $\sim 20 \div 28\%$ of the total gas, depending on the sub-sample mass. This leads to an increase in the total amount of gas, not well matched by the best fit suggested from low-z observations.

  - Previous studies have shown that AGN feedback affects the evolution of baryon and gas fraction in galaxy clusters (Lapi et al., 2005; Castro et al., 2021; Ragagnin et al., 2022; Ayromlou et al., 2022). In our work, we examine the relationship between the feedback energy (Eq. 5.8) and the depletion parameter (see Fig. 5.13 and Tab. 5.2), finding a high level of correlation between the evolution of the cold gas phase and the stellar depletion parameter. The gas, hot gas phase, and gas metallicity are found to be anti-correlated with the evolving feedback energy. The gas depletion parameter also showed a dependency on the correlation with the mass of the galaxy clusters. We also compare different models of AGN feedback implemented in numerical simulations (see Fig. 5.15) and we conclude that further observational investigations are needed to determine the best AGN feedback model. The analysis of gas metallicity and

stellar depletion parameter (see Fig. 5.11 and Fig. 5.12) indicates that an early enrichment scenario (see Biffi et al., 2017, 2018c) likely accounts for the trends with mass and redshift. In the central regions of galaxy clusters, the redshift evolution of gas metallicity accounts for less than 20% in less massive objects and less than 10% in the most massive ones. Additionally, the stellar depletion parameter decreases by a factor of 2, independently of the mass of the galaxy clusters, suggesting that recent star-formation processes have a negligible impact on the enrichment of the gas metallicity.

– **In summary, our study (recently accepted at the time of this writing) suggests that the ratio between the different phases of baryons in halos, as well as the gas chemical composition, is primarily controlled by the time-integrated effect of AGN feedback, which influences the halo properties starting from high redshifts and out to very large radii, with important consequences on the cosmological use of these systems.**

For sake of completeness, the reader may find a more detailed description of the findings I presented in the original papers. Furthermore, some useful numerical and fitting results are discussed in Chapt. 8.

Chapter 7

The future perspectives

Galaxy clusters and groups represent unique laboratories to test our knowledge about many different physical processes. The low density of gas in the outskirts of galaxy clusters makes them difficult to detect with X-ray telescopes, due to their faintness. However, cosmological simulations suggest that these regions should be active with gas accretion and ongoing mergers with smaller sub-clusters and gas clumps. There is a wide range of physics at play in these outskirts, which differ significantly from the physics in the cores of clusters that have been studied extensively in the past.

There are several limitations of current cosmological hydrodynamical simulations in the modeling the physics of cluster outskirts (see Walker, Lau 2022 for details). Modern simulations often lack sophisticated treatments of non-thermal energy components, such as magnetic fields and cosmic rays, which can become increasingly important in the cluster outskirts, due to the radial drop of the gas thermal energy. The physical processes involved in modeling the physics of cluster outskirts also span a wide range of physical scales. To improve the modeling of largely non-equilibrium physics in cluster outskirts, higher mass and spatial resolution are needed in simulations. Additionally, high-resolution simulations are needed to resolve the full turbulence cascade, small-scale gas clumps, and merger and accretion shocks. To anticipate data from upcoming surveys of galaxy clusters, future efforts will have to focus on improving the multi-scale modeling, with small-box and high-resolution simulations to study small-scale accretion physics in detail, large-box low-resolution simulations to sample the range of cluster mass accretion histories, and physically motivated sub-grid models to bridge the simulations of large and small scales.

From an observational point of view, more powerful X-ray observatories with greater effective area, low and stable background and high spatial resolution are needed to make further progress. eROSITA* (launched in 2019) promises to signif-

*https://erosita.mpe.mpg.de

icantly improve our understanding of cluster outskirts by providing measurements out to $2R_{200,c}$, and by investigating the connection of cosmic web filaments to clusters. On the other hand, XRISM[†] (expected launch date: May 2023) is supposed to recover and improve scopes of the HITOMI mission, focusing on the cluster's core (inside $\sim R_{2500,c}$) and investigating the consequences of the interactions between ICM and infalling structures. ATHENA[‡], which is planned to launch in the late 2030s, will allow the direct measurement of turbulence and bulk motions up to the clusters' outskirts. Other prospective future missions such as Lynx[§], AXIS[¶] or HUBS[‖] would offer high spatial and spectral resolution and low background noise that would be beneficial for observations of cluster outskirts. These future missions will increase the sensitivity by a factor of 50 which will allow us to reveal the full picture of the way the cluster outskirts connect with the cosmic web.

In the following, I present some possible extensions related to the works presented in this Thesis.

Can we solve the hydrostatic mass bias?

Starting from the findings and the advanced filtering techniques discussed in Angelinelli et al. (2020), it will be possible to test the persistence of the relations identified in non-radiative simulations when different physical schemes are adopted in the simulations. Using samples of galaxy clusters and groups extracted from *Magneticum* simulations and the iterative small-scale filtering techniques, it will be possible to verify the impact of feedback processes in the evolution of turbulent motions in the central regions of the simulated halos. In this respect, future observations, e.g., with LOFAR and SKA may be able to provide important clues to the presence of significant cosmic rays and relativistic particles, i.e. non-thermal pressure in dynamically disturbed systems. Thanks to numerical simulations, such out-of-equilibrium conditions may be linked to the presence of turbulent motions, as observations have also begun to establish the quantitative link between observed radio power in radio halos to the turbulent energy budget of the ICM, inferred from the amount of fluctuations in X-ray surface brightness (e.g. Eckert et al., 2017b). This will be key for the cosmological use of galaxy clusters in future X-ray surveys (e.g. with eROSITA, see for example Zandanel et al. 2018). Furthermore, future pointed exposures of the ICM in X-rays will enable the calibration of the $\alpha_{\rm HS}$-α relation by measuring the level of gas turbulence with the next generation of instruments having high spectral resolution capabilities (e.g. XRISM/Resolve - see Ishisaki et al. 2018 and scientific applications in Kitayama et al. 2014 - and

[†] https://xrism.isas.jaxa.jp/en/
[‡] https://www.the-athena-x-ray-observatory.eu/
[§] https://www.lynxobservatory.com/
[¶] https://axis.astro.umd.edu/
[‖] http://hubs.phys.tsinghua.edu.cn/en/

ATHENA/X-IFU - description in Barret et al. 2018, and discussion of some scientific cases related to the one presented here in Roncarelli et al. 2018a, Vazza et al. 2019, Clerc et al. 2019, Cucchetti et al. 2019). Moreover, by including different physical processes, it will be possible to study the non-thermal pressure support given by AGN or stellar feedback, magnetic fields and all the other sources of non-thermal phenomena and compare these contributions with the one given by turbulent motion, to understand the relative impact of each of them on the hydrostatic mass bias (see Nelson et al., 2014a; Biffi et al., 2016b, for the analysis of the impact of different non-thermal components) and to validate different theoretical models (Eckert et al., 2019; Ettori, Eckert, 2022)

Synthetic X-ray observations: what will we observe using ATHENA?

As already introduced in Sect. 4.2.5, I developed a procedure that involves both the instruments that will be on board the ATHENA mission. Even if nowadays it is not clear which will be the final design of such instruments, the procedure I developed is still useful. Indeed, the idea of using WFI to detect matter clumps located in the external regions of massive galaxy clusters and making a follow-up observation with X-IFU is quite independent of the final configurations of these instruments. Indeed, in the algorithm that I developed, the instrumental configuration is completely determined by the RMF and ARF matrices that are released by the ATHENA consortium. Changing the configuration of the instruments will affect the results that I will achieve. Indeed, as already discussed, the external regions of galaxy clusters and groups are characterised by low X-rays emissivity and the background becomes important to understand what will be observed and what will not. The results that I presented in Sect. 4.2.5 are obtained using the last available configuration for WFI and X-IFU before the de-scoped suffered by the mission in 2022. Once the final design of the instruments will be released to the community, I will integrate the new RMF and ARF files and I will determine the physical proprieties of matter clumps that would be observed by the ATHENA satellite. In this respect, it would be useful to understand the observational limits of ATHENA and possible sources of uncertainties that the instruments will introduce in the analysis, comparing the results obtained from the pipeline and the cosmological simulations which will be used as input of these simulated observations. Moreover, to have realistic predictions, it will be important to use as input of the pipeline more sophisticated and modern cosmological simulations. Indeed, it is clear that physical processes such as feedback and cooling, highly affect the physical proprieties of matter clumps and the surrounding medium, impacting also their observability. Having realistic constraints in this respect it will be crucial to determine the best observational candidates and maximise the information that will be achieved by the observations.

How to detect X-ray structures at very low SNR?

As a first result of the pipeline described above, I verified that with the current and next future X-ray observatories, the detection of matter clumps and small structures around galaxy clusters is still very challenging. Indeed, the signal-to-noise ratio (SNR) that characterises these structures is often very low, on the order of the unit or below. In this regime, developing sophisticated numerical and observational techniques are fundamental.

Important steps in the treatment of the observational background in radio band using Machine Learning techniques have been discussed by Gheller, Vazza (2022). The authors present the use of a techniques called Convolutional Denoising Autoencoder to "denoise" synthetic images of state-of-the-art radio telescopes in order to detect faint, diffused radio sources predicted to characterise the radio cosmic web. The denoising process addresses the reduction of random instrumental noise and the minimization of additional spurious artefacts. The effectiveness and accuracy of the method are analysed for different kinds of corrupted input images, along with their computational performance. The authors also note that specific attention has been devoted to creating realistic mock observations for the training, using cosmological numerical simulations, to generate images. The autoencoder is effective at denoising complex images and identifying faint objects at the limits of instrumental sensitivity. It can efficiently scale on large datasets using high-performance computing solutions, in a fully automated way, and can accurately perform image segmentation, identifying low brightness outskirts of diffused sources, proving to be a viable solution for detecting challenging extended objects hidden in noisy radio observations. Starting from this work, we are now working to extend this technique also to mock X-ray observations from cosmological simulations (see Fig. 7.1). The input of the training dataset is the *Box2b* of *Magneticum* simulations. Indeed, the simulated volume is $\sim 650^3\ Mpc^3/h$ and from the single *Box2b* we can extract $\sim 10^5$ independently halos. This allows us sufficient statistics to perform tests on the autoencoder technology and understand the effectiveness of the application of the denoising procedure on X-rays images. Preliminary tests suggest that our procedure could resolve sources with a signal-to-noise ratio on the order of $0.1 \div 0.2$.

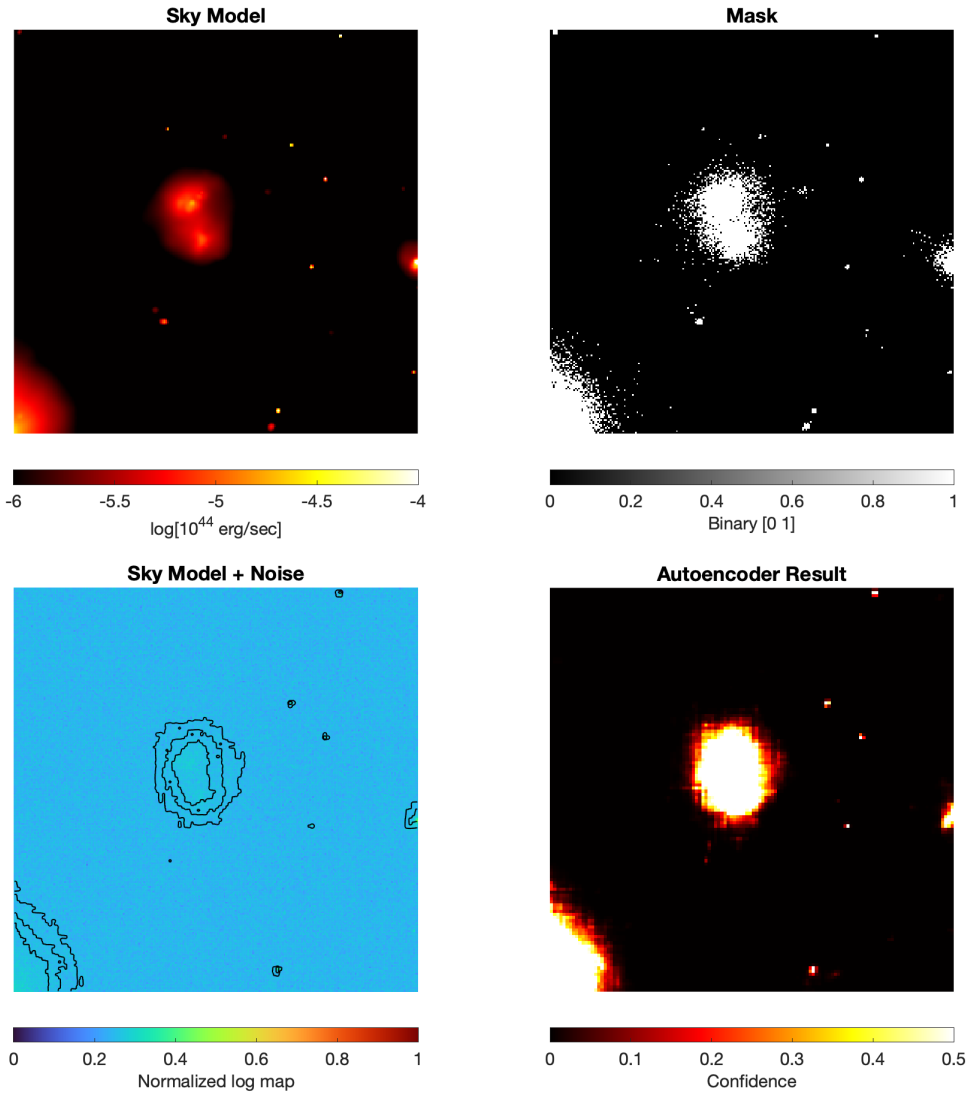

Figure 7.1: Convolutional Denoising Autoencoder applied to mock X-rays image (maps produced by Dr. C. Gheller). (Top left) X-rays emission map in 10^{44} [erg/s] of the source. (Top right) Mask needed in the training phase of the algorithm; in each pixel, given a defined threshold, it expresses the presence (tagged with 1) or the absence (tagged with 0) of the source. (Bottom left) Normalised X-rays emission map of the combination of source and background; the contours represent the emission identified by the autoencoder algorithm. (Bottom right) Result of the autoencoder algorithm; in each pixel, it represents the possibility of the presence of a source.

Chapter 8

Appendices

In this chapter, we collect all the appendixes of the papers presented above. Each section title refers to the chapter that the appendix completes.

8.1 Chapter 3: Testing the relation between filtering scale and non-thermal pressure

As detailed in the main text (Sec.3.1.2) our iterative scheme to measure the local turbulent velocity field requires predicting the increase of the local rms velocity as a function of the smoothing scale, w, i.e $.\delta v^2 \propto w^f$. In Kolmogorov theory, such exponent should be $f = 2/3$, yet we tested to what extent the standard Kolmogorov theory of turbulence applies to our data and studied the relation between the value of α measured at the reference radius of $R_{200,c}$ (α_{200}) as a function of different fixed smoothing scale. If we apply the standard relation between rms velocity and turbulent scale (e.g. $\sigma^2 \propto \mathrm{L}^{\frac{2}{3}}$) in the stationary subsonic turbulent regime described by Kolmogorov theory, we expect that the relation should approximately follow:

$$\alpha_{200} = a \cdot w^f, \tag{8.1}$$

where w is the value of smoothing scale in physical quantities and a and f are the parameters obtained from Kolmogorov's theory (Kolmogorov, 1941). The expected value for f is close to $\frac{2}{3}$ for stationary and subsonic turbulence. However, the ICM is not such an idealised environment because of density stratification, self-gravity and non-stationary flow patterns, which can lead to deviations from 2/3.

Fig. 8.1 shows the pressure ratio, α_{200}, versus the smoothing scale computed of our set of clusters at $z = 0$, after computing the local turbulent velocity field for increasing smoothing scales, w. The trend is measured to be very similar across our sample and can be fitted by a unique power law.

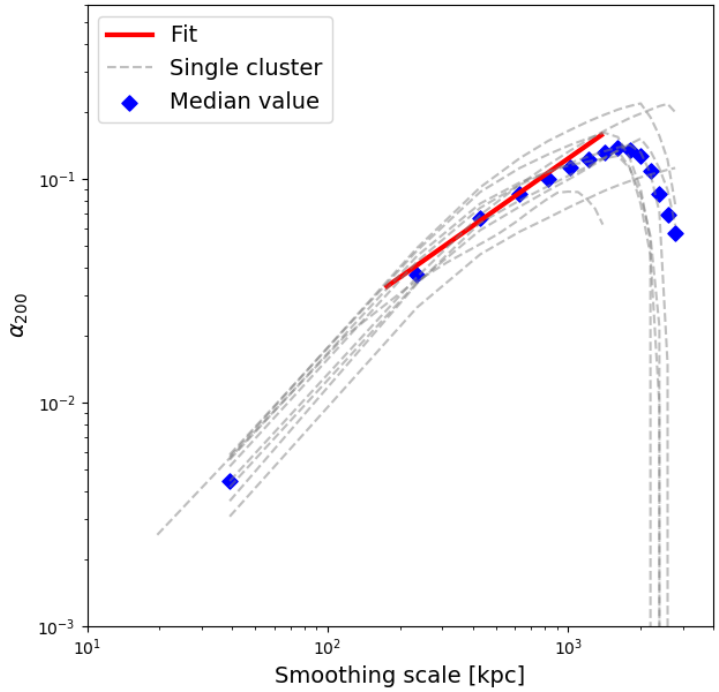

Figure 8.1: Relation between smoothing scales and α_{200} for the sample of clusters at $z = 0$. The blue points represent the median values of α_{200} at different smoothing scales for the used sample of clusters. The solid red line gives the power-law fit obtain explained in Sect. 3.1.2.

We fit the data to Eq. 8.1 and obtain $a \simeq 6 \cdot 10^{-3}$ and $f \simeq 0.77$, which is the fiducial value we adopted to stop the iterations in our method in the Chapt. 3, as in Eq. 3.4. The value for f is reasonably close to $2/3$ and is consistent with the fact that the power spectra of the velocity field in simulated galaxy clusters are typically steeper than Kolmogorov's slope because of the stratified cluster atmosphere (Vazza et al., 2011a). Only the scales below ~ 100 kpc show hints of a steepening, which may partially be ascribed to numerical dissipation in the PPM scheme, which is expected to dampen the velocities on scales close to a few times the spatial resolution (e.g, Porter, Woodward 1994). For scales larger than ~ 8 times the numerical resolution (≥ 200 kpc) these effects do not occur and the relation between α and the smoothing scale is well fitted by Kolmogorov's spectrum. Since a number of physical and numerical effects may affect the dynamics of the turbulent flow on $< 100 - 200$ kpc, with these simulations it is hard to tell the different effects apart. In the following, we focus mostly on the dynamics of turbulence on scales > 100 kpc, which are also the ones that dominate the non-thermal pressure support. On scales greater than ~ 1 Mpc, the spectra show a drop where the peak of the Kolmogorov spectrum

is reached. The exponent f in Eq. 8.1 is calculated in the inertial range of the Kolmogorov spectrum, from $\sim$ 200 to $\sim$ 800 kpc, so we can use this value for the multi-scale adaptive filtering.

8.2 Chapter 4: Numerical resolution effects on clumping factor and clump number density

We tested the effect of the spatial and force resolution on the measure of the clumping factor and on the number of identified clumps, to understand how much are the findings of our Chapt. 4 restricted to the particular adopted resolution. To this end, we analysed four different re-simulations of the same cluster of $M_{500,c} = 8.5\times10^{14}\ M_{\odot}$ and $R_{500,c} = 1.4$ Mpc, obtained for an increasing level of maximum adaptive mesh refinement, as in Vazza et al. (2018b). The adaptive mesh refinement follows the local gas over-density, and the maximum resolution goes from 128 kpc in the lowest resolution case, to 8 kpc in the highest resolution run adopted here (see Fig. 8.2 for the related density maps and detected clumps).

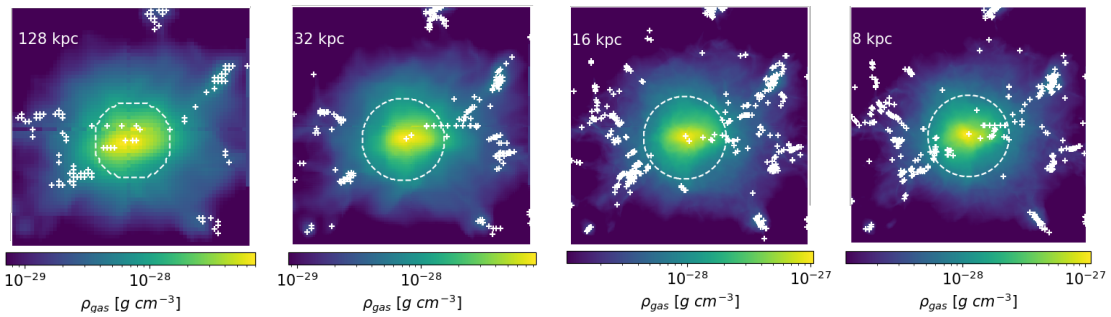

Figure 8.2: Projected gas density for the test cluster, at four different levels of numerical resolution (top left: 128 kpc; top right: 32 kpc; bottom left: 16 kpc; bottom right: 8 kpc). The dashed circle represent $R_{500,c}$, while the white crosses are the centre of the identified clumps.

We followed the same procedures of Chapt. 4 and computed the radial profiles of gas clumping factor and clumps as a function of resolution (Fig. 8.3).

It can be noticed that in the central regions (up to $\sim 2.5R_{500,c}$), the clumping factor is weakly affected by changes in numerical resolution. However, in the external regions, the differences introduced by the AMR levels account for less than 30% of the clumping factor at any radii. This trend ensures that the evaluation of the clumping factor is weakly affected by the simulations' numerical resolution - at least for the non-radiative gas physics used in this work.

Second, we tested the effects of numerical resolution on the clumps' number density. Using the same AMR level adopted for the clumping factor, we use ten

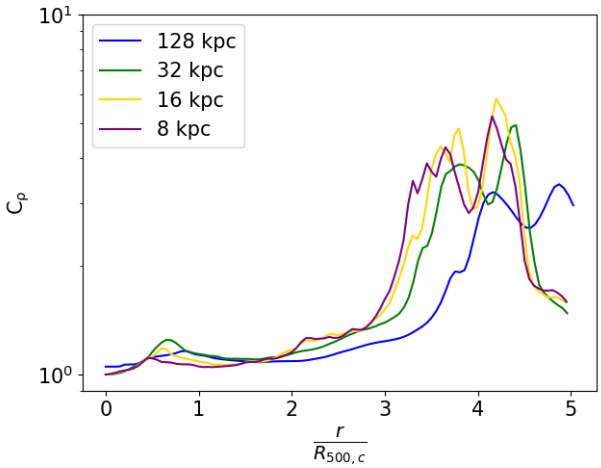

Figure 8.3: Clumping factor for the test cluster at different levels of numerical resolution.

equally spaced radial shells from $R_{500,c}$ up to $5R_{500,c}$. From Fig. 8.4, we notice that by increasing the numerical resolution, the clumps number density increases. In particular, we observe a difference of factor $\sim$3 between the lower numerical resolution and the higher one. However, we also notice that from 16 kpc to 8 kpc, the median values computed in the inner regions (from centre to $2.5R_{500,c}$) and the outer ones (from $2.5R_{500,c}$ and $5R_{500,c}$) are quite constant. The observed trend is exactly as in Chapt. 4, and the relatively little evolution with resolution suggests that spatial resolution of the cluster sample used in Chapt. 4 ($\sim$ 19.6 comoving kpc) is suitable to study clumps and clumping free from numerical artefacts.

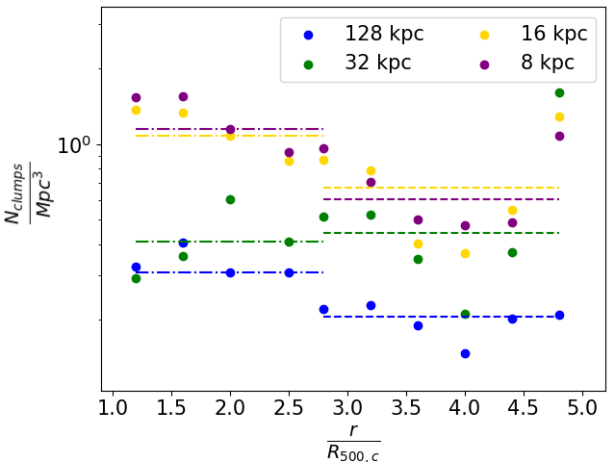

Figure 8.4: Clumps' number density for the same cluster at different levels of numerical resolution in the function of radial distance from the cluster's centre. The dot-dashed lines represent the median value computed between $R_{500,c}$ and $2.5R_{500,c}$, while the dashed ones represent the median value computed from $2.5R_{500,c}$ to $5R_{500,c}$. The colour-coding of these lines is the same adopted for the dots.

8.3 Chapter 5: Estimates and fitting parameters of the depletion factors in the local Universe

We provide the best-fit parameters obtained from the fitting function:

$$Y_i = \alpha \cdot w^{\beta} \cdot x^{\gamma+\delta*w} \tag{8.2}$$

where $w = M_{500,c}/5 \cdot 10^{14}\ h^{-1}M_{\odot}$, $x = r/R_{500,c}$, while α, β, γ and δ are the free parameters, that are quoted in Tab. 8.1.

	$Y_{\rm bar}$	$Y_{\rm gas}$	$Y_{\rm hot}$
α	0.900 ± 0.003	0.733 ± 0.004	0.724 ± 0.004
β	0.123 ± 0.002	0.223 ± 0.003	0.261 ± 0.003
γ	0.233 ± 0.005	0.674 ± 0.008	0.756 ± 0.009
δ	-0.217 ± 0.015	-0.708 ± 0.022	-0.810 ± 0.022
$\tilde{\chi}^2$	0.43	0.75	0.97
$\tilde{e}$	2%	4%	5%
e_{max}	23%	24%	30%

Table 8.1: Best-fit parameters and related standard errors, for the functional form Eq. 8.2 fitted on $Y_{\rm bar}$, $Y_{\rm gas}$ and $Y_{\rm hot}$. The values of the reduced χ^2 ($\tilde{\chi}^2$), the median and the maximum deviation of the model from the data ($\tilde{e}$ and e_{max}, respectively) are also quoted.

The set of parameters $(\alpha, \beta, \gamma, \delta) = (0.90, 0.12, 0.23, -0.22)$ provides a description within 2% of $Y_{\rm bar}$ (see Fig. 8.5).

Being our findings potentially useful to make predictions and comparisons with observational work, we confine our fitting produce in a radial range similar to the one available for present and near future X-rays observations and limited to the central regions of our analysis, from $0.5R_{500,c}$ to $2.5R_{500,c}$. The functional form is able to well reproduce the behaviour of $Y_{\rm bar}$ at all considered masses, as also shown by the $\tilde{\chi}^2$ and values of the median and the maximum deviation of the model from the data ($\tilde{e}$ and e_{max}, respectively) quoted in Tab. 8.1. However, for the $Y_{\rm gas}$ and $Y_{\rm hot}$, we note that our fitting procedure gives less strong results than for the $Y_{\rm bar}$ case. We use the dispersion around the mean profile as the weight to evaluate χ^2.

We provide here details on the values of the depletion parameters under investigations in different mass bins and at various radii (see Tab. 8.2).

		$R_{500,c}$	$3R_{500,c}$	$5R_{500,c}$	$10R_{500,c}$
A	Y_{bar}	$0.51^{+0.09}_{-0.06}$	$0.70^{+0.06}_{-0.05}$	$0.83^{+0.05}_{-0.01}$	$0.95^{+0.04}_{-0.02}$
	Y_{gas}	$0.27^{+0.06}_{-0.03}$	$0.57^{+0.05}_{-0.03}$	$0.73^{+0.05}_{-0.03}$	$0.86^{+0.05}_{-0.03}$
	Y_{hot}	$0.22^{+0.03}_{-0.02}$	$0.48^{+0.05}_{-0.07}$	$0.53^{+0.06}_{-0.08}$	$0.46^{+0.14}_{-0.10}$
	Y_{cold}	$0.06^{+0.03}_{-0.02}$	$0.10^{+0.01}_{-0.02}$	$0.21^{+0.04}_{-0.06}$	$0.41^{+0.08}_{-0.10}$
	Y_{star}	$0.24^{+0.03}_{-0.03}$	$0.12^{+0.01}_{-0.01}$	$0.11^{+0.01}_{-0.01}$	$0.09^{+0.01}_{-0.01}$
	Z_{tot}	$0.24^{+0.07}_{-0.02}$	$0.17^{+0.05}_{-0.06}$	$0.21^{+0.21}_{-0.05}$	$0.22^{+0.12}_{-0.03}$
B	Y_{bar}	$0.63^{+0.08}_{-0.04}$	$0.85^{+0.03}_{-0.05}$	$0.93^{+0.01}_{-0.02}$	$0.98^{+0.01}_{-0.02}$
	Y_{gas}	$0.42^{+0.07}_{-0.05}$	$0.72^{+0.04}_{-0.05}$	$0.82^{+0.02}_{-0.02}$	$0.89^{+0.01}_{-0.03}$
	Y_{hot}	$0.37^{+0.03}_{-0.03}$	$0.67^{+0.02}_{-0.03}$	$0.73^{+0.03}_{-0.03}$	$0.64^{+0.08}_{-0.05}$
	Y_{cold}	$0.04^{+0.06}_{-0.02}$	$0.04^{+0.02}_{-0.01}$	$0.09^{+0.02}_{-0.03}$	$0.26^{+0.05}_{-0.11}$
	Y_{star}	$0.21^{+0.04}_{-0.01}$	$0.12^{+0.01}_{-0.01}$	$0.10^{+0.01}_{-0.01}$	$0.09^{+0.01}_{-0.01}$
	Z_{tot}	$0.29^{+0.09}_{-0.06}$	$0.25^{+0.05}_{-0.06}$	$0.26^{+0.04}_{-0.02}$	$0.20^{+0.04}_{-0.05}$
C	Y_{bar}	$0.72^{+0.04}_{-0.07}$	$0.90^{+0.02}_{-0.03}$	$0.95^{+0.03}_{-0.02}$	$0.99^{+0.01}_{-0.01}$
	Y_{gas}	$0.53^{+0.03}_{-0.07}$	$0.78^{+0.01}_{-0.03}$	$0.85^{+0.03}_{-0.02}$	$0.90^{+0.01}_{-0.01}$
	Y_{hot}	$0.50^{+0.03}_{-0.06}$	$0.74^{+0.01}_{-0.03}$	$0.76^{+0.04}_{-0.03}$	$0.65^{+0.08}_{-0.06}$
	Y_{cold}	$0.03^{+0.01}_{-0.01}$	$0.04^{+0.02}_{-0.01}$	$0.08^{+0.03}_{-0.02}$	$0.24^{+0.07}_{-0.07}$
	Y_{star}	$0.18^{+0.02}_{-0.01}$	$0.11^{+0.01}_{-0.01}$	$0.10^{+0.01}_{-0.01}$	$0.09^{+0.01}_{-0.01}$
	Z_{tot}	$0.28^{+0.07}_{-0.05}$	$0.27^{+0.06}_{-0.05}$	$0.25^{+0.04}_{-0.02}$	$0.21^{+0.08}_{-0.07}$
D	Y_{bar}	$0.87^{+0.03}_{-0.04}$	$0.93^{+0.01}_{-0.02}$	$0.99^{+0.01}_{-0.01}$	$1.00^{+0.01}_{-0.01}$
	Y_{gas}	$0.69^{+0.04}_{-0.04}$	$0.82^{+0.02}_{-0.02}$	$0.88^{+0.01}_{-0.01}$	$0.91^{+0.01}_{-0.01}$
	Y_{hot}	$0.67^{+0.04}_{-0.05}$	$0.79^{+0.01}_{-0.02}$	$0.81^{+0.01}_{-0.01}$	$0.68^{+0.03}_{-0.02}$
	Y_{cold}	$0.02^{+0.01}_{-0.01}$	$0.03^{+0.01}_{-0.01}$	$0.07^{+0.01}_{-0.01}$	$0.23^{+0.02}_{-0.03}$
	Y_{star}	$0.17^{+0.02}_{-0.02}$	$0.11^{+0.01}_{-0.01}$	$0.11^{+0.01}_{-0.01}$	$0.09^{+0.01}_{-0.01}$
	Z_{tot}	$0.33^{+0.06}_{-0.04}$	$0.28^{+0.04}_{-0.08}$	$0.25^{+0.11}_{-0.08}$	$0.16^{+0.08}_{-0.04}$

Table 8.2: Baryons (Y_{bar}), gas (Y_{gas}), hot gas phase (Y_{hot}), cold gas phase (Y_{cold}) and stellar (Y_{star}) depletion factors and gas metallicity (Z_{tot}) computed at four different radii ($1, 3, 5$ and 10 times $R_{500,c}$) for four virial mass bins ($A: \ 10^{13} < M_{vir}/h^{-1}M_{\odot} < 2 \cdot 10^{13}$ ($4.2 \cdot 10^{12} < M_{500,c}/h^{-1}M_{\odot} < 1.2 \cdot 10^{13}$); $B: \ 5 \cdot 10^{13} < M_{vir}/h^{-1}M_{\odot} < 6 \cdot 10^{13}$ ($1.6 \cdot 10^{13} < M_{500,c}/h^{-1}M_{\odot} < 3.6 \cdot 10^{13}$); $C: \ 10^{14} < M_{vir}/h^{-1}M_{\odot} < 2 \cdot 10^{14}$ ($6.3 \cdot 10^{13} < M_{500,c}/h^{-1}M_{\odot} < 10^{14}$); $D: \ M_{vir}/h^{-1}M_{\odot} > 5 \cdot 10^{14}$ ($M_{500,c}/h^{-1}M_{\odot} > 2.4 \cdot 10^{14}$)). Errors are given as 16th and 84th distributions percentiles. Note that the depletion factors are computed within the given radii, differently from the metallicity values which are given within a spherical shell (considering the same reference radii).

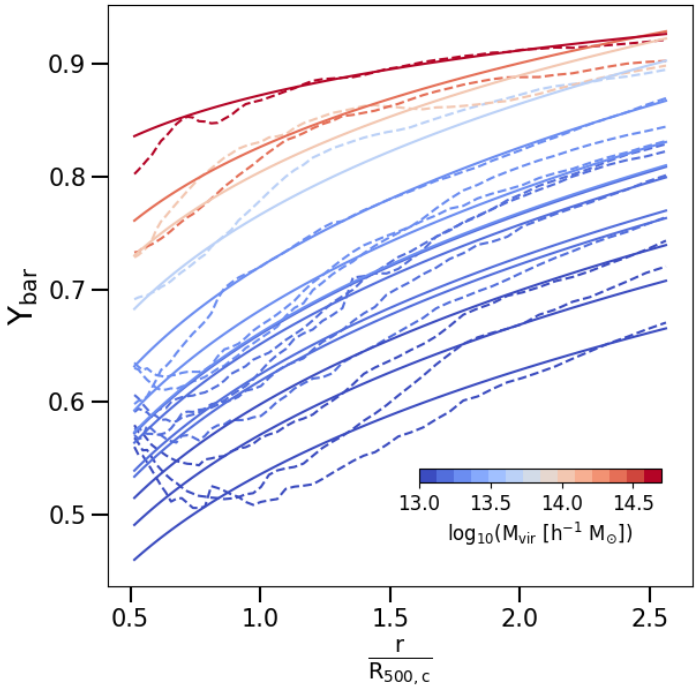

Figure 8.5: Radial profiles of baryon depletion, from $0.5R_{500,c}$ up to $2.5R_{500,c}$. The dashed lines represent the median profiles in each mass bin, according to the legend in the bottom-right corner. The solid lines are the fit performed according to functional form Eq. 8.2, with the same colour scale of median profiles.

8.4 Chapter 5: Depletion factors estimations and fitting results at different redshifts

We provide within Tab. 8.3 (see also Fig. 8.6) the best-fit parameters obtained from the fitting function:

$$Y_i = \alpha \cdot w^{\beta} \cdot x^{\gamma+\delta*w+\epsilon*(1+z)} \tag{8.3}$$

where $w = M_{500,c}/5 \cdot 10^{14}\ h^{-1}M_{\odot}$, $x = r/R_{500,c}$, z is the redshift, while α, β, γ, δ and ϵ are the free parameters. Our best-fit values are able to provide a description within 2% for the baryon depletion parameter and within 3% for gas and hot gas phase ones.

Following our previous work *PaperI*, we limit our fitting produce in a radial range comparable with the one of present and near future X-rays observations, focusing in the central regions of our analysis, from $0.5R_{500,c}$ to $2.5R_{500,c}$. The functional form is able to well reproduce the behaviour of all the depletion parameters analysed, as shown by the $\tilde{\chi}^2$ and values of the median and the maximum deviation of the model from the data ($\tilde{e}$ and e_{max}, respectively). However, as already observed in *PaperI*, also in this case, for the $Y_{\rm gas}$ and $Y_{\rm hot}$ we note that our fitting procedure gives less strong results than for $Y_{\rm bar}$ case. We use the dispersion around the mean profile as

	$Y_{\rm bar}$	$Y_{\rm gas}$	$Y_{\rm hot}$
α	0.821 ± 0.001	0.660 ± 0.001	0.680 ± 0.001
β	-0.051 ± 0.001	0.015 ± 0.001	0.115 ± 0.001
γ	0.129 ± 0.006	0.315 ± 0.008	0.482 ± 0.008
δ	0.093 ± 0.007	-0.015 ± 0.008	-0.254 ± 0.008
ϵ	-0.050 ± 0.001	-0.029 ± 0.002	-0.047 ± 0.003
$\tilde{\chi}^2$	1.62	1.03	0.83
$\tilde{e}$	2%	3%	3%
e_{max}	17%	32%	28%

Table 8.3: Best-fit parameters and related standard errors, for the functional form Eq. 8.3 fitted on $Y_{\rm bar}$, $Y_{\rm gas}$ and $Y_{\rm hot}$. The values of the reduced χ^2 ($\tilde{\chi}^2$), the median and the maximum deviation of the model from the data ($\tilde{e}$ and e_{max}, respectively) are also quoted.

the weight to evaluate χ^2.

In Tab. 8.4 we report the details on the values of the depletion parameters under investigations in the less and the most massive bins and at four radii ($R_{500,\rm c}$, $3R_{500,\rm c}$, $5R_{500,\rm c}$ and $10R_{500,\rm c}$) and for four different redshifts (2.79, 1.71, 0.67 and 0.25).

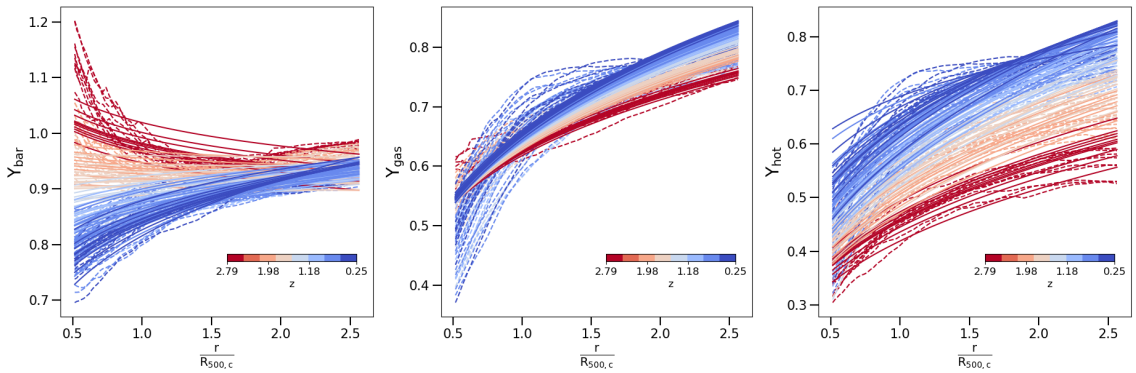

Figure 8.6: Radial profiles of baryon (left), gas (centre) and hot gas phase (right) depletion, from $0.5R_{500,\rm c}$ up to $2.5R_{500,\rm c}$. The dashed lines represent the median profiles of each mass bin at each redshift, according to the colourbar in the bottom right corner. The solid lines are the fit performed according to functional form Eq. 8.3, with the same colour scale of median profiles.

z		Less massive sub-sample				Most massive sub-sample			
		$R_{500,c}$	$3R_{500,c}$	$5R_{500,c}$	$10R_{500,c}$	$R_{500,c}$	$3R_{500,c}$	$5R_{500,c}$	$10R_{500,c}$
2.79		$5.8 \times 10^{12} \leq M_{500,c}/M_{\odot} \leq 9.7 \times 10^{12}$				$2.5 \times 10^{13} \leq M_{500,c}/M_{\odot} \leq 5.0 \times 10^{13}$			
	$Y_{\rm bar}$	$0.99^{+0.02}_{-0.05}$	$0.99^{+0.01}_{-0.02}$	$1.0^{+0.01}_{-0.01}$	$1.0^{+0.01}_{-0.01}$	$0.96^{+0.01}_{-0.02}$	$0.99^{+0.01}_{-0.01}$	$1.0^{+0.01}_{-0.01}$	$1.00^{+0.01}_{-0.01}$
	$Y_{\rm gas}$	$0.64^{+0.02}_{-0.06}$	$0.78^{+0.02}_{-0.03}$	$0.82^{+0.02}_{-0.01}$	$0.88^{+0.01}_{-0.01}$	$0.63^{+0.02}_{-0.03}$	$0.79^{+0.01}_{-0.02}$	$0.84^{+0.01}_{-0.01}$	$0.90^{+0.01}_{-0.01}$
	$Y_{\rm hot}$	$0.45^{+0.02}_{-0.04}$	$0.55^{+0.02}_{-0.06}$	$0.44^{+0.05}_{-0.03}$	$0.27^{+0.04}_{-0.05}$	$0.50^{+0.02}_{-0.06}$	$0.57^{+0.04}_{-0.02}$	$0.46^{+0.04}_{-0.02}$	$0.27^{+0.02}_{-0.01}$
	$Y_{\rm cold}$	$0.18^{+0.05}_{-0.03}$	$0.25^{+0.03}_{-0.06}$	$0.38^{+0.04}_{-0.06}$	$0.62^{+0.06}_{-0.05}$	$0.13^{+0.04}_{-0.01}$	$0.22^{+0.03}_{-0.04}$	$0.38^{+0.02}_{-0.04}$	$0.63^{+0.01}_{-0.03}$
	$Y_{\rm star}$	$0.33^{+0.09}_{-0.04}$	$0.20^{+0.03}_{-0.01}$	$0.18^{+0.01}_{-0.02}$	$0.11^{+0.01}_{-0.01}$	$0.33^{+0.07}_{-0.03}$	$0.20^{+0.02}_{-0.01}$	$0.16^{+0.02}_{-0.01}$	$0.10^{+0.01}_{-0.01}$
	$Z_{\rm tot}$	$0.05^{+0.04}_{-0.03}$	$0.03^{+0.27}_{-0.02}$	$0.07^{+0.20}_{-0.05}$	$0.02^{+0.27}_{-0.02}$	$0.09^{+0.11}_{-0.03}$	$0.03^{+0.09}_{-0.02}$	$0.03^{+0.10}_{-0.02}$	$0.02^{+0.04}_{-0.01}$
1.71		$1.2 \times 10^{13} \leq M_{500,c}/M_{\odot} \leq 3.4 \times 10^{13}$				$6.0 \times 10^{13} \leq M_{500,c}/M_{\odot} \leq 1.5 \times 10^{14}$			
	$Y_{\rm bar}$	$0.91^{+0.03}_{-0.08}$	$0.97^{+0.02}_{-0.03}$	$0.99^{+0.01}_{-0.01}$	$1.00^{+0.01}_{-0.01}$	$0.91^{+0.03}_{-0.01}$	$0.98^{+0.01}_{-0.01}$	$1.00^{+0.01}_{-0.01}$	$1.00^{+0.01}_{-0.01}$
	$Y_{\rm gas}$	$0.64^{+0.02}_{-0.09}$	$0.80^{+0.02}_{-0.01}$	$0.85^{+0.02}_{-0.01}$	$0.89^{+0.01}_{-0.01}$	$0.68^{+0.02}_{-0.01}$	$0.82^{+0.01}_{-0.01}$	$0.86^{+0.01}_{-0.01}$	$0.90^{+0.01}_{-0.01}$
	$Y_{\rm hot}$	$0.53^{+0.03}_{-0.08}$	$0.67^{+0.03}_{-0.01}$	$0.62^{+0.03}_{-0.02}$	$0.41^{+0.03}_{-0.05}$	$0.61^{+0.02}_{-0.01}$	$0.72^{+0.02}_{-0.02}$	$0.65^{+0.02}_{-0.04}$	$0.43^{+0.04}_{-0.05}$
	$Y_{\rm cold}$	$0.09^{+0.03}_{-0.03}$	$0.12^{+0.03}_{-0.02}$	$0.23^{+0.04}_{-0.03}$	$0.49^{+0.04}_{-0.05}$	$0.07^{+0.01}_{-0.01}$	$0.10^{+0.02}_{-0.02}$	$0.21^{+0.05}_{-0.02}$	$0.47^{+0.06}_{-0.05}$
	$Y_{\rm star}$	$0.26^{+0.04}_{-0.03}$	$0.17^{+0.01}_{-0.02}$	$0.14^{+0.01}_{-0.01}$	$0.10^{+0.01}_{-0.01}$	$0.23^{+0.02}_{-0.01}$	$0.16^{+0.01}_{-0.01}$	$0.13^{+0.01}_{-0.01}$	$0.10^{+0.01}_{-0.01}$
	$Z_{\rm tot}$	$0.22^{+0.17}_{-0.06}$	$0.17^{+0.17}_{-0.10}$	$0.15^{+0.08}_{-0.10}$	$0.07^{+0.25}_{-0.02}$	$0.19^{+0.03}_{-0.07}$	$0.09^{+0.11}_{-0.04}$	$0.11^{+0.08}_{-0.04}$	$0.07^{+0.14}_{-0.04}$
0.67		$6.0 \times 10^{13} \leq M_{500,c}/M_{\odot} \leq 1.0 \times 10^{14}$				$2.3 \times 10^{14} \leq M_{500,c}/M_{\odot} \leq 4.6 \times 10^{14}$			
	$Y_{\rm bar}$	$0.81^{+0.05}_{-0.01}$	$0.93^{+0.01}_{-0.01}$	$0.98^{+0.01}_{-0.02}$	$1.00^{+0.01}_{-0.01}$	$0.92^{+0.02}_{-0.02}$	$0.96^{+0.02}_{-0.02}$	$0.99^{+0.01}_{-0.01}$	$1.00^{+0.01}_{-0.01}$
	$Y_{\rm gas}$	$0.60^{+0.07}_{-0.07}$	$0.80^{+0.01}_{-0.02}$	$0.87^{+0.01}_{-0.02}$	$0.90^{+0.01}_{-0.01}$	$0.73^{+0.01}_{-0.02}$	$0.82^{+0.01}_{-0.01}$	$0.87^{+0.01}_{-0.01}$	$0.90^{+0.01}_{-0.01}$
	$Y_{\rm hot}$	$0.56^{+0.07}_{-0.01}$	$0.76^{+0.01}_{-0.02}$	$0.77^{+0.02}_{-0.01}$	$0.62^{+0.01}_{-0.05}$	$0.70^{+0.02}_{-0.02}$	$0.78^{+0.01}_{-0.01}$	$0.78^{+0.01}_{-0.01}$	$0.63^{+0.06}_{-0.07}$
	$Y_{\rm cold}$	$0.04^{+0.01}_{-0.01}$	$0.04^{+0.01}_{-0.01}$	$0.10^{+0.02}_{-0.01}$	$0.28^{+0.05}_{-0.01}$	$0.03^{+0.01}_{-0.01}$	$0.04^{+0.01}_{-0.01}$	$0.09^{+0.03}_{-0.03}$	$0.27^{+0.07}_{-0.07}$
	$Y_{\rm star}$	$0.21^{+0.01}_{-0.02}$	$0.13^{+0.01}_{-0.01}$	$0.12^{+0.01}_{-0.01}$	$0.09^{+0.01}_{-0.01}$	$0.19^{+0.01}_{-0.01}$	$0.13^{+0.01}_{-0.01}$	$0.12^{+0.01}_{-0.01}$	$0.09^{+0.01}_{-0.01}$
	$Z_{\rm tot}$	$0.34^{+0.03}_{-0.04}$	$0.28^{+0.14}_{-0.04}$	$0.17^{+0.08}_{-0.03}$	$0.14^{+0.05}_{-0.04}$	$0.34^{+0.08}_{-0.06}$	$0.23^{+0.10}_{-0.04}$	$0.18^{+0.11}_{-0.05}$	$0.21^{+0.09}_{-0.09}$
0.25		$6.0 \times 10^{13} \leq M_{500,c}/M_{\odot} \leq 1.9 \times 10^{14}$				$4.6 \times 10^{14} \leq M_{500,c}/M_{\odot} \leq 7.5 \times 10^{14}$			
	$Y_{\rm bar}$	$0.84^{+0.02}_{-0.01}$	$0.93^{+0.02}_{-0.01}$	$0.98^{+0.01}_{-0.02}$	$1.00^{+0.01}_{-0.01}$	$0.92^{+0.01}_{-0.04}$	$0.93^{+0.02}_{-0.01}$	$0.99^{+0.01}_{-0.01}$	$1.00^{+0.01}_{-0.01}$
	$Y_{\rm gas}$	$0.67^{+0.01}_{-0.04}$	$0.81^{+0.02}_{-0.01}$	$0.88^{+0.01}_{-0.02}$	$0.90^{+0.01}_{-0.01}$	$0.75^{+0.03}_{-0.04}$	$0.81^{+0.03}_{-0.01}$	$0.87^{+0.01}_{-0.01}$	$0.90^{+0.01}_{-0.01}$
	$Y_{\rm hot}$	$0.64^{+0.01}_{-0.04}$	$0.78^{+0.02}_{-0.01}$	$0.80^{+0.02}_{-0.01}$	$0.68^{+0.07}_{-0.04}$	$0.73^{+0.03}_{-0.04}$	$0.79^{+0.02}_{-0.01}$	$0.82^{+0.01}_{-0.01}$	$0.70^{+0.02}_{-0.03}$
	$Y_{\rm cold}$	$0.02^{+0.01}_{-0.01}$	$0.03^{+0.01}_{-0.01}$	$0.07^{+0.01}_{-0.01}$	$0.22^{+0.04}_{-0.08}$	$0.02^{+0.01}_{-0.01}$	$0.02^{+0.01}_{-0.01}$	$0.05^{+0.02}_{-0.01}$	$0.21^{+0.03}_{-0.02}$
	$Y_{\rm star}$	$0.18^{+0.02}_{-0.01}$	$0.12^{+0.01}_{-0.01}$	$0.11^{+0.01}_{-0.01}$	$0.09^{+0.01}_{-0.01}$	$0.17^{+0.01}_{-0.02}$	$0.12^{+0.01}_{-0.01}$	$0.11^{+0.01}_{-0.01}$	$0.09^{+0.01}_{-0.01}$
	$Z_{\rm tot}$	$0.32^{+0.08}_{-0.06}$	$0.25^{+0.09}_{-0.06}$	$0.25^{+0.09}_{-0.09}$	$0.19^{+0.06}_{-0.05}$	$0.34^{+0.07}_{-0.06}$	$0.23^{+0.06}_{-0.03}$	$0.21^{+0.14}_{-0.05}$	$0.18^{+0.05}_{-0.05}$

Table 8.4: Baryons ($Y_{\rm bar}$), gas ($Y_{\rm gas}$), hot gas phase ($Y_{\rm hot}$), cold gas phase ($Y_{\rm cold}$) and stellar ($Y_{\rm star}$) depletion parameters and gas metallicity (Z_{tot}) computed at four different radii ($1, 3, 5$ and 10 times $R_{500,\rm c}$) for the less massive sub-sample (left side) and the most massive one (right side), in each of the four different redshifts ($2.79, 1.70, 0.67$ and 0.25). Errors are given as 16th and 84th distributions percentiles. Note that the depletion parameters are computed within the given radii, differently from the metallicity values which are given within a spherical shell (considering the same reference radii).

Bibliography

Adhikari Susmita, Dalal Neal, Chamberlain Robert T. Splashback in accreting dark matter halos // J. Cosmology Astropart. Phys.. XI 2014. 2014, 11. 019–019.

Akino Daichi, Eckert Dominique, Okabe Nobuhiro, Sereno Mauro, Umetsu Keiichi, Oguri Masamune, Gastaldello Fabio, Chiu I. Non, Ettori Stefano, Evrard August E., Farahi Arya, Maughan Ben, Pierre Marguerite, Ricci Marina, Valtchanov Ivan, McCarthy Ian, McGee Sean, Miyazaki Satoshi, Nishizawa Atsushi J., Tanaka Masayuki. HSC-XXL: Baryon budget of the 136 XXL groups and clusters // PASJ. II 2022. 74, 1. 175–208.

Allen Steven W., Evrard August E., Mantz Adam B. Cosmological Parameters from Observations of Galaxy Clusters // ARA&A. IX 2011. 49, 1. 409–470.

Anders E., Grevesse N. Abundances of the elements: Meteoritic and solar // Geochimica Cosmochimica Acta. I 1989. 53, 1. 197–214.

Angelinelli M., Ettori S., Dolag K., Vazza F., Ragagnin A. Mapping 'out-of-the-box' the properties of the baryons in massive halos // A&A. VII 2022. 663. L6.

Angelinelli M., Ettori S., Vazza F., Jones T. W. Proprieties of clumps and filaments around galaxy clusters // A&A. IX 2021. 653. A171.

Angelinelli M., Vazza F., Giocoli C., Ettori S., Jones T. W., Brunetti G., Brüggen M., Eckert D. Turbulent pressure support and hydrostatic mass bias in the intracluster medium // MNRAS. IV 2020. 495, 1. 864–885.

Arnaud K. A. XSPEC: The First Ten Years // Astronomical Data Analysis Software and Systems V. 101. I 1996. 17. (Astronomical Society of the Pacific Conference Series).

Asplund Martin, Grevesse Nicolas, Sauval A. Jacques, Scott Pat. The Chemical Composition of the Sun // ARA&A. IX 2009. 47, 1. 481–522.

Aung Han, Nagai Daisuke, Lau Erwin T. Shock and splash: gas and dark matter halo boundaries around ΛCDM galaxy clusters // MNRAS. XII 2021. 508, 2. 2071–2078.

Ayromlou Mohammadreza, Nelson Dylan, Pillepich Annalisa. Feedback reshapes the baryon distribution within haloes, in halo outskirts, and beyond: the closure radius from dwarfs to massive clusters // arXiv e-prints. XI 2022. arXiv:2211.07659.

Barret Didier, Lam Trong Thien, den Herder Jan-Willem, Piro Luigi, Cappi Massimo, Houvelin Juhani, Kelley Richard, Mas-Hesse J. Miguel, Mitsuda Kazuhisa, Paltani Stéphane, Rauw Gregor, Rozanska Agata, Wilms Joern, Bandler Simon, Barbera Marco, Barcons Xavier, Bozzo Enrico, Ceballos Maria Teresa, Charles Ivan, Costantini Elisa, Decourchelle Anne, den Hartog Roland, Duband Lionel, Duval Jean-Marc, Fiore Fabrizio, Gatti Flavio, Goldwurm Andrea, Jackson Brian, Jonker Peter, Kilbourne Caroline, Macculi Claudio, Mendez Mariano, Molendi Silvano, Orleanski Piotr, Pajot François, Pointecouteau Etienne, Porter Frederick, Pratt Gabriel W., Prêle Damien, Ravera Laurent, Sato Kosuke, Schaye Joop, Shinozaki Keisuke, Thibert Tanguy, Valenziano Luca, Valette Véronique, Vink Jacco, Webb Natalie, Wise Michael, Yamasaki Noriko, Douchin Françoise, Mesnager Jean-Michel, Pontet Bernard, Pradines Alice, Branduardi-Raymont Graziella, Bulbul Esra, Dadina Mauro, Ettori Stefano, Finoguenov Alexis, Fukazawa Yasushi, Janiuk Agnieszka, Kaastra Jelle, Mazzotta Pasquale, Miller Jon, Miniutti Giovanni, Naze Yael, Nicastro Fabrizio, Scioritino Salavtore, Simonescu Aurora, Torrejon Jose Miguel, Frezouls Benoit, Geoffray Hervé, Peille Philippe, Aicardi Corinne, André Jérôme, Daniel Christophe, Clénet Antoine, Etcheverry Christophe, Gloaguen Emilie, Hervet Gilles, Jolly Antoine, Ledot Aurélien, Paillet Irwin, Schmisser Roseline, Vella Bruno, Damery Jean-Charles, Boyce Kevin, Dipirro Mike, Lotti Simone, Schwander Denis, Smith Stephen, Van Leeuwen Bert-Joost, van Weers Henk, Clerc Nicolas, Cobo Beatriz, Dauser Thomas, Kirsch Christian, Cucchetti Edoardo, Eckart Megan, Ferrando Philippe, Natalucci Lorenzo. The ATHENA X-ray Integral Field Unit (X-IFU) // Space Telescopes and Instrumentation 2018: Ultraviolet to Gamma Ray. 10699. VII 2018. 106991G. (Society of Photo-Optical Instrumentation Engineers (SPIE) Conference Series).

Beck A. M., Murante G., Arth A., Remus R. S., Teklu A. F., Donnert J. M. F., Planelles S., Beck M. C., Förster P., Imgrund M., Dolag K., Borgani S. An improved SPH scheme for cosmological simulations // MNRAS. I 2016. 455, 2. 2110–2130.

Bertschinger E. Self-similar secondary infall and accretion in an Einstein-de Sitter universe // ApJS. V 1985. 58. 39–65.

Biffi V., Borgani S., Murante G., Rasia E., Planelles S., Granato G. L., Ragone-Figueroa C., Beck A. M., Gaspari M., Dolag K. On the Nature of Hydrostatic Equilibrium in Galaxy Clusters // ApJ. VIII 2016a. 827. 112.

Biffi V., Borgani S., Murante G., Rasia E., Planelles S., Granato G. L., Ragone-Figueroa C., Beck A. M., Gaspari M., Dolag K. On the Nature of Hydrostatic Equilibrium in Galaxy Clusters // ApJ. VIII 2016b. 827. 112.

Biffi V., Dolag K., Böhringer H. Investigating the velocity structure and X-ray observable properties of simulated galaxy clusters with PHOX // MNRAS. I

2013. 428, 2. 1395–1409.

Biffi V., Dolag K., Merloni A. AGN contamination of galaxy-cluster thermal X-ray emission: predictions for eRosita from cosmological simulations // MNRAS. XII 2018a. 481, 2. 2213–2227.

Biffi V., Mernier F., Medvedev P. Enrichment of the Hot Intracluster Medium: Numerical Simulations // Space Sci. Rev.. XII 2018b. 214, 8. 123.

Biffi V., Planelles S., Borgani S., Fabjan D., Rasia E., Murante G., Tornatore L., Dolag K., Granato G. L., Gaspari M., Beck A. M. The history of chemical enrichment in the intracluster medium from cosmological simulations // MNRAS. VI 2017. 468, 1. 531–548.

Biffi V., Planelles S., Borgani S., Rasia E., Murante G., Fabjan D., Gaspari M. The origin of ICM enrichment in the outskirts of present-day galaxy clusters from cosmological hydrodynamical simulations // MNRAS. V 2018c. 476, 2. 2689–2703.

Biffi Veronica, Dolag Klaus, Reiprich Thomas H., Veronica Angie, Ramos-Ceja Miriam E., Bulbul Esra, Ota Naomi, Ghirardini Vittorio. The eROSITA view of the Abell 3391/95 field: Case study from the Magneticum cosmological simulation // A&A. V 2022. 661. A17.

Binney James, Tremaine Scott. Galactic Dynamics: Second Edition. 2008.

Bonafede A., Brüggen M., Rafferty D., Zhuravleva I., Riseley C. J., van Weeren R. J., Farnes J. S., Vazza F., Savini F., Wilber A., Botteon A., Brunetti G., Cassano R., Ferrari C., de Gasperin F., Orrú E., Pizzo R. F., Röttgering H. J. A., Shimwell T. W. LOFAR discoveryof radio emission in MACS J0717.5+3745 // MNRAS. VIII 2018. 478. 2927–2938.

Bonafede A., Feretti L., Murgia M., Govoni F., Giovannini G., Dallacasa D., Dolag K., Taylor G. B. The Coma cluster magnetic field from Faraday rotation measures // A&A. IV 2010. 513. A30+.

Bond J. Richard, Kofman Lev, Pogosyan Dmitry. How filaments of galaxies are woven into the cosmic web // Nature. IV 1996. 380, 6575. 603–606.

Bonjean V., Aghanim N., Salomé P., Douspis M., Beelen A. Gas and galaxies in filaments between clusters of galaxies. The study of A399-A401 // A&A. I 2018. 609. A49.

Bourne Martin A., Sijacki Debora. AGN jet feedback on a moving mesh: cocoon inflation, gas flows and turbulence // MNRAS. XII 2017. 472, 4. 4707–4735.

Branchini E., Ursino E., Corsi A., Martizzi D., Amati L., den Herder J. W., Galeazzi M., Gendre B., Kaastra J., Moscardini L., Nicastro F., Ohashi T., Paerels F., Piro L., Roncarelli M., Takei Y., Viel M. Studying the Warm Hot Intergalactic Medium with Gamma-Ray Bursts // ApJ. V 2009. 697, 1. 328–344.

Brighenti F., Mathews W. G. Heated Cooling Flows // ApJ. VII 2002. 573. 542–561.

Brüggen M. Equilibrium Models of Galaxy Clusters with Cooling, Heating, and Conduction // ApJ. VIII 2003. 593. 700–704.

Brüggen M., Hoeft M., Ruszkowski M. X-Ray Line Tomography of AGN-induced Motion in Clusters of Galaxies // ApJ. VII 2005. 628. 153–159.

Brunetti G., Jones T. W. Cosmic Rays in Galaxy Clusters and Their Nonthermal Emission // International Journal of Modern Physics D. III 2014. 23. 1430007–98.

Brunetti G., Lazarian A. Acceleration of primary and secondary particles in galaxy clusters by compressible MHD turbulence: from radio haloes to gamma-rays // MNRAS. I 2011. 410. 127–142.

Brunetti Gianfranco, Vazza Franco. Second-order Fermi Reacceleration Mechanisms and Large-Scale Synchrotron Radio Emission in Intracluster Bridges // Phys. Rev. Lett.. Feb 2020. 124, 5. 051101.

Bryan G. L., Norman M. L., O'Shea B. W., Abel T., Wise J. H., Turk M. J., Reynolds D. R., Collins D. C., Wang P., Skillman S. W., Smith B., Harkness R. P., Bordner J., Kim J.-h., Kuhlen M., Xu H., Goldbaum N., Hummels C., Kritsuk A. G., Tasker E., Skory S., Simpson C. M., Hahn O., Oishi J. S., So G. C., Zhao F., Cen R., Li Y., Enzo Collaboration . ENZO: An Adaptive Mesh Refinement Code for Astrophysics // ApJS. IV 2014. 211. 19.

Bryan G. L., Norman M. L., Stone J. M., Cen R., Ostriker J. P. A piecewise parabolic method for cosmological hydrodynamics // Computer Physics Communications. VIII 1995. 89. 149–168.

Bryan Greg L., Norman Michael L. Statistical Properties of X-Ray Clusters: Analytic and Numerical Comparisons // ApJ. III 1998. 495, 1. 80–99.

Bulbul Esra, Randall Scott W., Bayliss Matthew, Miller Eric, Andrade-Santos Felipe, Johnson Ryan, Bautz Mark, Blanton Elizabeth L., Forman William R., Jones Christine, Paterno-Mahler Rachel, Murray Stephen S., Sarazin Craig L., Smith Randall K., Ezer Cemile. Probing the Outskirts of the Early-Stage Galaxy Cluster Merger A1750 // ApJ. II 2016. 818, 2. 131.

Cassano R., Brunetti G. Cluster mergers and non-thermal phenomena: a statistical magneto-turbulent model // MNRAS. III 2005. 357. 1313–1329.

Castro Tiago, Borgani Stefano, Dolag Klaus, Marra Valerio, Quartin Miguel, Saro Alexandro, Sefusatti Emiliano. On the impact of baryons on the halo mass function, bias, and cluster cosmology // MNRAS. I 2021. 500, 2. 2316–2335.

Cautun M., van de Weygaert R., Jones B. J. T., Frenk C. S. Evolution of the cosmic web // MNRAS. VII 2014. 441. 2923–2973.

Cen Renyue, Ostriker Jeremiah P. Where Are the Baryons? // ApJ. III 1999. 514, 1. 1–6.

Chiu I., Mohr J., McDonald M., Bocquet S., Ashby M. L. N., Bayliss M., Ben-

son B. A., Bleem L. E., Brodwin M., Desai S., Dietrich J. P., Forman W. R., Gangkofner C., Gonzalez A. H., Hennig C., Liu J., Reichardt C. L., Saro A., Stalder B., Stanford S. A., Song J., Schrabback T., Šuhada R., Strazzullo V., Zenteno A. Baryon content of massive galaxy clusters at $0.57 < z < 1.33$ // MNRAS. I 2016. 455, 1. 258–275.

Churazov E., Khabibullin I., Lyskova N., Sunyaev R., Bykov A. M. Tempestuous life beyond R_{500}: X-ray view on the Coma cluster with SRG/eROSITA. I. X-ray morphology, recent merger, and radio halo connection // A&A. VII 2021. 651. A41.

Churazov E., Vikhlinin A., Zhuravleva I., Schekochihin A., Parrish I., Sunyaev R., Forman W., Böhringer H., Randall S. X-ray surface brightness and gas density fluctuations in the Coma cluster // MNRAS. IV 2012. 421. 1123–1135.

Clerc Nicolas, Cucchetti Edoardo, Pointecouteau Etienne, Peille Philippe. Towards mapping turbulence in the intra-cluster medium. I. Sample variance in spatially-resolved X-ray line diagnostics // A&A. IX 2019. 629. A143.

Colella P., Woodward P. R. // Journal of Computational Physics. IX 1984. 54. 174–201.

Connor Thomas, Zahedy Fakhri S., Chen Hsiao-Wen, Cooper Thomas J., Mulchaey John S., Vikhlinin Alexey. COS Observations of the Cosmic Web: A Search for the Cooler Components of a Hot, X-Ray Identified Filament // ApJ. X 2019. 884, 1. L20.

Corasaniti P. S., Achitouv I. Toward a Universal Formulation of the Halo Mass Function // Phys. Rev. Lett.. VI 2011. 106, 24. 241302.

Crain Robert A., Schaye Joop, Bower Richard G., Furlong Michelle, Schaller Matthieu, Theuns Tom, Dalla Vecchia Claudio, Frenk Carlos S., McCarthy Ian G., Helly John C., Jenkins Adrian, Rosas-Guevara Yetli M., White Simon D. M., Trayford James W. The EAGLE simulations of galaxy formation: calibration of subgrid physics and model variations // MNRAS. VI 2015. 450, 2. 1937–1961.

Cucchetti E., Clerc N., Pointecouteau E., Peille P., Pajot F. Towards mapping turbulence in the intra-cluster medium. II. Measurement uncertainties in the estimation of structure functions // A&A. IX 2019. 629. A144.

Danforth Charles W., Shull J. Michael. The Low-z Intergalactic Medium. I. O VI Baryon Census // ApJ. V 2005. 624, 2. 555–560.

Dauser Thomas, Falkner Sebastian, Lorenz Maximilian, Kirsch Christian, Peille Philippe, Cucchetti Edoardo, Schmid Christian, Brand Thorsten, Oertel Mirjam, Smith Randall, Wilms Jörn. SIXTE: a generic X-ray instrument simulation toolkit // A&A. IX 2019. 630. A66.

Davé Romeel, Anglés-Alcázar Daniel, Narayanan Desika, Li Qi, Rafieferantsoa

Mika H., Appleby Sarah. SIMBA: Cosmological simulations with black hole growth and feedback // MNRAS. VI 2019. 486, 2. 2827–2849.

Davé Romeel, Cen Renyue, Ostriker Jeremiah P., Bryan Greg L., Hernquist Lars, Katz Neal, Weinberg David H., Norman Michael L., O'Shea Brian. Baryons in the Warm-Hot Intergalactic Medium // ApJ. V 2001. 552, 2. 473–483.

Davies Jonathan J., Crain Robert A., Oppenheimer Benjamin D., Schaye Joop. The quenching and morphological evolution of central galaxies is facilitated by the feedback-driven expulsion of circumgalactic gas // MNRAS. I 2020. 491, 3. 4462–4480.

De Boni C., Serra A. L., Diaferio A., Giocoli C., Baldi M. The Mass Accretion Rate of Galaxy Clusters: A Measurable Quantity // ApJ. II 2016. 818. 188.

Dehnen Walter, Aly Hossam. Improving convergence in smoothed particle hydrodynamics simulations without pairing instability // MNRAS. IX 2012. 425, 2. 1068–1082.

Desjacques Vincent. Environmental dependence in the ellipsoidal collapse model // MNRAS. VIII 2008. 388, 2. 638–658.

Despali G., Giocoli C., Angulo R. E., Tormen G., Sheth R. K., Baso G., Moscardini L. The universality of the virial halo mass function and models for non-universality of other halo definitions // MNRAS. III 2016. 456. 2486–2504.

Dolag K., Borgani S., Murante G., Springel V. Substructures in hydrodynamical cluster simulations // MNRAS. X 2009. 399, 2. 497–514.

Dolag K., Borgani S., Schindler S., Diaferio A., Bykov A. M. Simulation Techniques for Cosmological Simulations // Space Sci. Rev.. II 2008. 134, 1-4. 229–268.

Dolag K., Hansen F. K., Roncarelli M., Moscardini L. The imprints of local superclusters on the Sunyaev-Zel'dovich signals and their detectability with Planck // MNRAS. X 2005a. 363, 1. 29–39.

Dolag K., Jubelgas M., Springel V., Borgani S., Rasia E. Thermal Conduction in Simulated Galaxy Clusters // ApJ. V 2004. 606, 2. L97–L100.

Dolag K., Komatsu E., Sunyaev R. SZ effects in the Magneticum Pathfinder simulation: comparison with the Planck, SPT, and ACT results // MNRAS. XII 2016. 463, 2. 1797–1811.

Dolag K., Mevius E., Remus R.-S. Distribution and Evolution of Metals in the Magneticum Simulations // Galaxies. VIII 2017. 5. 35.

Dolag K., Schindler S., Govoni F., Feretti L. Correlation of the magnetic field and the intra-cluster gas density in galaxy clusters // A&A. XI 2001. 378. 777–786.

Dolag K., Stasyszyn F. An MHD GADGET for cosmological simulations // MNRAS. X 2009. 398. 1678–1697.

Dolag K., Vazza F., Brunetti G., Tormen G. // MNRAS. XII 2005b. 364. 753–772.

Dolag K., Vazza F., Brunetti G., Tormen G. Turbulent gas motions in galaxy cluster simulations: the role of smoothed particle hydrodynamics viscosity // MNRAS. XII 2005c. 364. 753–772.

Domínguez-Fernández P., Vazza F., Brüggen M., Brunetti G. Dynamical evolution of magnetic fields in the intracluster medium // MNRAS. VI 2019. 486. 623–638.

Donnert J., Vazza F., Brüggen M., ZuHone J. Magnetic Field Amplification in Galaxy Clusters and Its Simulation // Space Sci. Rev.. XII 2018. 214. 122.

Duffy Alan R., Schaye Joop, Kay Scott T., Dalla Vecchia Claudio, Battye Richard A., Booth C. M. Impact of baryon physics on dark matter structures: a detailed simulation study of halo density profiles // MNRAS. VII 2010. 405, 4. 2161–2178.

Eckert D., Ettori S., Coupon J., Gastaldello F., Pierre M., Melin J. B., Le Brun A. M. C., McCarthy I. G., Adami C., Chiappetti L., Faccioli L., Giles P., Lavoie S., Lefèvre J. P., Lieu M., Mantz A., Maughan B., McGee S., Pacaud F., Paltani S., Sadibekova T., Smith G. P., Ziparo F. The XXL Survey. XIII. Baryon content of the bright cluster sample // A&A. VI 2016. 592. A12.

Eckert D., Ettori S., Pointecouteau E., Molendi S., Paltani S., Tchernin C. The XMM cluster outskirts project (X-COP) // Astronomische Nachrichten. III 2017a. 338. 293–298.

Eckert D., Gaspari M., Vazza F., Gastaldello F., Tramacere A., Zimmer S., Ettori S., Paltani S. On the Connection between Turbulent Motions and Particle Acceleration in Galaxy Clusters // ApJ. VII 2017b. 843. L29.

Eckert D., Ghirardini V., Ettori S., Rasia E., Biffi V., Pointecouteau E., Rossetti M., Molendi S., Vazza F., Gastaldello F., Gaspari M., De Grandi S., Ghizzardi S., Bourdin H., Tchernin C., Roncarelli M. Non-thermal pressure support in X-COP galaxy clusters // A&A. Jan 2019. 621. A40.

Eckert D., Jauzac M., Shan H., Kneib J.-P., Erben T., Israel H., Jullo E., Klein M., Massey R., Richard J., Tchernin C. Warmhot baryons comprise 510 per cent of filaments in the cosmic web // Nature. XII 2015a. 528. 105–107.

Eckert D., Roncarelli M., Ettori S., Molendi S., Vazza F., Gastaldello F., Rossetti M. Gas clumping in galaxy clusters // MNRAS. III 2015b. 447, 3. 2198–2208.

Eckert Dominique, Gaspari Massimo, Gastaldello Fabio, Le Brun Amandine M. C., O'Sullivan Ewan. Feedback from Active Galactic Nuclei in Galaxy Groups // Universe. V 2021. 7, 5. 142.

Eckmiller H. J., Hudson D. S., Reiprich T. H. Testing the low-mass end of X-ray scaling relations with a sample of Chandra galaxy groups // A&A. XI 2011. 535. A105.

Einstein Albert. Die Feldgleichungen der Gravitation // Sitzungsberichte der

Königlich Preussischen Akademie der Wissenschaften. I 1915. 844–847.

Eke Vincent R., Cole Shaun, Frenk Carlos S. Cluster evolution as a diagnostic for Omega // MNRAS. IX 1996. 282. 263–280.

Ettori S. The physics inside the scaling relations for X-ray galaxy clusters: gas clumpiness, gas mass fraction and slope of the pressure profile // MNRAS. I 2015. 446, 3. 2629–2639.

Ettori S., Dolag K., Borgani S., Murante G. The baryon fraction in hydrodynamical simulations of galaxy clusters // MNRAS. I 2006. 365, 3. 1021–1030.

Ettori S., Eckert D. Tracing the non-thermal pressure and hydrostatic bias in galaxy clusters // A&A. I 2022. 657. L1.

Ettori S., Ghirardini V., Eckert D., Pointecouteau E., Gastaldello F., Sereno M., Gaspari M., Ghizzardi S., Roncarelli M., Rossetti M. Hydrostatic mass profiles in X-COP galaxy clusters // A&A. I 2019. 621. A39.

Ettori S., Lovisari L., Eckert D. $i(cm)z$, a semi-analytic model for the thermodynamic properties in galaxy clusters: calibrations with mass and redshift, and implication for the hydrostatic bias // arXiv e-prints. XI 2022. arXiv:2211.03082.

Fabian A. C. Observational Evidence of Active Galactic Nuclei Feedback // ARA&A. IX 2012. 50. 455–489.

Fabjan D., Borgani S., Tornatore L., Saro A., Murante G., Dolag K. Simulating the effect of active galactic nuclei feedback on the metal enrichment of galaxy clusters // MNRAS. I 2010. 401. 1670–1690.

Faltenbacher A., Allgood B., Gottlöber S., Yepes G., Hoffman Y. Imprints of mass accretion on properties of galaxy clusters // MNRAS. IX 2005. 362. 1099–1108.

Freeman P. E., Kashyap V., Rosner R., Lamb D. Q. A Wavelet-Based Algorithm for the Spatial Analysis of Poisson Data // ApJS. I 2002. 138, 1. 185–218.

Fryxell B., Olson K., Ricker P., Timmes F. X., Zingale M., Lamb D. Q., MacNeice P., Rosner R., Truran J. W., Tufo H. FLASH: An Adaptive Mesh Hydrodynamics Code for Modeling Astrophysical Thermonuclear Flashes // ApJS. XI 2000. 131, 1. 273–334.

Fusco-Femiano R. Results from the SuperModel Analysis of the X-COP Galaxy Clusters Sample // arXiv e-prints. II 2019.

Fusco-Femiano R., Lapi A. Non-thermal pressure in the outskirts of Abell 2142 // MNRAS. III 2018. 475. 1340–1346.

Galárraga-Espinosa Daniela, Aghanim Nabila, Langer Mathieu, Tanimura Hideki. Properties of gas phases around cosmic filaments at z=0 in the Illustris-TNG simulation // arXiv e-prints. X 2020. arXiv:2010.15139.

Galárraga-Espinosa Daniela, Langer Mathieu, Aghanim Nabila. Relative distribution of dark matter, gas, and stars around cosmic filaments in the IllustrisTNG

simulation // A&A. V 2022. 661. A115.

Gaspari M., Churazov E., Nagai D., Lau E. T., Zhuravleva I. The relation between gas density and velocity power spectra in galaxy clusters: High-resolution hydrodynamic simulations and the role of conduction // A&A. IX 2014. 569. A67.

Gaspari M., McDonald M., Hamer S. L., Brighenti F., Temi P., Gendron-Marsolais M., Hlavacek-Larrondo J., Edge A. C., Werner N., Tozzi P., Sun M., Stone J. M., Tremblay G. R., Hogan M. T., Eckert D., Ettori S., Yu H., Biffi V., Planelles S. Shaken Snow Globes: Kinematic Tracers of the Multiphase Condensation Cascade in Massive Galaxies, Groups, and Clusters // ApJ. II 2018. 854. 167.

Gaspari M., Melioli C., Brighenti F., D'Ercole A. The dance of heating and cooling in galaxy clusters: three-dimensional simulations of self-regulated active galactic nuclei outflows // MNRAS. II 2011. 411. 349–372.

Gastaldello Fabio, Simionescu Aurora, Mernier Francois, Biffi Veronica, Gaspari Massimo, Sato Kosuke, Matsushita Kyoko. The Metal Content of the Hot Atmospheres of Galaxy Groups // Universe. VI 2021. 7, 7. 208.

Gheller C., Vazza F. Convolutional deep denoising autoencoders for radio astronomical images // MNRAS. I 2022. 509, 1. 990–1009.

Ghirardini V., Eckert D., Ettori S., Pointecouteau E., Molendi S., Gaspari M., Rossetti M., De Grandi S., Roncarelli M., Bourdin H., Mazzotta P., Rasia E., Vazza F. Universal thermodynamic properties of the intracluster medium over two decades in radius in the X-COP sample // A&A. I 2019. 621. A41.

Ghirardini V., Ettori S., Eckert D., Molendi S., Gastaldello F., Pointecouteau E., Hurier G., Bourdin H. The XMM Cluster Outskirts Project (X-COP): Thermodynamic properties of the Intracluster Medium out to R_200 in Abell 2319 // ArXiv e-prints. VIII 2017.

Ghirardini V., Ettori S., Eckert D., Molendi S., Gastaldello F., Pointecouteau E., Hurier G., Bourdin H. The XMM Cluster Outskirts Project (X-COP): Thermodynamic properties of the intracluster medium out to R_{200} in Abell 2319 // A&A. VI 2018. 614. A7.

Ghizzardi Simona, Molendi Silvano, van der Burg Remco, De Grandi Sabrina, Bartalucci Iacopo, Gastaldello Fabio, Rossetti Mariachiara, Biffi Veronica, Borgani Stefano, Eckert Dominique, Ettori Stefano, Gaspari Massimo, Ghirardini Vittorio, Rasia Elena. Iron in X-COP: Tracing enrichment in cluster outskirts with high accuracy abundance profiles // A&A. II 2021. 646. A92.

Giocoli C., Tormen G., Sheth R. K. Formation times, mass growth histories and concentrations of dark matter haloes // MNRAS. V 2012a. 422. 185–198.

Giocoli C., Tormen G., Sheth R. K. Formation times, mass growth histories and concentrations of dark matter haloes // MNRAS. V 2012b. 422. 185–198.

Giocoli Carlo, Tormen Giuseppe, van den Bosch Frank C. The population of dark matter subhaloes: mass functions and average mass-loss rates // MNRAS. VI 2008. 386, 4. 2135–2144.

Godunov Sergei K., Bohachevsky I. Finite difference method for numerical computation of discontinuous solutions of the equations of fluid dynamics // Matematičeskij sbornik. 1959. 47(89), 3. 271–306.

Gonzalez Anthony H., Sivanandam Suresh, Zabludoff Ann I., Zaritsky Dennis. Galaxy Cluster Baryon Fractions Revisited // ApJ. XI 2013. 778, 1. 14.

Gunn James E., Gott III J. Richard. On the Infall of Matter Into Clusters of Galaxies and Some Effects on Their Evolution // ApJ. VIII 1972. 176. 1.

Gupta N., Saro A., Mohr J. J., Dolag K., Liu J. SZE observables, pressure profiles and centre offsets in Magneticum simulation galaxy clusters // MNRAS. VIII 2017. 469, 3. 3069–3087.

Guzzo L., Scodeggio M., Garilli B., Granett B. R., Fritz A., Abbas U., Adami C., Arnouts S., Bel J., Bolzonella M., Bottini D., Branchini E., Cappi A., Coupon J., Cucciati O., Davidzon I., De Lucia G., de la Torre S., Franzetti P., Fumana M., Hudelot P., Ilbert O., Iovino A., Krywult J., Le Brun V., Le Fèvre O., Maccagni D., Małek K., Marulli F., McCracken H. J., Paioro L., Peacock J. A., Polletta M., Pollo A., Schlagenhaufer H., Tasca L. A. M., Tojeiro R., Vergani D., Zamorani G., Zanichelli A., Burden A., Di Porto C., Marchetti A., Marinoni C., Mellier Y., Moscardini L., Nichol R. C., Percival W. J., Phleps S., Wolk M. The VIMOS Public Extragalactic Redshift Survey (VIPERS). An unprecedented view of galaxies and large-scale structure at $0.5 < z < 1.2$ // A&A. VI 2014. 566. A108.

Haider M., Steinhauser D., Vogelsberger M., Genel S., Springel V., Torrey P., Hernquist L. Large-scale mass distribution in the Illustris simulation // MNRAS. IV 2016. 457, 3. 3024–3035.

Hallman E. J., Motl P. M., Burns J. O., Norman M. L. Challenges for Precision Cosmology with X-Ray and Sunyaev-Zeldovich Effect Gas Mass Measurements of Galaxy Clusters // ApJ. IX 2006. 648. 852–867.

Henden Nicholas A., Puchwein Ewald, Shen Sijing, Sijacki Debora. The FABLE simulations: a feedback model for galaxies, groups, and clusters // MNRAS. X 2018. 479, 4. 5385–5412.

Henden Nicholas A., Puchwein Ewald, Sijacki Debora. The baryon content of groups and clusters of galaxies in the FABLE simulations // MNRAS. X 2020. 498, 2. 2114–2137.

Hirschmann Michaela, Dolag Klaus, Saro Alexandro, Bachmann Lisa, Borgani Stefano, Burkert Andreas. Cosmological simulations of black hole growth: AGN luminosities and downsizing // MNRAS. VIII 2014. 442, 3. 2304–2324.

Hitomi Collaboration , Aharonian F., Akamatsu H., Akimoto F., Allen S. W., Anabuki N., Angelini L., Arnaud K., Audard M., Awaki H., Axelsson M., Bamba A., Bautz M., Blandford R., Brenneman L., Brown G. V., Bulbul E., Cackett E., Chernyakova M., Chiao M., Coppi P., Costantini E., de Plaa J., den Herder J.-W., Done C., Dotani T., Ebisawa K., Eckart M., Enoto T., Ezoe Y., Fabian A. C., Ferrigno C., Foster A., Fujimoto R., Fukazawa Y., Furuzawa A., Galeazzi M., Gallo L., Gandhi P., Giustini M., Goldwurm A., Gu L., Guainazzi M., Haba Y., Hagino K., Hamaguchi K., Harrus I., Hatsukade I., Hayashi K., Hayashi T., Hayashida K., Hiraga J., Hornschemeier A., Hoshino A., Hughes J., Iizuka R., Inoue H., Inoue Y., Ishibashi K., Ishida M., Ishikawa K., Ishisaki Y., Itoh M., Iyomoto N., Kaastra J., Kallman T., Kamae T., Kara E., Kataoka J., Katsuda S., Katsuta J., Kawaharada M., Kawai N., Kelley R., Khangulyan D., Kilbourne C., King A., Kitaguchi T., Kitamoto S., Kitayama T., Kohmura T., Kokubun M., Koyama S., Koyama K., Kretschmar P., Krimm H., Kubota A., Kunieda H., Laurent P., Lebrun F., Lee S.-H., Leutenegger M., Limousin O., Loewenstein M., Long K. S., Lumb D., Madejski G., Maeda Y., Maier D., Makishima K., Markevitch M., Matsumoto H., Matsushita K., McCammon D., McNamara B., Mehdipour M., Miller E., Miller J., Mineshige S., Mitsuda K., Mitsuishi I., Miyazawa T., Mizuno T., Mori H., Mori K., Moseley H., Mukai K., Murakami H., Murakami T., Mushotzky R., Nagino R., Nakagawa T., Nakajima H., Nakamori T., Nakano T., Nakashima S., Nakazawa K., Nobukawa M., Noda H., Nomachi M., O'Dell S., Odaka H., Ohashi T., Ohno M., Okajima T., Ota N., Ozaki M., Paerels F., Paltani S., Parmar A., Petre R., Pinto C., Pohl M., Porter F. S., Pottschmidt K., Ramsey B., Reynolds C., Russell H., Safi-Harb S., Saito S., Sakai K., Sameshima H., Sato G., Sato K., Sato R., Sawada M., Schartel N., Serlemitsos P., Seta H., Shidatsu M., Simionescu A., Smith R., Soong Y., Stawarz L., Sugawara Y., Sugita S., Szymkowiak A., Tajima H., Takahashi H., Takahashi T., Takeda S., Takei Y., Tamagawa T., Tamura K., Tamura T., Tanaka T., Tanaka Y., Tanaka Y., Tashiro M., Tawara Y., Terada Y., Terashima Y., Tombesi F., Tomida H., Tsuboi Y., Tsujimoto M., Tsunemi H., Tsuru T., Uchida H., Uchiyama H., Uchiyama Y., Ueda S., Ueda Y., Ueno S., Uno S., Urry M., Ursino E., de Vries C., Watanabe S., Werner N., Wik D., Wilkins D., Williams B., Yamada S., Yamaguchi H., Yamaoka K., Yamasaki N. Y., Yamauchi M., Yamauchi S., Yaqoob T., Yatsu Y., Yonetoku D., Yoshida A., Yuasa T., Zhuravleva I., Zoghbi A. The quiescent intracluster medium in the core of the Perseus cluster // Nature. VII 2016. 535. 117–121.

Hitomi Collaboration , Aharonian Felix, Akamatsu Hiroki, Akimoto Fumie, Allen Steven W., Angelini Lorella, Audard Marc, Awaki Hisamitsu, Axelsson Magnus, Bamba Aya, Bautz Marshall W., Blandford Roger, Brenneman Laura W., Brown Gregory V., Bulbul Esra, Cackett Edward M., Canning Rebecca E. A.,

Chernyakova Maria, Chiao Meng P., Coppi Paolo S., Costantini Elisa, de Plaa Jelle, de Vries Cor P., den Herder Jan-Willem, Done Chris, Dotani Tadayasu, Ebisawa Ken, Eckart Megan E., Enoto Teruaki, Ezoe Yuichiro, Fabian Andrew C., Ferrigno Carlo, Foster Adam R., Fujimoto Ryuichi, Fukazawa Yasushi, Furuzawa Akihiro, Galeazzi Massimiliano, Gallo Luigi C., Gandhi Poshak, Giustini Margherita, Goldwurm Andrea, Gu Liyi, Guainazzi Matteo, Haba Yoshito, Hagino Kouichi, Hamaguchi Kenji, Harrus Ilana M., Hatsukade Isamu, Hayashi Katsuhiro, Hayashi Takayuki, Hayashi Tasuku, Hayashida Kiyoshi, Hiraga Junko S., Hornschemeier Ann, Hoshino Akio, Hughes John P., Ichinohe Yuto, Iizuka Ryo, Inoue Hajime, Inoue Shota, Inoue Yoshiyuki, Ishida Manabu, Ishikawa Kumi, Ishisaki Yoshitaka, Iwai Masachika, Kaastra Jelle, Kallman Tim, Kamae Tsuneyoshi, Kataoka Jun, Katsuda Satoru, Kawai Nobuyuki, Kelley Richard L., Kilbourne Caroline A., Kitaguchi Takao, Kitamoto Shunji, Kitayama Tetsu, Kohmura Takayoshi, Kokubun Motohide, Koyama Katsuji, Koyama Shu, Kretschmar Peter, Krimm Hans A., Kubota Aya, Kunieda Hideyo, Laurent Philippe, Lee Shiu-Hang, Leutenegger Maurice A., Limousin Olivier, Loewenstein Michael, Long Knox S., Lumb David, Madejski Greg, Maeda Yoshitomo, Maier Daniel, Makishima Kazuo, Markevitch Maxim, Matsumoto Hironori, Matsushita Kyoko, McCammon Dan, McNamara Brian R., Mehdipour Missagh, Miller Eric D., Miller Jon M., Mineshige Shin, Mitsuda Kazuhisa, Mitsuishi Ikuyuki, Miyazawa Takuya, Mizuno Tsunefumi, Mori Hideyuki, Mori Koji, Mukai Koji, Murakami Hiroshi, Mushotzky Richard F., Nakagawa Takao, Nakajima Hiroshi, Nakamori Takeshi, Nakashima Shinya, Nakazawa Kazuhiro, Nobukawa Kumiko K., Nobukawa Masayoshi, Noda Hirofumi, Odaka Hirokazu, Ohashi Takaya, Ohno Masanori, Okajima Takashi, Ota Naomi, Ozaki Masanobu, Paerels Frits, Paltani Stéphane, Petre Robert, Pinto Ciro, Porter Frederick S., Pottschmidt Katja, Reynolds Christopher S., Safi-Harb Samar, Saito Shinya, Sakai Kazuhiro, Sasaki Toru, Sato Goro, Sato Kosuke, Sato Rie, Sawada Makoto, Schartel Norbert, Serlemtsos Peter J., Seta Hiromi, Shidatsu Megumi, Simionescu Aurora, Smith Randall K., Soong Yang, Stawarz Łukasz, Sugawara Yasuharu, Sugita Satoshi, Szymkowiak Andrew, Tajima Hiroyasu, Takahashi Hiromitsu, Takahashi Tadayuki, Takeda Shin'ichiro, Takei Yoh, Tamagawa Toru, Tamura Takayuki, Tanaka Keigo, Tanaka Takaaki, Tanaka Yasuo, Tanaka Yasuyuki T., Tashiro Makoto S., Tawara Yuzuru, Terada Yukikatsu, Terashima Yuichi, Tombesi Francesco, Tomida Hiroshi, Tsuboi Yohko, Tsujimoto Masahiro, Tsunemi Hiroshi, Tsuru Takeshi Go, Uchida Hiroyuki, Uchiyama Hideki, Uchiyama Yasunobu, Ueda Shutaro, Ueda Yoshihiro, Uno Shin'ichiro, Urry C. Megan, Ursino Eugenio, Wang Qian H. S., Watanabe Shin, Werner Norbert, Wilkins Dan R., Williams Brian J., Yamada Shinya, Yamaguchi Hiroya, Yamaoka Kazutaka, Yamasaki Noriko Y., Yamauchi Makoto, Yamauchi Shigeo, Yaqoob Tahir, Yatsu

Yoichi, Yonetoku Daisuke, Zhuravleva Irina, Zoghbi Abderahmen. Atmospheric gas dynamics in the Perseus cluster observed with Hitomi // PASJ. Mar 2018. 70, 2. 9.

Huchra John P., Macri Lucas M., Masters Karen L., Jarrett Thomas H., Berlind Perry, Calkins Michael, Crook Aidan C., Cutri Roc, Erdoğdu Pirin, Falco Emilio, George Teddy, Hutcheson Conrad M., Lahav Ofer, Mader Jeff, Mink Jessica D., Martimbeau Nathalie, Schneider Stephen, Skrutskie Michael, Tokarz Susan, Westover Michael. The 2MASS Redshift Survey—Description and Data Release // ApJS. IV 2012. 199, 2. 26.

Ishisaki Y., Ezoe Y., Yamada S., Ichinohe Y., Fujimoto R., Takei Y., Yasuda S., Ishida M., Yamasaki N. Y., Maeda Y., Tsujimoto M., Iizuka R., Koyama S., Noda H., Tamagawa T., Sawada M., Sato K., Kitamoto S., Hoshino A., Brown G. V., Eckart M. E., Hayashi T., Kelley R. L., Kilbourne C. A., Leutenegger M. A., Mori H., Okajima T., Porter F. S., Soong Y., McCammon D., Szymkowiak A. E. Resolve Instrument on X-ray Astronomy Recovery Mission (XARM) // Journal of Low Temperature Physics. XII 2018. 193, 5-6. 991–995.

Jee M. J., Dawson K. S., Hoekstra H., Perlmutter S., Rosati P., Brodwin M., Suzuki N., Koester B., Postman M., Lubin L., Meyers J., Stanford S. A., Barbary K., Barrientos F., Eisenhardt P., Ford H. C., Gilbank D. G., Gladders M. D., Gonzalez A., Harris D. W., Huang X., Lidman C., Rykoff E. S., Rubin D., Spadafora A. L. Scaling Relations and Overabundance of Massive Clusters at z ˜ 1 from Weak-lensing Studies with the Hubble Space Telescope // ApJ. VIII 2011. 737. 59.

Kaiser N. Evolution and clustering of rich clusters // MNRAS. IX 1986. 222. 323–345.

Kay S. T., Thomas P. A., Jenkins A., Pearce F. R. Cosmological simulations of the intracluster medium // MNRAS. XII 2004. 355. 1091–1104.

Kitayama T., Bautz M., Markevitch M., Matsushita K., Allen S., Kawaharada M., McNamara B., Ota N., Akamatsu H., de Plaa J., Galeazzi M., Madejski G., Main R., Miller E., Nakazawa K., Russell H., Sato K., Sekiya N., Simionescu A., Tamura T., Uchida Y., Ursino E., Werner N., Zhuravleva I., ZuHone J. ASTRO-H White Paper - Clusters of Galaxies and Related Science // arXiv e-prints. XII 2014. arXiv:1412.1176.

Kolmogorov A. The Local Structure of Turbulence in Incompressible Viscous Fluid for Very Large Reynolds' Numbers // Akademiia Nauk SSSR Doklady. 1941. 30. 301–305.

Komatsu E., Smith K. M., Dunkley J., Bennett C. L., Gold B., Hinshaw G., Jarosik N., Larson D., Nolta M. R., Page L., Spergel D. N., Halpern M., Hill R. S., Kogut A., Limon M., Meyer S. S., Odegard N., Tucker G. S., Weiland J. L., Wollack

E., Wright E. L. Seven-year Wilkinson Microwave Anisotropy Probe (WMAP) Observations: Cosmological Interpretation // ApJS. II 2011. 192. 18.

Kravtsov Andrey V., Borgani Stefano. Formation of Galaxy Clusters // ARA&A. IX 2012. 50. 353–409.

Kravtsov Andrey V., Nagai Daisuke, Vikhlinin Alexey A. Effects of Cooling and Star Formation on the Baryon Fractions in Clusters // ApJ. VI 2005. 625, 2. 588–598.

Lapi A., Cavaliere A., Menci N. Intracluster and Intragroup Entropy from Quasar Activity // ApJ. I 2005. 619, 1. 60–72.

Lau E. T., Kravtsov A. V., Nagai D. Residual Gas Motions in the Intracluster Medium and Bias in Hydrostatic Measurements of Mass Profiles of Clusters // ApJ. XI 2009. 705. 1129–1138.

Lau Erwin T., Gaspari Massimo, Nagai Daisuke, Coppi Paolo. Physical Origins of Gas Motions in Galaxy Cluster Cores: Interpreting Hitomi Observations of the Perseus Cluster // ApJ. XI 2017. 849, 1. 54.

Libeskind Noam I., van de Weygaert Rien, Cautun Marius, Falck Bridget, Tempel Elmo, Abel Tom, Alpaslan Mehmet, Aragón-Calvo Miguel A., Forero-Romero Jaime E., Gonzalez Roberto, Gottlöber Stefan, Hahn Oliver, Hellwing Wojciech A., Hoffman Yehuda, Jones Bernard J. T., Kitaura Francisco, Knebe Alexander, Manti Serena, Neyrinck Mark, Nuza Sebastián E., Padilla Nelson, Platen Erwin, Ramachandra Nesar, Robotham Aaron, Saar Enn, Shand arin Sergei, Steinmetz Matthias, Stoica Radu S., Sousbie Thierry, Yepes Gustavo. Tracing the cosmic web // MNRAS. I 2018. 473, 1. 1195–1217.

Limber D. Nelson. Effects of Intracluster Gas and Duct upon the Virial Theorem. // ApJ. IX 1959. 130. 414.

Lotz Marcel, Dolag Klaus, Remus Rhea-Silvia, Burkert Andreas. Rise and fall of post-starburst galaxies in Magneticum Pathfinder // MNRAS. IX 2021. 506, 3. 4516–4542.

Lotz Marcel, Remus Rhea-Silvia, Dolag Klaus, Biviano Andrea, Burkert Andreas. Gone after one orbit: How cluster environments quench galaxies // MNRAS. X 2019. 488, 4. 5370–5389.

Lovisari L., Reiprich T. H., Schellenberger G. Scaling properties of a complete X-ray selected galaxy group sample // A&A. I 2015. 573. A118.

Lustig Peter, Strazzullo Veronica, Remus Rhea-Silvia, D'Eugenio Chiara, Daddi Emanuele, Burkert Andreas, De Lucia Gabriella, Delvecchio Ivan, Dolag Klaus, Fontanot Fabio, Gobat Raphael, Mohr Joseph J., Onodera Masato, Pannella Maurilio, Pillepich Annalisa, Renzini Alvio. Massive quiescent galaxies at $z \sim 3$: a comparison of selection, stellar population and structural properties with simulation predictions // arXiv e-prints. I 2022. arXiv:2201.09068.

Martizzi Davide, Vogelsberger Mark, Artale Maria Celeste, Haider Markus, Torrey Paul, Marinacci Federico, Nelson Dylan, Pillepich Annalisa, Weinberger Rainer, Hernquist Lars, Naiman Jill, Springel Volker. Baryons in the Cosmic Web of IllustrisTNG - I: gas in knots, filaments, sheets, and voids // MNRAS. VII 2019. 486, 3. 3766–3787.

Maughan B. J., Jones L. R., Ebeling H., Scharf C. The evolution of the cluster X-ray scaling relations in the Wide Angle ROSAT Pointed Survey sample at 0.6 z 1.0 // MNRAS. I 2006. 365. 509–529.

Mazzotta P., Rasia E., Moscardini L., Tormen G. Comparing the temperatures of galaxy clusters from hydrodynamical N-body simulations to Chandra and XMM-Newton observations // MNRAS. Oct 2004. 354, 1. 10–24.

McCarthy Ian G., Schaye Joop, Bird Simeon, Le Brun Amandine M. C. The BAHAMAS project: calibrated hydrodynamical simulations for large-scale structure cosmology // MNRAS. III 2017. 465, 3. 2936–2965.

Mernier F., de Plaa J., Werner N., Kaastra J. S., Raassen A. J. J., Gu L., Mao J., Urdampilleta I., Truong N., Simionescu A. Mass-invariance of the iron enrichment in the hot haloes of massive ellipticals, groups, and clusters of galaxies // MNRAS. VII 2018. 478, 1. L116–L121.

Miniati F. The Matryoshka Run: A Eulerian Refinement Strategy to Study the Statistics of Turbulence in Virialized Cosmic Structures // ApJ. II 2014. 782. 21.

Minkowski H. Das Relativitätsprinzip // Annalen der Physik. I 1915. 352, 15. 927–938.

Monaghan J. J. Smoothed particle hydrodynamics. // ARA&A. I 1992. 30. 543–574.

Monaghan J. J. SPH and Riemann Solvers // Journal of Computational Physics. IX 1997. 136, 2. 298–307.

Monaghan J. J., Gingold R. A. Shock Simulation by the Particle Method SPH // Journal of Computational Physics. XI 1983. 52, 2. 374–389.

Morandi A., Limousin M., Rephaeli Y., Umetsu K., Barkana R., Broadhurst T., Dahle H. Triaxiality and non-thermal gas pressure in Abell 1689 // MNRAS. X 2011. 416. 2567–2573.

Mostoghiu Robert, Arthur Jake, Pearce Frazer R., Gray Meghan, Knebe Alexander, Cui Weiguang, Welker Charlotte, Cora Sofía A., Murante Giuseppe, Dolag Klaus, Yepes Gustavo. The Three Hundred Project: The gas disruption of infalling objects in cluster environments // MNRAS. I 2021.

Murgia M., Govoni F., Feretti L., Giovannini G., Dallacasa D., Fanti R., Taylor G. B., Dolag K. Magnetic fields and Faraday rotation in clusters of galaxies // A&A. IX 2004. 424. 429–446.

Naab Thorsten, Ostriker Jeremiah P. Theoretical Challenges in Galaxy Formation

// ARA&A. VIII 2017. 55, 1. 59–109.

Nagai D., Kravtsov A. V., Vikhlinin A. Effects of Galaxy Formation on Thermodynamics of the Intracluster Medium // ApJ. X 2007. 668. 1–14.

Nagai D., Lau E. T. Gas Clumping in the Outskirts of ΛCDM Clusters // ApJ. IV 2011. 731. L10.

Nelson Dylan, Pillepich Annalisa, Springel Volker, Weinberger Rainer, Hernquist Lars, Pakmor Rüdiger, Genel Shy, Torrey Paul, Vogelsberger Mark, Kauffmann Guinevere, Marinacci Federico, Naiman Jill. First results from the IllustrisTNG simulations: the galaxy colour bimodality // MNRAS. III 2018. 475, 1. 624–647.

Nelson Dylan, Springel Volker, Pillepich Annalisa, Rodriguez-Gomez Vicente, Torrey Paul, Genel Shy, Vogelsberger Mark, Pakmor Ruediger, Marinacci Federico, Weinberger Rainer, Kelley Luke, Lovell Mark, Diemer Benedikt, Hernquist Lars. The IllustrisTNG simulations: public data release // Computational Astrophysics and Cosmology. V 2019. 6, 1. 2.

Nelson K., Lau E. T., Nagai D. Hydrodynamic Simulation of Non-thermal Pressure Profiles of Galaxy Clusters // ApJ. IX 2014a. 792. 25.

Nelson Kaylea, Lau Erwin T., Nagai Daisuke, Rudd Douglas H., Yu Liang. Weighing Galaxy Clusters with Gas. II. On the Origin of Hydrostatic Mass Bias in ΛCDM Galaxy Clusters // ApJ. Feb 2014b. 782, 2. 107.

Nicastro F., Kaastra J., Krongold Y., Borgani S., Branchini E., Cen R., Dadina M., Danforth C. W., Elvis M., Fiore F., Gupta A., Mathur S., Mayya D., Paerels F., Piro L., Rosa-Gonzalez D., Schaye J., Shull J. M., Torres-Zafra J., Wijers N., Zappacosta L. Observations of the missing baryons in the warm-hot intergalactic medium // Nature. VI 2018. 558, 7710. 406–409.

Nugent Jenna M., Dai Xinyu, Sun Ming. Suzaku Measurements of Hot Halo Emission at Outskirts for Two Poor Galaxy Groups: NGC 3402 and NGC 5129 // ApJ. VIII 2020. 899, 2. 160.

Okabe Nobuhiro, Futamase Toshifumi, Kajisawa Masaru, Kuroshima Risa. Subaru Weak-lensing Survey of Dark Matter Subhalos in the Coma Cluster: Subhalo Mass Function and Statistical Properties // ApJ. IV 2014. 784, 2. 90.

Oppenheimer Benjamin D., Babul Arif, Bahé Yannick, Butsky Iryna S., McCarthy Ian G. Simulating Groups and the IntraGroup Medium: The Surprisingly Complex and Rich Middle Ground between Clusters and Galaxies // Universe. VI 2021. 7, 7. 209.

Ota N., Nagai D., Lau E. T. Constraining hydrostatic mass bias of galaxy clusters with high-resolution X-ray spectroscopy // PASJ. VI 2018. 70. 51.

Overzier Roderik A. The realm of the galaxy protoclusters. A review // A&ARv. XI 2016. 24, 1. 14.

Parrish I. J., McCourt M., Quataert E., Sharma P. Turbulent pressure support in the outer parts of galaxy clusters // MNRAS. I 2012. 419. L29–L33.

Peebles P. J. E. Large-scale background temperature and mass fluctuations due to scale-invariant primeval perturbations // ApJ. XII 1982. 263. L1–L5.

Pillepich Annalisa, Nelson Dylan, Hernquist Lars, Springel Volker, Pakmor Rüdiger, Torrey Paul, Weinberger Rainer, Genel Shy, Naiman Jill P., Marinacci Federico, Vogelsberger Mark. First results from the IllustrisTNG simulations: the stellar mass content of groups and clusters of galaxies // MNRAS. III 2018a. 475, 1. 648–675.

Pillepich Annalisa, Nelson Dylan, Hernquist Lars, Springel Volker, Pakmor Rüdiger, Torrey Paul, Weinberger Rainer, Genel Shy, Naiman Jill P., Marinacci Federico, Vogelsberger Mark. First results from the IllustrisTNG simulations: the stellar mass content of groups and clusters of galaxies // MNRAS. III 2018b. 475, 1. 648–675.

Planck Collaboration , Ade P. A. R., Aghanim N., Arnaud M., Ashdown M., Atrio-Barandela F., Aumont J., Baccigalupi C., Balbi A., Banday A. J., al. et. Planck intermediate results. V. Pressure profiles of galaxy clusters from the Sunyaev-Zeldovich effect // A&A. II 2013. 550. A131.

Planck Collaboration , Ade P. A. R., Aghanim N., Arnaud M., Ashdown M., Aumont J., Baccigalupi C., Banday A. J., Barreiro R. B., Bartlett J. G., Bartolo N., Battaner E., Battye R., Benabed K., Benoît A., Benoit-Lévy A., Bernard J. P., Bersanelli M., Bielewicz P., Bock J. J., Bonaldi A., Bonavera L., Bond J. R., Borrill J., Bouchet F. R., Boulanger F., Bucher M., Burigana C., Butler R. C., Calabrese E., Cardoso J. F., Catalano A., Challinor A., Chamballu A., Chary R. R., Chiang H. C., Chluba J., Christensen P. R., Church S., Clements D. L., Colombi S., Colombo L. P. L., Combet C., Coulais A., Crill B. P., Curto A., Cuttaia F., Danese L., Davies R. D., Davis R. J., de Bernardis P., de Rosa A., de Zotti G., Delabrouille J., Désert F. X., Di Valentino E., Dickinson C., Diego J. M., Dolag K., Dole H., Donzelli S., Doré O., Douspis M., Ducout A., Dunkley J., Dupac X., Efstathiou G., Elsner F., Enßlin T. A., Eriksen H. K., Farhang M., Fergusson J., Finelli F., Forni O., Frailis M., Fraisse A. A., Franceschi E., Frejsel A., Galeotta S., Galli S., Ganga K., Gauthier C., Gerbino M., Ghosh T., Giard M., Giraud-Héraud Y., Giusarma E., Gjerløw E., González-Nuevo J., Górski K. M., Gratton S., Gregorio A., Gruppuso A., Gudmundsson J. E., Hamann J., Hansen F. K., Hanson D., Harrison D. L., Helou G., Henrot-Versillé S., Hernández-Monteagudo C., Herranz D., Hildebrandt S. R., Hivon E., Hobson M., Holmes W. A., Hornstrup A., Hovest W., Huang Z., Huffenberger K. M., Hurier G., Jaffe A. H., Jaffe T. R., Jones W. C., Juvela M., Keihänen E., Keskitalo R., Kisner T. S., Kneissl R., Knoche J., Knox L., Kunz M., Kurki-Suonio H., Lagache G., Lähteenmäki A., Lamarre J. M., Lasenby A., Lattanzi M., Lawrence

C. R., Leahy J. P., Leonardi R., Lesgourgues J., Levrier F., Lewis A., Liguori M., Lilje P. B., Linden-Vørnle M., López-Caniego M., Lubin P. M., Macías-Pérez J. F., Maggio G., Maino D., Mandolesi N., Mangilli A., Marchini A., Maris M., Martin P. G., Martinelli M., Martínez-González E., Masi S., Matarrese S., McGehee P., Meinhold P. R., Melchiorri A., Melin J. B., Mendes L., Mennella A., Migliaccio M., Millea M., Mitra S., Miville-Deschênes M. A., Moneti A., Montier L., Morgante G., Mortlock D., Moss A., Munshi D., Murphy J. A., Naselsky P., Nati F., Natoli P., Netterfield C. B., Nørgaard-Nielsen H. U., Noviello F., Novikov D., Novikov I., Oxborrow C. A., Paci F., Pagano L., Pajot F., Paladini R., Paoletti D., Partridge B., Pasian F., Patanchon G., Pearson T. J., Perdereau O., Perotto L., Perrotta F., Pettorino V., Piacentini F., Piat M., Pierpaoli E., Pietrobon D., Plaszczynski S., Pointecouteau E., Polenta G., Popa L., Pratt G. W., Prézeau G., Prunet S., Puget J. L., Rachen J. P., Reach W. T., Rebolo R., Reinecke M., Remazeilles M., Renault C., Renzi A., Ristorcelli I., Rocha G., Rosset C., Rossetti M., Roudier G., Rouillé d'Orfeuil B., Rowan-Robinson M., Rubiño-Martín J. A., Rusholme B., Said N., Salvatelli V., Salvati L., Sandri M., Santos D., Savelainen M., Savini G., Scott D., Seiffert M. D., Serra P., Shellard E. P. S., Spencer L. D., Spinelli M., Stolyarov V., Stompor R., Sudiwala R., Sunyaev R., Sutton D., Suur-Uski A. S., Sygnet J. F., Tauber J. A., Terenzi L., Toffolatti L., Tomasi M., Tristram M., Trombetti T., Tucci M., Tuovinen J., Türler M., Umana G., Valenziano L., Valiviita J., Van Tent F., Vielva P., Villa F., Wade L. A., Wandelt B. D., Wehus I. K., White M., White S. D. M., Wilkinson A., Yvon D., Zacchei A., Zonca A. Planck 2015 results. XIII. Cosmological parameters // A&A. IX 2016. 594. A13.

Planck Collaboration , Aghanim N., Akrami Y., Ashdown M., Aumont J., Baccigalupi C., Ballardini M., Banday A. J., Barreiro R. B., Bartolo N., Basak S., Battye R., Benabed K., Bernard J. P., Bersanelli M., Bielewicz P., Bock J. J., Bond J. R., Borrill J., Bouchet F. R., Boulanger F., Bucher M., Burigana C., Butler R. C., Calabrese E., Cardoso J. F., Carron J., Challinor A., Chiang H. C., Chluba J., Colombo L. P. L., Combet C., Contreras D., Crill B. P., Cuttaia F., de Bernardis P., de Zotti G., Delabrouille J., Delouis J. M., Di Valentino E., Diego J. M., Doré O., Douspis M., Ducout A., Dupac X., Dusini S., Efstathiou G., Elsner F., Enßlin T. A., Eriksen H. K., Fantaye Y., Farhang M., Fergusson J., Fernandez-Cobos R., Finelli F., Forastieri F., Frailis M., Fraisse A. A., Franceschi E., Frolov A., Galeotta S., Galli S., Ganga K., Génova-Santos R. T., Gerbino M., Ghosh T., González-Nuevo J., Górski K. M., Gratton S., Gruppuso A., Gudmundsson J. E., Hamann J., Handley W., Hansen F. K., Herranz D., Hildebrandt S. R., Hivon E., Huang Z., Jaffe A. H., Jones W. C., Karakci A., Keihänen E., Keskitalo R., Kiiveri K., Kim J., Kisner T. S., Knox L., Krachmalnicoff N., Kunz M., Kurki-Suonio H., Lagache G., Lamarre J. M., Lasenby A.,

Lattanzi M., Lawrence C. R., Le Jeune M., Lemos P., Lesgourgues J., Levrier F., Lewis A., Liguori M., Lilje P. B., Lilley M., Lindholm V., López-Caniego M., Lubin P. M., Ma Y. Z., Macías-Pérez J. F., Maggio G., Maino D., Mandolesi N., Mangilli A., Marcos-Caballero A., Maris M., Martin P. G., Martinelli M., Martínez-González E., Matarrese S., Mauri N., McEwen J. D., Meinhold P. R., Melchiorri A., Mennella A., Migliaccio M., Millea M., Mitra S., Miville-Deschênes M. A., Molinari D., Montier L., Morgante G., Moss A., Natoli P., Nørgaard-Nielsen H. U., Pagano L., Paoletti D., Partridge B., Patanchon G., Peiris H. V., Perrotta F., Pettorino V., Piacentini F., Polastri L., Polenta G., Puget J. L., Rachen J. P., Reinecke M., Remazeilles M., Renzi A., Rocha G., Rosset C., Roudier G., Rubiño-Martín J. A., Ruiz-Granados B., Salvati L., Sandri M., Savelainen M., Scott D., Shellard E. P. S., Sirignano C., Sirri G., Spencer L. D., Sunyaev R., Suur-Uski A. S., Tauber J. A., Tavagnacco D., Tenti M., Toffolatti L., Tomasi M., Trombetti T., Valenziano L., Valiviita J., Van Tent B., Vibert L., Vielva P., Villa F., Vittorio N., Wandelt B. D., Wehus I. K., White M., White S. D. M., Zacchei A., Zonca A. Planck 2018 results. VI. Cosmological parameters // A&A. IX 2020. 641. A6.

Planelles S., Borgani S., Dolag K., Ettori S., Fabjan D., Murante G., Tornatore L. Baryon census in hydrodynamical simulations of galaxy clusters // MNRAS. V 2013. 431, 2. 1487–1502.

Porter D. H., Jones T. W., Ryu D. Vorticity, Shocks, and Magnetic Fields in Subsonic, ICM-like Turbulence // ApJ. IX 2015. 810. 93.

Porter D. H., Woodward P. R. High-resolution simulations of compressible convection using the piecewise-parabolic method // ApJS. VII 1994. 93. 309–349.

Pratt G. W., Arnaud M., Biviano A., Eckert D., Ettori S., Nagai D., Okabe N., Reiprich T. H. The Galaxy Cluster Mass Scale and Its Impact on Cosmological Constraints from the Cluster Population // Space Sci. Rev.. II 2019. 215. 25.

Press William H., Schechter Paul. Formation of Galaxies and Clusters of Galaxies by Self-Similar Gravitational Condensation // ApJ. II 1974. 187. 425–438.

Ragagnin A., Andreon S., Puddu E. Simulation view of galaxy clusters with low X-ray surface brightness // A&A. X 2022. 666. A22.

Ragagnin Antonio, Dolag Klaus, Moscardini Lauro, Biviano Andrea, D'Onofrio Mauro. Dependency of halo concentration on mass, redshift and fossilness in Magneticum hydrodynamic simulations // MNRAS. VII 2019. 486, 3. 4001–4012.

Rasia E., Ettori S., Moscardini L., Mazzotta P., Borgani S., Dolag K., Tormen G., Cheng L. M., Diaferio A. Systematics in the X-ray cluster mass estimators // MNRAS. VII 2006. 369. 2013–2024.

Rasia Elena, Lau Erwin T., Borgani Stefano, Nagai Daisuke, Dolag Klaus, Avestruz Camille, Granato Gian Luigi, Mazzotta Pasquale, Murante Giuseppe, Nelson

Kaylea, Ragone-Figueroa Cinthia. Temperature Structure of the Intracluster Medium from Smoothed-particle Hydrodynamics and Adaptive-mesh Refinement Simulations // ApJ. VIII 2014a. 791, 2. 96.

Rasia Elena, Lau Erwin T., Borgani Stefano, Nagai Daisuke, Dolag Klaus, Avestruz Camille, Granato Gian Luigi, Mazzotta Pasquale, Murante Giuseppe, Nelson Kaylea, Ragone-Figueroa Cinthia. Temperature Structure of the Intracluster Medium from Smoothed-particle Hydrodynamics and Adaptive-mesh Refinement Simulations // ApJ. VIII 2014b. 791, 2. 96.

Rau A., Meidinger N., Nandra K., Porro M., Barret D., Santangelo A., Schmid C., Struder L., Tenzer C., Wilms J., Amoros C., Andritschke R., Aschauer F., Bahr A., Gunther B., Furmetz M., Ott B., Perinati E., Rambaud D., Reiffers J., Treis J., von Kienlin A., Weidenspointner G. The Hot and Energetic Universe: The Wide Field Imager (WFI) for Athena+ // arXiv e-prints. VIII 2013. arXiv:1308.6785.

Reiprich T. H., Veronica A., Pacaud F., Ramos-Ceja M. E., Ota N., Sanders J., Kara M., Erben T., Klein M., Erler J., Kerp J., Hoang D. N., Brüggen M., Marvil J., Rudnick L., Biffi V., Dolag K., Aschersleben J., Basu K., Brunner H., Bulbul E., Dennerl K., Eckert D., Freyberg M., Gatuzz E., Ghirardini V., Käfer F., Merloni A., Migkas K., Nandra K., Predehl P., Robrade J., Salvato M., Whelan B., Diaz-Ocampo A., Hernandez-Lang D., Zenteno A., Brown M. J. I., Collier J. D., Diego J. M., Hopkins A. M., Kapinska A., Koribalski B., Mroczkowski T., Norris R. P., O'Brien A., Vardoulaki E. The Abell 3391/95 galaxy cluster system. A 15 Mpc intergalactic medium emission filament, a warm gas bridge, infalling matter clumps, and (re-) accelerated plasma discovered by combining SRG/eROSITA data with ASKAP/EMU and DECam data // A&A. III 2021. 647. A2.

Reiprich T. H., Veronica A., Pacaud F., Ramos-Ceja M. E., Ota N., Sanders J., Kara M., Erben T., Klein M., Erler J., Kerp J., Hoang D. N., Brüggen M., Marvil J., Rudnick L., Biffi V., Dolag K., Aschersleben J., Basu K., Brunner H., Bulbul E., Dennerl K., Eckert D., Freyberg M., Gatuzz E., Ghirardini V., Käfer F., Merloni A., Migkas K., Nandra K., Predehl P., Robrade J., Salvato M., Whelan B., Diaz-Ocampo A., Hernandez-Lang D., Zenteno A., Brown M. J. I., Collier J. D., Diego J. M., Hopkins A. M., Kapinska A., Koribalski B., Mroczkowski T., Norris R. P., O'Brien A., Vardoulaki E. The Abell 3391/95 galaxy cluster system: A 15 Mpc intergalactic medium emission filament, a warm gas bridge, infalling matter clumps, and (re-) accelerated plasma discovered by combining SRG/eROSITA data with ASKAP/EMU and DECam data // arXiv e-prints. XII 2020. arXiv:2012.08491.

Ricker P. M., Dodelson S., Lamb D. Q. COSMOS: A Hybrid N-Body/Hydrodynamics Code for Cosmological Problems // ApJ. VI 2000. 536,

1. 122–143.

Robson Dylan, Davé Romeel. Redshift evolution of galaxy group X-ray properties in the SIMBA simulations // MNRAS. II 2023. 518, 4. 5826–5842.

Roediger E., Brüggen M. Ram pressure stripping of disc galaxies orbiting in clusters - I. Mass and radius of the remaining gas disc // MNRAS. X 2007. 380. 1399–1408.

Roncarelli M., Ettori S., Borgani S., Dolag K., Fabjan D., Moscardini L. Large-scale inhomogeneities of the intracluster medium: improving mass estimates using the observed azimuthal scatter // MNRAS. VII 2013. 432. 3030–3046.

Roncarelli M., Gaspari M., Ettori S., Biffi V., Brighenti F., Bulbul E., Clerc N., Cucchetti E., Pointecouteau E., Rasia E. Measuring turbulence and gas motions in galaxy clusters via synthetic Athena X-IFU observations // A&A. X 2018a. 618. A39.

Roncarelli M., Gaspari M., Ettori S., Biffi V., Brighenti F., Bulbul E., Clerc N., Cucchetti E., Pointecouteau E., Rasia E. Measuring turbulence and gas motions in galaxy clusters via synthetic Athena X-IFU observations // A&A. X 2018b. 618. A39.

Ruszkowski M., Oh S. P. Galaxy motions, turbulence and conduction in clusters of galaxies // MNRAS. VI 2011. 414. 1493–1507.

Ryu D., Kang H., Cho J., Das S. Turbulence and Magnetic Fields in the Large-Scale Structure of the Universe // Science. V 2008. 320. 909–.

Ryu D., Ostriker J. P., Kang H., Cen R. A cosmological hydrodynamic code based on the total variation diminishing scheme // ApJ. IX 1993. 414. 1–19.

Salvati Laura, Douspis Marian, Ritz Anna, Aghanim Nabila, Babul Arif. Mass bias evolution in tSZ cluster cosmology // arXiv e-prints. Jan 2019. arXiv:1901.03096.

Schaye Joop, Crain Robert A., Bower Richard G., Furlong Michelle, Schaller Matthieu, Theuns Tom, Dalla Vecchia Claudio, Frenk Carlos S., McCarthy I. G., Helly John C., Jenkins Adrian, Rosas-Guevara Y. M., White Simon D. M., Baes Maarten, Booth C. M., Camps Peter, Navarro Julio F., Qu Yan, Rahmati Alireza, Sawala Till, Thomas Peter A., Trayford James. The EAGLE project: simulating the evolution and assembly of galaxies and their environments // MNRAS. I 2015. 446, 1. 521–554.

Schaye Joop, Dalla Vecchia Claudio, Booth C. M., Wiersma Robert P. C., Theuns Tom, Haas Marcel R., Bertone Serena, Duffy Alan R., McCarthy I. G., van de Voort Freeke. The physics driving the cosmic star formation history // MNRAS. III 2010. 402, 3. 1536–1560.

Schrabback T., Applegate D., Dietrich J. P., Hoekstra H., Bocquet S., Gonzalez A. H., von der Linden A., McDonald M., Morrison C. B., Raihan S. F., Allen S. W., Bayliss M., Benson B. A., Bleem L. E., Chiu I., Desai S., Foley R. J., de

Haan T., High F. W., Hilbert S., Mantz A. B., Massey R., Mohr J., Reichardt C. L., Saro A., Simon P., Stern C., Stubbs C. W., Zenteno A. Cluster mass calibration at high redshift: HST weak lensing analysis of 13 distant galaxy clusters from the South Pole Telescope Sunyaev-Zel'dovich Survey // MNRAS. II 2018. 474. 2635–2678.

Schuecker P., Finoguenov A., Miniati F., Böhringer H., Briel U. G. Probing turbulence in the Coma galaxy cluster // A&A. XI 2004. 426. 387–397.

Shi X., Komatsu E. Analytical model for non-thermal pressure in galaxy clusters // MNRAS. VII 2014. 442. 521–532.

Shi Xun, Komatsu Eiichiro, Nagai Daisuke, Lau Erwin T. Analytical model for non-thermal pressure in galaxy clusters - III. Removing the hydrostatic mass bias // MNRAS. Jan 2016. 455, 3. 2936–2944.

Shi Xun, Komatsu Eiichiro, Nelson Kaylea, Nagai Daisuke. Analytical model for non-thermal pressure in galaxy clusters - II. Comparison with cosmological hydrodynamics simulation // MNRAS. Mar 2015. 448, 1. 1020–1029.

Simionescu A., Werner N., Mantz A., Allen S. W., Urban O. Witnessing the growth of the nearest galaxy cluster: thermodynamics of the Virgo Cluster outskirts // MNRAS. VIII 2017. 469, 2. 1476–1495.

Springel V. The cosmological simulation code GADGET-2 // MNRAS. XII 2005. 364. 1105–1134.

Springel V., Hernquist L. Cosmological smoothed particle hydrodynamics simulations: the entropy equation // MNRAS. VII 2002. 333. 649–664.

Springel Volker. E pur si muove: Galilean-invariant cosmological hydrodynamical simulations on a moving mesh // MNRAS. I 2010. 401, 2. 791–851.

Springel Volker, Di Matteo Tiziana, Hernquist Lars. Modelling feedback from stars and black holes in galaxy mergers // MNRAS. VIII 2005. 361, 3. 776–794.

Springel Volker, Pakmor Rüdiger, Pillepich Annalisa, Weinberger Rainer, Nelson Dylan, Hernquist Lars, Vogelsberger Mark, Genel Shy, Torrey Paul, Marinacci Federico, Naiman Jill. First results from the IllustrisTNG simulations: matter and galaxy clustering // MNRAS. III 2018. 475, 1. 676–698.

Springel Volker, White Simon D. M., Tormen Giuseppe, Kauffmann Guinevere. Populating a cluster of galaxies - I. Results at [formmu2]z=0 // MNRAS. XII 2001. 328, 3. 726–750.

Starobinsky A. A. Dynamics of phase transition in the new inflationary universe scenario and generation of perturbations // Physics Letters B. XI 1982. 117, 3-4. 175–178.

Steinborn Lisa K., Dolag Klaus, Comerford Julia M., Hirschmann Michaela, Remus Rhea-Silvia, Teklu Adelheid F. Origin and properties of dual and offset active

galactic nuclei in a cosmological simulation at z=2 // MNRAS. V 2016. 458, 1. 1013–1028.

Steinmetz Matthias, White Simon D. M. Two-body heating in numerical galaxy formation experiments // MNRAS. VII 1997. 288, 3. 545–550.

Stone James M., Norman Michael L. ZEUS-2D: A Radiation Magnetohydrodynamics Code for Astrophysical Flows in Two Space Dimensions. I. The Hydrodynamic Algorithms and Tests // ApJS. VI 1992. 80. 753.

Subramanian K., Shukurov A., Haugen N. E. L. Evolving turbulence and magnetic fields in galaxy clusters // MNRAS. III 2006. 366. 1437–1454.

Sugawara Yuuki, Takizawa Motokazu, Itahana Madoka, Akamatsu Hiroki, Fujita Yutaka, Ohashi Takaya, Ishisaki Yoshitaka. Suzaku observations of the outskirts of the galaxy cluster Abell 3395, including a filament toward Abell 3391 // PASJ. XII 2017. 69, 6. 93.

Sun M., Voit G. M., Donahue M., Jones C., Forman W., Vikhlinin A. Chandra Studies of the X-Ray Gas Properties of Galaxy Groups // ApJ. III 2009. 693, 2. 1142–1172.

Tanimura H., Aghanim N., Bonjean V., Malavasi N., Douspis M. Density and temperature of cosmic-web filaments on scales of tens of megaparsecs // A&A. V 2020. 637. A41.

Tanimura H., Aghanim N., Douspis M., Malavasi N. X-ray emission from cosmic web filaments in SRG/eROSITA data // A&A. XI 2022. 667. A161.

Tegmark Max, Blanton Michael R., Strauss Michael A., Hoyle Fiona, Schlegel David, Scoccimarro Roman, Vogeley Michael S., Weinberg David H., Zehavi Idit, Berlind Andreas, Budavari Tamás, Connolly Andrew, Eisenstein Daniel J., Finkbeiner Douglas, Frieman Joshua A., Gunn James E., Hamilton Andrew J. S., Hui Lam, Jain Bhuvnesh, Johnston David, Kent Stephen, Lin Huan, Nakajima Reiko, Nichol Robert C., Ostriker Jeremiah P., Pope Adrian, Scranton Ryan, Seljak Uroš, Sheth Ravi K., Stebbins Albert, Szalay Alexander S., Szapudi István, Verde Licia, Xu Yongzhong, Annis James, Bahcall Neta A., Brinkmann J., Burles Scott, Castander Francisco J., Csabai Istvan, Loveday Jon, Doi Mamoru, Fukugita Masataka, Gott III J. Richard, Hennessy Greg, Hogg David W., Ivezić Željko, Knapp Gillian R., Lamb Don Q., Lee Brian C., Lupton Robert H., McKay Timothy A., Kunszt Peter, Munn Jeffrey A., O'Connell Liam, Peoples John, Pier Jeffrey R., Richmond Michael, Rockosi Constance, Schneider Donald P., Stoughton Christopher, Tucker Douglas L., Vand en Berk Daniel E., Yanny Brian, York Donald G., SDSS Collaboration . The Three-Dimensional Power Spectrum of Galaxies from the Sloan Digital Sky Survey // ApJ. V 2004. 606, 2. 702–740.

Tormen Giuseppe. The assembly of matter in galaxy clusters // MNRAS. VI 1998. 297, 2. 648–656.

Tornatore L., Borgani S., Dolag K., Matteucci F. Chemical enrichment of galaxy clusters from hydrodynamical simulations // MNRAS. XII 2007. 382, 3. 1050–1072.

Tornatore L., Borgani S., Springel V., Matteucci F., Menci N., Murante G. Cooling and heating the intracluster medium in hydrodynamical simulations // MNRAS. VII 2003. 342. 1025–1040.

Tripp Todd M., Aracil Bastien, Bowen David V., Jenkins Edward B. The O VI Absorbers toward PG 0953+415: High-Metallicity, Cosmic-Web Gas Far from Luminous Galaxies // ApJ. VI 2006. 643, 2. L77–L82.

Truong N., Rasia E., Biffi V., Mernier F., Werner N., Gaspari M., Borgani S., Planelles S., Fabjan D., Murante G. Mass-metallicity relation from cosmological hydrodynamical simulations and X-ray observations of galaxy groups and clusters // MNRAS. IV 2019. 484, 2. 2896–2913.

Valdarnini R. A Multifiltering Study of Turbulence in a Large Sample of Simulated Galaxy Clusters // ApJ. Mar 2019a. 874, 1. 42.

Valdarnini R. A multifiltering study of turbulence in a large sample of simulated galaxy clusters // arXiv e-prints. Feb 2019b. arXiv:1902.07291.

Vallés-Pérez David, Planelles Susana, Quilis Vicent. On the accretion history of galaxy clusters: temporal and spatial distribution // MNRAS. XII 2020. 499, 2. 2303–2318.

Vallés-Pérez David, Planelles Susana, Quilis Vicent. Troubled cosmic flows: turbulence, enstrophy, and helicity from the assembly history of the intracluster medium // MNRAS. VI 2021. 504, 1. 510–527.

Vazza F., Angelinelli M., Jones T. W., Eckert D., Brüggen M., Brunetti G., Gheller C. The turbulent pressure support in galaxy clusters revisited // MNRAS. Nov 2018a. 481. L120–L124.

Vazza F., Brüggen M., Gheller C. Thermal and non-thermal traces of AGN feedback: results from cosmological AMR simulations // MNRAS. I 2013a. 428. 2366–2388.

Vazza F., Brunetti G., Brüggen M., Bonafede A. Resolved magnetic dynamo action in the simulated intracluster medium // MNRAS. II 2018b. 474, 2. 1672–1687.

Vazza F., Brunetti G., Gheller C. Shock waves in Eulerian cosmological simulations: main properties and acceleration of cosmic rays // MNRAS. V 2009. 395. 1333–1354.

Vazza F., Brunetti G., Gheller C., Brunino R., Brüggen M. Massive and refined. II. The statistical properties of turbulent motions in massive galaxy clusters with high spatial resolution // A&A. V 2011a. 529. A17+.

Vazza F., Dolag K., Ryu D., Brunetti G., Gheller C., Kang H., Pfrommer C. A comparison of cosmological codes: properties of thermal gas and shock waves in

large-scale structures // MNRAS. XII 2011b. 418, 2. 960–985.

Vazza F., Eckert D., Simionescu A., Brüggen M., Ettori S. Properties of gas clumps and gas clumping factor in the intra-cluster medium // MNRAS. II 2013b. 429, 1. 799–814.

Vazza F., Ettori S., Roncarelli M., Angelinelli M., Brüggen M., Gheller C. Detecting shocked intergalactic gas with X-ray and radio observations // arXiv e-prints. Mar 2019. arXiv:1903.04166.

Vazza F., Jones T. W., Brüggen M., Brunetti G., Gheller C., Porter D., Ryu D. Turbulence and vorticity in Galaxy clusters generated by structure formation // MNRAS. I 2017. 464. 210–230.

Vazza F., Roediger E., Brueggen M. Turbulence in the ICM from mergers, cool-core sloshing and jets: results from a new multi-scale filtering approach // ArXiv e-prints 1202.5882. II 2012.

Vogelsberger Mark, Genel Shy, Springel Volker, Torrey Paul, Sijacki Debora, Xu Dandan, Snyder Greg, Nelson Dylan, Hernquist Lars. Introducing the Illustris Project: simulating the coevolution of dark and visible matter in the Universe // MNRAS. X 2014. 444, 2. 1518–1547.

Vogt C., Enßlin T. A. A Bayesian view on Faraday rotation maps Seeing the magnetic power spectra in galaxy clusters // A&A. IV 2005. 434. 67–76.

Voit G. Mark. Tracing cosmic evolution with clusters of galaxies // Reviews of Modern Physics. IV 2005. 77, 1. 207–258.

Walker Stephen, Lau Erwin. Cluster outskirts and their connection to the cosmic web // arXiv e-prints. II 2022. arXiv:2202.07056.

Walker Stephen, Simionescu Aurora, Nagai Daisuke, Okabe Nobuhiro, Eckert Dominique, Mroczkowski Tony, Akamatsu Hiroki, Ettori Stefano, Ghirardini Vittorio. The Physics of Galaxy Cluster Outskirts // Space Sci. Rev.. I 2019. 215, 1. 7.

Weinberger Rainer, Springel Volker, Pakmor Rüdiger. The AREPO Public Code Release // ApJS. VI 2020. 248, 2. 32.

Werner N., Finoguenov A., Kaastra J. S., Simionescu A., Dietrich J. P., Vink J., Böhringer H. Detection of hot gas in the filament connecting the clusters of galaxies Abell 222 and Abell 223 // A&A. V 2008. 482, 3. L29–L33.

Wicker R., Douspis M., Salvati L., Aghanim N. Constraining the mass and redshift evolution of the hydrostatic mass bias using the gas mass fraction in galaxy clusters // arXiv e-prints. IV 2022. arXiv:2204.12823.

Wiersma Robert P. C., Schaye Joop, Theuns Tom, Dalla Vecchia Claudio, Tornatore Luca. Chemical enrichment in cosmological, smoothed particle hydrodynamics simulations // MNRAS. X 2009. 399, 2. 574–600.

Wittor D., Jones T., Vazza F., Brüggen M. Evolution of vorticity and enstrophy in the intracluster medium // MNRAS. XI 2017. 471. 3212–3225.

Young Sam, Komatsu Eiichiro, Dolag Klaus. Testing the Sunyaev-Zeldovich-based tomographic approach to the thermal history of the Universe with pressure-density cross correlations: Insights from the Magneticum simulation // Phys. Rev. D. X 2021. 104, 8. 083538.

Zandanel F., Fornasa M., Prada F., Reiprich T. H., Pacaud F., Klypin A. Multi-Dark clusters: galaxy cluster mock light-cones, eROSITA, and the cluster power spectrum // MNRAS. X 2018. 480. 987–1005.

Zhang Congyao, Churazov Eugene, Dolag Klaus, Forman William R., Zhuravleva Irina. Encounters of merger and accretion shocks in galaxy clusters and their effects on intracluster medium // MNRAS. V 2020. 494, 3. 4539–4547.

Zhuravleva I., Churazov E., Kravtsov A., Lau E. T., Nagai D., Sunyaev R. Quantifying properties of ICM inhomogeneities // MNRAS. II 2013. 428. 3274–3287.

Zhuravleva I., Churazov E., Schekochihin A. A., Allen S. W., Arévalo P., Fabian A. C., Forman W. R., Sanders J. S., Simionescu A., Sunyaev R., Vikhlinin A., Werner N. Turbulent heating in galaxy clusters brightest in X-rays // Nature. XI 2014. 515. 85–87.

Zhuravleva I. V., Churazov E. M., Sazonov S. Y., Sunyaev R. A., Dolag K. Resonant scattering in galaxy clusters for anisotropic gas motions on various spatial scales // Astronomy Letters. III 2011. 37. 141–153.

ZuHone J. A., Miller E. D., Bulbul E., Zhuravleva I. What Do the Hitomi Observations Tell Us About the Turbulent Velocities in the Perseus Cluster? Probing the Velocity Field with Mock Observations // ApJ. II 2018. 853. 180.